HitSpooling: An Improvement for the Supernova Neutrino Detection System in IceCube

Thesis submitted by

David Freiherr Heereman von Zuydtwyck

for the degree of Doctor of Science at the
Université Libre de Bruxelles

Bruxelles, June 1st 2015

ULB
UNIVERSITÉ
LIBRE
DE BRUXELLES

ICECUBE

Promoteur:
Prof. Dr. Kael D. Hanson

Supervisory Committee:
Prof. Dr. Pierre Marage (President)
Dr. Nicolas Chamel
Prof. Dr. Kael D. Hanson

Members of Jury:
Prof. Dr. Kael D. Hanson
Dr. Nicolas Chamel (President)
Dr. Gilles De Lentdecker (Secretary)
Prof. Dr. Lutz Köpke
Prof. Dr. Catherine De Clercq

To Maria & Adrian, the sources of joy, love and happiness in my life.

Abstract

The IceCube Neutrino Observatory consists of a lattice of 5160 photomultiplier tubes (PMTs) which monitor one cubic kilometer of deep Antarctic ice at the geographic South Pole. IceCube was primarily designed to detect neutrinos of energies greater than $\mathcal{O}(100\,\mathrm{GeV})$. Due to subfreezing ice temperatures, the photomultipliers' dark noise rates are particularly low which enables IceCube to search for neutrinos from galactic supernovae by detecting bursts of MeV neutrinos emitted during the core collapse and for several seconds following. For that purpose, a dedicated online supernova DAQ system records the total number of hits in the detector, without any further information from the PMTs, and generates supernova candidate triggers in case of a significant detector rate enhancement. A new feature to the standard DAQ, called HitSpooling, was implemented in IceCube during this thesis. The HitSpooling system is implemented in the standard DAQ system and buffers the complete raw data stream of the photomultipliers for several hours or days. By reading out time periods of HitSpool data around supernova candidate triggers, generated by the online supernova DAQ system, we overcome the limitations of the latter and have access to the entire information of the detector in case of a supernova. Furthermore, HitSpool data is a powerful source for studying and understanding the noise behavior of the detector as well as background processes coming from atmospheric muons. The idea of HitSpooling was developed in the scope of this thesis and is the basis of the work at hand. The developed interface between the standard DAQ and the supernova DAQ system is presented. The correlated dark noise component in optical modules of IceCube is quantified for the first time and possible explanations are discussed. The possibility of identifying triggering and subthreshold atmospheric muons in HitSpool data and subtracting them from a possible supernova signal is analyzed. Furthermore, the conversion from HitSpool data to supernova DAQ type data was developed which allows for a comparison of both data types with respect to lightcurves and significances of selected supernova candidate triggers.

Résumé

L'observatoire des neutrinos IceCube consiste en 5160 photomultiplicateurs déployés dans un kilomètre cube de glace dans les couches profondes de l'Antarctique au Pôle Sud géographique. Ce télescope d'un nouveau type a été conçu pour détecter des neutrinos d'énergies supérieures à $\mathcal{O}(100\,\text{GeV})$. Néanmoins, grâce aux températures négatives, photomultiplicateurs sont caractérisés par un taux de bruit particulièrement faible et permettent dès lors la recherche de neutrinos originaires de supernovae galactiques au travers de la détection de neutrinos d'énergies de l'ordre du MeV émis pendant l'effondrement du coeur de la supernova et plusieurs secondes après celui-ci. Dans ce cadre, une nouvelle méthode d'acquisition de données, dénommée HitSpooling a été implémentée. Par la mise en mémoire tampon du flux complet de données brutes et l'extraction des fenêtres temporelles générées autour de déclenchements obtenues grâce au supernova trigger, nous avons accès aux données les plus complètes possibles fournies par le détecteur en cas de supernova. De plus, la méthode du HitSpooling est un puissant outil pour l'étude et la compréhension du bruit au sein du détecteur autant que pour celles des processus de bruit de fond des muons atmosphériques. L'idée du HitSpooling a été développée dans le cadre de ce travail de doctorat et est la base de notre étude. L'interface ainsi développée entre le système standard d'acquisition de données et le système d'acquisition de données spécifiques au supernova est présentée dans ce document. La composante du bruit corrélé des modules optiques digitaux d'IceCube est quantifiée pour la première fois et de possibles explications sont discutées. La possibilité d'identifier des muons atmosphériques sous le seuil de détection habituelle grâce au HitSpooling et le soustraction de celui-ci à un possible signal de supernova est également analysée. Enfin, la transformation des données issues du HitSpooling en flux de données du type du système d'acquisition de données des supernovae a été développée et offre ainsi la possibilité d'une comparaison entre ces deux types de données pour courbes de luminosité et seuil de significativité de candidats sélectionnés de supernovae.

Contents

Introduction 1
Supernovae and the Birth of Neutrino Astronomy . . . 1
Thesis Overview . . . 3

I Theory 5

1 Neutrinos 7
1.1 Neutrino Properties . . . 7
1.1.1 Quantum Numbers . . . 8
1.1.2 Neutrino Families . . . 8
1.1.3 Neutrino Chirality, Helicity and Mass . . . 9
1.2 Neutrino Mixing and Oscillations . . . 10
1.2.1 Neutrino Mixing . . . 11
1.2.2 Neutrino Mass Splitting . . . 11
1.2.3 Neutrino Oscillations . . . 11
1.3 Low Energy Neutrino Interactions in Ice . . . 15
1.3.1 Inverse Beta Decay (IBD) . . . 15
1.3.2 Neutrino-Electron Scattering . . . 18
1.3.3 Interactions with Oxygen . . . 20
1.4 Neutrino Detection in Ice . . . 21
1.4.1 Energy Loss of e^+ and e^- in Ice . . . 21
1.4.2 Cherenkov Effect . . . 22

2 Supernovae 25
2.1 Stellar Evolution . . . 25
2.1.1 Star Formation . . . 25
2.1.2 Stellar Burning Stages . . . 26
2.2 Core-Collapse Supernova . . . 30
2.2.1 Prerequisites . . . 30
2.2.2 Neutrino Driven Explosion Mechanism . . . 32

2.3 Neutrino Emission . . . 36
2.3.1 Lightcurve . . . 36
2.3.2 Energy Spectrum . . . 38
2.4 Results from Modern Simulations . . . 40
2.4.1 SASI . . . 40
2.4.2 LESA . . . 43
2.5 Galactic Supernova Rate . . . 46
2.6 Lessons from SN1987A . . . 48

II Detector 51

3 The IceCube Neutrino Observatory 53
3.1 The IceCube Detector . . . 53
3.2 The Digital Optical Module . . . 55
3.2.1 Photomultiplier Tube . . . 55
3.2.2 DOM Mainboard . . . 56
3.3 Surface Data Acquisition . . . 59
3.3.1 StringHub & DOMHub . . . 59
3.3.2 Trigger System . . . 62
3.3.3 EventBuilder . . . 64
3.3.4 SecondaryBuilder . . . 64
3.3.5 Control Framework . . . 64
3.4 Basic Online Data Processing . . . 67
3.4.1 Waveform Calibration . . . 67
3.4.2 Waveform Feature Extraction . . . 67
3.4.3 Event Reconstruction . . . 68

4 Supernova Detection in IceCube 71
4.1 Supernova Data Acquisition System - SNDAQ . . . 71
4.1.1 Detection Method . . . 71
4.1.2 Real-Time Analysis Method . . . 73
4.1.3 Supernova Alert Message . . . 74
4.2 Supernova Signal in IceCube . . . 76
4.2.1 Effective Volume . . . 76
4.2.2 Neutrino Flux . . . 80
4.2.3 Signal Hit Rate . . . 80
4.2.4 SNDAQ Signal: Physics Capabilities . . . 83

4.2.5 Detection Range 86
4.3 Other Supernova Neutrino Detectors 86

5 HitSpooling - A New Data Stream in IceCube 91
5.1 The HitSpool Concept 91
5.1.1 HitSpool Raw Data Format 92
5.2 HitSpool Interface 94
5.2.1 Requirements and Solutions in the Interface 94
5.2.2 Messaging Architecture 96
5.2.3 SNDAQ HitSpool Data Requests 96
5.3 HitSpool Data Processing in IceTray 98
5.4 HitSpool Data Verification 101
5.4.1 Trigger Threshold 101

6 Backgrounds in IceCube 103
6.1 Atmospheric Muons 103
6.1.1 Cosmic Rays 103
6.1.2 Air Showers 104
6.1.3 Consequences of In-Ice Atmospheric Muons 104
6.1.4 Temperature Effects 107
6.2 DOM Noise 108
6.2.1 Prepulses and Afterpulses 108
6.2.2 Uncorrelated Noise 109
6.2.3 Correlated Noise 112
6.3 Correlated Noise Studies with HitSpool Data 112
6.3.1 Definitions 113
6.3.2 Burst Size Distribution 114
6.3.3 Burst Rate 114
6.3.4 Burst Duration 115
6.3.5 Inner Interval Distribution 116
6.3.6 Temperature Dependence 116
6.3.7 Discussion of Physical Explanations 116

III Analysis 119

7 Identification of Subthreshold Atmospheric Muons in IceCube 121
7.1 Subthreshold Atmospheric Muons in Simulation 121

7.1.1 Simulation Framework: IceSim 121
7.1.2 Atmospheric Muons in Simulation 124
7.2 Potential of Identification of Subthreshold Muons via Splitter Algorithms . . . 131
7.2.1 Overall Performance 132
7.2.2 Muons in Hit Clusters 138
7.2.3 Noise Engine Agreement 138
7.3 Application of Muon Identification to HitSpool Data 142
7.3.1 Resulting Hit Rates 142

8 HitSpooling for Supernova Detection 145
8.1 Scaler Production from HitSpool data 145
8.2 Supernova Candidate Significance 148
8.2.1 Scalers with Deadtime 148
8.2.2 Triggering Muon Correction 151
8.2.3 Subthreshold Muon Correction 151
8.3 Supernova Candidate Lightcurves 155
8.3.1 All Hits 156
8.3.2 Deadtime Application 156
8.3.3 Triggering Muon Correction 156
8.3.4 Subthreshold Muon Correction 158
8.4 Outlook 160
8.4.1 Investigation of Supernova Candidate Trigger from 2014-08-16 160

9 Conclusions and Outlook 165
9.1 Summary of Results 165
9.2 Outlook 167
9.2.1 Supernova Characteristics 167
9.2.2 Fast Radio Bursts 168
9.2.3 Dark Matter 168

IV Appendix 171

A HitSpool Data Format 173

B HitSpool Interface Operation Manual 179

Introduction

Supernovae and the Birth of Neutrino Astronomy

When John N. Bahcall[1] was asked about the importance of the detection of neutrinos from supernovae he summarized it perfectly:

> These neutrino observations are so exciting and significant that I think we're about to see the birth of an entirely new branch of astronomy: neutrino astronomy. Supernova explosions that are invisible to us because of dust clouds may occur in our galaxy as often as once every 10 years, and neutrino bursts could give us a way to study them.

This statement was made in the context of the first detection of extra-solar only weakly interacting particles, neutrinos, from a supernova in 1987 (SN1987A). In fact, the detection of 19 neutrino events in 3 different detectors provided a unique opportunity for modern theories of supernova formation to be tested against observation of this fascinating and certainly most violent phenomenon in the universe. A supernova signalizes the final phase in the life of a massive star when the nuclear fusion processes are terminated in the star's central region. Due to the gravitational attraction, the core collapses to incompressible densities on which the infalling matter is reflected and a shock wave is formed. From modern simulations we know that neutrinos play the most important role in this scenario since they carry away about 99 % of the released gravitational energy and thus are essential in the progress and the final explosion of the stellar collapse. Although SN1987A marked the beginning of neutrino astronomy three decades ago, it is needless to say that the history of supernova observations did not start only after the postulation of the neutrino by Wolfgang Pauli[2] in 1933. Optical observations of these outstanding events, whose sudden radiated luminosity can outshine the entire galaxy they are hosted in, date as far back as to the year 185 CE. Other discoveries like Brahe's supernova (SN1572)[3] and the observation of a supernova remnant by Kepler[4] (SN1604) marked milestones in astronomy. The centrality of supernova explosions in astronomical considerations was not always as obvious as it seems today. When Baade[5] and Zwicky[6] published their famous papers in 1934 and coined the term *super-nova*, according to the luminosity increase compared to the more common *novae*, they hypothesized not only the existence of neutron stars but also connected them to the origin of cosmic rays [1, 2] which can be seen as one of the most prescient conclusions in science history [3]. Although most of the quantitative results presented by Baade and Zwicky have not survived, their concepts could not have been more accurate. Today we know that supernova remnants leave neutron stars, as it was first observed in 1965 in the crab nebula [4] that is formed by the remains of a stellar

[1] John Norris Bachall ($\star$1934, †2005), American astrophysicist

[2] Wolfgang Ernst Pauli ($\star$1900, †1958), Austrian-Swiss theoretical physicist

[3] Tycho Brahe ($\star$1546, †1601), Danish nobleman and astronomer)

[4] Johannes Kepler ($\star$1571, †1630), German mathematician and astronomer

[5] Wilhelm Heinrich Walter Baade ($\star$1893, †1960), German astronomer

[6] Fritz Zwicky ($\star$1898, †1974), Swiss astronomer

explosion. Furthermore, the stellar material ejected is likely to be an origin of cosmic rays [5]. Additionally, and not less important, supernovae are essential for stellar forming regions by providing the trigger for the collapse of interstellar clouds. The maybe most prominent fact is the established assumption that the unique environment inside the star during the supernova formation is the universal source for the production of all elements heavier than iron [6]. The observation of neutrinos from supernovae is not only advantageous for the understanding of the internal processes during the stellar explosion but is also driven by another compelling argument. Unlike the obvious observation method via telescopes detecting photons, either in the optical regime or in x-rays, the detection of neutrinos does not suffer from deflection or absorption between source and observer. Since neutrinos interact primarily through the weak force, they rarely interact at all with matter. Hence interstellar magnetic fields and dust do not prevent neutrinos from traveling on straight tracks through the universe. This transforms neutrinos to perfect cosmic messengers of supernova physics in multiple ways. On the one hand, they can be used as an early warning system for an optical signal, as it was observed several hours after the neutrinos in the case of SN1987A. On the other hand, neutrinos might even be the only observation channel when photons are absorbed by interstellar material or deflected by inter stellar magnetic fields on their way. The rare interactions of neutrinos with matter are not only a benefit but also a challenge in building experiments to detect them since massive amounts of interaction material are required. In order to cope with this challenge, the IceCube Neutrino Observatory was built at the geographic South Pole where a cubic kilometer of ice was instrumented with over 5000 sensors, so-called photomultipliers (PMTs). By measuring the light emitted from charged by-product of neutrino interactions with ice molecules, IceCube is able to indirectly observe neutrinos from supernovae with unmatched high statistics. Although IceCube was primarily built with the intention, which is already successfully achieved [7,8], to detect cosmic neutrinos with energies as high as $\mathcal{O}(1\,\mathrm{PeV})$, it is also the world's largest experiment for observing supernova neutrinos of energies $\mathcal{O}(10\,\mathrm{MeV})$. Due to the optical properties of the ultra-transparent Antarctic ice, the noise hit rate of the optical sensors is extremely low. This is the key for observing low energy neutrinos in IceCube which is based on a collective noise rate enhancement originating from the burst of low energy neutrinos flushing through the detector. Supernovae are expected to happen only a few times per century in our galaxy and detecting such a rare event would provide a priceless and unique insight in its internal mechanism of which we still know so little. Since the detection method for supernova neutrinos in IceCube is based on a hit rate increase without taking other observables from the detecting PMTs into account, valuable improvements are possible in multiple ways which were the motivation for this thesis. For that purpose, a new data stream called HitSpool was developed, that buffers all raw data hits of the PMTs for several hours. By extracting HitSpool data for a time period around a significant hit rate increase, triggered by the online supernova data acquisition system, we overcome the limitations of the latter and have access to the entire information of the detector in case of a supernova. HitSpool is a powerful data source for studying and understanding not only the noise behavior of the detector but also background processes coming from atmospheric muons. The author was engaged not only in realizing the interface of HitSpool data to the supernova system but also responsible for the processing and analysis of HitSpool data with respect to noise characteristics and signals from atmospheric muons which not only contaminate a possible supernova detection but can also mimic a signal and launch triggers of the supernova system. Especially the contributions from atmospheric muons that pass the detector without being noticed by the standard trigger system are accessible in HitSpool data and are investigated with focus on the benefit for supernova neutrino analysis. An overview of the thesis is outlined in the following section.

Thesis Overview

This dissertation comprises of three parts which are outlined in the following.

Theory

The very first chapter spans the theoretical framework of neutrino physics needed to provide the necessary understanding for the detection and analysis of neutrinos in the IceCube detector. The basic properties of neutrinos in the Standard Model of Particle Physics are explained and the concepts of neutrino mixing and the resulting flavor oscillations is introduced. With an emphasis on low energy neutrino interactions in ice and the resulting charged particles this chapter covers the theoretical background of neutrino processes in ice before we demonstrates how the positrons and electrons resulting from these interactions produce the Cherenkov photons that are detected by IceCube. Chapter 2 is dedicated to the description of stellar life and death. In the first part we review the evolution of stars from their creation until their final nuclear fusion phase. At the end of its life a star has used all its nuclear power in its core and it collapses due to its mass. This is the beginning of the most energetic and brightest events in the universe: supernovae. We address the aspects of the most popular model of the gravitational core-collapse supernova mechanism in detail with an emphasis on the neutrino production before we cover the phenomenology of the lightcurve and energies of these neutrinos in detail. This is followed by an overview of result from modern simulations which can be compared to the history-making detection of supernova neutrinos more than two decades ago, in 1987, which concludes this chapter.

Detector

Chapter 3 describes the macroscopic design of the IceCube neutrino observatory before we go into the microscopic details of its hardware components. The chapter is concluded by a section about the standard data streams and data processing tools. This is covered in great detail in order to enable the reader to put the following technical aspects of the author's work in the right context. In Chapter 4 we give an overview of the supernova data acquisition system (SNDAQ). Our expectations of how a supernova signal should look like and the calculations done in order to derive these estimations are presented and an overview of supernova signals in other experiments is given. Chapter 5 introduces HitSpool which is a multi-purpose raw data buffer with the primary goal to improve the data acquisition for supernova neutrino analysis. The basic concept of the system as well as the HitSpool Interface developed for HitSpool data taking is explained. In the last section the details of HitSpool data processing for following analyses are summarized. Since a profound understanding of the background in the detector is essential for an optimal supernova neutrino detection performance, Chapter 6 gives a summary of the state-of-the-art knowledge of background sources in the detector. The first section is dedicated to atmospheric muons that are produced in air showers of cosmic rays in our atmosphere. The second section deals with the instruments' intrinsic dark noise and reviews its most important characteristics. A specific component of the dark noise, the non-thermal emission, is studied in detail from HitSpool data, presented in the final section.

Analysis

In Chapter 7, we investigate low energy atmospheric muons that pass IceCube without being noticed by the trigger system. Such subthreshold muons are of particular interest for the supernova detection since they contaminate and even mimic a possible signal. In the first section, the detector response to simulated atmospheric muons is studied using untriggered simulation data. The influence and characteristics of subthreshold muons compared to triggering muons is quantified. Simulations also help to interpret the results from techniques developed to identify these muons in experimental data which is presented in the second section. The final part of this chapter presents the results of atmospheric muon identification in HitSpool data. Finally, Chapter 8 presents the results of HitSpool data, collected by the HitSpool Interface , processed to SNDAQ type data, so-called scalers. In the development of this thesis, multiple HitSpool data sets around high significant supernova candidate triggers were collected. The additional information provided by HitSpool raw data enables us to produce scaler data in which hits caused by triggering muons can be identified as well as to some extent those hits originating from subthreshold muons. This chapter demonstrates the feasibility of producing lightcurves as well as significances for supernova candidates from HitSpool data. The processing of HitSpool data to scalers is presented in the first section and is compared to SNDAQ. The significances of the supernova candidate triggers are calculated from HitSpool data with a comparison to the corresponding results from SNDAQ in the second section. The resulting lightcurves of the various scaler types of one exemplary data set are the topic of the third section. Finally, the last section presents an outlook of possible causes for a particular data set with an outstanding high significance even after all muon corrections applied.

Part I

Theory

1

Neutrinos

This chapter spans the theoretical framework of neutrino physics needed to provide the necessary understanding of detection and analysis of neutrinos in the ICECUBE *detector. The basic properties of neutrinos in the Standard Model of Particle Physics are explained in section 1.1 while section 1.2 highlights the concepts of neutrino mixing and the resulting flavor oscillations. With an emphasis on low energy neutrino interactions in ice and the resulting charged particles, section 1.3 covers the theoretical background of a neutrino process in ice before 1.4 demonstrates how the positrons and electrons resulting from these interactions produce the Cherenkov photons that are detected by* ICECUBE*.*

1.1 Neutrino Properties

Neutrinos are part of the Standard Model[1] that describes the interactions of elementary particles, the fermions. Processes between particles are mediated by vector bosons which correspond to the generators of the local symmetry groups $SU(3) \otimes SU(2) \otimes U(1)$, the basis of the Standard Model. The $SU(3)$ group represents the strong force with eight generators, the *gluons*, responsible for exchanging *color*, the conserved quantity in the field theory of quantum chromodynamics. Electroweak interactions are given by the gauge theory of the groups $SU(2) \otimes U(1)$, with the former representing the weak force that conserves the *weak isospin*, whereas the electromagnetic force has characteristics of the latter and conserves *weak hypercharge*, a linear combination of the electric charge with the third component of the weak isospin. In this theory, the mediators are two charged $W^{\pm}$ and two neutral states, Z^0 and γ. The neutral bosons arise from linear combinations of the neutral representation of the W of the weak interactions and A of quantum electrodynamics with the weak mixing angle θ_W describing the intensity of mixing between them. With the help of the so-called *Brout-Englert-Higgs* scalar field, a mechanism is introduced that provides mass to the Z^0 , W^+ and W^- whereas the neutral photon γ is left massless. Neutrinos are only under the influence of the electroweak force. The following lays out the basic characteristic of these interesting

---

[1] For more details on the Standard Model of Particle Physics, the reader might be directed to the established textbooks, for example [9, 10], in general or to modern reviews of Neutrino Physics in particular, as given for example in [11–13] on which the aspects covered here are mostly based.

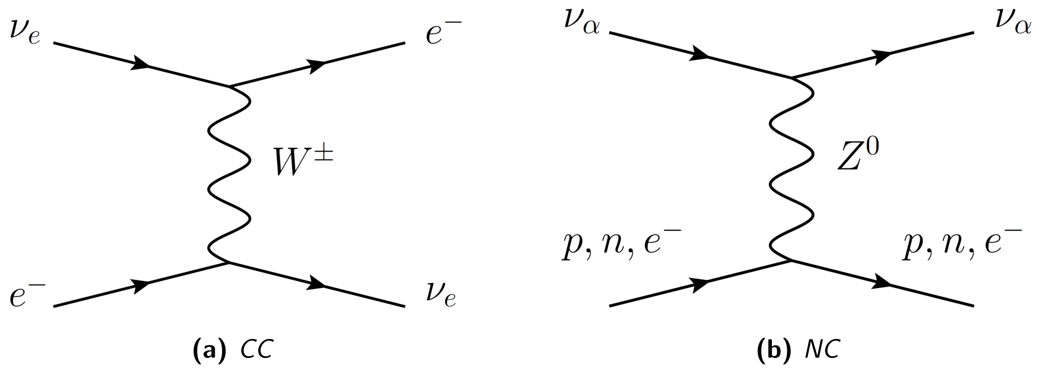

(a) *CC* **(b)** *NC*

Figure 1.1: *Feynman diagrams for charged current (CC, left) and neutral current (NC, right) neutrino interactions [14].*

particles.

1.1.1 Quantum Numbers

The neutrino is a spin $\frac{1}{2}$ fermion that does not carry any electric charge nor magnetic moment and thus interacts only via the weak force. Neutrinos appear in three flavor states ν_e, ν_μ and ν_τ, matching the flavor of the charged lepton it couples to in a weak interaction via the exchange of a $W^\pm$, also called charged-current interactions (CC). In neutral-current interactions (NC), i.e. a process involving the exchange of a Z^0 boson, the flavor of the neutrino is not predictable. Figure 1.1 shows the Feynman diagrams for both processes.

A preserved quantity in weak processes is the *weak isospin*, or more precisely its third component, I_3, which is related to the weak hypercharge mentioned before. Left-handed leptons, see Section 1.1.3, can be grouped in doublets:

$$\begin{pmatrix}\nu_e\\ e\end{pmatrix}\begin{pmatrix}\nu_\mu\\ \mu\end{pmatrix}\begin{pmatrix}\nu_\tau\\ \tau\end{pmatrix} \tag{1.1}$$

where the charge leptons (e, μ, τ) with $I_3 = -1/2$ always transform into their duplet partners (ν_e, ν_μ, ν_τ) of weak isopsin $I_3 = +1/2$ and vice-versa.

1.1.2 Neutrino Families

The above mentioned neutral weak interaction channel enables one to measure the number of neutrino families in an indirect way. The Z^0 can decay hadronically with a decay width Γ_h and letponically with a decay width Γ_l for charged leptons and Γ_ν for neutral ones, respectively. Since the decay width represents the summed probability of the final particles to be produced, additional lepton families enhance the changes of observing them. Although neutrinos leave a particle-detector without a trace, this "invisible" Z-decay width $\Gamma_{inv} = N_\nu \Gamma_\nu$ gives a handle on the number of neutrino families N_ν. Exploiting the fact that the ratio Γ_{inv}/Γ_l can be determined with higher precision than Γ_{inv} alone, the number of neutrino families can be derived:

$$\frac{\Gamma_{inv}}{\Gamma_l} = N_\nu \left(\frac{\Gamma_\nu}{\Gamma_l}\right)_{\mathrm{SM}} \quad , \tag{1.2}$$

where $\left(\frac{\Gamma_\nu}{\Gamma_l}\right)_{\mathrm{SM}}$ is derived from Standard Model predictions. The left side of equation 1.2 can be expressed in terms of the total hadronic cross-section depending only on measurable decay widths and the mass of the Z^0 [15]. This high precision measurement was performed at the Large Electron Positron collider (LEP) with the result shown in figure 1.2. The best fit to the combined data of more than 17 million produced Z^0 events results in $N_\nu = 2.9840 \pm 0.0082$ in agreement with the observed three lepton families.

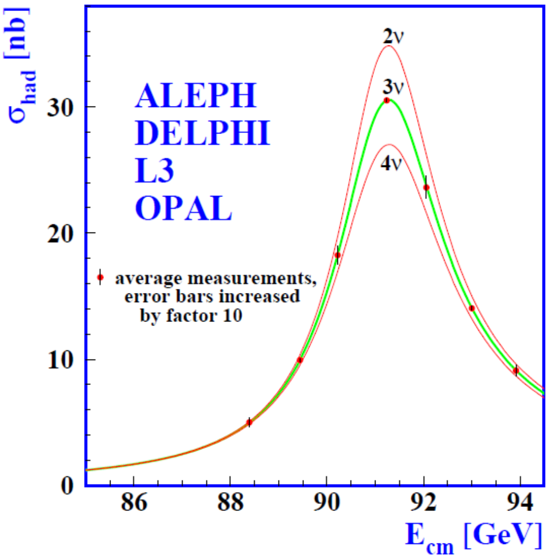

Figure 1.2: *Combined measurement of the hadronic production cross section around Z^0 mass as obtained by the LEP experiments OPAL, DELPHI, L3 and ALEPH. The data is best fit by the prediction arising from three (light) neutrino species [15].*

1.1.3 Neutrino Chirality, Helicity and Mass

At the time the Standard Model was proposed, experimental results indicated that neutrinos are massless. The reason for that lies in the helicity h of the particles which is defined as the projection of the spin $\vec{s}$ onto its momentum $\vec{p}$:

$$h = \frac{\vec{s} \cdot \vec{p}}{|\vec{s} \cdot \vec{p}|} \quad , \tag{1.3}$$

which is a variable quantity for massive particles depending on both the particles' speed and the observer's velocity. If the particle is massless and hence travels with the speed of light, the helicity is conserved and equal to the chirality of the particle. The helicity of the neutrino was firstly measured by Goldhaber *et al* [16] in an experiment where electron capture in an unpolarized $^{152}\mathrm{Eu}$ nucleus results in the emission of a photon and a neutrino. A back-to-back emission of the photon and the neutrino gives the angular momentum of the initial state by the sum of the spin of the neutrino and the polarization of the photon. Since the initial angular momentum is given by the spin of the electron, $\pm\frac{1}{2}$, and the polarization of the photon was measured to take only particular values, the helicity of the neutrino was determined to be $-\frac{1}{2}$ or left-handed and $+\frac{1}{2}$ or right-handed for anti-neutrinos, respectively. A massive particle needs two chiral components to be fully described. The results from the above mentioned experiment show that in nature only neutrinos with single chiral components are observed, i.e.

left-handed neutrinos and right-handed anti-neutrinos. This reveals the possibility of neutrinos being massless. The postulation of massless neutrinos in the Standard Model is consistent with results from experiments that try to measure the neutrino mass directly of which none was successful until today. The best limits on the neutrino mass come from experiments measuring the tail of the energy spectrum of the emitted electron of a tritium $\beta-$decay:

$$^{3}\mathrm{H} \longrightarrow \mathrm{He}^{3} + e^{-} + \overline{\nu}_{e} \qquad . \tag{1.4}$$

The most precise results for the neutrino mass in this process are $m_{\overline{\nu}_e} = 2.1\,\mathrm{eV}$ [17] and $m_{\overline{\nu}_e} = 2.2\,\mathrm{eV}$ [18], respectively. A new experiment named KATRIN, currently under construction, aims for a sub-eV sensitivity [19] in search for the absolute neutrino mass scale.

The efforts made in order to identify a finite nonzero neutrino mass are strongly supported by results from experiments that observed the appearance or disappearance of a certain neutrino flavor. Due to nonzero neutrino masses and neutrino mixing, the existence of neutrino oscillations [20], explained in section 1.2, is expected and confirmed by results from solar neutrinos measurements [21–24], atmospheric neutrinos [25, 26], neutrinos from accelerators [27, 28] and reactor based experiments [29, 30]. This hypothesis is also supported by cosmological observations [31, 32] that are in favor of a nonzero sum of the three neutrino mass states:

$$\sum m_{\nu} < 0.23\,\mathrm{eV} \qquad .$$

The fact that neutrinos have a finite mass is the only discovery made so far beyond the Standard Model.

Since the neutrino is electrically neutral, there are two possibilities provided by the Standard Model in order to give mass to neutrinos. Neutrinos may be *Dirac* type [33], in which case they behave like other standard model fermions. Speaking in terms of quantum field theory, a Dirac mass term in the Schroedinger Lagrangian describes the coupling between left- and right-handed chiral neutrino states. Therefore, a Dirac neutrino must have a (yet undiscovered) right-handed component in order to generate mass. The other possibility for neutral fermions to gain mass is given by the *Majorana* approach [34]. In this case, the right-handed state is identified with the antiparticle of the left-handed state which is obviously only possible for neutral particles and would violate the empirical law of lepton number conservation. Based on the current status of experimental evidence, it is impossible to judge whether massive neutrinos are Dirac or Majorana type fermions.

1.2 Neutrino Mixing and Oscillations

Neutrinos emitted in a supernova explosion are under the influence of oscillations. The probability of detecting a certain neutrino flavor changes periodically during its path from the source to the observer. This so-called neutrino oscillations effect plays an important role in the efforts of detecting and understanding potential supernova neutrino signals on earth. The first requirement for oscillations are finite non-zero and non-equal masses for the particles in question, as discussed in the previous section. Another condition is given when the interaction eigenstates of a particles do not correspond to one specific mass eigenstate but are rather a mixture of multiple mass eigenstates. As we saw in section 1.1, mixing is possible in weak interactions of the Standard Model and described by a mixing angle. Since neutrinos are only interacting weakly, mixing of neutrino mass eigenstates and oscillations of flavor eigenstates are the consequence.

1.2.1 Neutrino Mixing

The flavor eigenstates of neutrinos, ν_α, are defined by the flavor of the charged lepton $\alpha = e, \mu, \tau$ they couple to in weak interactions. Due to the fact that neutrinos are only indirectly detectable, the flavor eigenstate does not necessarily represent a well-defined mass of the particle as opposed to charged leptons [9, 35]. As a matter of fact, an observable flavor eigenstate ν_α can be expressed as being a superposition of mass eigenstates ν_i, with $i = 1, 2, 3$:

$$\nu_\alpha = \sum_{i=1,2,3} U^*_{\alpha i} \nu_i \qquad , \tag{1.5}$$

where $U^*_{\alpha i}$ are elements of the unitary *PMNS*[2] matrix U [36, 37]:

$$U = \begin{pmatrix} 1 & 0 & 0 \\ 0 & c_{23} & s_{23} \\ 0 & -s_{23} & c_{23} \end{pmatrix} \begin{pmatrix} c_{13} & 0 & e^{-i\delta} s_{13} \\ 0 & 1 & 0 \\ -e^{i\delta} s_{13} & 0 & c_{13} \end{pmatrix} \begin{pmatrix} c_{12} & s_{12} & 0 \\ -s_{12} & c_{12} & 0 \\ 0 & 0 & 1 \end{pmatrix} \begin{pmatrix} e^{i\rho_1} & 0 & 0 \\ 0 & e^{i\rho_2} & 0 \\ 0 & 0 & 1 \end{pmatrix} \tag{1.6}$$

The elements c an s in the matrix represent the cosine and sine functions with their arguments being three mixing angles between the two mass eigenstates indicated in the subscript. Experimental derived values of these parameters are shown in table 1.1. One complex phase is present (δ) in the Dirac case while two more appear (ρ_1 and ρ_2) if the neutrino is of Majorana type.

1.2.2 Neutrino Mass Splitting

Neutrino mixing and oscillations are only partly determined by the above mentioned mixing angles. The squared mass differences of the mass eigenstates are needed for a full description of the picture. Due to the unknown sign of Δm^2_{32}, two independent mass squared differences or *mass splittings* are possible, as shown in figure 1.3.

This is known as the *neutrino mass hierarchy problem* with the normal mass order ($m_1 < m_2 < m_3$) and the inverted hierarchy ($m_3 < m_1 < m_2$) being equally possible. The best fit values for the squared mass differences are shown in figure 1.3 and table 1.1.

1.2.3 Neutrino Oscillations

The dependence of neutrino flavor oscillations on the mixing angles and squared mass differences of the massive eigenstates is reflected best in the transition probability $P_{\nu_\alpha \to \nu_\beta}(L)$, i.e. the probability for an initial neutrino of flavor α to be found in flavor state β after a given distance L. In vacuum this is given by[3]:

$$P_{\nu_\alpha \to \nu_\beta}(L) = \sum_{kj} U^*_{\alpha k} U_{\beta k} U_{\alpha j} U^*_{\beta j} e^{-i \frac{\Delta m_{\mathrm{kj}2}}{2E} L} \qquad , \tag{1.7}$$

---

[2] An acronym that stands for the founders of the idea of neutrino oscillations: Pontecorvo, Maki, Nakagawa and Sakata.

[3] The interested reader might refer to [9] for the calculations for deriving the oscillations probabilities.

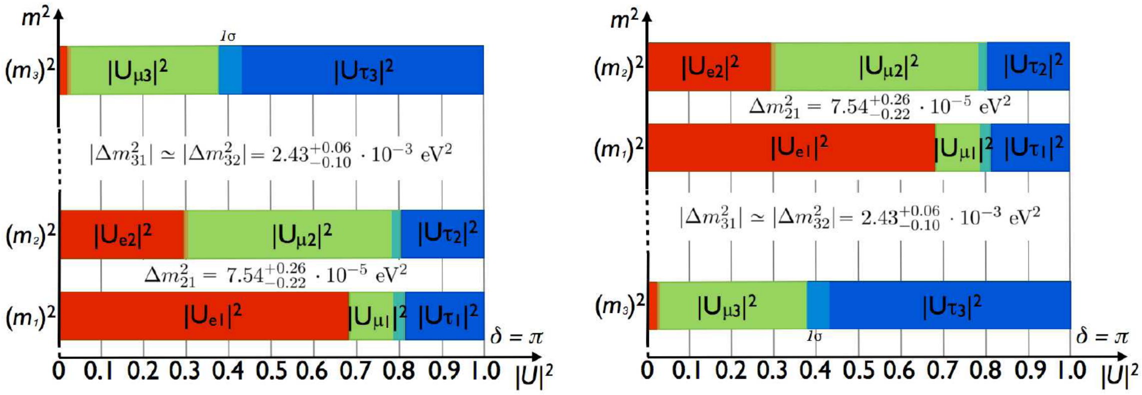
m^2
$(m_3)^2$
1σ
$|U_{\mu 3}|^2$
$|U_{\tau 3}|^2$
$|\Delta m^2_{31}| \simeq |\Delta m^2_{32}| = 2.43^{+0.06}_{-0.10} \cdot 10^{-3}$ eV^2
$(m_2)^2$
$|U_{e2}|^2$
$|U_{\mu 2}|^2$
$|U_{\tau 2}|^2$
$\Delta m^2_{21} = 7.54^{+0.26}_{-0.22} \cdot 10^{-5}$ eV^2
$(m_1)^2$
$|U_{e1}|^2$
$|U_{\mu 1}|^2$
$|U_{\tau 1}|^2$
$\delta = \pi$
0 0.1 0.2 0.3 0.4 0.5 0.6 0.7 0.8 0.9 1.0
$|U|^2$

(a) *Normal hierarchy* **(b)** *Inverted hierarchy*

Figure 1.3: *Illustration of the configurations of neutrino mass splitting in the case of normal mass hierarchy and inverted mass hierarchy [14].*

Table 1.1: *Best fit values (assuming a normal mass hierarchy) with 3σ band for neutrino oscillation parameters resulting from a global analysis of data from multiple experiments [14, 38, 39].*

Parameter	Best Fit Value
$sin^2\theta_{12}$	$0.307^{+0.018}_{-0.016}$
Δm^2_{21}	$7.45^{+0.26}_{-0.22} \cdot 10^{-5}\mathrm{eV}^2$
$sin^2\theta_{23}$	$0.386^{+0.034}_{-0.021}$
$\|\Delta m^2_{31}\| \simeq \|\Delta m^2_{32}\|$	$2.43^{+0.06}_{-0.10} \cdot 10^{-3}\mathrm{eV}^2$
$sin^2\theta_{13}$	0.0241 ± 0.0025
δ	?

with $\Delta m^2_{\mathrm{kj}} = m^2_{\mathrm{k}} - m^2_{\mathrm{j}}$ and E being the initial neutrino's energy. A more descriptive representation can be achieved when considering the two-neutrino case, which is absolutely sufficient in order to demonstrate neutrino oscillations. The PMNS matrix reduces to 2×2 dimensions with only one mixing angle and one effective mass squared difference:

$$P^{2\nu}_{\nu_\alpha \to \nu_\beta}(L, E) = \sin^2(2\theta)\sin^2\left(\frac{\Delta m^2}{4E} L\right) \tag{1.8}$$

In the quest of detecting neutrinos from supernovae, two complex media are involved: the exploding star that produces the neutrinos and the Earth that the neutrinos might cross before being detected by any ground based experiment. For neutrino oscillations in matter, several new aspects have to be considered. In general, neutrinos are coherently forward scattered off of the electrons, protons and neutrons in matter due to an effective potential [9, 35, 40]

$$V_{\mathrm{eff}} = \begin{cases} \sqrt{2}G_{\mathrm{F}}n_e & \text{if} \quad \nu = \nu_e \\ -\sqrt{2}G_{\mathrm{F}}n_e & \text{if} \quad \nu = \overline{\nu}_e \end{cases} , \tag{1.9}$$

where G_F is the Fermi-constant and $n_e = n_b \Upsilon_e$ is the electron density defined by the baryon number n_b and the number of leptons per baryon Υ_e. Since in matter there are not enough abundant muons and tauons to provide a contribution to form a significant potential for the other neutrino generations, it is sufficient to only consider the dominant effective potential for electron neutrinos and to remain in the two generation mixing scenario. The interaction potential is different for each neutrino type and results in a new mixing angle and mass squared difference compared to the scenario in vacuum. Therefore, a neutrino flavor transition can become maximal in matter where the effective mixing might be small in vacuum. This is known as the *Mikheev-Smirnov-Wolfenstein* or MSW effect [41].

If one assumed a constant electron density n_e along the trajectory of the neutrino, as it can be done for neutrinos crossing the Earth's mantel [42, 43], the two-neutrino flavor transition probability in matter is given by:

$$P^{2\nu\mathrm{matter}}_{\nu_\alpha \to \nu_\beta} = \sin^2(2\theta_M)\sin^2\left(\frac{\Delta m^2_M}{4E}L\right) \qquad , \tag{1.10}$$

in analogy to the case in vacuum but with the effective oscillation parameters for matter Δm^2_M and θ_M. While the assumption of a constant electron density might be sufficient for the Earth matter effect, this does not hold true for neutrinos produced in stars where a non-zero density gradient is present. The stellar matter oscillation effect leads to a transition probability inside the dense object of the form [35]:

$$P_{\nu_e \to \nu_\mu} = \frac{1}{2} - \frac{1}{2}\cos(2\theta_c)\cos(2\theta_M) + P_{\nu_1 \to \nu_2}\cos(2\theta_c)\cos(2\theta_M) \tag{1.11}$$

where θ_c stands for the mixing angle for neutrinos produced at the center of the star and θ_M is the effective mixing angle as mentioned before. The additional $P_{\nu 1 \to \nu 2}$ -term reflects the fact that even mass eigenstates mix in the case of a non-homogeneous density profile.

At the boundary between matter and vacuum, e.g. at the surface of the star, the electron density goes to zero while $\theta_M \to \theta$ and $\Delta m^2_M \to \Delta m^2$. Thus from equation 1.11 it can be deduced that neutrinos leave massive objects in mass eigenstates and are not affected by oscillations any further when traveling through vacuum [35, 44].

With this very simplified picture of neutrino oscillations at production (equation 1.11) and detection site (equation 1.10), and additional considerations that are about to follow, one can derive the initial neutrino flux modified due to neutrino oscillations. The picture drawn here follows the work of [45] considering a three-generation neutrino mixing scenario. Without going into the details of supernova neutrino evolution at the moment, this is covered in chapter 2 extensively, the central region of the star is assumed to be the neutrino production zone. This is the region of highest densities ($\rho > 10 \times 10^5\,\mathrm{g\,cm^{-3}}$), all mixing of neutrinos is highly suppressed and almost unambiguous assignment between flavor and mass eigenstates is present:

$$\begin{array}{llll} \nu_e = \nu_3 & \nu_\mu = \nu_1 & \nu_\tau = \nu_2 & \mathrm{NH} \\ \overline{\nu}_e = \nu_1 & \overline{\nu}_\mu = \nu_2 & \overline{\nu}_\tau = \nu_3 & \mathrm{NH} \\ \nu_e = \nu_2 & \nu_\mu = \nu_1 & \nu_\tau = \nu_3 & \mathrm{IH} \\ \overline{\nu}_e = \nu_3 & \overline{\nu}_\mu = \nu_2 & \overline{\nu}_\tau = \nu_1 & \mathrm{IH} \end{array} \tag{1.12}$$

with different mapping for normal (NH) and inverted hierarchy (IH). The initial neutrino fluxes $\Phi^0_{\nu_\alpha}$ $(\alpha = e, \mu, \tau)$ emitted from this central region below the so-called *neutrino-sphere* (see Section 2.2.2) coincide with the fluxes of the corresponding mass eigenstates Φ^0_k with $k = 1, 2, 3$ as indicated in equation 1.12.

In regions of greater radii of the collapsing star, the densities are lower, neutrinos do start to mix and are subject to two MSW-resonances, i.e. maxima in the transition probability[4], when diffusing through the surface which modifies the above solution to the fluxes. The MSW effect predicts resonances at high densities $\rho_H \approx 10^3 - 10^4\,\mathrm{g\,cm^{-3}}$ and low densities, $\rho_L \approx 10^1 - 10^2\,\mathrm{g\,cm^{-3}}$, which can be treated as being spatially separated. While in the low density region the probability for flavor transition tends to zero due to the given values of the mixing angles and mass squared differences, the high density, or *H-resonance*, contributes a flavor transition probability $0 < P_H < 1$ and a modified mapping compared to equation 1.12.

The neutrino fluxes at the surface of the collapsing star, and thus the fluxes expected at the Earth, can be summarized [45] as:

$$\begin{pmatrix} \Phi_{\nu_e} \\ \Phi_{\overline{\nu}_e} \\ 4\Phi_{\nu_x} \end{pmatrix} = \begin{pmatrix} p & 0 & 1-p \\ 0 & \overline{p} & 1-\overline{p} \\ 1-p & 1-\overline{p} & 2+p+\overline{p} \end{pmatrix} \begin{pmatrix} \Phi^0_{\nu_e} \\ \Phi^0_{\overline{\nu}_e} \\ \Phi^0_{\nu_x} \end{pmatrix} \quad , \tag{1.13}$$

with ν_x representing ν_μ, ν_τ and the corresponding anti-particles, respectively. The survival probabilities, i.e. the probability to find the neutrino in the same flavor, for neutrinos are given by p and for anti-neutrinos by $\overline{p}$:

$$\begin{array}{lll} p = |U_{e3}|^2 & \overline{p} = \cos^2(\theta_{12}) & \mathrm{NH} \\ p = \cos^2(\theta_{12}) & \overline{p} = |U_{e3}|^2 & \mathrm{IH} \end{array} \quad , \tag{1.14}$$

with the parameters from equation 1.6.

Using this parametrization one can write the neutrino fluxes at the detector Φ^Dafter taking possible flavor oscillation inside the Earth's mantel into account:

$$\begin{pmatrix} \Phi^D_{\nu_e} \\ \Phi^D_{\overline{\nu}_e} \\ 4\Phi^D_{\nu_x} \end{pmatrix} = \begin{pmatrix} p^D & 0 & 1-p^D \\ 0 & \overline{p}^D & 1-\overline{p}^D \\ 1-p^D & 1-\overline{p}^D & 2+p^D+\overline{p}^D \end{pmatrix} \begin{pmatrix} \Phi^0_{\nu_e} \\ \Phi^0_{\overline{\nu}_e} \\ \Phi^0_{\nu_x} \end{pmatrix} \quad , \tag{1.15}$$

where p^D and $\overline{p}^D$ representing now the survival probabilities from both stellar matter and Earth matter effect (considering only neutrinos traveling through the Earth mantel) [35, 43]:

$$\begin{aligned} p^D &\simeq P_H \left[\sin^2\theta + \frac{\epsilon \sin^2(2\theta)}{(\epsilon - \cos(2\theta))^2 + \sin^2(2\theta)} sin^2\left(\frac{\pi z}{L_M}\right)\right] \begin{cases} 0 < P_H < 1(\mathrm{NH}) \\ P_H = 1(\mathrm{IH}) \end{cases} \\ \overline{p}^D &\simeq \overline{P}_H \left[\sin^2\theta + \frac{\epsilon \sin^2(2\theta)}{(\epsilon - \cos(2\theta))^2 + \sin^2(2\theta)} sin^2\left(\frac{\pi z}{L_M}\right)\right] \begin{cases} \overline{P}_H = 1(\mathrm{NH}) \\ 0 < \overline{P}_H < 1(\mathrm{IH}) \end{cases} \end{aligned} \tag{1.16}$$

The effects of oscillation in the Earth described by Δm^2_M are contained in

$$\begin{aligned} \epsilon &= \frac{2EV_{\mathrm{eff}}}{\Delta m^2_M} \\ L_M &= \frac{4\pi E}{\Delta m^2_M} \quad , \end{aligned} \tag{1.17}$$

---

[4] which still can be negligibly small

where E is the energy of the neutrino, V_{eff} the effective potential from equation 1.9 and L_M stands for the distance traveled by the neutrinos inside the Earth. Stellar matter effects are accounted for in P_H and $\overline{P}_H$, respectively while neutrino transport in vacuum is described by the mixing angle θ. All oscillation effects described here are summarized in the above modified initial neutrino flux of equation 1.15 and have to be taken into account when estimating any signal coming from supernova neutrinos in a detector like IceCube , which is covered in chapter 4. It was just recently found by the authors of [46] that, besides the demonstrated standard oscillation scenarios, non-linear effects caused by neutrino-neutrino interactions lead to a collective flavor transformation near the supernova core. This arises from neutrinos interacting not only with the background matter but also with the present gas of neutrinos and anti-neutrinos in the collapsing star. While it is believed that these *collective oscillation effects* play a major role in the case of an inverted mass hierarchy, and even precede the ordinary matter effects, they basically vanish in the normal mass hierarchy case [47]. More details on that can be found in [48–51] and references therein.

1.3 Low Energy Neutrino Interactions in Ice

As we will see in chapter 2, core-collapse supernovae emit neutrinos of energies of $\mathcal{O}(10\,\text{MeV})$. This section is dedicated to explain the necessary details of neutrino interaction in the medium that IceCube uses to detect them.

1.3.1 Inverse Beta Decay (IBD)

Inverse β-decay of anti electron neutrinos on free protons of hydrogen nuclei:

$$\overline{\nu}_e + p \longrightarrow n + e^+ \tag{1.18}$$

is the main interaction channel for supernova neutrinos in ice with a contribution of $\sim 93\%$ of the total interaction rate depending on the underlying oscillation scenario. This process dominates the cross-sections of neutrinos in ice up to an energy of $\sim$ 60 MeV, see figure 1.6. In principle, this reaction would be possible also for other neutrino flavors and heavier leptons in the final state. Since the energy regime of supernova neutrinos, $E_\nu \sim \text{MeV}$, does not reach the mass limit of the muon or tau lepton, only IBD with positrons and electrons in the final state is considered here.

The energy threshold E_ν^{min} above which this process is possible is given by the masses of the involved particles:

$$E_\nu^{\text{min}}(\overline{\nu}_e + p \longrightarrow n + e^+) > m_e + m_n - m_p = m_e + \Delta m_{np} \approx 1.806\,\text{MeV} \quad , \tag{1.19}$$

with $\Delta m_{np} \approx 1.293$ MeV being the abbreviated nucleon mass difference. In order to derive the detector response of IceCube , which will be covered in chapter 4.2, one needs to calculate the total and differential cross-sections. The derivations below follow closely the explanations given in [52]. The differential cross-section can be written as:

$$\frac{d\sigma}{dt}(E_\nu, E_e) = \frac{G_{\text{F}}^2 \cos^2\theta_C}{2\pi} \frac{1}{(s - m_p^2)^2} |\mathcal{M}^2| \quad , \tag{1.20}$$

with G_{F} being the Fermi-coupling constant for weak interactions and $\cos\theta_C = 0.97425$ [37] the cosine of the *Cabbibo*-angle, expressing the probability of an up-type valence quark of the proton to change into a down-type quark forming a neutron in the final state. The energy dependence is hidden in the *Mandelstam*-variables expressing the four momenta $p = (E, \overrightarrow{p})$ conservation in scattering processes:

$$s = (p_{\overline{\nu}_e} - p_{e^+})^2 = (p_p - p_n)^2 \tag{1.21a}$$

$$t = (p_{\overline{\nu}_e} - p_p)^2 = (p_{e^+} + p_n)^2 \tag{1.21b}$$

$$u = (p_{\overline{\nu}_e} - p_n)^2 = (p_p - p_{e^+})^2 \quad . \tag{1.21c}$$

Equation 1.21a is mentioned explicitly in 1.20 and all three are contained in the scattering matrix $\mathcal{M}$ which can be approximated by:

$$\begin{aligned} |\mathcal{M}^2| \simeq \; & \mathrm{M}^2(f_1^2 - g_1^2)(t - m_e^2) - \\ & \mathrm{M}^2 \Delta m_{np}(f_1^2 + f_g^2) - \\ & 2m^2 \Delta m_{np} \mathrm{M} g_1 (f_1 - f_2) - \\ & (s-u) t g_1 (f_1 + f_2) + \\ & \frac{1}{4}(s-u)^2 (f_1^2 + g_1^2) \end{aligned} \tag{1.22}$$

with the dimensional and constant form-factors $f_1 \simeq 1.778$, $f_2 \simeq 6.588$ and $g_1 \simeq -1.270$ and $\mathrm{M} = (m_n + m_p)/2$ the average nucleon mass.

The differential cross-section of equation 1.20 can be expressed with the desired positron and neutrino energy dependence if one uses the proton's rest frame and rewrites the Mandelstam variables:

$$\begin{aligned} s &= 2m_p - E_\nu + m_p^2 \\ u &= s - 2m_p(E_\nu + E_e) + m_e^2 \\ t &= m_n^2 - m_p^2 - 2m_p(E_\nu - E_e) \\ . \end{aligned} \tag{1.23}$$

Using these expressions in equation 1.22 and substituting the corresponding factors in equation 1.20 results in:

$$\frac{d\sigma}{dE_e}\left(\frac{E_\nu}{E_e}\right) = 2m_p \frac{d\sigma}{dt}(E_\nu, E_e) \quad , \tag{1.24}$$

if $E_\nu \geq E_\nu^{min}$. Integrating over the energy range of the positron reveals the total cross-section:

$$\sigma(E_\nu) = \int_{E_{min}}^{E_{max}} dE_e \frac{d\sigma}{dE_e}(e_\nu, E_e) \quad . \tag{1.25}$$

The positron energy E_e can now be described in terms of the neutrino energy and the scattering angle θ_s [52]:

$$E_e = \frac{1}{\kappa}\left[(E_\nu - \delta)(\epsilon + 1) + \cos\theta_s \sqrt{(E_\nu - \delta)^2 - m_e^2 \cdot \kappa}\right] \tag{1.26}$$

where

$$\delta \equiv \frac{m_n^2 - m_p^2 - m_e^2}{2m_p} \quad , \quad \epsilon = \frac{E_\nu}{m_p} \quad , \quad \kappa = (1+\epsilon)^2 - (\epsilon \cos\theta_{scat})^2 \quad .$$

Since the positron energy spectrum is not discrete but follows a continuous distribution due to nucleon recoil effects of the participating nucleon, it is natural to compute the average positron energy which can be approximated with an accuracy better than 1% for energies below 100 MeV to be

$$\langle E_e \rangle \approx (E_\nu - \delta)\left(\frac{E_\nu}{E_\nu + m_p} - 1\right) \quad . \tag{1.27}$$

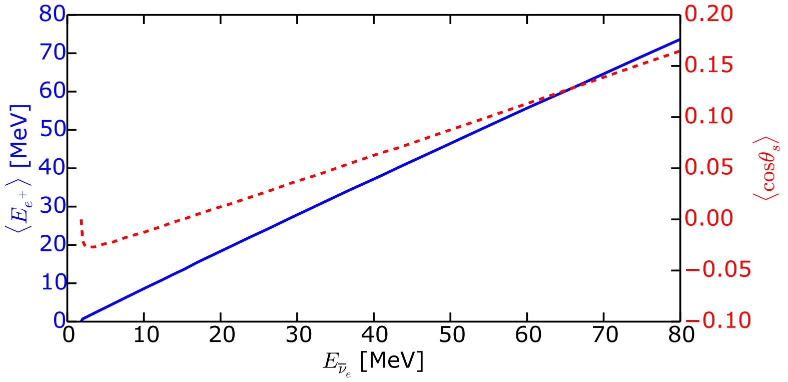

Figure 1.4: *Average energy* $\langle E_{e^+} \rangle$ *(blue and left axis) and cosine of the scattering angle* $\langle \cos\theta_s \rangle$ *(red and right axis) for the resulting positron in the inverse* β *process of an anti-electron neutrino with energy* $E_{\overline{\nu}_e}$ *[52, 53].*

In figure 1.4, a graphical representation of equation 1.26 is shown where E_e and θ_s are plotted against the relevant neutrino energy range for supernova neutrinos up to a few tens of MeV. In principle, one can use the scattering angle dependence of the positron energy in order to track the primary neutrino and its source. Since in ICECUBE the deposition of light by the resulting Cherenkov photons, see section 1.4.2, is spherical and locally very bounded in this energy regime, an individual event tracing is not possible. Therefore, the precise evolution of θ_s can be satisfyingly approximated by a flat distribution.

Finally, the resulting total number of events N_e in the detection medium and the distribution in positron energy depend on the number of target protons and the neutrino energy dependent flux model Φ_ν:

$$N_{e^+} = N_p \int dE_\nu \frac{d\Phi_\nu}{dE_\nu}\sigma(E_\nu) \quad \text{and} \quad \frac{dN_{e^+}}{dE_e} = N_p \int dE_\nu \frac{d\Phi_\nu}{dE_\nu}\frac{d\sigma}{dE_\nu} \tag{1.28}$$

An example for such an energy distribution can be seen in figure 1.5, where a few simplifications were assumed that do not effectively change the basic result [54]. A detailed explanation of the supernova neutrino flux parametrization is outlined in chapter 2.3.2. For now it is sufficient to mention that, given a naive approximation for the total cross-section [55], the positron spectrum nearly follows a Gamma function as it is the case for the primary neutrinos.

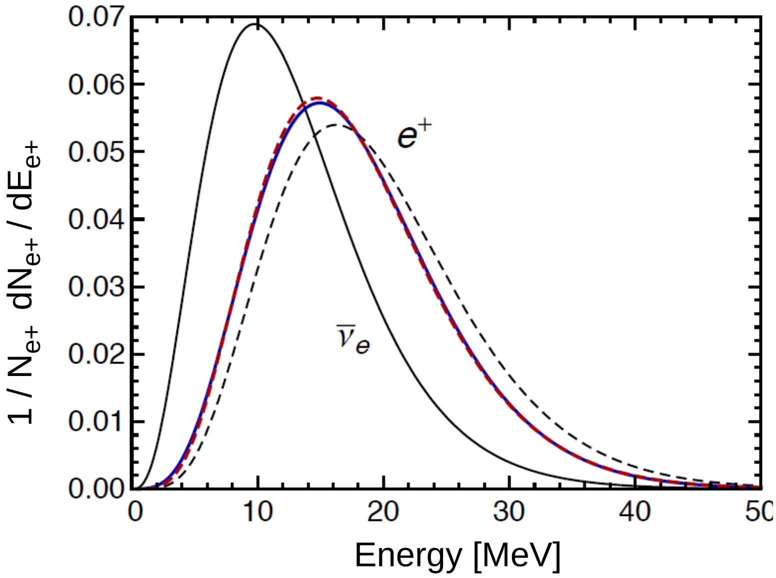

Figure 1.5: *Normalized distributions for energies of* $\overline{\nu}_e$ *(black solid line) with mean energy* $\langle E_\nu \rangle = 13\,\mathrm{MeV}$ *and resulting positron (solid blue line) from inverse* β*-decay interactions [54]. Approximating the positron spectrum with a Gamma distribution gives the red dashed line. Assuming a naive IBD cross-section, ignoring recoil effects and the proton-neutron mass difference results in the black dashed line.*

The fact that $\langle E_{e^+} \rangle = 17.9\,\mathrm{MeV} > \langle E_{\overline{\nu}_e} \rangle = 13\,\mathrm{MeV}$ is a direct consequence of the total cross-section (equation 1.25) being proportional to the squared neutrino energy. Although neutrinos with energies above average are less abundant they are more likely to interact which results in more positrons in the corresponding energy range.

Neutron Capture

Together with the final positron, a neutron is produced in the IBD. Shortly after production, on time-scales $\mathcal{O}(100\,\mu\mathrm{s})$, the neutron will be thermalized and be captured on hydrogen $(n + ^1\mathrm{H} \longrightarrow ^2\mathrm{H} + \gamma)$ creating deuterium and emission of a γ-ray of 2.225 MeV [56, 57]. When traveling through the ice, the photon may undergo Compton-Scattering. The released electron follows a well defined energy distribution [58, 59]:

$$
\begin{aligned}
p(E_{e^-}) \sim & (E_\gamma - E_{e^-})^{-2} E_\gamma^{-3} \\
& - (2 + 2\frac{E_\gamma}{m_e} - \frac{E_\gamma^2}{m_e^2})(E_\gamma - E_{e^-})^{-1} E_\gamma^{-3} \\
& + \left(\frac{E_\gamma}{m_e} + 1\right) E_\gamma^{-4} - m_e^{-2} E_\gamma^{-3} E_{e^-}
\end{aligned}
\tag{1.29}
$$

1.3.2 Neutrino-Electron Scattering

Elastic scattering by neutrinos of all flavors happens on the orbital electrons of water-molecules:

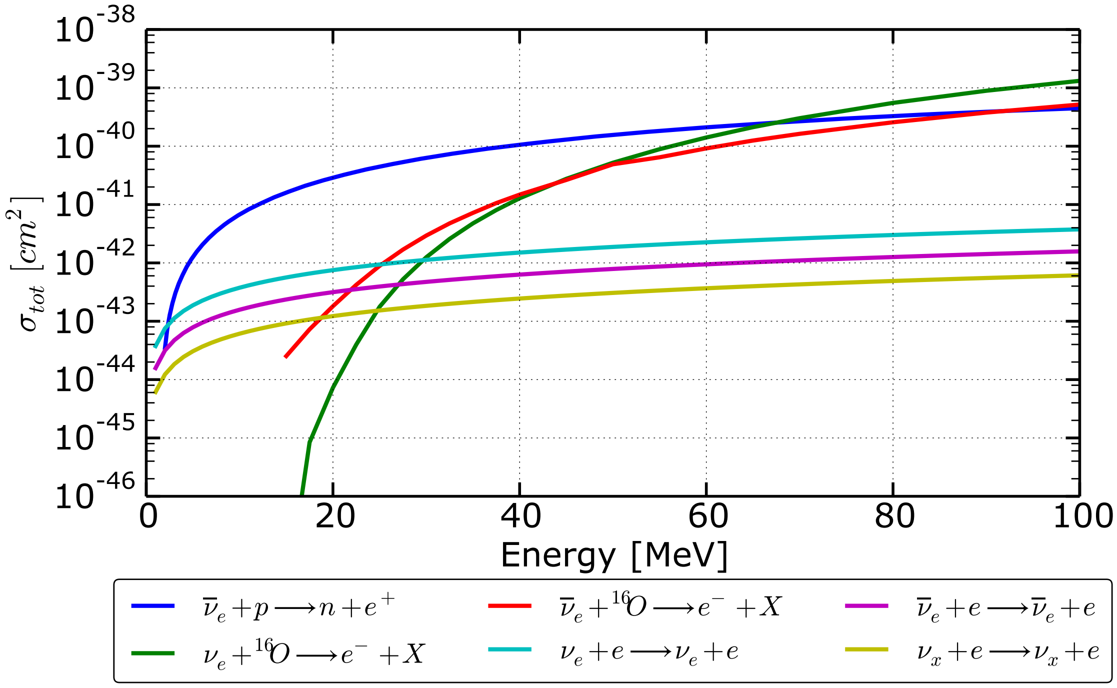

Figure 1.6: *Total cross-section as a function of energy for most relevant interaction of low energy neutrinos in ice [52, 60, 61].*

$$\begin{array}{llll} \nu_e + e^- \longrightarrow \nu_e + e^- & (\mathrm{CC}, \mathrm{NC}) & \nu_{\mu,\tau} + e^- \longrightarrow \nu_{\mu,\tau} + e^- & (\mathrm{NC}) \\ \overline{\nu}_e + e^- \longrightarrow \overline{\nu}_e + e^- & (\mathrm{CC}, \mathrm{NC}) & \overline{\nu}_{\mu,\tau} + e^- \longrightarrow \overline{\nu}_{\mu,\tau} + e^- & (\mathrm{NC}) \end{array} \tag{1.30}$$

Regarding ν_e and $\overline{\nu_e}$, these processes can occur via charged and neutral current exchange whereas the heavier flavors only undergo the neutral current interaction due to lepton number conservation. ICECUBE uses the cross-sections computed by [60] under the assumption that the transfer of momentum is very small compared to the masses of the mediators of the weak force ($|q^2| \ll m_{W^\pm, Z^0}$):

$$\sigma(E_\nu) = \frac{2G_\mathrm{F}^2 m_e E_\nu}{\pi} \left[\epsilon_\mp^2 + \frac{1}{3}\epsilon_\pm^2 - \frac{1}{2}\frac{m_e}{E_\nu}\epsilon_+\epsilon_- \right] \tag{1.31}$$

and

$$\frac{d\sigma}{dx}(E_\nu, E_e) = \frac{2G_\mathrm{F}^2 m_e E_\nu}{\pi} \left[\epsilon_\mp^2 + \epsilon_\pm^2 (1-x)^2 - \frac{1}{2}\frac{m_e}{E_\nu} x \epsilon_+\epsilon_- \right] \quad , \tag{1.32}$$

for the differential cross-section respectively , where

$$\epsilon_+ = \sin^2\theta_\mathrm{W} \quad \text{and} \quad \epsilon_- = \begin{cases} -\frac{1}{2} - \sin^2\theta_\mathrm{W} & \text{for} \quad \nu = \nu_e, \overline{\nu}_e \\ \frac{1}{2} - \sin^2\theta_\mathrm{W} & \text{for} \quad \nu = \nu_{\mu,\tau}, \overline{\nu}_{\mu,\tau} \end{cases} \tag{1.33}$$

expresses the dependence on the Weinberg-angle θ_W and $x = (E_e - m_e)/E_\nu$ describes the transfer of momentum to the electron. As can be seen in figure 1.6, the electron scattering is about two orders of magnitude less frequent compared to IBD interactions with ice. This is due to the cross-section being only linear dependent on the energy whereas the IBD has a squared energy dependence. For neutrino energies up to $\sim 30\,\text{MeV}$, electron scattering by electron neutrinos ($\nu_e + e \longrightarrow \nu_e + e$) is the most important interaction channel to detect ν_e from a supernova.

1.3.3 Interactions with Oxygen

Interactions of neutrinos with the oxygen of the water molecules are very complex due to the non-trivial substructure of the latter. Since IceCube is sensitive only to interaction with electrons and positrons in the final state at these energies [5], we concentrate on the charge current processes [58, 61–63]:

$$\nu_e + {}^{16}\mathrm{O} \longrightarrow \begin{cases} {}^{15}\mathrm{O} + e^- + p \\ {}^{15}\mathrm{O}^* + e^- + p + \gamma \\ {}^{14}\mathrm{N}^* + e^- + 2p \end{cases} \tag{1.34}$$

$$\overline{\nu}_e + {}^{16}\mathrm{O} \longrightarrow \begin{cases} {}^{15}\mathrm{N} + e^+ + n \\ {}^{16}\mathrm{N} + e^+ \\ {}^{15}\mathrm{N}^* + e^+ + n + \gamma \end{cases} \tag{1.35}$$

Interactions with oxygen contribute the higher fraction of ν_e processes above $\sim 30\,\text{MeV}$ in particular and dominate the overall cross-section of neutrinos in ice above $\sim 70\,\text{MeV}$ in general. Due to their relatively high energy threshold, 13 MeV for ν_e and 18 MeV for $\overline{\nu}_e$, interactions of this type occur far more rarely than IBD given an energy spectrum of the incident neutrinos of $\mathcal{O}(10\,\text{MeV})$ as it is the case for neutrinos emitted by a supernova (see chapter 2.3.2). The energy dependent total cross-section can be parametrized [64]:

$$\sigma(E_\nu) = \mathrm{A} \cdot \left[E_\nu^{\mathrm{B}} - \mathrm{C}^{1/4}\right]^{\mathrm{D}} \quad , \tag{1.36}$$

where the primary neutrino energy E_ν needs to be provided in units of MeV and the parameters A,B,C and D are resulting from fits which are summarized in Table 1.2.

Table 1.2: *Parameters A,B,C, and D from the total cross-section of relevant neutrino interaction with oxygen resulting from fits [64, 65]*

Reaction	A	B	C	D
ν_e CC (equation 1.34)	$4.7 \times 10^{-40}\,\text{cm}^2$	$\frac{1}{4}$	15	6
$\overline{\nu}_e$ CC (equation 1.35)	$3.1 \times 10^{-40}\,\text{cm}^2$	0.223	8.0	5.9

The total cross-section for both reaction types is displayed in 1.6 over the expected energy range of the incident neutrino. The natural abundance of other isotopes of oxygen, like ${}^{17}\mathrm{O}$ and ${}^{18}\mathrm{O}$, and deuterium in the ice deviates from zero. With ${}^{16}\mathrm{O}$ being the most abundant among them, representing $\sim 0.2\,\%$ of natural oxygen [62], it is clear that the these interactions would only be relevant if the incident neutrino energy is below the ${}^{16}\mathrm{O}$ threshold of 13 MeV.

---

[5] Neutral current interactions produce protons in the final state which are not detectable in detectors like IceCube because their energy is not above the Cherenkov threshold (see section 1.4.2) for producing detectable photons.

Since the combined cross-section of all three of these processes in this energy range is below $\sim 3 \times 10^{-43}\,\text{cm}^2$ the contribution would still be rather small.

1.4 Neutrino Detection in Ice

Detecting neutrinos in ice is realized in a twofold indirect way. First, low energy neutrinos interact via processes describe in the previous section. The charged by-products of these reactions are assumed to carry most of the incident neutrino's energy. Along their way through the ice, these charged leptons loose energy which is explained in the next section. As long as their velocity is still above a certain threshold, these secondaries emit *Cherenkov* photons. When using water or ice as interaction medium, photomultipliers can be implemented to detect these light signals. ICECUBE exploit this very concept by using the antarctic ice-cap at the South Pole for searching for neutrinos. Table 1.3 summarizes the relevant interaction channels for low energy neutrinos and their contribution to the envisioned signal based on the mentioned coss-sections and assumption about the neutrino production inside the stars [66]. The quantities of the Cherenkov effect important with respect to a supernova signal are dealt with in section 1.4.2.

Table 1.3: *Relevant reactions for low energy neutrinos in ice via inverse β-decay [52], electron scattering [60] and reaction on oxygen [61, 67, 68] with their signal fraction and corresponding uncertainty [66] assuming a normal mass hierarchy.*

Reaction	Proportion of Signal	Uncertainty
$\overline{\nu}_e + p \longrightarrow n + e^+$ (IBD)	$\sim$ 94 %	$<$ 1 %
$\nu_e + e^- \longrightarrow \nu_e + e^-$	$\sim$ 1.7 %	$<$ 1 %
$\overline{\nu}_e + e^- \longrightarrow \overline{\nu}_e + e^-$	$\sim$ 0.5 %	$<$ 1 %
$\nu_x + e^- \longrightarrow \nu_x + e^-$	$\sim$ 0.5 %	$<$ 1 %
$\overline{\nu}_e + {}^{16}\mathrm{O} \longrightarrow e^+ + \mathrm{X}$	1.3 %	$<$ 30 %
$\nu_e + {}^{16}\mathrm{O} \longrightarrow e^+ + \mathrm{X}$	1.5 %	$<$ 30 %

1.4.1 Energy Loss of e^+ and e^- in Ice

Charged particle in matter loose energy when ionizing the material they are traveling in as well as due to radiation. The situation for incident particles over a wide energy range is depicted in figure 1.7. Ionization, i.e. the liberation of an electron from an atom via energy transfer of the incident particle, is the dominating process over a large fraction of the displayed energy range. The basic formulation of the theory by Bethe and Bloch [69, 70] describes the energy loss per path length for relativistic heavy charged particles. For electrons and positrons the situation is somewhat different compared to heavy particles with respect to spin, charge and kinematics in general. The fact that the incident electron can not be distinguished from the electron it ionizes modifies the energy loss rate, see [71] for more details. The average energy loss for positrons and electrons is then given by [72] :

$$-\frac{dE_{e^\pm}}{dx} = \frac{\kappa}{\beta^2}\frac{\mathrm{Z}}{\mathrm{A}} \cdot \mathrm{B}(\beta, \gamma, \mathrm{I}) \quad . \tag{1.37}$$

In order to derive this compact presentation, material constants like Avogadro's number, electron mass and radius are summarized in $\kappa = 2\pi \mathrm{N}_A m_e r_e^2$. The number of electrons per target molecule and the corresponding mass number are denoted with Z and A, respectively. The function $\mathrm{B}(\beta, \gamma, I)$ represents the dependence on the velocity of the incident particle $\beta = v/c$, the Lorentz-factor $\gamma = (1-\beta^2)^{-\frac{1}{2}}$ and the average ionization energy of the target I. Slightly different expression of $\mathrm{B}(\beta, \gamma, I)$ were found for electrons and positrons. Electron-electron scattering interactions are determined by the *Møller* cross-section whereas the *Bahbah* equation characterizes positron interactions on electrons [73]. For high Lorentz-factors $\mathrm{B}(\beta, \gamma, I)$ is proportional to $\ln \gamma$ in both cases. Additionally to energy loss via ionization, bremsstrahlung becomes an important contribution starting at energies of $\mathcal{O}(1\,\mathrm{MeV})$. This type of radiation arises from the electric field of a nucleus decelerating the incoming charged particle which radiates a photon due to energy conservation. As shown in figure 1.7, the bremsstrahlung effect on energy loss of positrons in ice increases linearly with energy of the incident particle whereas the ionization loss rate rises logarithmically. In the range of the energy spectrum of supernova neutrinos, a few tens of MeV, ionization dominates over bremsstrahlung.

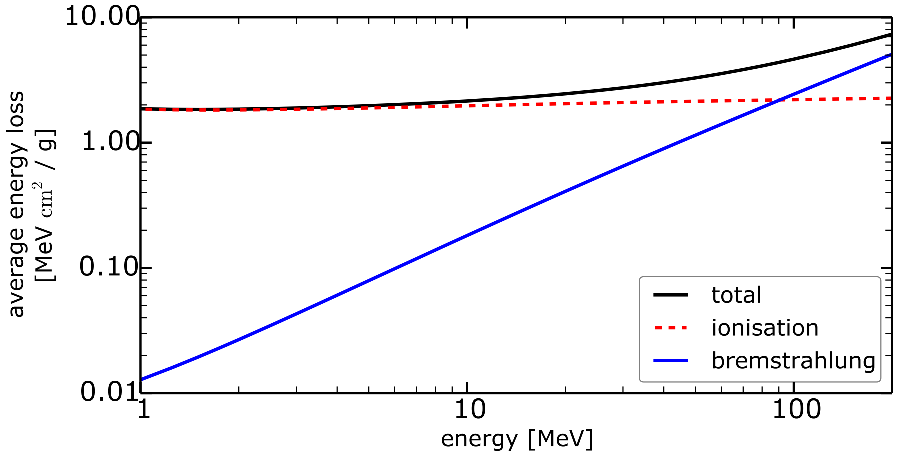

Figure 1.7: *Energy loss of positrons in ice normalized to the inverted density* ($\mathrm{cm}^2\,\mathrm{g}^{-1}$) *over the energy range of a few tens of MeV [74].*

1.4.2 Cherenkov Effect

Cherenkov radiation [76, 77] is a relativistic effect that can be seen as a result of the fundamental law of energy and momentum conservation when a charged particle travels through a dielectric medium with a velocity faster than the speed of light in that material.

Electromagnetic waves in a medium travel with a wavelength dependent phase velocity $c_{ph}(\lambda)$ that is smaller than the speed of light in vacuum c due to the refractive index $n(\lambda) = c/c_{ph} > 1$. For charged particles traversing the medium with a velocity $v > c/n$, energy conservation allows for the emission of photons, $e \longrightarrow e + \gamma$.

From classical electrodynamics one knows that charged particles polarize the material they travel through inducing time-varying dipole fields in the molecules. These electromagnetic fields do not interfere constructively as long as the particle's velocity is smaller than the speed of light in the medium, see left panel of figure 1.8. If the particle's velocity exceeds that limit, the wavefronts interfere constructively resulting in the emission of electromagnetic radiation, so-called *Cherenkov* photons, see right panel in figure 1.8. Based on the fundamental energy-momentum relation and also supported by the depicted geometry in figure 1.8, the

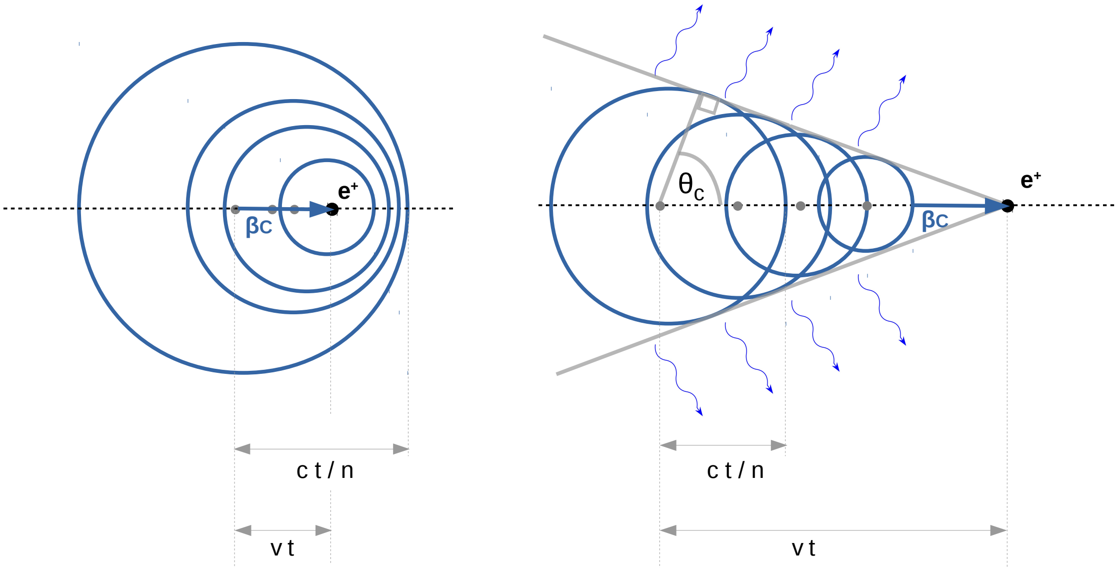

Figure 1.8: *Spherical wavelets (blue circles) of the diploe field created by a charged particle traveling with a velocity less (left panel) or greater (right panel) than the speed of light in that medium. An electromagnetic "shock" wave appears for $\beta c > c'$. Since in ice the index of refraction is almost independent of the wavelength, Cherenkov photons are emitted perpendicular to the wave front [75].*

characteristic angle θ_{ch} can be derived which depends only on the particle velocity and the refractive index of the medium:

$$\cos\theta_{\text{ch}} = \frac{c}{v \cdot n(\lambda)} \tag{1.38}$$

In the case of IceCube , the minimum kinetic energy for producing Cherenkov photons by electrons or positrons traveling in ice, which has a refractive index of typically $n_{\text{ice}} \approx 1.32$ for wavelength around 400 nm, is given by $\beta = 1/n$ and $\theta_{\text{ch}} = 0$, which results in:

$$E_e^{min} = (\gamma - 1)m_e c^2 = \left(\frac{1}{\sqrt{1 - \frac{1}{n^2}}} - 1 \right) m_e c^2 = 0.252\,\text{MeV} \tag{1.39}$$

for electrons and positrons, respectively (with the usual expressions β and γ from relativistic kinematics and the electron mass m_e). The basis for measuring low energy electrons and positrons in IceCube is the relation between the average number of produced Cherenkov photons $\bar{\text{N}}_\gamma$ and the incident particle's energy. This is accomplished in two steps. First, the Frank-Tamm formula [78] provides the differential number of photons that depends on the incident lepton's track length x and the wavelength of emitted photons λ:

$$\frac{d^2N}{dx d\lambda} = \frac{2\pi\alpha z^2}{\lambda^2}\left[1 - (\beta n(\lambda))^{-2}\right] \tag{1.40}$$

or, equivalently,

$$\frac{d^2N}{dEdx} = \frac{\alpha z^2}{\hbar c}\sin^2\theta_{\mathrm{ch}}(E) \approx 370\sin^2\theta_{\mathrm{ch}}(E)\mathrm{eV}^{-1}\,\mathrm{cm}^{-1} + \epsilon(E) \qquad , \tag{1.41}$$

which expresses the number of photons produced per unit track length of the positron and per unit energy of the photon [37]. For the detection with photomultipliers, the work function $\epsilon(E)$ of the bi-alkali photo-cathode has to be added in order to calculated the number of original Cherenkov photons from the resulting photo-electrons (p.e.).

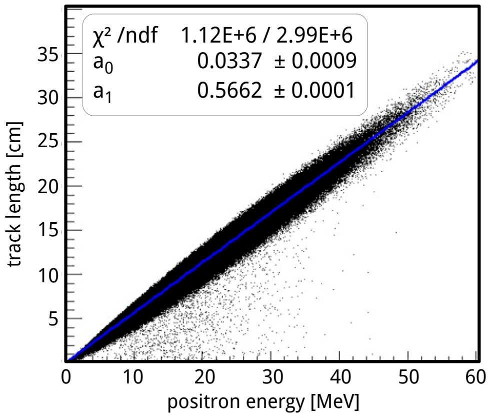

Figure 1.9: *Positron track length vs positron energy [65].*

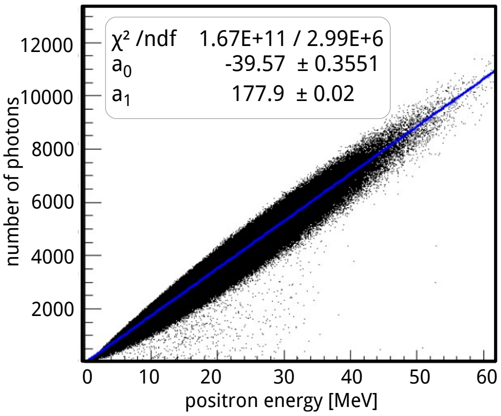

Figure 1.10: *Cherenkov photons vs positron energy [65].*

In order to find the average track length for a positron / electron in ice, a GEANT4 [79, 80] simulation was performed [65], see figure 1.9. A linear dependence of the track length as a function of the positron's energy is clearly visible with an average track $\bar{\mathrm{x}} = 0.57\,\mathrm{cm\,MeV}^{-1}$. With this at hand, and integrating over a reasonable wavelength range of 300 nm - 600 nm, the average number of Cherenkov photons is:

$$\bar{\mathrm{N}}_\gamma = 2\alpha\pi\left[1-(\beta n(\lambda))^{-2}\right]\bar{\mathrm{x}}\int_{300\mathrm{nm}}^{600\mathrm{nm}}\frac{d\lambda}{\lambda^2} = 325.4\cdot\bar{\mathrm{x}}\left[\mathrm{cm}^{-1}\right] \approx 185\left[E_e\mathrm{MeV}^{-1}\right] \tag{1.42}$$

In terms of detected photo-electrons in a photomultiplier, this translates to

$$\frac{dN}{dr} = 370\int_{300\mathrm{nm}}^{600\mathrm{nm}} dE\sin^2\theta_{\mathrm{ch}}(E)\epsilon(E) \approx 45\,\mathrm{p\,e}\,/\mathrm{cm}\cdot 0.57\,\mathrm{cm\,MeV}^{-1} = 25\,\mathrm{p\,e}\,/\mathrm{MeV} \tag{1.43}$$

This result is in good agreement with the outcome of the above mentioned simulation study [65] with an average value for generated Cherenkov photons of 178 per MeV positron energy, see figure 1.10.

After dealing with the properties of neutrinos involved in detecting them, we now turn towards the stars and see how they can transform into a pure neutrino event: a core-collapse supernova.

2

Supernovae

This chapter is dedicated to the description of stellar life and death. In the first part we review the evolution of stars from their creation until their final nuclear fusion phase. At the end of its life a star has used all its nuclear power in its core and it collapses due to its mass. This is the beginning of the most energetic and brightest events in the universe: supernovae. We address the aspects of the most popular model of the gravitational core-collapse supernova mechanism in detail in section 2.2 with an emphasis on the neutrino production before we cover the phenomenology of the lightcurve and energies of these neutrinos in detail in section 2.3. This is followed by an overview of result from modern simulations which can be compared to the history-making detection of supernova neutrinos more than two decades ago, in 1987, which concludes this chapter.

2.1 Stellar Evolution

The detailed physics behind the birth of a star are complex and beyond the scope of this thesis. Therefore, this section outlines the most important feature only. For a more detailed discussion about the life of a star one may refer to [81–86].

2.1.1 Star Formation

Stars are known to be born in interstellar clouds of matter which extend their dimensions up to several parsecs[1]. Main constituents of this interstellar medium (ISM) are hydrogen and helium. Traces of heavier elements (C, O, Ne, Mg, Fe and their ions) produced in older stellar explosions as well as dust, cosmic ray particles and magnetic or radiation fields are less abundant ingredients of the ISM. At the moment when the gravitational energy becomes greater than the thermal energy of the cloud, contraction of the ISM sets in. The minimal mass of a gravitationally unstable cloud depends on its temperature T and radius R and is parameterized in the so-called *Jeans criterion*:

---

[1] A parsec (pc), an abbreviation for *parallax of an arcsecond*, is defined as the distance of an imaginary observer to the sun who would see the average sun-earth distant, the astronomical unit, as being one arcsecond. $1\,\text{pc} \approx 3.261\,56\,\text{ly} = 3.0857 \times 10^{6}\,\text{m}$

$$M_{Jeans} \geq \frac{2kTR}{G\overline{\mu} \cdot m_H} \quad . \tag{2.1}$$

Here, $\overline{\mu}$ represents the average atomic mass number, m_H is the mass of a hydrogen atom, k the Boltzmann-Constant and the Gravitational-constant is given by G. With equation 2.1 it is clear that a low temperature and a large spatial spread of the cloud favor collapse. At a temperature of 10 K (the speed of sound then is about 0.2 km s^{-1}) and a number density for a cloud of hydrogen of $n \leq 10^4$ cm^{-3} the Jeans radius is 0.2 pc and the Jeans mass is 1.6 $\mathrm{M}_\odot$ (solar mass[2]. A shock wave front from a former supernova could be a possible explanation for an over-density or local compression of the ISM above the critical density. Since the gravitational pull in the region under consideration is now greater than the thermal pressure of the gas, the cloud collapses while density and pressure in its interior increase. At this time, photons can still escape and reduce effectively the energy sum of the cloud. The cloud becomes opaque at densities $\rho \approx 10^{-13}$ g cm^{-3} , its potential energy cannot be released any longer through radiation and the cooling via photons stops. The temperature in the medium starts to rise due to adiabatic compression which decelerates the collapse and builds the begin of the *proto-star*. Molecular hydrogen H_2 starts dissociating at temperatures $\mathrm{T} \approx$ 1800 K. Since energy is consumed in this process, the temperature and the pressure in the proto-star decrease and the collapse accelerates again. This goes on until all H_2 is dissociated and the rising temperature and gaseous pressure slow down the speed of the infalling ISM. One can speak of the formation of a *young stellar object* (YSO) as soon as $T \approx 6000K$ in the proto-star is reached. This is the start of dissociation of atomic hydrogen and decreases the gaseous pressure in the ISM which ensures the collapse to proceed. Density and temperature rise now decelerating the collapse once more. During the next million years the YSO slowly accretes matter which leads to an increasing temperature t_{core} . When the core holds a temperature of $\mathrm{t}_{\mathrm{core}} \approx 10^6$ K, deuterium fusion can start (*T-Tauri phase*) and finally, at $\mathrm{t}_{\mathrm{core}} \approx 3.5 \times 10^7$ K, hydrogen burning sets in. This marks the star's entrance into the *main-sequence*.

2.1.2 Stellar Burning Stages

The best way to classify stars is to categorize them by their surface temperatures and observed luminosities. The first diagram of this type was developed by Ejnar Hertzsprung and Henry Norris Russell and therefore carries their name, see Figure 2.1. A main feature of this diagram is the just mentioned main-sequence. Furthermore, a classification by spectral type (i.e. surface temperature) is displayed where for example one can find our Sun to be of type G.

The burning stages a star goes through and the type of death it has to face are mostly determined by the star's initial mass but also by other factors. If the *metallicity*[3] in the star is high, more photons will be trapped inside and the medium is more opaque increasing the mass-loss rate [89] which affects the composition of the envelopes of the star and its surface temperature. During its burning phases the gravitational force of stellar matter pointing inwards and the thermal pressure of fusion processes opposing it are at equilibrium. At the end of every burning phase, the fusion in the core stops, contraction sets in and continues until the gravitational pressure and temperature of the core are high enough to initialize the next burning stage. The core starts a new burning cycle but the former fusion process continues in the core surrounding layer. With every fusion step the core mass increases, leading to a

---

[2] In astronomy it is widely used to measure weights in terms of solar masses $\mathrm{M}_\odot$. $1\,\mathrm{M}_\odot \approx 2 \times 10^{30}$ kg [83]

[3] The metallicity of an object describes the fraction of its matter made up by elements heavier than hydrogen and helium.

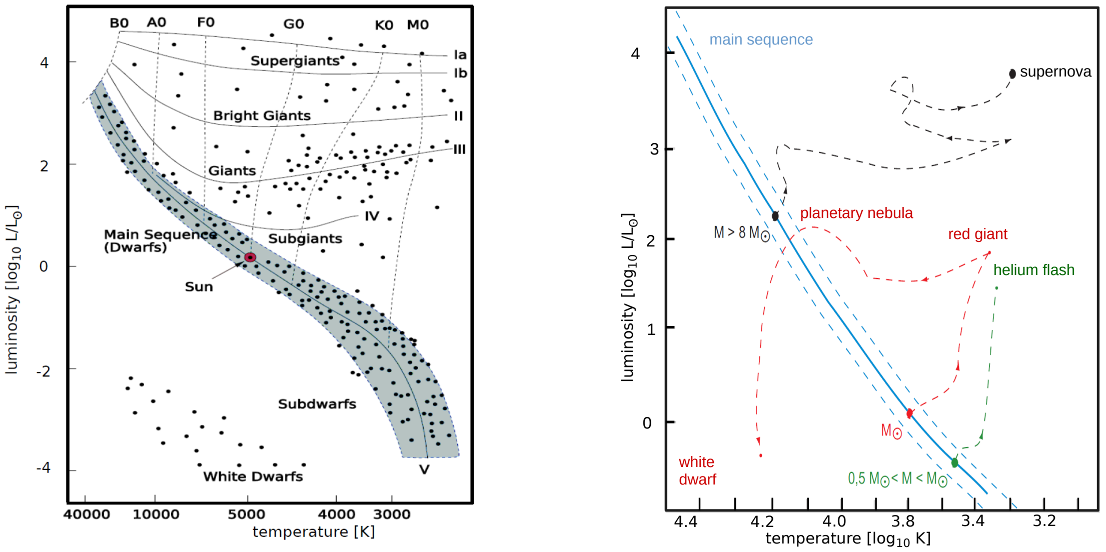

Figure 2.1: *The Hertzsprung-Russell diagram on the left [87] shows stars with their luminosity (in units of solar luminosity) as a function of theirs surface temperature. The right plot shows a sub-region of the Hertzsprung-Russel diagram with evolutionary tracks for a selected set of initial masses of stars after their main sequence period [63, 87, 88]. The colored dashed lines show from the main sequence for different stellar mass regimes.*

higher pressure which enables the star to overcome higher energy thresholds and to enter more burning phases. Furthermore, the core temperature and density rise at each stage which increases the luminosity of photons and neutrinos [90].

When a star has finished its very first fusion process, it leaves the main sequence. Low-mass stars, i.e. $\leq 0.3\,\mathrm{M}_\odot$, will never reach the ignition temperature for helium burning and collapse to a white dwarf after going through instability phases. If the star has a mass up to $1.4\,\mathrm{M}_\odot$, helium burning starts explosively (*helium flash*) but without disrupting the star since its energy is absorbed in the surrounding layers. The star settles in the giant branch. When the central helium is exhausted, the fusion process moves on to an outer shell, the outer part expands and the star loses a fraction of its mass. The expanding envelope forms a planetary nebula (PN) and the remaining core builds a white dwarf, see Figure 2.1.

Intermediate-mass stars ($2.3\,\mathrm{M}_\odot$ to $8\,\mathrm{M}_\odot$) have a higher core temperature and a lower density and thus starting their helium burning non-catastrophically [88]. Stars with masses greater than eleven solar masses go through all fusion stages whereas stars lighter down to eight solar masses can achieve only some elementary burning processes [91]. The cycle of possible fusion processes ends at the latest with fusion of silicon to iron. Any fusion of heavier elements would be endothermic and hence is disfavored. A summary of all stages can be found in table 2.1 for an exemplary $15\,\mathrm{M}_\odot$ star.

Most stars in our universe reside in the hydrogen burning phase which is also the longest stage. For example, our Sun happens to be in this very first stage and will continue to be for about another five billion years before all core hydrogen is used and helium fusion starts. For hydrogen burning, two different reaction chains are possible. The *proton-proton cycle*, where the most common channel of hydrogen production is the ppI channel:

Table 2.1: *The various fusion stages of a massive star. With every next burning stage (from top down) the process becomes faster, hotter, denser and brighter [90]*

Fuel	Ash	Duration	Temp. $[10^9\,\mathrm{K}]$	Density $[\mathrm{g\,cm^{-3}}]$	Luminosity $[L_\odot]$	Neutrino Luminosity $[L_{\nu,\odot}]$
H	He	11 Myr	0.035	5.8	28×10^3	1.8×10^3
He	C, O	2 Myr	0.18	1.4×10^3	44×10^3	1.9×10^3
C	Ne, Mg	2 kyr	0.81	2.8×10^5	72×10^3	3.7×10^5
Ne	O, Mg	0.7 yr	1.6	1.2×10^7	75×10^3	1.4×10^8
O, Mg	Si, S, Ar, Ca	2.6 yr	1.9	8.8×10^6	75×10^3	9.1×10^8
Si, S, Ar, Ca	Fe, Ni, Cr, Ti, ...	18 d	3.3	4.8×10^7	75×10^3	1.3×10^{11}
Fe, Ni, Cr, Ti, ...	Neutron Star	~ 1 s	7.1	7.3×10^9	75×10^3	3.6×10^{15}

$$
\begin{aligned}
p + p &\longrightarrow {}^2\mathrm{H} + e^+ + \nu_e \\
{}^2\mathrm{H} + p &\longrightarrow {}^3\mathrm{He} + \gamma \\
{}^3\mathrm{He} + {}^3\mathrm{He} &\longrightarrow {}^4\mathrm{He} + 2p
\end{aligned}
\tag{2.2}
$$

which is favored by low mass stars. The *CNO cycle*:

$$
\begin{aligned}
p + {}^{12}\mathrm{C} &\longrightarrow {}^{13}\mathrm{N} + \gamma \quad \text{and} \;\; e^+ + {}^{13}\mathrm{N} \longrightarrow {}^{13}\mathrm{C} + \nu \\
p + {}^{13}\mathrm{C} &\longrightarrow {}^{14}\mathrm{N} + \gamma \quad \text{and} \;\; p + {}^{14}\mathrm{N} \longrightarrow {}^{15}\mathrm{O} + \gamma \\
e^+ + {}^{15}\mathrm{O} &\longrightarrow {}^{15}\mathrm{N} + \nu \quad \text{and} \;\; p + {}^{15}\mathrm{N} \longrightarrow {}^{12}\mathrm{C} + \alpha
\end{aligned}
\tag{2.3}
$$

plays a more important role in higher mass stars ($> 1.3 M_\odot$), ending with the production of doubly ionized helium atoms, i.e. alpha particles. At a temperature $t_{core} \approx 1.7 \times 10^7$ K both processes happen equally often continue for a time-span of $\mathcal{O}(10 \times 10^9\,\mathrm{y})$.

With the start of helium burning, a star enters the second and already last fusion phase of its evolution that can be identified in the Hertzsprung-Russel diagram. The stars leave the main-sequence towards the upper part and enter the giant region. In order to efficiently gain energy, the star now commences fusion processes involving alpha-particles:

$$
\alpha + \alpha + \alpha \longrightarrow {}^{12}\mathrm{C} \text{ and } \alpha + {}^{12}C \longrightarrow {}^{16}O + \gamma \qquad , \tag{2.4}
$$

which can least for few million years. When the core region has burned all its fuel, the fusion process "relocates" itself to outer layers where the necessary element is still abundant. This holds for all possible fusion phases and is the reason for an onion-like shell structure of the star, see Figure 2.2.

The advanced fusion processes in the core happen too quickly for the surrounding evolution to keep up. However, convection of the core material to the surface ensures the distribution

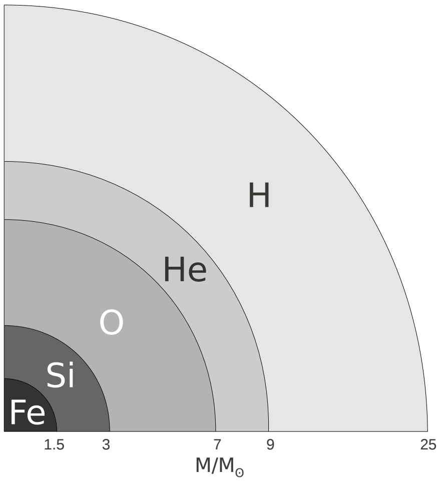

Figure 2.2: *Shell-structure of a massive star. Transition regions between the layers are left out for simplicity.*

of elements, produced in the core, to other regions. If a star's initial mass is high enough, carbon burning follows the helium fusion lasting for a few thousand years:

$$^{12}\mathrm{C} + ^{12}\mathrm{C} \longrightarrow {}^{24}\mathrm{Mg}^* \begin{array}{cc} \nearrow & ^{23}\mathrm{Mg} + n \\ \longrightarrow & ^{20}\mathrm{Ne} + \alpha \\ \searrow & ^{23}\mathrm{Na} + p \end{array} \tag{2.5}$$

where the excited magnesium decays equally often to neon or sodium and in only about 5% of all times in magnesium itself. Since neutrons, protons and α interact further, the core then consists mainly of oxygen, neon and magnesium. Without any fusion process at its center, the stars center contracts again and reaches $t_{core} \approx 10^9$ K. Photo dissociation of neon is now possible which results finally in the production of even more neon and magnesium but also silicon via the reaction with the previously produced helium:

$$^{20}\mathrm{Ne} + \gamma \longrightarrow {}^{16}\mathrm{O} + {}^{4}\mathrm{He} \text{ and } {}^{4}\mathrm{He} + \begin{cases} ^{16}\mathrm{O} & \longrightarrow {}^{20}\mathrm{Ne} \\ ^{20}\mathrm{Ne} & \longrightarrow {}^{24}\mathrm{Mg} + \gamma \\ ^{24}\mathrm{Mg} & \longrightarrow {}^{28}\mathrm{Si} + \gamma \end{cases} \tag{2.6}$$

and continues for less than one year of the star's lifetime. For the next phase, oxygen burning, photo-disintegration could again be the driving mechanism but in the environment of a massive star oxygen fusion is favored at this temperature ($t_{core} \approx 2 \times 10^9$ K):

$$^{16}\mathrm{O} + {}^{16}\mathrm{O} \longrightarrow \begin{cases} ^{32}\mathrm{S} + \gamma \\ ^{31}\mathrm{S} + n \\ ^{31}\mathrm{P} + p \\ ^{28}\mathrm{Si} + {}^{4}\mathrm{He} \end{cases} \tag{2.7}$$

which lasts for a few years. Sulfur and silicon are the most abundant elements in the ashes of oxygen burning in the star. Following oxygen, silicon burning rings in the end of the star.

This reaction chain is not a straightforward fusion process but rather determined by photodisintegration and alpha processes that lead to creation of nickel and iron which takes a few days only:

$$^{28}\mathrm{Si} + ^{4}\mathrm{He} \longrightarrow \, ^{32}\mathrm{S} + ^{4}\mathrm{He} \ldots \, ^{56}\mathrm{Ni} + \gamma \longrightarrow \, ^{52}\mathrm{Fe} + ^{4}\mathrm{He} \tag{2.8}$$

As the silicon abundance decreases, the burning stops and the star will finally reach its last episode.

2.2 Core-Collapse Supernova

The gravitationally induced catastrophic collapse of the iron core is the inevitable end of the live of stars between $8\,\mathrm{M}_{\odot}$ and $150\,\mathrm{M}_{\odot}$. When there is no fuel left to burn int he stars inner region, no force stands anymore against the inwards directed gravity and the region starts to collapse.

This matter flow increases the the inner iron core's density until it reaches nucleon level. The electron degeneracy is the only force left opposing the in-falling matter and stabilizes the region against further compression. Converging matter bounces back from the just formed *proto-neutron star* and a hydrodynamic shock is launched. At the beginning, the shock progresses through the outer core but loses energy due to the dissociation of heavy nuclei at the wave front and neutrino dissipation from the the post-shock region [92]. The necessary revival of the shock in order to lead to a core-collapse supernova (CCSN) has been topic of intensive research for many decades (e.g. [93] and references therein). Several models describing the possible nature of the responsible CCSN mechanism have been developed since the 1960's. This sections aims to provide an overview of possible star death scenarios and different observational features of supernova before concentrating on the most popular explosion mechanism: the neutrino-driven core-collapse supernova [94].

2.2.1 Prerequisites

For historical reasons, the classification of the different supernova types is based on their observational feature in their lightcurves [95] rather than on the underlying mechanisms. If the observed spectrum does not have any hydrogen lines, astronomers call it a *type* I Supernova and otherwise a stellar explosion of *type* II. Among these two groups further classifications can be made. An explosion of a star that has lost its hydrogen outer shell earlier provides characteristic Helium lines (*type* Ia) or no Helium lines at all (*type* Ic) if it also lost its helium envelope before.

A special case are the Supernova of *type* Ia. They are not caused by the neutrino driven core-collapse mechanism, explained in detail in the next section, but are the result of thermonuclear reactions [96]. Originating from a white dwarf and a red giant, i.e. a binary star system. The white dwarf in this scenario is the remnant of a low-mass star that accretes matter from the expanded hydrogen shell of its companion. This goes on until the Chandrasekhar mass-limit is reached and the white dwarf collapse due to its mass. Unlike in type II progenitor stars, these white dwarf still contains carbon and oxygen which enables the ignition of nuclear burning and lead to fragmentation of the nuclear elements. The underlying physics for the fusion are still under debate with two burning processes in the main focus, detonation and deflagration. The

Table 2.2: *Overview of main differences of thermonuclear and core-collapse supernovae.*

	Supernova Class	
	Thermonuclear	Core-Collapse
Stellar mass	$< 8\,\mathrm{M}_\odot$	$> 8\,\mathrm{M}_\odot$
Evolution	highly developed	expanded shells
Fusion	explosive C + O burning	burning by compression
Stellar system	binary	single (binary for type Ib, Ic)
Final stage	complete disruption	neutron star or black hole
ν production	feeble	strong

delayed detonation model [97] explains the observational quantities, such as the lightcurve, in the best manner. In these recent models, the white dwarf never reaches Chandrasekhar mass M_{CH} and collapse does not commence in this way but rather rises the temperature in the core due to increasing pressure and density [97]. Holding a mass of about 0.99 M_{CH} convection sets in. The heat transfer leads to the ignition of a thermonuclear flame, known as deflagration, which moves at subsonic speeds outwards being supported by carbon fusion and initiating oxygen fusion shortly after. In a standard main-sequence star, the resulting increasing in thermal pressure would be balanced by cooling via expansion. This regulation is not possible for white dwarfs as their degeneracy pressure is independent of temperature. This starts a runaway fusion reaction that could result into a supersonic detonation [98]. Despite the still unsolved mystery of this fusion, heavier elements are expected to be produced. All this happens on very short time scales ($\mathcal{O}$(s)) [99], releasing enough energy , $\mathcal{O}(2 \times 10^{44}$ J), [100] to disrupt the star. The fact that type *Ia* supernovae are among the brightest of all types and have a very stable and well defined lightcurve supports the idea that they originate from similar objects, carbon-oxygen white dwarfs. These features are used in order to measure distances in the universe which is the basis of the proof for an accelerating expanding universe which was awarded the Nobel Prize in 2011 [101, 102].

In the same way that the life of a star is determined by its mass and metallicity also is its death. The initial mass of the star is an obvious prerequisite whereas the metallicity is linked to the mass loss rate during the stellar burning phases and therefore influences the conditions indirectly. Figure 2.3 provides an overview of all varieties of stellar death. In the case when the star's initial mass is smaller than about eight solar masses, it will not end at all in a stellar explosion but as a white dwarf [4], independent of its metallicity. White dwarfs are believed to be the final stage of evolution in the life of a red giant that has already shed its outer layers. The left over core forms the white dwarf and consists mostly of carbon and oxygen, the ashes of its last fusion process in the core. The main differences between thermonuclear and core-collapse supernovae are depicted in table 2.2.

With increasing initial mass, $8\mathrm{M}_\odot \lesssim M_* \lesssim 10\mathrm{M}_\odot$, the first type of stars resulting in a core-collapse supernova has not yet the potential to go through all fusion stage and therefore its core consists only of oxygen, neon and magnesium. The collapse of these ONeMg-core stars is triggered by rapid electron capture on Ne and Mg, therefore also called *electron capture supernovae* (ECSN), and is estimated to be the reason for an explosion in 30% of all cases [103]. For an initial mass between $10\mathrm{M}_\odot$ and $25\mathrm{M}_\odot$, the iron core collapse is the source of the explosion. At higher masses, $25M_{\odot} \leq M_{*} \leq 260M_{\odot}$, the metallicity plays an increasingly important role. For example, a star initially as heavy as $35\,\mathrm{M}_{\odot}$, could either end up as a Supernova of type Ib, Ic, IIb, IIL or IIp, depending on the abundance of heavy elements in its composition. As a matter of fact, the stars at these masses are so heavy that they can form a black hole when the supernova explosion falls back. In simulations it has been found that the initial characteristics of a star beginning its life at the main sequence determine the success of the SN explosion regarding a massive star with $40\,\mathrm{M}_{\odot}$ [93]. Even heavier stars but with lower metallicity than the sun are predetermined to end their lives in a totally different way, namely through direct black hole formation.

---

[4] Characterised by their surprisingly high temperature, resulting in a white spectrum, and by their low luminosity, coming from a small surface, these stars are called white dwarfs.

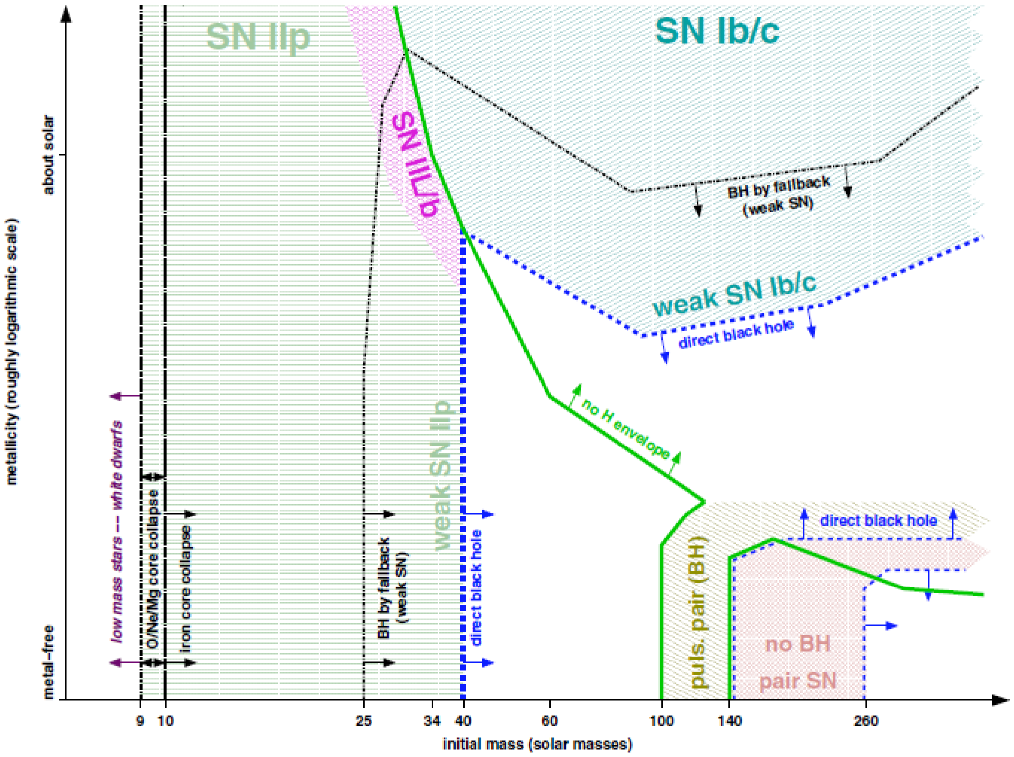
metallicity (roughly logarithmic scale)
about solar
metal-free
low mass stars -- white dwarfs
O/Ne/Mg core collapse
iron core collapse
SN IIp
BH by fallback
(weak SN)
weak SN IIp
direct black hole
SN IIL/b
SN Ib/c
BH by fallback
(weak SN)
weak SN Ib/c
direct black hole
no H envelope
puls. pair (BH)
direct black hole
no BH
pair SN
9
10
25
34
40
60
100
140
260
initial mass (solar masses)

Figure 2.3: *Final fate of non-rotating stars depending on their initial mass (horizontal axis) and initial metallicity (vertical axis) [89]. As opposed to the straight limit at $9M_{\odot}$, more recent calculations [104] define the minimum mass of stars for ending in a CCSN to be about $8.3M_{\odot}$ and depending slightly on its metallicity.*

2.2.2 Neutrino Driven Explosion Mechanism

Initial Phase

The inactive iron core at the center no longer provides any fusion pressure and is only stabilized because of the degeneracy pressure of relativistic electrons. This stability is only guaranteed up to the *Chandrasekhar mass limit*:

$$M_{\mathrm{Ch}} = 5.83\,\overline{\Upsilon}_e^2 \left[1 + \left(\frac{\overline{s}_e}{\pi \overline{\Upsilon}_e^2} \right)^2 \right] , \tag{2.9}$$

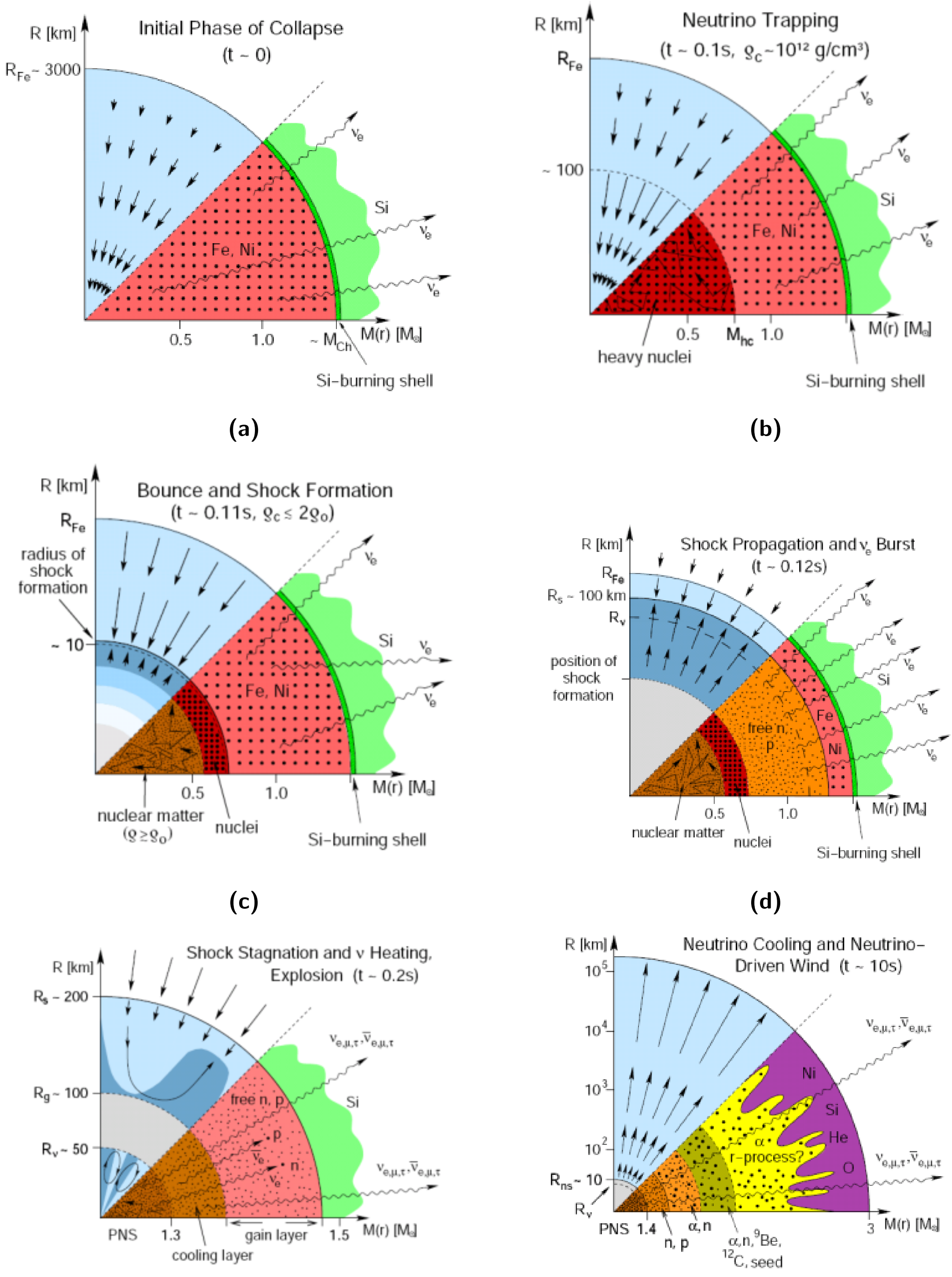
R [km]
Initial Phase of Collapse
(t ~ 0)
R_{Fe} ~ 3000
ν_e
Si
Fe, Ni
0.5
1.0
~ M_{Ch}
M(r) [$M_\odot$]
Si–burning shell
R [km]
Neutrino Trapping
(t ~ 0.1s, ϱ_c~10^{12} g/cm³)
R_{Fe}
~ 100
Si
Fe, Ni
0.5
M_{hc}
1.0
M(r) [$M_\odot$]
heavy nuclei
Si–burning shell
R [km]
Bounce and Shock Formation
(t ~ 0.11s, $\varrho_c \lesssim 2\varrho_0$)
R_{Fe}
radius of shock formation
~ 10
Si
Fe, Ni
0.5
1.0
M(r) [$M_\odot$]
nuclear matter ($\varrho \geq \varrho_0$)
nuclei
Si–burning shell
R [km]
Shock Propagation and ν_e Burst
(t ~ 0.12s)
R_{Fe}
R_s ~ 100 km
R_ν
position of shock formation
free n, p
Fe
Ni
Si
0.5
1.0
M(r) [$M_\odot$]
nuclear matter
nuclei
Si–burning shell
R [km]
Shock Stagnation and ν Heating, Explosion (t ~ 0.2s)
R_s ~ 200
R_g ~ 100
R_ν ~ 50
$\nu_{e,\mu,\tau}, \bar{\nu}_{e,\mu,\tau}$
free n, p
p
n
ν_e
Si
PNS
1.3
gain layer
1.5
M(r) [$M_\odot$]
cooling layer
R [km]
Neutrino Cooling and Neutrino–Driven Wind (t ~ 10s)
10^5
10^4
10^3
10^2
R_{ns} ~ 10
R_ν
$\nu_{e,\mu,\tau}, \bar{\nu}_{e,\mu,\tau}$
Ni
Si
He
O
α
r–process?
PNS
1.4
α, n
n, p
α, n, ^{9}Be, ^{12}C, seed
3
M(r) [$M_\odot$]

(a) **(b)**

(c) **(d)**

(e) **(f)**

Figure 2.4: *Schematics of the evolution steps in a core-collapse supernova via the neutrino-driven delayed explosion mechanism. Nuclear composition and processes are indicated in the lower half of each panel whereas the upper half shows the direction of matter flow, indicated by arrows [94]. Detailed explanation is to be found in the text.*

where the dependence of the just mentioned electrons is reflected in $\overline{\Upsilon}_{\rm e}$, the mean electron fraction per baryon, and $\overline{s}_e$ which describes the mean entropy of the electrons. At this time, matter still accumulates on the core, coming from outer regions of the star where fusion processes still take place. When the temperature in the core reaches $T_c \approx 5 \times 10^9$ K and the density exceeds 10^{10} g cm^{-3}, photo-dissociation of iron sets in and reduces the thermal pressure.

Electron capture on free iron nuclei sets in via:

$$e^- + {}^{56}Fe \longrightarrow {}^{56}Mn + \nu_e \tag{2.10}$$

because the Fermi energy of electrons is high enough to overcome the mass difference between the nuclei[5]. Furthermore, β-decay is now possible:

$$e^- + p \longrightarrow n + \nu_e \qquad . \tag{2.11}$$

Both processes reduce the electron pressure because the produced neutrinos can still freely leave the core region. Figure 2.4a depicts this initial phase.

Collapse and Neutrino Trapping

The three processes describes above, electron capture, photo-dissociation and β-decay, pull energy from the core and reduce the electron density. The collapse accelerates which is caused by a diminished electron entropy $\overline{s}_e$ and smaller electron density fraction $\overline{\Upsilon}_e$. At densities of $\rho \approx 10^{12}$ g cm^{-3}, an electron's diffusion time through the core, caused by scattering on nuclei, exceeds the collapse time. In other words, the mean free path of the neutrinos produced in electron capture becomes smaller than the core radius and the neutrinos are trapped inside. The outer core region of the star are kept unaffected of the collapse until the pressure and density become so high that the inner core collapse velocity is proportional to its radius. This is the time when the outer core regions start to collapse at free-fall time scale[6] Due to the matter density gradient in the core, there is a region of radius R_ν above which neutrinos still can freely escape, the so-called *neutrino sphere*. This radius can be imagined as being the optical neutrino depth at which the average number of scattering interaction is $2/3$. Neutrinos produced in scattering and β-reactions above this threshold radius R_ν leave the core region unaffected, see Figure 2.4b.

Core Bounce & Prompt Shock

The collapse proceeds now without disturbance until nuclear densities of $\rho_{core} \approx 3.5 \times 10^{14}$ g cm^{-3} are reached in the core. At this level, the degeneracy pressure stops the collapse and the proto-neutron star forms. As the region now became incompressible, the in-falling matter is promptly stopped and rebounds (see Figure 2.4c). An outward going shock wave transverses the in-falling matter and supports the dissociation of nuclei into free nucleons, consuming about $8.8 MeV$ per nucleon and leading to a deceleration of the shock. If the shock front has stopped the collapse and proceeds until the outer burning shells of the star, the shock wave could trigger a direct explosion of the star. However, this so-called *prompt shock* scenario is disfavored by all state-of-the-art simulations as the energy available to the shock seems to be consumed totally by dissociation of heavy nuclei in the outer core region.

---

[5] Fermi Energy of electrons: $\mu_e = (3\pi^2 n_e)^{\frac{1}{3}} \hbar c = 11.1\,\text{MeV} \left(\frac{\rho \Upsilon_e}{10^{10}\,\text{g cm}^{-3}}\right)$ which is greater than the mass difference $m_{\rm Mn} - m_{\rm Fe} = 3.7$ MeV

[6] The time it takes for a heavy object to collapse if no other forces come into play besides its own gravity.

Shock Propagation & ν_e Burst

Due to the huge amount of free protons, a high number of electron neutrinos, created via electron capture, follow just behind the shock front:

$$e^- + p \longrightarrow n + \nu_e \tag{2.12}$$

At the moment when the shock radius reaches the neutrino sphere, a vast amount of these neutrinos will escape on a timescale of $\mathcal{O}(5\,\mathrm{ms})$, as shown in Figure 2.4d. This so-called *deleptonization peak* holds a neutrino luminosity of approximately 3.5×10^{53} erg/s [105]. A complete overview of neutrino luminosity features will be given in chapter 2.3.1.

Shock Stagnation, ν Heating and Explosion

The neutronization process from equation 2.12 weakens the shock propagation. Pair production and thus positron capture on free neutrons are now possible because of a lower electron degeneracy in the post-shock region:

$$e^+ + n \longrightarrow p + \overline{\nu}_e \tag{2.13}$$

Additionally, other neutrino flavors are generated in the *cooling layer* via pair annihilation:

$$e^- + e^+ \longrightarrow \nu_{e,\mu,\tau} + \overline{\nu}_{e,\mu,\tau} \tag{2.14}$$

Although the neutrino production from electron positron annihilation is about ten thousand times less likely than the production of two photons[7], the latter cannot escape due to the present matter densities and hence do not add to the cooling. The last neutrino production channel contributing to cooling in this region is nucleon bremsstrahlung:

$$N + N' \longrightarrow N + N' + \nu_{e,\mu,\tau} + \overline{\nu}_{e,\mu,\tau} \qquad . \tag{2.15}$$

At about 200 ms after the initialization of the collapse, the shock stalls at a radius between 100 km and 200 km. This defines a region of neutrino absorption, the so-called (energy) gain layer, or *neutrino heating* region where neutrinos deposit energy via the very inverse process of equation 2.13:

$$\begin{aligned} \nu_e + n &\longrightarrow e^- + p \\ \overline{\nu}_e + p &\longrightarrow e^+ + n\,. \end{aligned} \tag{2.16}$$

Figure 2.4e shows the exact position of the just mentioned regions. If the energy transfer of neutrinos, being produced by the cooling PNS, to free protons and neutrons in the gain layer is high enough, the shock will be re-initiated [106]. In the end, this *delayed neutrino-heating mechanism* [107, 108] is the driving force for the final burst although not more than SI1% of the total neutrino energy will be transferred in this way. The shock front will reach the outer layers and lead finally to the supernova explosion of the star at timescales of order 100 ms after the revival. In fact, it is the fine-tuning of these opposing processes, neutrino moderating in the cooling layer and heating in the gain layer, that determines a successful explosion. A deceleration of the infalling matter can only be caused by a strong heating which on the other side increases the time for absorption of neutrino energy. The increased time span results in a more efficient energy deposition by neutrinos. This positive feedback of a strong heating cycle can initiate the explosion. On the other hand, strong neutrino cooling decreases the chance for a stellar explosion because it increases the speed of infalling material and shortens the reheating time span.

---

[7] This estimated relation results from comparing the Feynman diagrams for both processes. The probability of $e^- + e^+ \longrightarrow \gamma + \gamma$ is proportional to the electromagnetic coupling constant $\alpha_{\mathrm{EM}} \approx 1/137$. The neutrino production has a probability proportional to the weak coupling $\alpha_{\mathrm{weak}} \approx 10^{-6}$ and hence resulting in a cross-section difference of $\mathcal{O}(10^4)$.

PNS Cooling

Neutrino production inside the PNS, equations 2.13,2.14 and 2.15, continues for several seconds. Energy input by these neutrinos into the shock wave region, equation 2.16, supports the shock propagation to reach finally, typically after a couple of hours, the outer layers of the star. The PNS formed in the core is now gravitationally decoupled from the envelope and, as a result of the cooling, shrinks down to a radius of about 20 km in less then a second after the bounce (see Figure 2.4f). Due to this compression the exterior heats up. The PNS still keeps accreting matter which results in even more neutrinos being emitted. At about 10 seconds after the core bounce, the thermal energy produced in this so-called *Kelvin-Helmholtz evolution* can penetrate from the outer regions inside the core. This energy transfer results in the release of the still trapped neutrinos behind the neutrino sphere radius in the PNS region where $T \approx 25\,\text{MeV}$. The temperature of the neutron star continuously cools down due to the neutrino emission and all neutrinos will be release as the core becomes completely transparent for them at $T \approx 2\,\text{MeV} \approx 2.4 \times 10^4\,\text{K}$. It is highly possible that this cooling process of the neutron star is the source for the production of heavier elements than iron in the surrounding layer where the shock front in passing through [6]. Since the neutron-to-proton ratio in the gain layer, see equation 2.16, depends on the ν_e and $\overline{\nu}_e$ capture by nucleons with the latter being more abundant at this point, it can be stated that the region above the PNS, also called *hot bubble*, is neutron-rich. This initial situation supports rapid neutron capture on heavy nuclei [109], also known as r-process. This is a chain reaction following the neutron drip line in the table of elements which happens much faster than the β-decays increasing atomic number resulting in a high abundance of unstable neutron-rich nuclei.

2.3 Neutrino Emission

In this section the neutrino phenomena related to the supernova are reviewed. The luminosity and mean energy of neutrinos produced in the core-collapse mechanism will be described with the help of results from early 2d and 3d simulations .

2.3.1 Lightcurve

As visible in Figure 2.5, one can determine four neutrino emission phases:

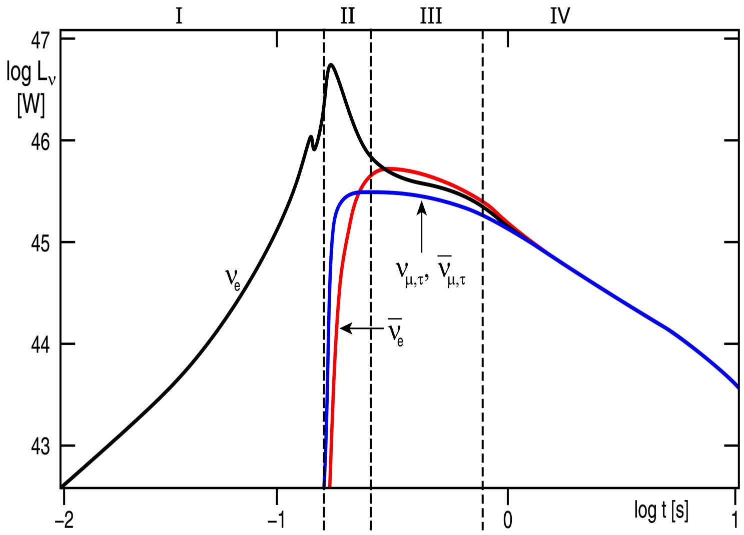

Figure 2.5: *Schematic drawing of the neutrino light curve during the development of the stars core from collapse to neutron star [110]. Neutrino luminosity and time are shown in logarithmic scales. See text for details.*

Neutrino Trapping

In the time before the collapse, electron capture on protons and neutrons is the production channel for neutrinos and generates only ν_e in the core. While these neutrinos make their way through the star via diffusion to the outer layers their energies thermalize due to inelastic scattering with electrons. At this point in time, the central temperature of the star is $T_c \approx 10^{10}$ K which results in a thermalization energy of a few MeV for the neutrinos. The ν_e luminosity reaches a significant level already during silicon burning. After the onset of the collapse, when the central density reaches $\rho_c \approx 10^{45}\,\mathrm{kg\,cm^{-3}}$, the nucleon scattering rate increases and the electron neutrinos are trapped inside the core which can be seen as a kink in the luminosity.

Deleptonization peak

This luminous burst of electron neutrinos happens when the ν_e, produced by electron capture on protons and neutrons just behind the shock front, break through the neutrino sphere R_ν which increases the luminosity for a few milliseconds, typically 5 ms to 7 ms [111]. This temporal evolution as well as the total amount of energy contained in the deleptonization peak, roughly 10^{51} erg, are independent of the mass of the progenitor star and even unaffected by the model used in simulation. This stable behavior is due to the fact that the core region can be treated separately from the shells because the core holds approximately the same mass in all scenarios and its homologous collapse doesn't affect the outer shells.

Accretion phase

The electron degeneracy is now decreased due to the deleptonization and photon-annihilation becomes more relevant resulting in an increased abundance of e^+e^--pairs. With the help of nucleon capture on the latter, ν_e and $\overline{\nu}_e$ are generated, respectively. Neutrinos of other types, ν_μ

and $\overline{\nu}_\mu$ as well as ν_τ and $\overline{\nu}_\tau$, are produced by bremsstrahlung on nuclei and e^+e^--annihilation. With these reactions, all neutrino types are now present in the luminosity spectrum in Figure 2.5. All common supernova models assume the heavier flavors to be produced in roughly equal quantities not favoring any of the μ or τ neutrinos. Due to the fact that the neutrino spheres of μ and τ neutrinos have smaller radii than the electron neutrino sphere, see section 2.3.2 for details, one can assume the following luminosity relation between the flavors after 20 ms [112]:

$$L_{\nu_e} \approx L_{\overline{\nu}_e} \approx 2L_{\nu_x} ,\nu_x \in (\nu_\mu, \overline{\nu}_\mu, \nu_\tau, \overline{\nu}_\tau) \tag{2.17}$$

These neutrino production reactions are kept alive by continuous and inwards oriented flow of matter. The stellar medium is heated up and compensates for the energy loss by neutrino emission. For a successful explosion of the star the deposited energy has not only to be the driving force for neutrino production but is also in charge of the acceleration of the outer layers of the star.

Cooling

Towards the end of the accretion phase the neutrinos diffusing from inner layers dominate the luminosity of the star ($t_{pb} \approx 500\mathrm{ms}$). Since the Kelvin-Helmholtz cooling starts outside the PNS it can take between $10 \ldots 60$ seconds before the central temperature drops below $T_c \approx 10^{10}\,\mathrm{K}$. The neutron star now becomes transparent for neutrinos. The PNS core region becomes denser, the neutronization of the core progresses and the luminosity of electron neutrinos decreases slowly. During this hydrostatic moderation more than 90% of the gravitational binding energy of the PNS is released via neutrino emission of all flavors.

2.3.2 Energy Spectrum

Besides the fact that the four phases explain well the basic neutrino luminosity picture one has to keep in mind that a profound understanding of the energy spectrum is important for any detection of supernova neutrinos. The following review is guided by [112].

The thermal energy spectrum of electrons and positrons in the stellar plasma also goes over to neutrinos due to inelastic scattering processes. In first approximation, this distribution follows a black body spectrum. In reality, several effects modify the spectral shape.

The opacity of ν_e and $\overline{\nu}_e$ are dominated by the just mentioned inelastic scattering processes in charge current interactions with nucleons: $\nu_e p \longrightarrow ne^+$ and $\overline{\nu}_e n \longrightarrow pe^-$. For a neutrino with a particular energy E_ν these reactions freeze out at a certain distance defining an energy dependent neutrino sphere. This results in a suppressed high energy tail, compared to the thermal spectrum of the same mean energy because the neutrino spheres reside at different temperatures. Since the atmosphere of the PNS is neutron-rich, the opacity of electron neutrinos is higher than for the corresponding anti-particles. Therefore, for a given E_ν, the $\overline{\nu}_e$ flux originates at deeper, i.e. hotter and energetically higher, layers than the ν_e flux. Consequently, the former encounter more interactions with the stellar plasma than lower energetic ones and create a narrower spectrum. Since a larger fraction of the $\overline{\nu}_e$ flux originates from higher energetic regions their mean energy is also higher. A similar but more complex picture also holds for the heavier flavors. Opacities are dominated by neutral current interactions, i.e. elastic scattering on nucleons ($\nu_{\mu,\tau}N \longrightarrow \nu_{\mu,\tau}N$), but are not considered to be efficient with respect to energy exchange. For ν_μ and ν_τ the main channels of energy exchange with the stellar plasma are elastic scattering on leptons, specially $\nu_{\mu,\tau}e^- \longrightarrow e^-\nu_{\mu,\tau}$, the recoil in nucleon scattering processes ($\nu_{\mu,\tau}N \longrightarrow \nu_{\mu,\tau}$) and inelastic scattering on nucleons ($\nu_{\mu,\tau}NN \longrightarrow \nu_{\mu,\tau}$), respectively. Furthermore, neutrino pair production processes take place, e.g caused by nucleon bremsstrahlung, $NN \longrightarrow NN\nu_{\mu,\tau}$. These reactions freeze out at different radii for a given E_ν so that one can define different spheres based on the underlying mechanisms. Among these regions, the largest sphere lays usually deeper inside the star than R_{ν_e}. From simulations one expects the following hierarchy of the time-integrated mean energies (robustness varies by the model applied):

$$\langle E_{\nu_\mu,\nu_\tau}\rangle > \langle E_{\overline{\nu}e}\rangle > \langle E_{\nu_e}\rangle \tag{2.18}$$

Over the last decades the modeling has improved constantly with the tendency of newer simulations producing somewhat cooler spectra and therefore fewer interaction events than older models. The fluxes are expected to have the approximate spectral form, parametrized by (e.g. [105, 112]):

$$f\left(E_\nu, \langle E_\nu\rangle(t), \alpha(t)\right) = N\left(\frac{E_\nu}{\langle E\rangle}\right)^\alpha \exp\left[-(\alpha+1)\frac{E_\nu}{\langle E\rangle}\right] \tag{2.19}$$

where α is often referred to as the "pinching parameter" because it controls the high-energy tail of the function, usually holding values $2 \leq \alpha \leq 5$. E_ν denotes the neutrino energy, $\langle E\rangle$ the mean neutrino energy and

$$N = \frac{(\alpha+1)^{\alpha+1}}{\langle E\rangle\Gamma(\alpha+1)} \tag{2.20}$$

is the normalization constant with the Gamma function Γ. Figure 2.6 shows an example of such a flux prediction, integrated over different time ranges. In general, the spectra of ν_e, $\overline{\nu}_e$ and ν_x are expected to have different mean energies $\langle E_\nu\rangle$ and α parameters and evolve in time.

The energy spectrum at any observer's site will be modified from the above original spectrum. Effects from neutrino oscillations (in stellar matter and inside the Earth,) see chapter 1.1, will imprint their signature as modulations in the spectrum which will provide us with hints about the neutrino oscillation parameters themselves as well as the supernova matter profile. A detailed discussion of the potential supernova neutrino signal in IceCube and the physics conclusions that can be drawn from it will be given in chapter 4.2.

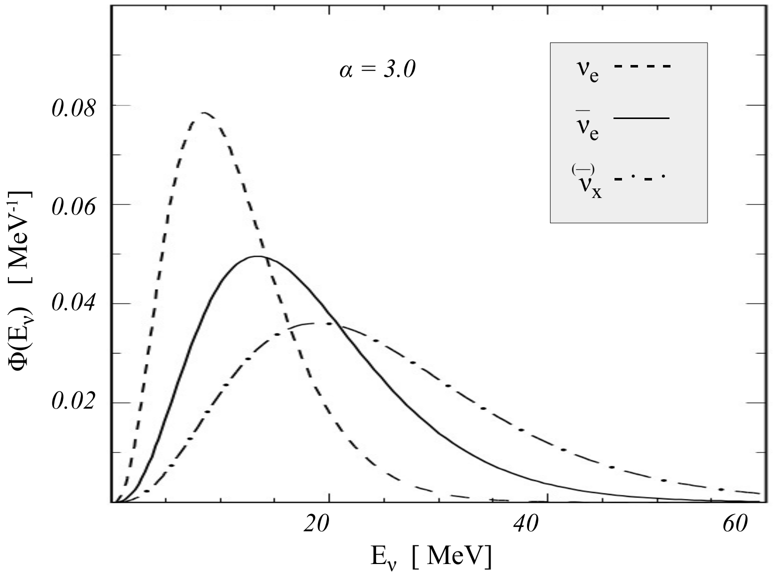

Figure 2.6: *Expected supernova neutrino energy spectra associated to the supernova neutrino burst as modeled in [113], averaged in the time interval for shock-wave effects ($t > 2s$) with shape parameter $\alpha = 3$ as defined in the parametrization in equation 2.19 .*

2.4 Results from Modern Simulations

The underlying processes that trigger the explosion of massive stars are still not understood in their details. All progress in understanding the complex mechanism of SNe is based on relativistic hydrodynamic simulations because the amount of neutrinos detected from a stellar explosion, see section 2.6, are too sparse to constrain the mechanism. So far, it was not possible to develop a satisfying standard model of core-collapse explosion. Amongst all possibilities the neutrino-heated scenario is favored because of its ability to trigger explosion in simulations of mid-range massive stars. This is due to the fact the models are not self-consistent because of unknown details in their equations of state (EoS) which combine matter composition with energy and pressure in the star. The input for the EoS is highly complex and depends on interactions via all four fundamental forces. The following section summarizes the challenges and result from the last decade of theoretical research.

2.4.1 SASI

It was not until the year 2003 that existing simulation models could predict a stellar explosion for stars heavier than $15\mathrm{M}_\odot$ and then only under very constrained circumstances, namely neutron-finger convective instabilities in the PNS (e.g. [114, 115]).

The authors of [116] found the right words to describe the situation when asking for the missing parts in the improved simulation models that still don't result in an explosion. They investigated two-dimensional hydrodynamic simulations with and without rotation performed by solving the Boltzmann equation for neutrino transport. Convections below the neutrino sphere and in the neutrino-heated region behind the shock could be observed but the models still did not explode. From their findings, the authors conclude that the models are missing physics, possibly related to the nuclear equation of state (EoS) used in the simulation [117] and weak interactions in the sub-nuclear regime. Furthermore, these results confirm the concerns that the success of previous simulations was only due to simplified assumptions of neutrino transport [118]. A possible solution to this fundamental problem was proposed by the authors of [119] who summarize their finding as *Standing Accretion Shock Instabilities* (SASI). The introduction of asymmetric perturbations by acoustic shock waves leads to growing turbulences in the post-shock region providing the necessary additional energy for letting the star explode. The problem with earlier simulations based on [118] was that the separation between the shock front and PNS surface was never sufficient for letting perturbations grow significantly enough to provoke instabilities because the chosen geometries were just too confined. The origin of the SASI, as described e.g. in [110], lies in the fact that the accretion shock is not stable and does not remain symmetric. It rather develops growing radial deformations due to small stochastic perturbations which are amplified via *Rayleigh-Taylor instabilities*. They arise when two substances of different density encounter small perturbations on their boundary layer. Due to accelerating forces[8], bubbles of hot gas rise up and colder, denser plasma sinks down in narrow tubes towards the PNS.

When transported towards the PNS, these fluctuations grow larger turbulences and temperature density variations as the matter current becomes more constricted to smaller radii. The result is an outwards oriented wave traveling back to the shock front with sonic speed against the in-falling matter. The sound waves hitting the accretion shock generate new perturbations resulting in even more turbulences in accretion flux. This creates a feedback process, where by a current of matter flowing inwards, hits the PNS surface and creates sound waves opposing it, amplifying each other. This stimulates oscillations of the shock front that are growing in time, see Figure 2.7, they are two-fold since they can be bi-polar modes and hemispherical.

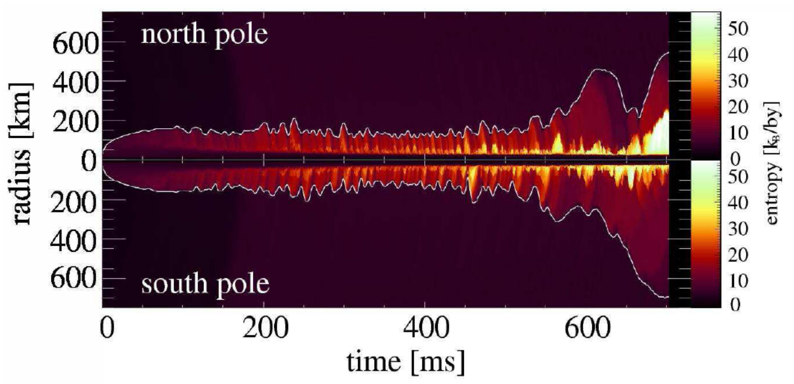

Figure 2.7: *Expansion and contraction of the shock until the start of the explosion of a 15 $M_\odot$ star progenitor simulation. Radial position of the shock near the north and south poles as a function of post-bounce time. The color scheme reflects the entropy per nucleon of the stellar plasma, i.e. hotter region due to neutrino heating. Clearly visible are amplitudes of the quasi-periodic and bi-polar (i.e. g-mode) vibration of the matter due to the SASI [120].*

These strong variations in the shock radius secondarily also create Rayleigh-Taylor instabilities in the accretion flow. In some simulations the explosion is driven mostly by another effect but also having its origin in the SASI. Sound waves coming from the pulsation of the PNS [121] dominate over the neutrino transport for being the driving force behind the explosion. In this *acoustic mechanism* the PNS itself starts to oscillate in so-called g-modes[9] due to anisotropic

---

[8] Not only gravity plays a role in the SN case. In outer stellar regions the pressure gradient is an even more important force for accelerating plasma layers against each other.

[9] Oscillations of spherical objects are parametrized by the Laplace equation for spherical harmonics where

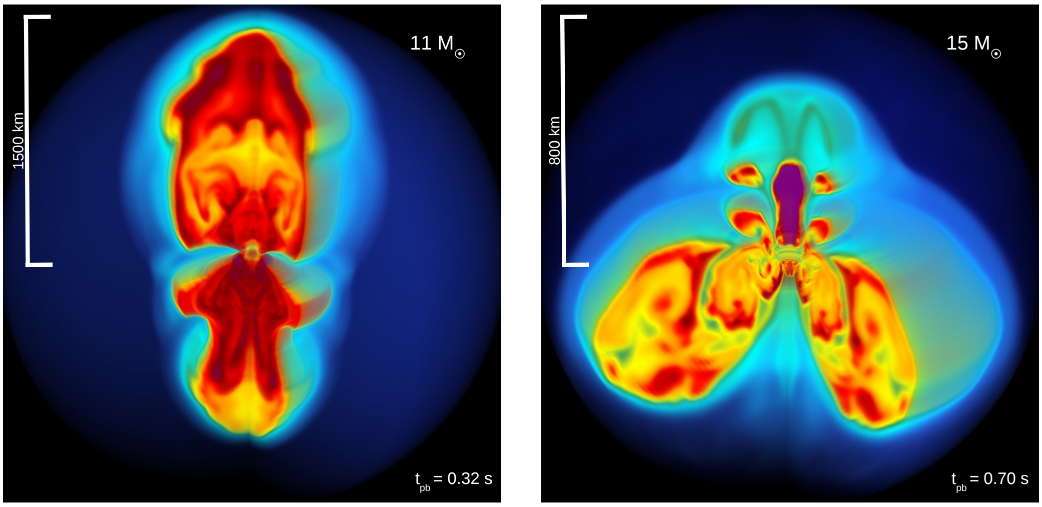

(a) **(b)**

Figure 2.8: *Snapshots from the evolution of supernova explosions in simulations from [120] for a non-rotating 11.2 $M_\odot$ in* **(a)** *and a rotating 15 $M_\odot$ model in* **(b)***, respectively. The color coding represents the entropy of the stellar gas (where blue means less and red means stronger heated gas). The times displayed are post-bounce time stamps.*

accretion of the impinging gas and sends pressure waves into its environment. Opposing to this scenario are the results from simulation of other authors who find that the acoustic energy input from both SASI effects to the developing blast is negligible compared to the neutrino energy deposition [120]. In summary one can say that the scientific community agrees on the following facts regarding the origin of the core-collapse supernova mechanism deducted from simulations:

1. The prompt shock scenario is ruled out.
2. The neutrino-driven mechanism, as explained in 2.2.2, is capable of explaining the explosion of light-mass $(8 - 10 M_\odot)$ stars that consist of an O-Ne-Mg core. These SNe are called electron capture Supernova (ECSN) because of the mechanism triggering the collapse.
3. Besides neutrino heating, multidimensional perturbation effects play an important role for heavier stars. Resulting strong vibrations keep the matter longer in the neutrino-heating region. Hence the energy of the neutrinos in this layer is higher and they can transfer more energy to the explosion and strengthen the heating mechanism.

The combination of these effects leads to an extremely asymmetrical shock front and finally to the explosion, as can be seen in Figure 2.8. The shock is visible as deformed sharp discontinuity between low-entropy, in-falling matter in the upstream region and high-entropy, boiling matter behind the shock (the shock front is situated at the transition from light to dark blue in the plots). Even though the lighter model doesn't rotate it also develops an extreme global asymmetry like the heavier one due to SASI. The symmetry with respect to the vertical axis results form the simulation being performed in 2 dimension only. Nevertheless, it is still

l denotes the degree and m stands for the order of oscillation. The mentioned gravity mode (g-mode) is describing the situation when $l = m = 1$.

not clear how much influence the acoustic effects resulting from the SASI really have on the delayed explosion of massive stars. At this point, more advanced simulations are needed to answer this ambiguity and to understand the processes of the explosion mechanism in more detail. One step towards this goal was recently made by three dimensional simulations where unexpected new features were found.

2.4.2 LESA

Recent 3-dimensional simulations show a new, spherical-symmetry breaking instability during the stalled-shock phase. It was observed that the lepton number flux, i.e. the difference between electron- and anti-electron neutrino emission $(F_{\nu_e} - F_{\overline{\nu}_e})$, emerges predominantly in one hemisphere. In this so called *Lepton-number Emission Self-sustained Asymmetry* [122], abbreviated LESA, the individual ν_e and $\overline{\nu}_e$ fluxes show a strong dipole pattern whereas the heavier flavor fluxes and the total luminosity remain almost spherically symmetric. The manifestations of this new phenomenon are summarized here, following [54, 122], concluded by an overview of the presently known symmetry breaking instabilities and their consequences.

Although this effect should not be unique to 3d simulations, it was not seen in previously performed lower dimensional simulations. Dipole asymmetry would be limited to the polar axis especially in two dimensional models . Artificial hemispherical differences arise because of this preferred symmetry axis where the simulation tends to project infalling matter either in- or outwards. Furthermore, sloshing motions of the shock front are directed along the axis strongly reinforcing the vibrations. Therefore, any hints of LESA in two dimensions might be present but masked by other effects.

The complete scenario of the LESA is a composition of several effects arising on the one hand in the post shock region and on the other hand inside the PNS, see Figure 2.9. The schematic drawing shows a cut through the center of the star at a time when the outwards propagating shock-front (solid black line) is turned into a standing accretion shock due to energy dissipating neutrinos and converging matter flow. In the region between the shock and the gain radius (gray dotted line) it comes to large-scale convective overturn (gray arrowed lines) because of a negative entropy gradient in the neutrino heating region [118] which is supported by Rayleigh-Taylor instabilities. Due to stochastic convective fluctuations, a dipolar deformation of the shock is provoked that deflects the accretion flow (red line) mostly towards one hemisphere. The shock radius is increased on the other hemisphere where the mass accretion rate is lower and the $\overline{\nu}_e$ flux is maximal, i.e. experiencing a minimal lepton-number flux. This situation is boosted by stronger neutrino heating due to the mean energy hierarchy $(\langle E_{\nu_e}\rangle < \langle E_{\overline{\nu}_e}\rangle)$ sustaining the strong convection on this side of the star. This positive feedback loop is the underlying force of the LESA. In the meanwhile *Ledoux* convection in the PNS below the neutrino sphere sets in. This material transfer is caused by neutrino losses that produce a inwards oriented deleptonization wave with a negative lepton number gradient [123]. The PNS develops pronounced convection in the hemisphere where the mass accretion rate of lepton-rich matter is larger[10] due to the previously explained deflection. Whereas the density distributions (red circular regions) around the mass center (black dot) stay spherical, a displacement of levels with constant electron fraction per baryon (Υ_e) can be observed (blue shapes) due to the anisotropic PNS convection. Even though the convective overturn behind the shock front is highly non-stationary and varies in time, these deformations persist and can last for multiple hundreds of milliseconds, even continuing during the SASI period. This results in a hemispheric asymmetry of the ν_e and $\overline{\nu}_e$ energy flux (brown and magenta arrows) that can reach between 20% to 30% deviation from their average values. Nevertheless, the overall sum of the fluxes is approximately uniform with a dipole variation only on the percent level. The nature of this interesting asymmetry implies that deviations of the neutrino luminosity from their average over all directions depend highly on the observers location. Figure 2.10 shows the expected result of the luminosity evolution for a 11.2 $M_\odot$ progenitor star's explosion. Strong alternations are visible for the ν_e and $\overline{\nu}_e$ luminosities, depending on the position of the observer relative to the star. The shown variation results when choosing the observers location to be along the axis of the greatest flux variation. The dipole pattern is clearly visible in ν_e (green line) and $\overline{\nu}_e$ (red line in figure). Although there is no SASI activity in this model, we see small and fast changing amplitude variations that are due to the large-scale convective overturn instability. The case is less distinct for heavier flavors.

---

[10] indicated in Figure 2.9 by the size of the black loops

A somewhat different scenario is visible in simulations for heavier progenitors that show extensive modulations in their corresponding amplitudes. These can be attributed to accretion variations caused by SASI spiral modes that in the end also lead to fluctuations in the neutrino emission. Among the performed simulations, the scenario is most impressively visible in the case of the 27 $M_\odot$ progenitor, see Figure 2.11. The plot shows clearly the LESA in between the first two SASI modes.

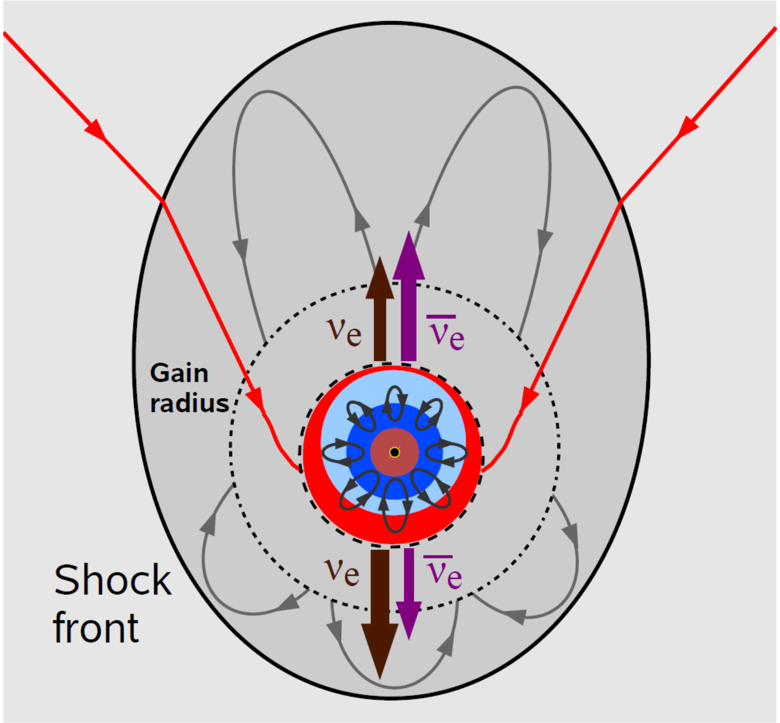

Figure 2.9: *Illustration of the self-sustained lepton-emission asymmetry. See text for explanations. Taken from [122].*

It has to be mentioned that this LESA phenomenon has to be observed by other research groups in order to ensure that it is not a numerical artifact of the simulation but real physics.

Table 2.3 summarizes the diverse mechanism of instabilities in the core-collpase supernova explosion.

Table 2.3: *Summary of spherical symmetry breaking instability processes in a core-collapse supernova ([122] and references therein). The convection-based instabilities are divided further by their region of appearance.*

Phenomenon	Location	Origin	Result
Prompt Postshock Convection	post shock region	hydrodynamic	gravitational wave emission
Ledoux Convection	post shock region	hydrodynamic	gravitational wave emission
Large-scale Convection	hydrodynamic	below stalled shock	increased neutrino-heating, delayed explosion possible
SASI	PNS & below shock front	hydrodynamic, acoustic	neutrino-heating, neutron-star kicks, quasi periodic neutrino emission, SN gravitational wave signal
LESA	PNS & below shock front	hydrodynamic, acoustic	dipole deformations of deleptonization flux, asymmetric PNS convection, asymmetric accretion, neutrino-heating

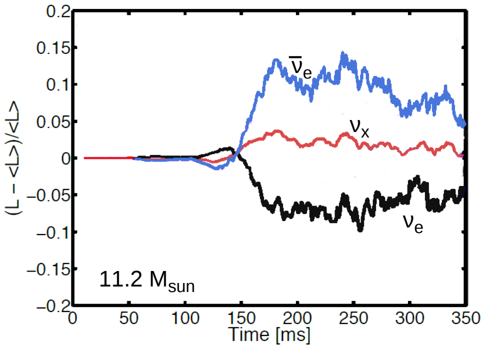

Figure 2.10: *Luminosity variations of a 11.2 $M_\odot$ progenitor for ν_e (black line), $\overline{\nu}_e$ (blue line) and ν_x $(x = \mu, \tau)$ (red line) relative to the time-dependent average over all directions $\langle L \rangle$ [54]. The observer location is chosen such that the flux variation is largest. The strong dipole pattern of the ν_e and $\overline{\nu}_e$ is clearly visible. There is no SASI in this simulation.*

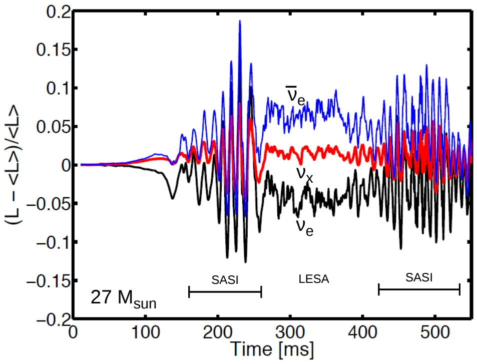

Figure 2.11: *Luminosity variations of a 27 $M_\odot$ progenitor for ν_e (black line), $\overline{\nu}_e$ (blue line) and ν_x $(x = \mu, \tau)$ (red line) relative to the time-dependent average over all directions $\langle L \rangle$ [54]. The observer location is chosen to be approximately in the plane where SASI develops. LESA activity is clearly visible although the line of sight does not coincide with the LESA axis.*

2.5 Galactic Supernova Rate

Several approaches can be taken to achieve estimating the core-collapse rate in our galaxy. The most natural would be to count the number of events observed in our home galaxy. Over the last millennium, the historic record contains six galactic events which implies a rather low rate. The most recent detected supernova remnant (SNR) originates from a type IIb explosion in the 17th century which is situated in the *Cassiopeia* constellation in our Milky Way. The sparsity of observations is most likely due to obscuration by the interstellar medium since the only detection channel of the past was in the optical regime. With neutrino detectors like IceCube this hurdle is overcome and we will discuss results of these type of detectors in detail in sections 4.2 and 4.3. Another conceivable approach is to count the events in other galaxies and compare to our home galaxy. This introduces selection effects because the supernova rate is not constant among different galaxy types. As the authors of [124] found, SNe are more common in spiral galaxies than in elliptic ones, see Figure 2.12. This holds true especially for type II SN which are closely related to the star formation rate (SFR) in the galaxy under investigation. By plugging in the luminosity for the SN rates of the same galaxy type one can deduce the SN rate in the Milkyway to 1.3 ± 0.9 [125].

A third way of solving this challenge is by counting objects that could be SN remnants. If one assumes that all CCSN either leave a pulsar or a black hole one derives a galactic core-sollpase SN rate of 3.2 to 3.7 per century [126]. Problems of this method are selection effects and the vague ratio of SNe to pulsars. The last method of calculating the galactic supernova rate to be mentioned here is the measurement of gamma-rays from galactic elements, i.e. ^{26}Al, ^{60}Fe or ^{44}Ti [127, 128]. All four of these techniques have their advantages and shortcomings and were investigated by variety of authors, as can be seen in Figure 2.13.

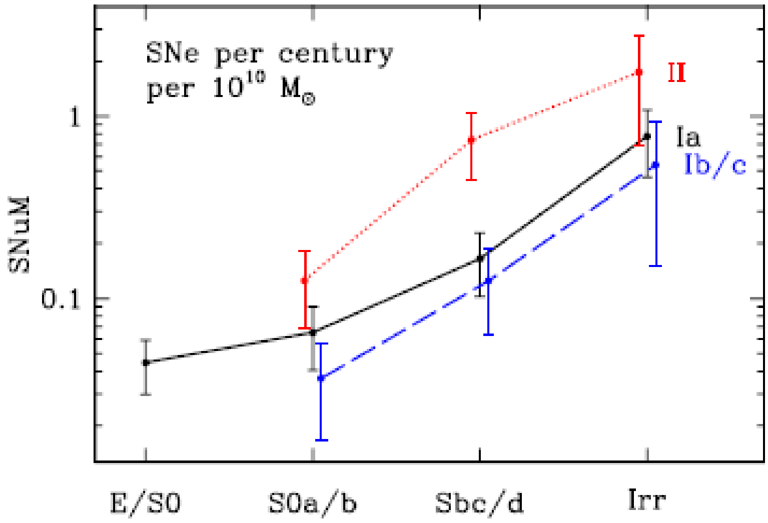

Figure 2.12: *Supernova rate depending on the morphology of the galaxy [124]. Values of core-collapse SN for elliptic galaxy types (E/S0) are particularly small and not plotted. For type Ib/c:* $SnM < 0.0093$ *and type II* $SnM < 0.013$, *respectively. S0a/b and Sbc/s stands for spiral galaxy types and Irr for irregular morphology , following Hubbles classification.*

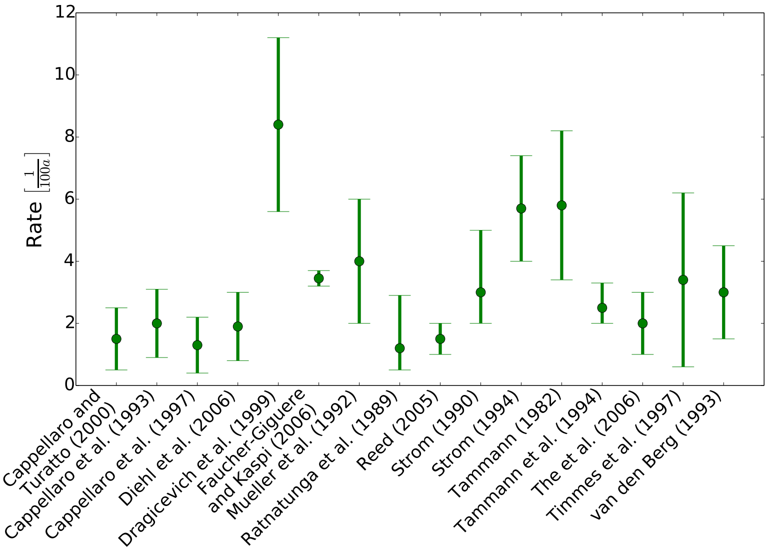

Figure 2.13: *Theorethical estimations of the rate of core-collapse supernovae in the Milkyway per century. References are partly mentioned in the text or can be find in [9]*

2.6 Lessons from SN1987A

The explosion of the 18 $\mathrm{M}_{\odot}$ massive blue supergiant *Sanduleak*, see Figure 2.14, in the Large Magellanic Cloud (LMC) produced the brightest ever detected supernova and the first one observed by naked eye since Kepler's supernova in 1604. Although this type II supernova did not happen in our galaxy but in the LMC, interesting conclusions could be drawn from the few events observed by several detectors. At 7:35 universal time on February 23rd 1987, the water-Cherenkov detectors IMB [129] and Kamiokande-II [130] registered neutrino events that were clearly attributed to SN1987A. Also the Baksan scintillator detector reported on the observation of events [131] which is in agreement with the others under the given temporal uncertainty. Further experiments active during that time, i.e. the Liquid-Scintillator-Detector (LSD) and the Homestake Solar Neutrino Experiment were not able to detect significant events. In total, 25 neutrinos made history for being the first directly detected extra-solar neutrinos.

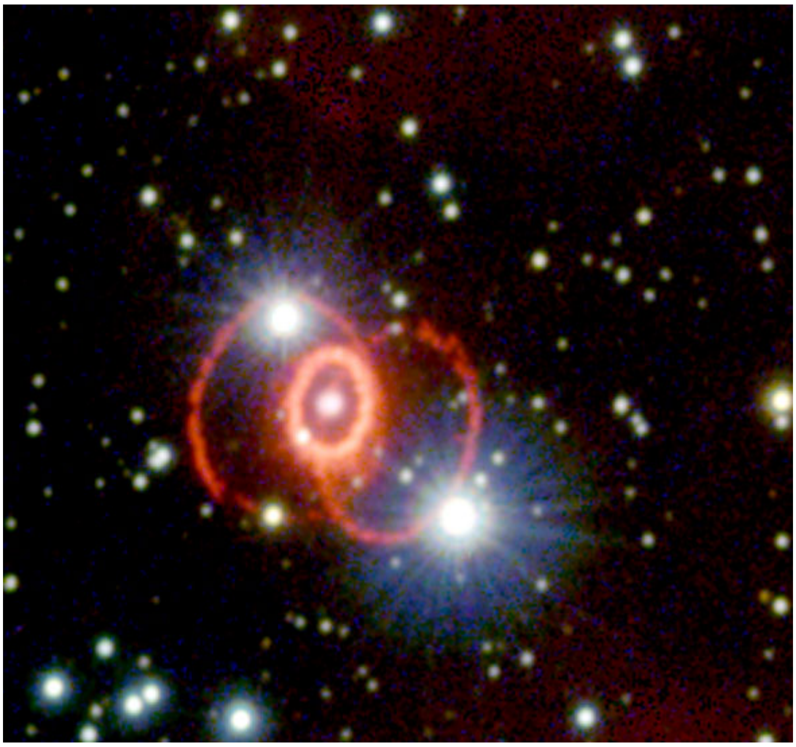

Figure 2.14: *This Hubble Space Telescope image, taken in February 1994, shows the full system of three rings of glowing gas surrounding supernova 1987A [132].*

Despite the low quantity of events, only 25 out of 10^{58} neutrinos emitted by the SN were detected, it was possible to draw basic conclusions about the underlying explosion mechanism and the released binding energy. From Figure 2.15 one can extract a maximal temporal distribution of the neutrino events of about 12.4 seconds. This is in good agreement with the standard picture of the core-collapse scenario where the diffusion of neutrino during the PNS cooling phase (see Section 2.2.2) lasts from seconds up to one minute. Since SN neutrinos do not follow exactly a blackbody distribution, as explained in 2.3.2, the effective temperature and luminosity of the observed $\overline{\nu}_e$ can be estimated via a Monte Carlo simulation of neutrino transport during the cooling phase which results in a thermalized neutrino energy T_ν and total energy of the anti-electron neutrino $E_{\overline{\nu}_e}$ [133]:

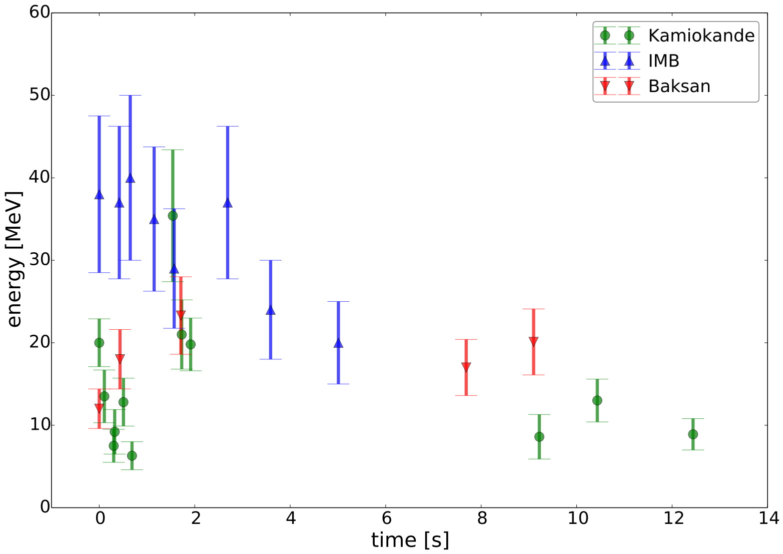

Figure 2.15: *Energies of all events detected at 7:35 UT on February 23, 1987 versus time.* $t = 0.0$ *is set as the time of the first event of each signal observed.*

$$T_\nu = 3.4^{+1.1}_{-0.8}\mathrm{MeV} \qquad \text{and} \qquad E_{\overline{\nu}_e} = 5.3^{+5.0}_{-2.6} \cdot 10^{52}\mathrm{ergs}, \tag{2.21}$$

with an overlap of 95% C.L. for the detections in Kamiokande and IMB. Furthermore, constraints on the anti-electron neutrino's electric charge and lifetime could be evaluated, as explained in detail in [134], resulting in an upper limit on its mass:

$$m_{\overline{\nu}_e} < 13\mathrm{eV}, \qquad \tau_{\overline{\nu}_e} \geq 2.5 \cdot 10^5\mathrm{s}\frac{m_{\overline{\nu}_e}}{\mathrm{eV}}, \qquad Q_{m_{\overline{\nu}_e}} < 10^{-18}e \qquad . \tag{2.22}$$

SN1987A was the start of modern supernova neutrino physics and, as one can imagine, triggered lots of research in the scientific community. It did not take long until the first simulation, modeled after SN1987A, was developed (e.g. [135]). A 1-dimensional numerical model was performed that simulates the average energy and luminosity of the emitted neutrinos from collapse onset until 18 seconds after core bounce [113]. Figure 2.16 shows the resulting time evolution for all neutrino flavors of this so-called *Lawrence-Livermore* model. Although these plots differ from more recent simulations, the result is highly remarkable given the fact that all input is derived from only a few neutrino events.

However, a larger number of detected events is crucially important for a more detailed understanding of SN explosions. The signatures will be seen in the time evolution of the neutrino luminosity and spectrum only in enough detail if the amount of events guarantees a statistical reconstruction of the temporal behavior. The IceCube detector is one of only two experiments worldwide that is able to provide such high statistics in case of a galactic explosion, with Super-Kamiokande being the other. The aim of the present work is to elaborate IceCube 's capability of providing answers for fundamental particle physics questions via the detection of supernova neutrinos.

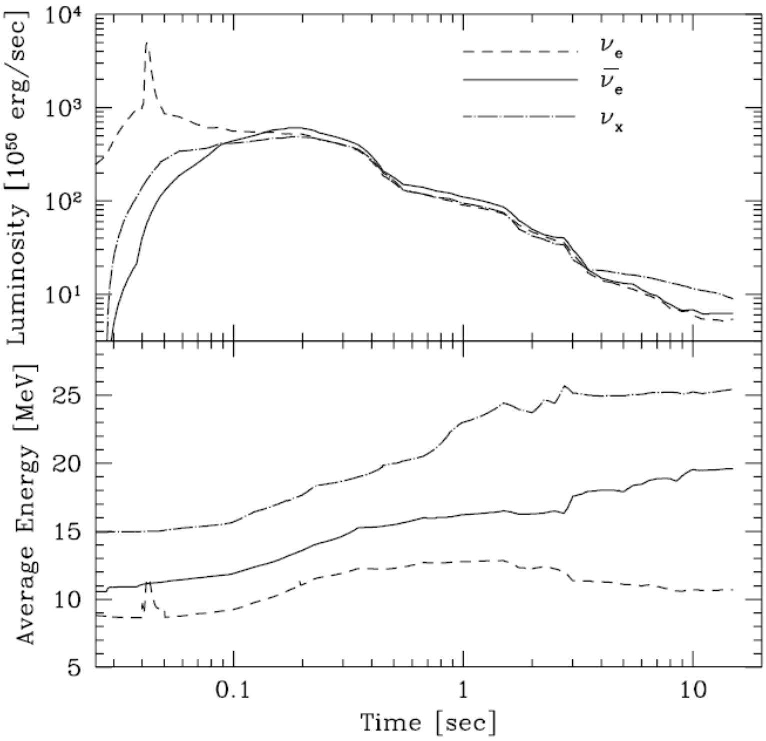

Figure 2.16: *First one-dimensional simulation of a supernova explosion from the onset of the collapse to 18 seconds after the core bounce. Neutrino luminosities and average energies are based on results from SN1987A whose progenitor is a main-sequence star of about* $20M_\odot$ *[113].*

Part II

Detector

3

The IceCube Neutrino Observatory

The IceCube Neutrino Observatory was primarily build with the intention to detect energy and direction of high energy neutrinos originating in sources outside the solar system and to characterize their properties. Thus the overall detector design, data acquisition and data processing are optimized towards that goal. The fact that it also enables us to search for low energy galactic supernova neutrinos gave rise to a dedicated supernova data stream which is covered separately in Chapter 4. In Section 3.1 of the present chapter the macroscopic design of the IceCube neutrino observatory is explained before we go into the microscopic details of its components in Section 3.2. Section 3.3 gives all the necessary details about the data streams and data processing.

3.1 The IceCube Detector

The IceCube Observatory is a kilometer-scale Cherenkov neutrino telescope with its main part being buried in the deep Antarctic ice sheet at the geographic South Pole, see Figure 3.1. The observatory consists of three parts that are dedicated to different scientific goals. The main array consists of 5160 light sensors, deployed between 1450 m and 2450 m below the ice surface and distributed over 86 strings in a hexagonal pattern. Each string supports 60 light sensors with integrated data acquisition, the so-called Digital Optical Modules (DOMs), see Section 3.2. The standard spacing of 125 m between strings and 17 m between DOMs is optimized on the primary scientific goal to detect high energy extra-solar neutrinos [7, 8]. Among the 86 strings, 78 are deployed following this scheme for the main detector of IceCube [136, 137]. The remaining 480 DOMs on 8 strings are deployed in the deep ice below a depth of 1750 m forming a denser instrumented volume. This sub-array, the *DeepCore* [138], with its inter-string spacings of 70 m and inter-DOM spacing of 7 m, is dedicated to the detection of atmospheric neutrinos, typically being lower in energy [139]. The observatory is completed by the *IceTop* air shower array [140], consisting of 81 stations, each hosting two frozen water tanks instrumented with two DOMs, for measuring cosmic rays in order to reveal their composition and characteristics [141]. The data from all DOMs are collected via kilometer long cables to the IceCube Laboratory (ICL) on the ice surface hosting the necessary IT environment for online data acquisition and processing, see Section 3.3. The

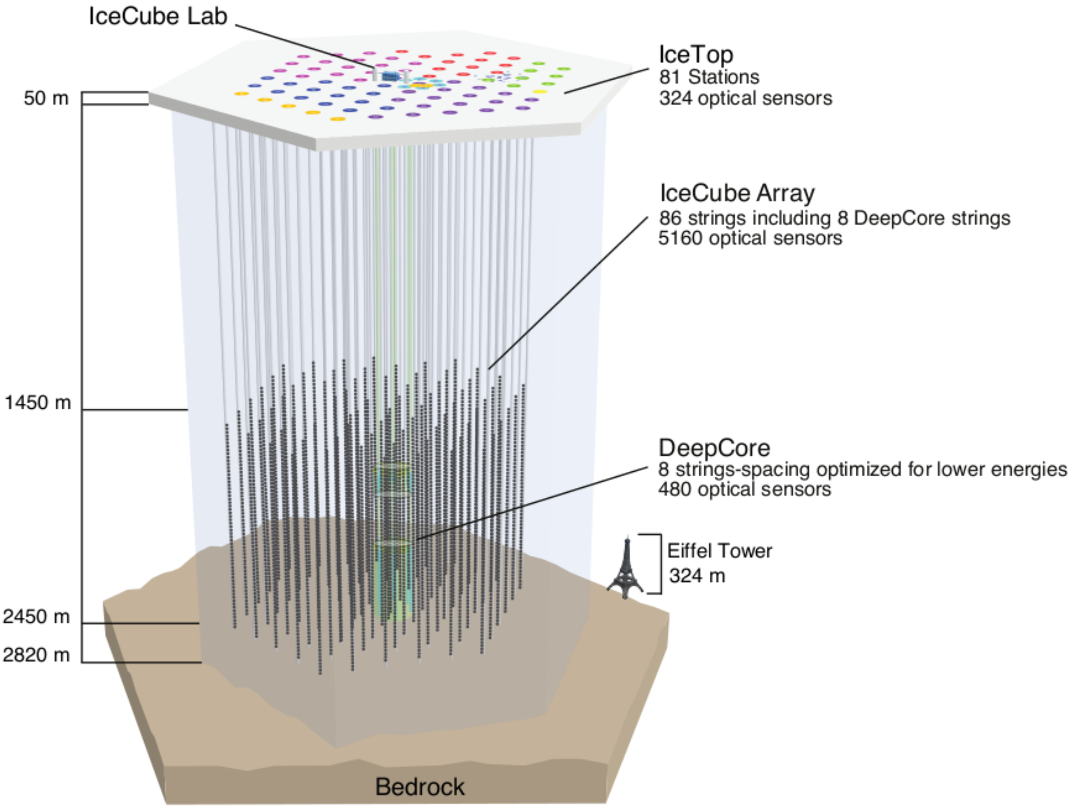
IceCube Lab
IceTop
81 Stations
324 optical sensors
IceCube Array
86 strings including 8 DeepCore strings
5160 optical sensors
DeepCore
8 strings-spacing optimized for lower energies
480 optical sensors
Eiffel Tower
324 m
50 m
1450 m
2450 m
2820 m
Bedrock

Figure 3.1: *The IceCube Neutrino Observatory with its sub-array DeepCore and the air shower array IceTop.*

geometric arrangement of the array is depicted in Figure 3.2. Details of the ice composition, including the so-called *dust layer* shown in Figure 3.2b, are presented in Section 4.2.1.

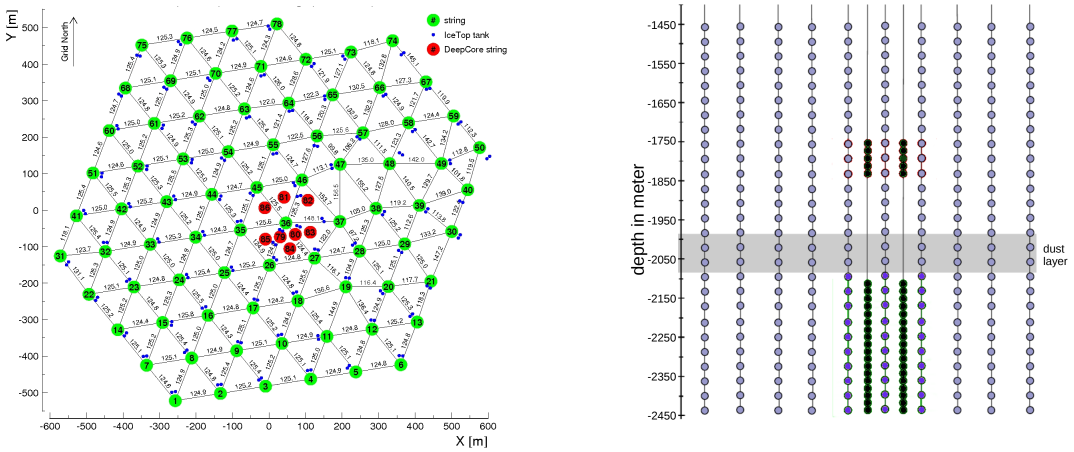
Y [m]
Grid North
500
400
300
200
100
0
-100
-200
-300
-400
-500
-600
-500
-400
-300
-200
-100
0
100
200
300
400
500
600
X [m]
string
IceTop tank
DeepCore string
depth in meter
-1450
-1550
-1650
-1750
-1850
-1950
-2050
-2150
-2250
-2350
-2450
dust layer

(a) *Footprint of* ICECUBE.

(b) *Side view, not to scale.*

Figure 3.2: *IceCube's top and side view. The origin of the x-y plane is set to the position of string 86. The vertical DOM position is shown on the right. DeepCore DOMs (black dots) are instrumented denser than DOMs on standard strings (blue dots) and elude the dust layer (gray band).*

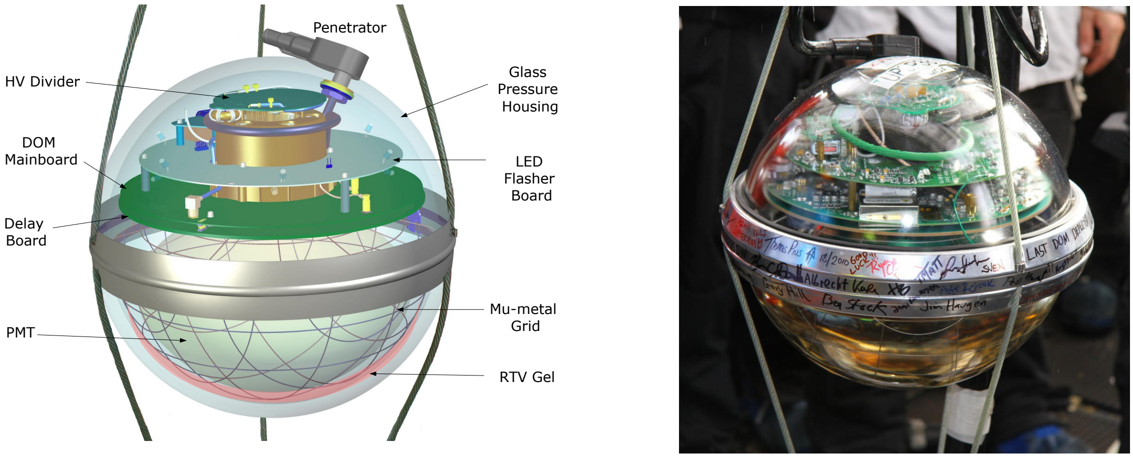

(a) *Schematic of the DOM*

(b) *Picture of the final deployed DOM in December 2010.*

Figure 3.3: *Technical drawing of the DOM and its main hardware components on the left. The picture on the right shows the final of 5160 deployed DOMs.*

3.2 The Digital Optical Module

The method used by IceCube for detecting particles is based on the Cherenkov effect, as explained in Section 1.4.2. Charged by-products of primary particles interacting in the ice emit photons if they travel faster than the local speed of light. The centerpieces of IceCube are the individual detection devices, the Digital Optical Modules (DOMs). They record these photons with a photomultiplier tube (PMT), described in Section 3.2.1 and the necessary readout electronics, see Section 3.2.2. The present section summarizes technical details of the DOM published in [142–144].

All hardware components of a DOM, as shown in Figure 3.3, are enclosed in a 13 mm thick pressurized glass sphere in order to protect them from humidity, temperature and especially the pressure arising from the refreezing drill-hole ice, that can be as high as 400 bar. Communication with the surface ICL but also with its neighboring DOMs as well as power supply for the DOM are realized via a penetrator connecting the DOM to its suspending cable. The high voltage (HV) divider inside the module transforms the low voltage input of 48 V to roughly 1400 V, needed for operating the PMT. The power consumption of the entire device is 3.5 W which results in a local heating of about 10° above the surrounding ice temperature. Furthermore, a flasher board is installed that holds twelve individually selectable LEDs capable of emitting pulses of $\mathcal{O}(10\,\mathrm{ns})$ duration. These beacons emit up to 1×10^9 single photon pulses and are not only used for calibrating the modules' position relative to each other but are also crucial for characterizing the optical properties of the ice.

3.2.1 Photomultiplier Tube

IceCube uses PMTs from Hamamatsu with a 25.4 cm (10") cathode surface [1]. The declared maximum quantum efficiency, i.e. the number of produced photoelectrons over the actually impacting photons, is given with 25 % at a photon wavelength of 390 nm and the optical acceptance reaching from 300 nm to 675 nm. In order to optically couple the PMT to the surrounding glass sphere, it is embedded in a silicon based gel. Furthermore, the PMT is surrounded by a Mu-metal cage that absorbs the magnetic flux of the low frequency varying magnetic field of the Earth and hence guarantees an undistorted signal. A photon reaching the PMT can be absorbed by the photo-cathode, releasing an electron that passes ten dynodes to reach a final amplification factor of about 10^7 [143]. Recognized as a change in voltage at the PMT's anode, the resulting signal is then passed to the DOM mainboard for further processing.

---

[1] Model reference number: R7081-02

3.2.2 DOM Mainboard

Figure 3.4 shows the electronic components of the DOM mainboard (DOM MB) where the signal processing from the PMT starts in the upper left corner of the diagram.

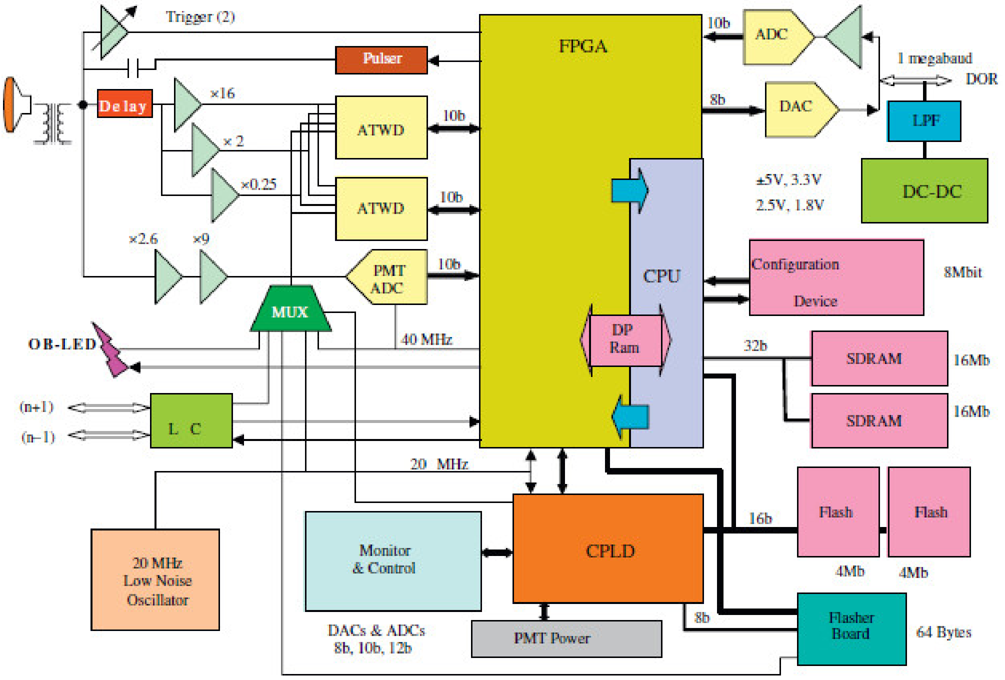
Trigger (2)
Pulser
FPGA
10b
ADC
1 megabaud
DOR
8b
DAC
LPF
De lay
×16
×2
×0.25
ATWD
10b
ATWD
10b
±5V, 3.3V
2.5V, 1.8V
DC-DC
×2.6
×9
PMT ADC
10b
CPU
Configuration Device
8Mbit
MUX
OB-LED
40 MHz
DP Ram
32b
SDRAM
16Mb
SDRAM
16Mb
(n+1)
(n–1)
L C
20 MHz
Flash
Flash
16b
4Mb
4Mb
20 MHz Low Noise Oscillator
Monitor & Control
CPLD
8b
Flasher Board
64 Bytes
DACs & ADCs 8b, 10b, 12b
PMT Power

Figure 3.4: *Block-diagram of the DOM mainboard components [142]. A photon hits the photomultiplier, which is in the upper left. This signal is split to the ATWD and fADC. The entire readout is controlled by the FPGA. Details about the waveform digitization are given in the text.*

Whenever the anode voltage of the PMT exceeds the 0.25 PE[2] threshold, one or more photons are detected and the waveform digitization is initiated. This trigger will be called a *Hit* or *DOMLaunch*.

The arriving signal is then divided among three processing lines:

Scaler This stream is dedicated to the supernova analysis in particular and is basically a simple Hit counter in a pre-defined time-binning. A software-wise integrated scaler summarizes asynchronously all discriminated PMT pulses in bins of 1.6384 ms and assigns a timestamp to it. The bin size results from a 16 bit buffer and the 40 MHz clock frequency.

---

[2] A PE (**P**hoto **E**lectron) defines the anode voltage level that a single photo electron holds after being amplified through all diode stages in the photo-mulitplier

This supernova scaler data are the basis of the supernova data acquisition and online analysis software (*SNDAQ*) which is explain in detail in the first section of Chapter 4.

ATWD Two of this custom design waveform digitization chips[3] are in place in order to reduce the deadtime arising from the readout period.The analog voltage is sampled at 290 MHz and is hold inside the ATWD by an array of 128 capacitors before it is digitizes by its internal ADC. This resolution translates to a maximum waveform duration of 426 ns in 3.3 ns wide bins. Opposed to more modern architectures, the ATWD has to be launched before the capacitors begin to sample the signal[4]. A delay board, mounted beneath the mainboard (see Figure 3.3), delays the PMT signal by the necessary launch-time of 72 ns. The ATWD has three input channels with different amplification levels in which the 128 samples are captured depending on the PMT output, see Figure 3.5. The digitization of the full waveform in the ATWD takes about 30 µs during which it is not available for data taking. An important criterion for keeping the waveform is the so-called *hard local coincidence* (HLC). It requires a next or next-to-next DOM also being hit within the local coincidence window of ± 1 µs. If none of the neighbors is hit in that time frame, we speak of a *soft local coincidence* (SLC) hit. The deadtime of 30 microseconds applies only for HLC hits where a record of the full waveform sample is kept. For SLC hits, the processing of the digitized waveform is aborted at the end of the local coincidence window. This results in a shorter deadtime of 2.45 µs originating from the LC condition and mainboard internal delays.

fADC The third signal line feeds the fADC[5] which scans the waveform continuously and converts it to a digital signal with a sampling rate of 40 MHz capturing 256 samples and covering a total time-window of 6.4 µs. An example waveform is given in the lower right panel of Figure 3.5. Although the fADC samples continuously, i.e. without deadtime, the firmware is organized such that a correspondence to an ATWD readout is required. Therefore, in the case of both ATWDs being busy with sampling waveforms, the fADC waveform is lost. The low resolution waveform provided by the fADC is fully available in HLC mode. In the case of the hit being of SLC type, only the highest value of the entries and its surrounding entries are stored with the Hit.

Table 3.1 summarizes the available readout modes. A compilation of minimum readout deadtimes between successive launches is given in Table 3.2. The advantage of having two ATDWs for readout becomes obvious when focusing on the minimum time between launches in the same chip (sequence ATWD AA or BB), that has the highest deadtime, i.e. 6.95 µs for the first launch being an SLC Hit or even 32.5 µs if the first hit was an HLC, respectively.

Table 3.1: *Readout modes of the IceCube Digital Optical Module [14].*

Readout mode	Condition	Sampling rate	Capture	Resolution
ATWD	HLC	290 MHz	128 samples	$\sim$ 3 ns
fADC	Above threshold	40 MHz	256 samples	25 ns

Besides the digitized waveforms, the mainboard generated information about the DOM's position in the array, its local-coincidence condition and, most importantly, its timestamp.

---

[3] **A**nalog **T**ransient **W**aveform **D**igitizer

[4] Hence the ICECUBE internal naming: Hit or *DOMLaunch*

[5] **f**ast **A**nalog to **D**igital **C**onverter

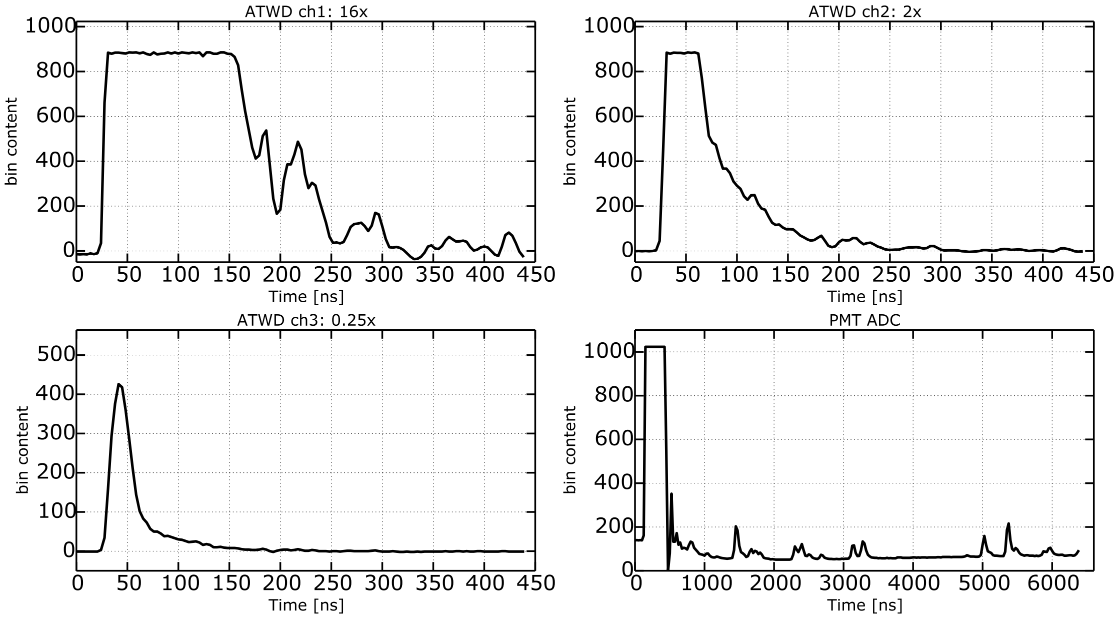

Figure 3.5: *ATWD and fADC digitized waveforms of a PMT hit. The ATWD provides 3 amplification channels with the bin content being either* 16×, 2× *or* 0.25× *the original.*

Table 3.2: *Minimum time differences between successive launches, i.e. deadtime, on a DOM Mainboard for all four possible readout sequences [145, 146].*

Launch Sequence	First Hit: SLC	First Hit: HLC	FADC	resulting Deadtime
ATWD AB (BA)	●	○	○	2.45 µs
ATWD AB (BA)	○	●	●	6.45 µs
ATWD AA (BB)	●	○	○	6.95 µs
ATWD AA (BB)	○	●	●	32.5 µs

A 40 MHz clock, local to each DOM, timestamps the Hit in combination with the *RAPcal*[6] method [142] to determine the relation of the local time at each DOM relative to the master clock on the surface. These transformed timestamps are given in UTC[7] time with a 0.1 ns precision. From the waveform information, either a peak sample for SLC hits or a complete readout for HLC Hits, the deposited charge can be calculated. The extracted charge Q in units of photoelectrons (PE) and the Hit's timestamp t, are the basic observables that are ultimately used for analyses by the collaboration. The Hit data are buffered on the DOM until the mainboard receives a readout request from the surface DAQ. Most DOMs record on average about 500 Hits per second, mostly from dark-noise photons. For high-quantum efficiency modules, the Hit rate is about 800 Hz. A detailed description of the instrumental noise is provided in Chapter 6.

---

[6] **R**eciprocal **A**ctive **P**ulsing **cal**ibration

[7] **U**niversal**T**ime**C**oordinated

3.3 Surface Data Acquisition

The ICL, situated on the surface above the IceCube array, hosts all necessary computational resources. Computers are mounted in 17 racks that can be accessed remotely from the Northern hemisphere to initiate DAQ runs and to monitor the detector. This is where all 86 cables from the strings meet. First, the Hits from the DOMs of each string are collected separately, in so-called StringHubs, as shown in Figure 3.6 and explained in the next section. The waveform information from the DOMs is buffered locally on the hubs and information from HLC Hits is forwarded to the multi-level trigger. In general, data transfer between components in the DAQ is realized via TCP streams over Gigabit-Ethernet. Different trigger settings are applied to Hits coming from in-ice and IceTop DOMs. If one or more triggers are formed, they are pushed to the GlobalTrigger where overlapping triggers are merged. The EventBuilder comes next in the data flow which receives requests from the trigger system and pulls the according data from the StringHubs in order to form a global *event*. Due to remote position of IceCube, data size is an important issue. A satellite connection with high bandwidth data transfer is only available for a few hours per day. Therefore, a highly compressed version of the data and only the interesting events are processed for transfer to the Northern hemisphere. This is realized in the *Processing and Filtering* (PnF) section of the online system. The most relevant parts of the IceCube surface DAQ (*pDAQ*) are explained in the following.

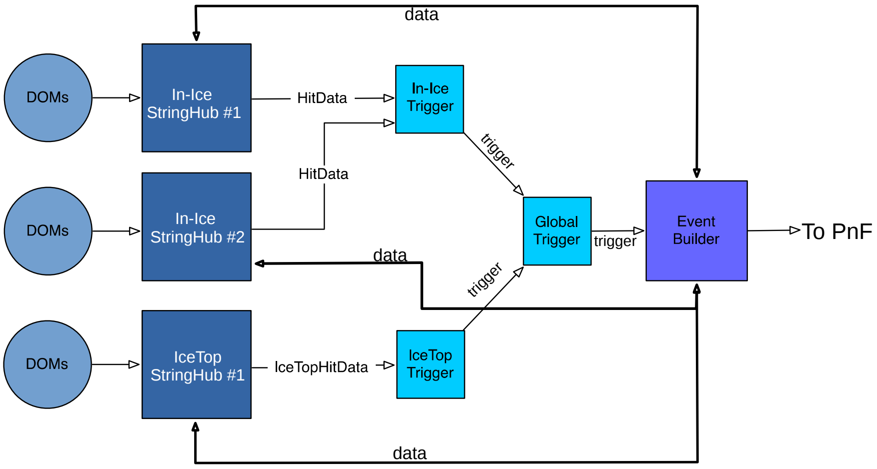

Figure 3.6: *IceCube Hit data flow diagram. Secondary data streams are omitted for simplicity. Thin lines indicate unidirectional data flow and thick lines stand for bi-directional communication.*

3.3.1 StringHub & DOMHub

The StringHub is the main software component of the so-called DOMHub to which all DOMs from one string are connected to. The DOMHub is based on an industrial PC, that handles communication and power supply to the DOMs. Each DOMHub accommodates eight DOM readout (*DOR*) cards with each one being able to host eight DOMs. The DOR cards handle all communications, time-calibration, data transfer and monitoring of the DOMs and communicate with the Hubs over a custom DOR protocol with a bandwidth of 1 Mbit/s. This major DAQ component, see Figure 3.7, has two separate functional sections. The front half, including the *DataCollector*, contains all of the code to talk to the DOMs and collect the

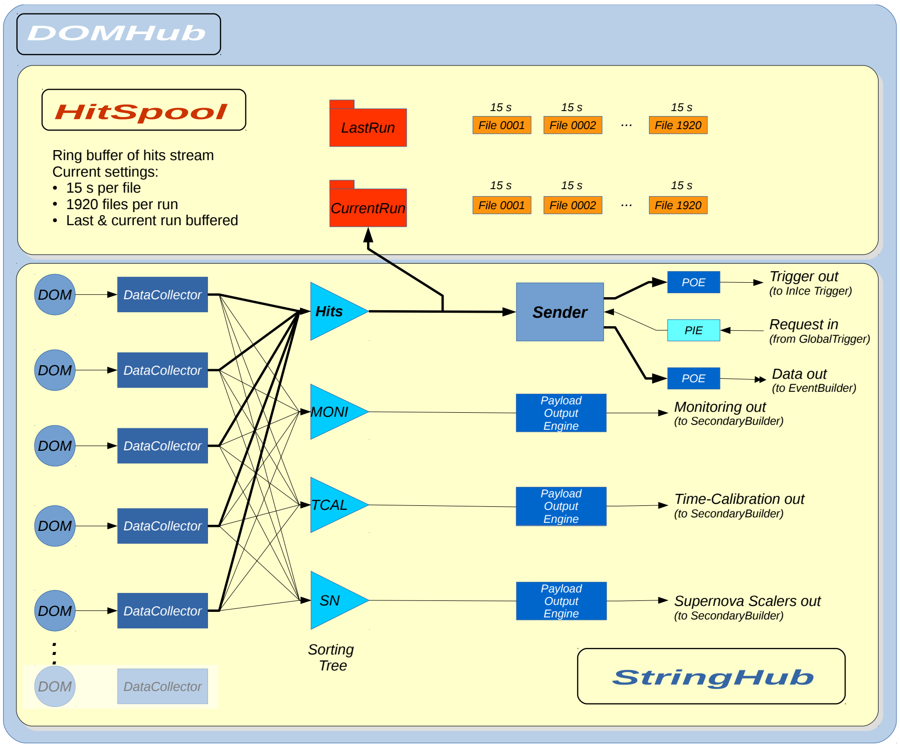
DOMHub
HitSpool
Ring buffer of hits stream
Current settings:
• 15 s per file
• 1920 files per run
• Last & current run buffered
LastRun
CurrentRun
15 s
File 0001
File 0002
...
File 1920
DOM
DataCollector
Hits
MONI
TCAL
SN
Sorting Tree
Sender
POE
PIE
Trigger out (to InIce Trigger)
Request in (from GlobalTrigger)
Data out (to EventBuilder)
Payload Output Engine
Monitoring out (to SecondaryBuilder)
Time-Calibration out (to SecondaryBuilder)
Supernova Scalers out (to SecondaryBuilder)
StringHub

Figure 3.7: *Diagram of the StringHub internals.*

data. The back end holds the *Sender* component which creates the trigger summaries from HLC tagged Hits, buffers Hit data and fulfills readout requests generated by the EventBuilder. Some components of the StringHub are explained in more detail in the following paragraphs.

Data Collector

Data from the DOMs of one string flow continuously to their DataCollectors. Inside the DataCollector, the *DOMApp* class handles the messaging between the StringHub and the DOR card which the DOM is connected to. The *Driver* class handles the interaction with the functionality exposed by the *DOR-driver* which is the kernel level device driver of the DOMHub's software. Besides the earlier mentioned Hits and Supernova scaler (*SN*) streams the DOM contains a stream of time-calibration data (*TCAL*) and monitoring data (*MONI*).

Data Stream Sorting

In order to merge and sort the 60 streams on a StringHub to one output stream, a cascaded binary sorting tree algorithm was developed [147], the so-called HKN1[8], see Figure 3.8. The minimal cell consists of two peers (*Left* and *Right*), a comparator and a sink. Objects pushed from outside into the peers are added to their first-in-first-out internal list. The lesser object of the two lists is pushed to the sink until the peers are empty. This procedure is easily adaptable to larger trees by connecting sinks as peers resulting in a 2^{N} input tree. This algorithm is proven to sort about 500.000 objects per second which is more than an order of magnitude above the average Hit rate of an entire string with 60 DOMs. All four sort engines run in

---

[8] An abbreviation for **H**anson-**K**rasberg-**N**-to-**1**.

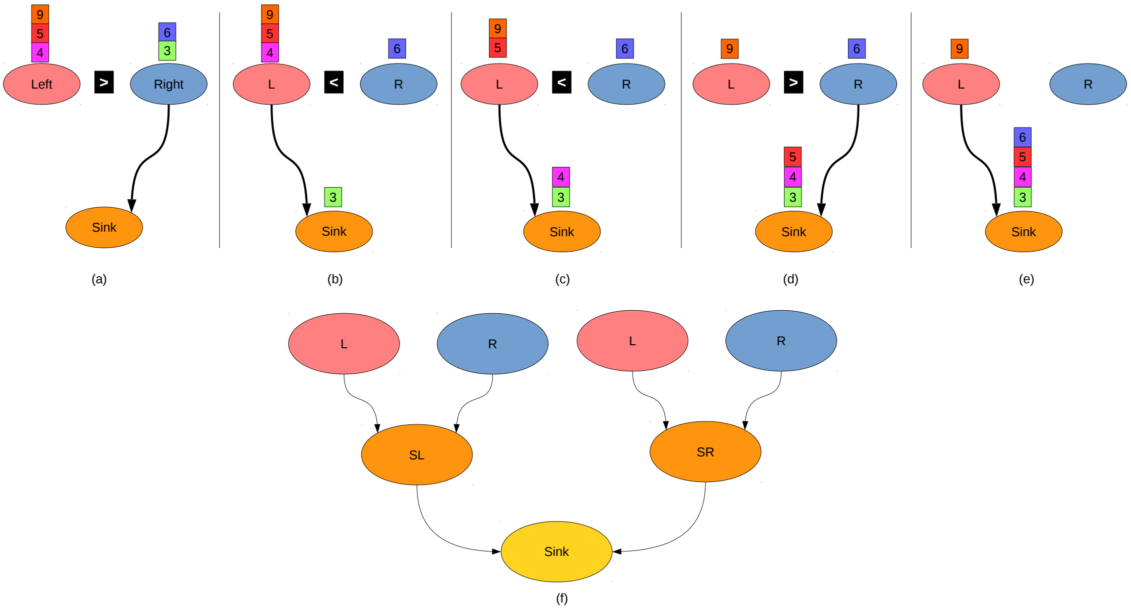

Figure 3.8: *Merge and Sort algorithm.*

threads in order to remain responsive to input while executing the tasks in background.

Sender

The sorted Hits stream is passed on to the Sender. This program is responsible for building trigger payloads and sending them to the trigger system. As we will see later on, the triggers only act on HLC hits. With an average HLC Hit rate per string in the order of $\mathcal{O}(10\,\mathrm{Hz})$, this stream is easily manageable by the HKN1 sorting tree. Inside the Sender, there is a request fulfillment engine consuming readout requests from the GlobalTrigger machine and DOM Hits from the StringHub. In case of a request, data payloads are formed in the payload output engine and are send to the EventBuilder.

Payloads

IceCube uses a custom design envelope for communicating the different data types and data requests such as Hits, MONI, SN or trigger information to other DAQ components. The minimum data packet of this protocol is called a *payload*. Payloads are byte streams in big-endian byte ordering starting with 4-byte holding the record length of the payload, another 4-byte payload identifier field and an 8-byte UTC timestamp. The remaining bytes are payload-dependent and can even contain entire payloads of other format. The basic Hit payload, for instance, has additionally information about the DOM number and recorded waveform. For packing the data in their corresponding payload type, the secondary streams (SN, TCAL and MONI) are fed to their corresponding payload output engines (POE) directly after the data collector. Hit related payloads are handled after the Sender component, explained earlier.

Untriggered Buffering: HitSpooling

Before the time-sorted Hit stream goes to the Sender, a copy of the data branches off to be written to disk as it is depicted in the upper part of Figure 3.7. The Hits are *spooled* to files in portions of 15 s inside a directory that can hold an entire standard DAQ run of eight hours, i.e. 1920 files. With the start of a new run, the content of the *currentRun* directory is moved to a *lastRun* and the spooling starts over. This untriggered buffered stream is independent of the main DAQ cycle and therefore a invaluable data source in case of a software crash in the DAQ. The HitSpool concept is a major topic in this thesis and is discussed in detail in Chapter 5.

3.3.2 Trigger System

The IceCube trigger algorithms operate by examining Hit payloads that contain the channel, i.e. the String and DOM number, as well as the time of the Hit. In general, triggers look for a certain minimal multiplicity of HLC hits in a certain time window and geometry. The trigger time window is set according to the time light needs to travel through the instrumented ice volume and is slighlty extended by a larger readout window in order to catch early and delayed light [148]. The already time-sorted hit streams from the strings are fed to the *Splicer* in the trigger system, see Figure 3.9a, based on the HKN1 algorithm, that sorts the hits globally. IceCube uses several trigger algorithms that can be run in parallel and on different sub-sets like in-ice DOMs, the *DeepCore* sub-array or on IceTop DOMs. The triggers form the front-line of the multi-level DAQ trigger system and feed the *GlobalTrigger*, the higher level component, see Fig 3.9b. The Global Trigger handler reads requests from other trigger handlers and groups concurrent requests into a single global request that is sent to the EventBuilder.

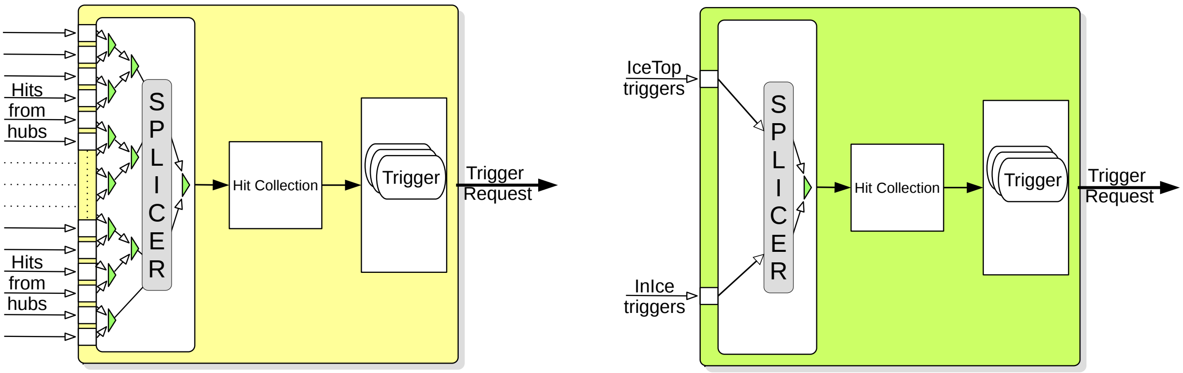

(a) *Diagram of the trigger system.* **(b)** *Details of the GlobalTrigger.*

Figure 3.9: *The trigger system. Triggers and GloablTrigger.*

Trigger Algorithms

Simple Multiplicity Trigger The *Simple Multiplicity Trigger* (SMT) is the most exploited trigger algorithm in IceCube. The only requirement for the SMT is a minimum number N of HLC hits in the detector within a sliding time window of $\mathcal{O}(1\,\mu\mathrm{s})$. The trigger window will be extended as long as the multiplicity condition is satisfied. With the multiplicity value N being tuned to the energy threshold of the different sub-detectors also the time window varies.

Volume Trigger The *Volume Trigger* is one of two triggers that imply locality conditions. For every hit DOM, the algorithm searches in a defined cylinder around that hit for a required abundance of HLC hits. In this way low energy events that do not satisfy the SMT conditions can still trigger the detector.

String Trigger uses a simpler locality condition when looking for HLC hits in DOMs on a single string in a certain time window. This trigger was developed in order to identify low energy muons passing vertically through the detector.

Fixed Rate Trigger (FRT) is the last trigger to be mentioned here. Every 30 s it reads out Hits from the full detector over a time window of 10 ms. It was implemented as a useful producer of minimum-bias samples for studies of DOM noise. In that sense it is the predecessor and motivation of HitSpool that can in principle record several hours or days of continuous data of the entire array.

Figure 3.10 shows a summary of the geometry requirements mentioned above and recalls the fundamental hit pair based on the local coincidence condition (HLC). The trigger parameters are summarized in Table 3.3.

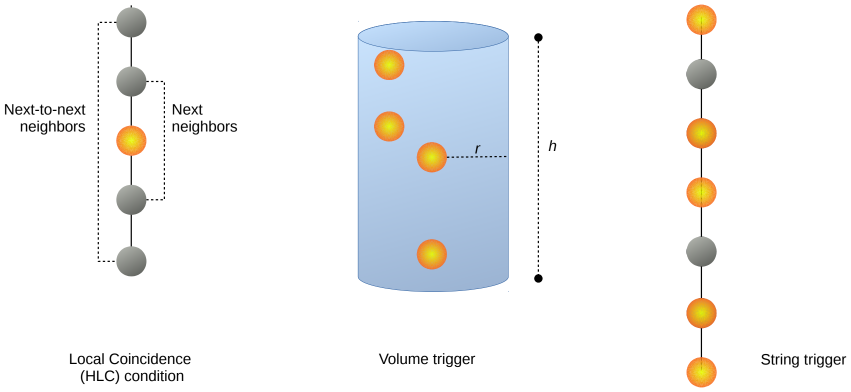

Figure 3.10: *Schematic representations of the geometry settings used for triggering in IceCube. Based on the fundamental hit pair, i.e. a hit within ±1 μs in (at least) one next or next-to-next neighbor around a hit DOM (left panel), the volume trigger (central panel) looks for four HLC hits in a given volume whereas the string trigger is fulfilled in case of five HLC hits on a single string.*

Table 3.3: *Trigger parameters and typical trigger rates [148].*

Trigger	DOM set	HLC hits	Window [μs]	Topology	Rate [Hz]
SMT8	in-ice	8	5	none	2100
SMT3	DeepCore	3	2.5	none	250
SMT6	IceTop	6	5	none	25
Volume	in-ice	8	5	cylinder ($r = 175$ m,$h = 75$ m)	3700
String	in-ice	5	1.5	7 adjacent DOMs on a string	2200
FRT	all	-	-	-	0.003

3.3.3 EventBuilder

This component reads the global requests, sent by the GlobalTrigger, that are uniquely numbered and contain the time window of interest to be readout. The Event Builder then extracts individual trigger requests and builds individual readout requests that are directed to the appropriate StringHubs. The Request Filler component of the Sender in the StringHub reads the requests and returns a (possibly empty) packet of all Hits in the given time window. Furthermore, the Sender uses these time markers to delete buffered data that is determined to be no longer in demand. The returned readout data payloads are assembled into events via collating them by their readout identification number that serves as an event number. When that number changes, an event is terminated and send out to the file dispatcher. The data files are usually written to disk by the dispatcher in chunks of 10 Mb and await pick-up from the PnF system.

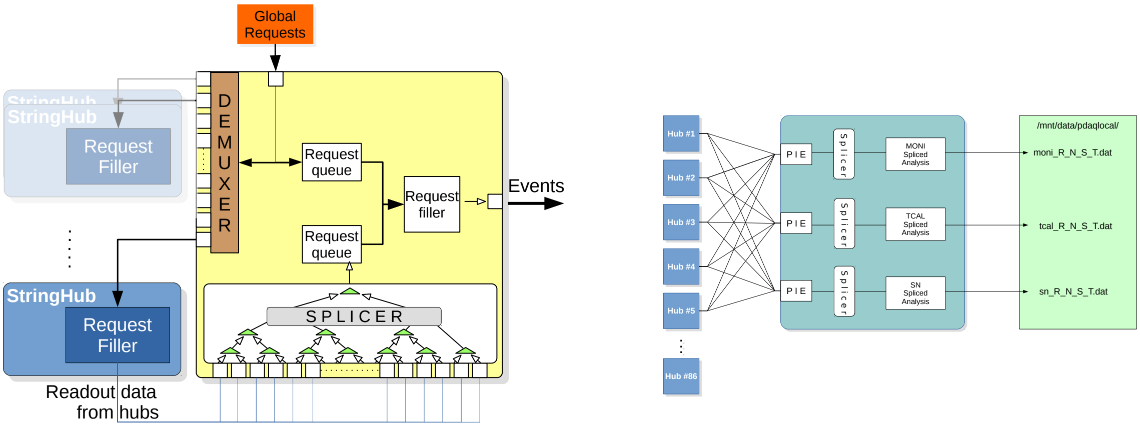
Global Requests
StringHub
Request Filler
StringHub
Request Filler
DEMUXER
Request queue
Request queue
Request filler
Events
SPLICER
Readout data from hubs
Hub #1
Hub #2
Hub #3
Hub #4
Hub #5
Hub #86
PIE
PIE
PIE
Splicer
Splicer
Splicer
MONI Spliced Analysis
TCAL Spliced Analysis
SN Spliced Analysis
/mnt/data/pdaqlocal/
moni_R_N_S_T.dat
tcal_R_N_S_T.dat
sn_R_N_S_T.dat

(a) *Diagram of the data flow in the EventBuilder.* **(b)** *Secondary Builder.*

Figure 3.11: *Secondary Builder and EventBuilder diagrams.*

3.3.4 SecondaryBuilder

Every stream that does not contain Hits is considered a *secondary* data source. The SecondaryBuilder, hosted on a dedicated machine at the ICL, basically consists of three Splicers that merge the monitoring, time-calibration and SN scaler streams emitted from the StringHubs.The analysis of each secondary stream is performed separately and summaries are stored on the file system, sorted by data type, run-number and other tags for bookkeeping. The online supernova analysis component (SNDAQ) running on the same machine, see Section 4.1, extracts the SN scalers from these files.

3.3.5 Control Framework

The IceCube DAQ system is deployed on a computing cluster with about one hundred data hubs and servers that have to be controlled and monitored. There are two levels of controlling. The distributed network control hosted on the *Command and Control* (CnC) server handles the low-level components (StringHubs, IceTopHubs, Triggers, GlobalTrigger, EventBuilder) with roughly one component per machine. On the user-level, *IceCubeLive* (I3Live) serves for operating and monitoring the detector with all its sub-systems. A simplyfied control flow diagram is shown in Figure 3.12 with details explained in the following.

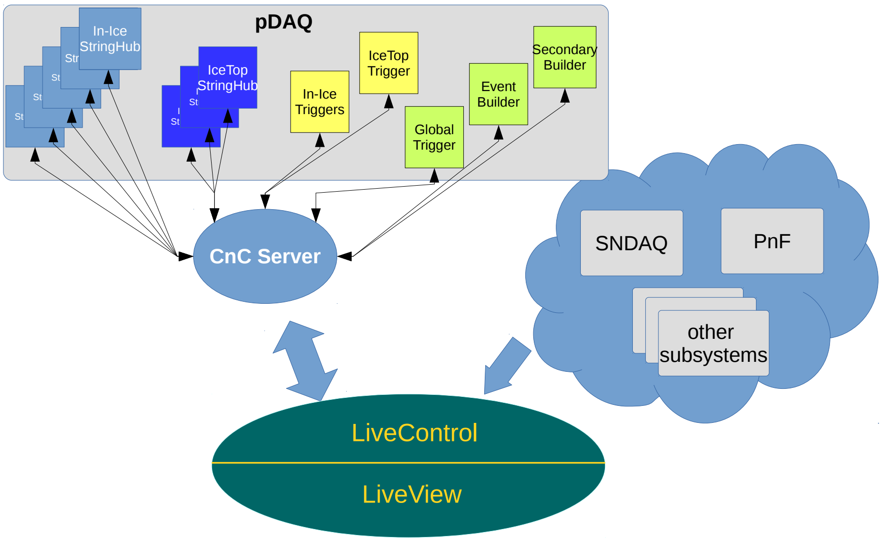

Figure 3.12: *Diagram of the control flow and its main components. The CnC server manages all control communications between the surface DAQ components and I3Live's control back end. Other sub-systems are directly connected to LiveControl and visualized via LiveView for the user.*

CnC Server

The (CnC) server directly controls the components of the surface DAQ system. It creates and manages sets of components through run cycles. The CnC server does not handle any physics or secondary data from the detector. It rather represents the front-end of the DAQ through which all control communications have to pass. The messaging protocol is based on XML-RPC. The CnC server is notified whenever a component starts running. During a DAQ run, it monitors all individual components and passes status information to I3Live. If problems are detected in a run, the run is stopped by the server.

I3Live

The IceCube Live system (I3Live) hosts the user interface for controlling runs. This mostly Python-based project is also the place where the monitoring of all sub-systems, such as the pDAQ, SNDAQ or PnF, is collected. It consists of two main components: LiveControl and LiveView. LiveControl is the control-point of I3Live for sub-systems and consists of a simple interface for control, monitoring and logging of the pDAQ. It is also responsible for generating and transmitting alerts from sub-systems, for example via e-mail to the responsible experts.

LiveView is the other building block of I3Live that receives alerts and status messages from LiveControl. This web-based user interface transmits control requests to LiveControl and shows the current state and history of the detector. There are two instances of LiveView running, one for monitoring by on-site experts and the other in the northern hemisphere for collaboration-wide access. From LiveControl, the monitoring messages are transfered in JSON[9] format via ZeroMQ [149] to the corresponding data base at Pole or in the North. ZeroMQ is a high-performance asynchronous messaging library for many languages and various transmission protocols like UDP, TCP etc. More details on that follow in Chapter 5.2 with the explanations of the HitSpool Interface that uses the same technique. For direct access to the detector and to perform special operations, I3Live has an extra command-line interface for experts.

---

[9] **J**ava**S**cript **O**bject **N**otation is a language independent text format, light-weighted and thus makes data-interchange easy.

3.4 Basic Online Data Processing

Due to the restricted transmission bandwidth of $\sim 105\,\mathrm{Gb}$ per day, the physics data stream, i.e. Hits data, needs further processing before it can be sent over satellite to the northern hemisphere for analysis. Only events that pass at least one of the online filter conditions are transmitted. Since the analyses performed in the framework of this thesis are not based on standard filtered data but on HitSpool data, details of standard filter techniques can be omitted here[10] and we focus on the data processing techniques of the dedicated *processing and filtering* (PnF) system.

PnF is hosted on a computing farm in the ICL that enables the system to process data and generate alerts in less than three minutes. The raw binary data provided by pDAQ, see Section 3.3, is transformed to an IceCube specific data type in a modular software framework, called *IceTray*. The basic data treatment for every Hit is an unfolding procedure that is conducted to determine the time, duration and number of photons of a signal in a DOM. Due to the finite time and voltage resolution of the DOM, it is possible to have more than only one photon recorded in a Hit. Therefore, the concept of *(reco)pulses* was introduced to describe the charge Q deposited in a DOM at a time t. In this sense, multiple pulses can be present in a Hit or DOMLaunch. This unfolding procedure provides the basic observables of the detector, the charge Q and time t of an event, which is the starting point of any standard analysis in IceCube. More details about basic processing steps are given below.

3.4.1 Waveform Calibration

The first processing step in the PnF system, after transforming the raw binary data into IceTray objects (DOMLaunches), is the application of calibrations to the waveforms. These calibration setting include:

- Subtraction of the PMT baseline from the ADC counts.
- Application of a bin-specific gain factor to obtain a voltage from the baseline-subtracted digitized waveform.
- Correction of the waveform start time for the transit time[11]
- Correction of droop effects that arise in the transformer that couples the PMT output to the DOM mainboard [151]

3.4.2 Waveform Feature Extraction

In theory, calibrated waveforms are sufficient in order to reconstruct the track of the incident particle. This becomes a lot more complex in reality where we have to deal with different digitizer channels and possible photon pile-up in a waveform. A solution to this problem is to reconstruct a photon arrival time at the photo-cathode before feeding this results to any track reconstruction algorithm. Defining a signal onset time only by a threshold-crossing is risky since parts of the deposited charge might be ignored in the multi-photon signal case. One solution to this problem was developed in [152] by unfolding the observed waveform into single photo-electron pulses. In this way, huge signals are described by a combination of multiple photons with their corresponding charge and arrival time. Examples of the results of this procedure can be seen in Figure 3.13. The resulting pulse series are used for all following event reconstructions.

---

[10] The interested reader might be directed to [150] for a summary of data filters used in IceCube

[11] The transit time is the average time it takes a pulse to propagate through the entire PMT. Waveforms from the second ATWD chip and the FADC are corrected for their delay with respect to the first ATWD chip.

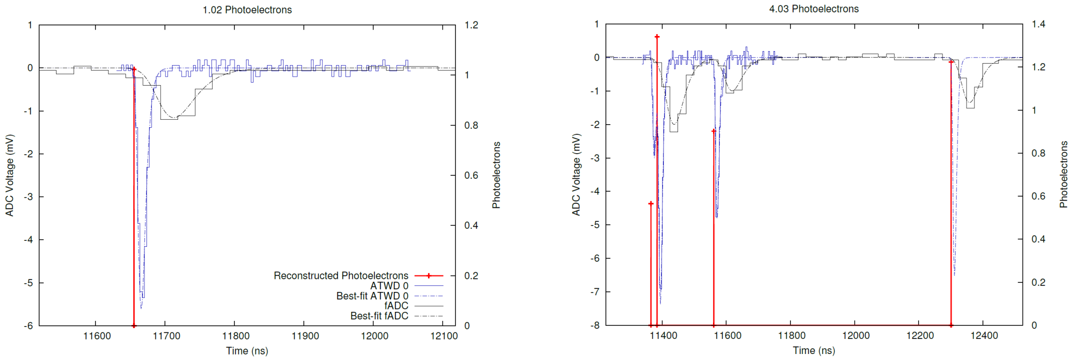

(a) *Single photon waveform* **(b)** *Multi photon waveform*

Figure 3.13: *Examples of waveform unfolding for both simple and complex waveforms. The lines marked Best-fit are predictions of the various digitizer read-outs given the reconstructed PMT hits. For a perfect reconstruction, and with no noise in the data, these lines would exactly match within the digitizer step. The vertical lines with crosses at the top represent the times and amplitudes of the unfolded pulses relative to the right-hand axis [153].*

3.4.3 Event Reconstruction

Due to limited computing power at the South Pole, only simple and fast event selection and reconstruction algorithm can be used online. Initially, hit cleaning techniques are applied in order to remove Hits arising from instrumental noise[12]. One of the first-guess algorithms is for instance an improved *linefit* [154, 155] that minimizes the sum of squared distances between a reconstructed track and the hit DOMs [156]. The pattern of hits associated to the event is treated as a plane wave moving through the detector, disregarding the geometry of Cherenkov radiation or optical scattering in the ice between emission and detection.

More computing intensive reconstruction techniques are performed offline after the data have arrived in the northern hemisphere. A summary of these energy and angular reconstruction techniques is presented in [153]. Two basic classes of events can be distinguished:

Tracks Track-like events, as in Figure 3.14, originate from a charged current interaction of a high-energy muon-neutrino with a nucleus ($\nu_\mu + N \longrightarrow \mu + X$), producing a muon with its typical Cherenkov cone along the track together with a hadronic cascade at the vertex. An angular reconstruction of such a muon track and hence the incident neutrino direction can reach a precision better than 1° which is confirmed by a pointing-resolution analysis of the moon shadow, presented in [157]. Due to the fact that these tracks often start outside the instrumented volume, they can be as long as a few kilometers for neutrinos of PeV energies, only a part of the full energy deposit is observed. The total muon energy can only be estimated indirectly from the differential energy loss rate inside the detector. Energy loss above the minimum-ionizing regime, typically ~ 1 TeV in IceCube, is highly dominated by stochastic processes such as bremstrahlung, photonuclear interactions and pair production resulting in large fluctuations in the amount of energy deposited for different muons of the same energy [153].

---

[12] This cleaning is inversely applied for the analysis of HitSpool data, with more details in Chapter 5, where one aims for the contrary, i.e. retrieving a pure noise Hit sample of the detector.

Cascades The second class of events are electro-magnetic or hadronic cascades from all neutrino flavors, resulting in a spherical light deposition in the detector, see Figure 3.15. Since the total light output of a cascade is directly proportional to its energy and the cascades are generally well contained in the detector, the energy reconstruction for such events is much more precise than for track-like events.

The average deposited energy resolution for both event types combined is $\sim 15\,\%$ [153].

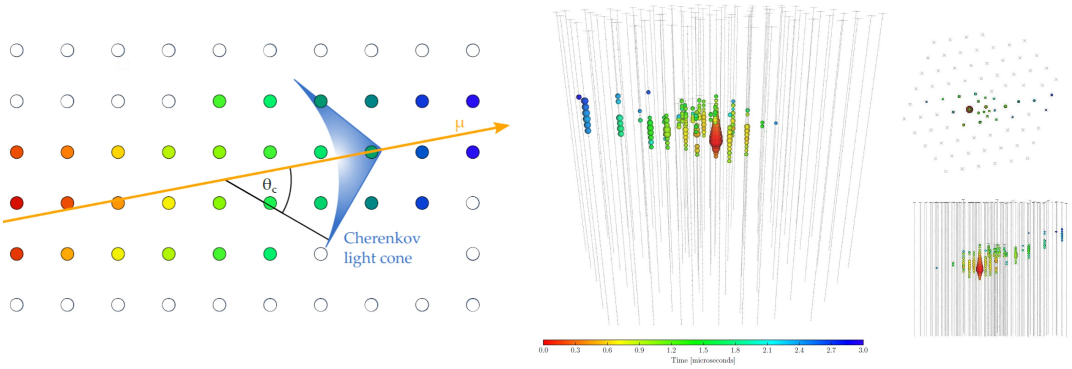

(a) Sketch of track-like topology

(b) Event in data

Figure 3.14: *Sketch of an event with track-like topology on the left and the recorded light of a track-like event on the right with a reconstructed energy of* $\sim$ 31 TeV *and an angular resolution better than* 1.2° *[8].*

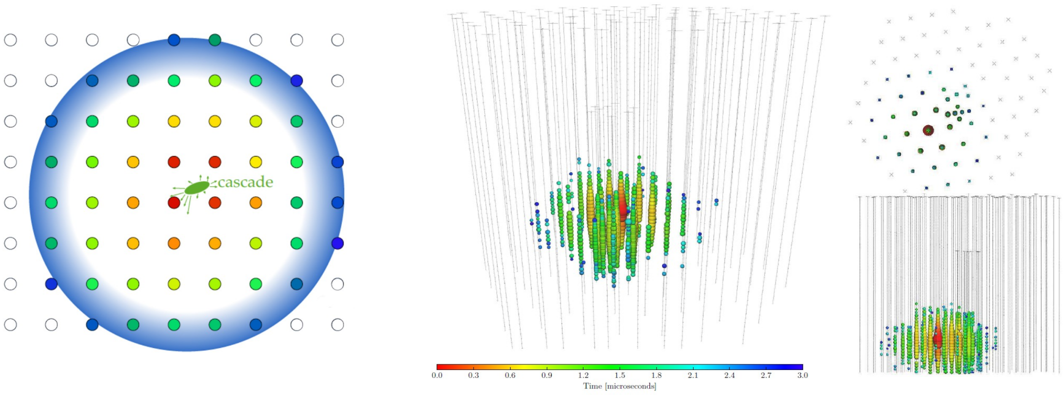

(a) Sketch of shower-like topology

(b) Event in data

Figure 3.15: *Sketch of an event with cascade-like topology on the left and the recorded light of a cascade-like event on the right with a reconstructed energy of* $\sim$ 130 TeV *and an angular resolution of* $\sim$ 8° *[8].*

4

Supernova Detection in IceCube

The first section gives an overview of the Supernova Data Acquisition System of ICECUBE. *Our expectations of how a supernova signal should look like and the calculations done in order to derive these estimations are presented in the second section. An overview of supernova signals in other experiments concludes the chapter.*

4.1 Supernova Data Acquisition System - SNDAQ

Since the energy threshold of ICECUBE is on the order of some hundreds of GeV, and thus at least four orders of magnitude above the supernova neutrino energy, a reconstruction of single events is not possible. Although the hit rate increase in individual DOMs is not significant enough for distinguishing between noise hits and supernova neutrino related hits, a signal will be detectable when considering the rate increase in the entire array [66]. The so-called *scaler data stream*, already mentioned in Section 3.2, is the basis for this dedicated supernova data acquisition system (SNDAQ).

4.1.1 Detection Method

ICECUBE was not designed with the primary intention to search for supernova neutrinos. Hence the detection method differs form the standard one. Depending on the supernova model and its distance to the detector, low energy neutrinos of $\mathcal{O}(10\,\text{MeV})$ will increase the hit rate in an individual DOM by a certain amount. In that sense, the supernova detection method of ICECUBE can be seen as a counting experiment with each DOM being a independent detector recording a time-dependent signal hit rate [66]:

$$R(t) = \epsilon_{\text{dt}} \cdot n_{\text{ice}} \int_0^\infty dE_\nu \Phi_\nu^{\text{D}}(E_\nu, t) \int_0^\infty dE_e \frac{d\sigma}{dE_e}(E_\nu, E_e) \cdot N_\gamma(E_e) V_{\text{eff}}^\gamma(E_e) \tag{4.1}$$

where n_{ice} is the target density and $\frac{d\sigma}{dE_e}(E_\nu, E_e)$ is the differential cross-section of a neutrino with energy E_ν interacting in the ice and producing an electron or positron of energy E_e. The number of radiated Cherenkov photons can be approximated to $N_\gamma \approx 178 \cdot E_e$ and depends on the lepton energy and the selected wavelength range, chosen to be between 300 nm and 600 nm. The effective volume for a single photon detection is given by V_{eff}^{γ}. The energy and time dependent neutrino flux at the detector is

$$\Phi_{\nu}^{\mathrm{D}} = \frac{\Phi_{\nu}(E_{\nu}, t)}{4\pi d^2} = \frac{L_{\mathrm{SN}}(t)}{4\pi d^2 \cdot \langle E_{\nu} \rangle(t)} \cdot f\left(E_{\nu}, \langle E_{\nu} \rangle(t), \alpha(t)\right) \tag{4.2}$$

where $\Phi_{\nu}(E_{\nu}, t)$ denotes the differential neutrino flux at the position of the earth at distance d from the supernova and $L_{\mathrm{SN}}(t)$ is the time-dependent supernova luminosity for neutrino $\nu = \overset{(-)}{\nu}_x$ where $x = e, \mu, \tau$ which is deduced from theory. The normalized energy distribution $f\left(E_{\nu}, \langle E_{\nu} \rangle(t), \alpha(t)\right)$ was already explained in Chapter 2, see equation 2.19. A possible modification of the neutrino flux due to flavor oscillation by the stellar matter and Earth matter effect, as discussed in Section 1.2, is highly sensitive to the incident angle of the neutrinos, the assumed supernova model and the corresponding neutrino properties. More details on that are given in Section 4.2.

In order to measure the signal hit rate $R(t)$, IceCube has a dedicated data stream, the supernova scalers, as explained in Section 3.2.2. This scaler data is produced by a firmware integrated counter that adds asynchronously all discriminated PMT pulses on each DOM for a defined interval length and assigns a timestamp. The interval length is given by the internal clock frequency and number of passed cycles:

$$\frac{2^{16}\ [\text{clock cycles}]}{40\ [\text{MHz}]} = 1.6384\ \text{ms} \qquad . \tag{4.3}$$

Hits in the DOMs are not only due to passage of cosmic radiations but can also be caused by instrumental noise. Chapter 6 will discuss in greater depth various sources of background noise in IceCube. For now, it is sufficient to point out that one can identify a hit-correlated noise contribution which can be effectively suppressed by adding a non-paralyzable deadtime to each hit of t_{dt} = 250 µs [63]. By adding Poissonian distributed signal to a measured sequence of noise hits it was found that the efficiency parameter in equation 4.1 is a function of the signal rate r_{SN} and the previously mentioned deadtime t_{dt} [66]

$$\epsilon_{\mathrm{dt}} \approx \frac{0.87}{1 + r_{\mathrm{SN}} \cdot t_{dt}} \qquad . \tag{4.4}$$

The deadtime is applied to the scalers directly at the DOM and only the filtered scalers are provided for the next stage of processing. At this low level, only pDAQ is communicating with the DOMs. The surface computers (*StringHubs*) read out the scalers of each DOM on the string approximately once every second[1]. In order to synchronize the entries per string, an absolute timestamp, provided by *RapCal* [142], is given to the first bin before merging the data per string. This forms the so-called *supernova payload*. The supernova payloads of all 86 strings are collected until a data size of 200 MB is reached which takes approximately two minutes. These files are then parsed in SNDAQ and quality-checks of their content are performed. This setup guarantees a high stability since both DAQ systems, pDAQ and SNDAQ, work mostly independent from each other.

Since the individual DOMs are asynchronously providing their scalers, it is essential to restructure the raw data and sort them in a global way. A binning of 2 ms was chosen in order to be able to re-arrange the data more easily in larger time periods. SNDAQ immediately rebins these data in 500 ms bins which are the basis of the later rebinnings of 1.5 s, 4 s and 10 s. Only if a trigger formed by SNDAQ is above a fixed (but arbitrary) threshold, will the system provide the finest binning of 2 ms (see Section 4.1.3).

---

[1] This amounts to approximately 612 bins per DOM on average: 1 s / 1.6348 ms = 611.695

4.1.2 Real-Time Analysis Method

The real-time analysis chain starts once the 500 ms binned raw data are produced by SNDAQ. The basic principle of the online analysis, inherited from IceCube 's precursor Amanda, is the search for a significant deviation of the collective averaged DOM rates from their mean values [66,158]. The rate enhancement is induced by Cherenkov photons which are radiated by electrons and positrons produced by supernova neutrino interactions in the ice (see chapter 1). Individual DOM rates R_i are caused by N_i pulses in the DOM scalers during a given time interval $\Delta t = 1.6348$ ms. These R_i, where $i = 1 \ldots N_{DOM}$, are rebinned twice (see previous section) before feeding them to the online analysis. The analyses for the higher binnings, 1.5 s, 4 s and 10 s, are performed in parallel to the 500 ms with each one having its own physics motivation as explained in Table 4.1.

Table 4.1: *SNDAQ's rebinning and their physics motivation.*

Scaler bin size	Motivation
500 ms	Looking for short bursts associated with black hole formation immediately after core-collapse of the star [93]
1.5 s	Covering the large neutrino flux as predicted in simulation like the Lawrence-Livermore model [113]
4.0 s	Proton-neutron star cooling phase emits neutrinos on an exponentially decreasing time-scale with a time constant $\tau \approx 3.8$ s [66]
10.0 s	Time span of neutrino detection from SN1987A, see Section 2.6

The distribution of the R_i can be described phenomenologically by a log-normal distribution if Δt is sufficiently large. For simplicity reasons, this distribution is approximated by a Gaussian which provides an expectation value for the rate $\langle R_i \rangle$ as well as for corresponding standard deviation σ_i. Both parameters are computed from a time-window of ±5 min around the analysis bin at t_0. In order to reduce the chance of a wide signal impacting the mean rates,

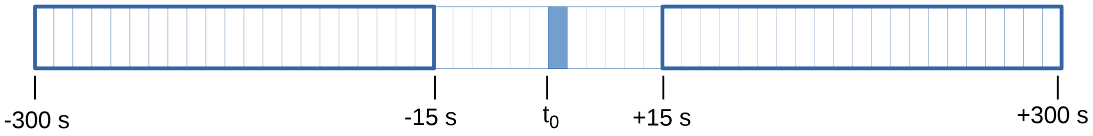

Figure 4.1: *Time range in the SNDAQ real-time analysis. A time-window of* ±5 min *around the analysis bin at* t_0*, surrounded by two exclusion zones of maximum* 15 s*, moves in steps of the smallest bin size (*500 ms*) and independently of the analysis bin size (*0.5 s, 1.5 s, 4 s *and* 10 s*).*

a zone of 15 s around the bin under investigation is ignored, see Figure 4.1. The step size of this sliding window procedure is 500 ms for all four analyses. The most likely rate deviation $\Delta\mu$ for all DOM noise rates R_i from their individual expectation value $\langle R_i\rangle$ can be derived by maximizing the likelihood

$$\mathcal{L}(\Delta\mu) = \prod_{i=1}^{N_{\mathrm{DOM}}} \frac{1}{\sqrt{2\pi}\cdot\langle\sigma_i\rangle} \exp\left(-\frac{(R_i - (\langle R_i\rangle + \epsilon_i\cdot\Delta\mu))^2}{2\langle\sigma_i\rangle^2}\right) \quad . \tag{4.5}$$

The individual DOM efficiency, ϵ_i, accounts for module specific parameters and depth dependent detection probabilities as resulting from the ice. Standard DOMs are normalized to $\epsilon_i = 1$ and high quantum efficiency DOMs to $\epsilon_i = 1.35$. Maximizing the likelihood analytically leads to $\Delta\mu$ and its approximate uncertainty $\sigma_{\Delta\mu}$:

$$\Delta\mu = \sigma^2_{\Delta\mu}\sum_{i=1}^{N_{\mathrm{DOM}}}\frac{\epsilon_i(R_i - \langle R_i\rangle)}{\langle\sigma_i\rangle^2} \qquad \text{where} \qquad \sigma^2_{\Delta\mu} = \left(\sum_{i=1}^{N_{\mathrm{DOM}}}\frac{\epsilon_i^2}{\langle\sigma_i\rangle^2}\right)^{-1} \tag{4.6}$$

Since each DOM contributes with the deviation of its expected noise rate corrected by a factor $\epsilon_i/\langle\sigma_i\rangle^2$, the collective rate deviation $\Delta\mu$ has the structure of a weighted sum. The *significance* of a suprenova candidate trigger is then defined as

$$\xi := \frac{\Delta\mu}{\sigma_{\Delta\mu}} \tag{4.7}$$

The distribution of recorded significances ξ is expected to follow a Gaussian behavior with unit width centered at zero if one assumes uncorrelated background noise and a large number of participating DOMs, see Figure 4.2. In reality, single cosmic ray showers can produce muons or muon bundles that trigger many optical modules and hence contribute to the background rate in ICECUBE. As we will see in detail in Chapter 6.1, cosmic ray muons contribute to the count rates of individual DOMs by only a few percent but clearly broaden the significance distribution as a function of detector size because the resulting hits are correlated across the detector. This results in a seasonally dependent width that has reached $\sigma = 1.5$ with 86 operating strings in the austral summer [159]. The effect can be reduced by an offline analysis that uses the fact that the number of coincident hits induced by muons in neighboring DOMs is recorded for all triggered events [160]. By decorrelating the muon induced hits from the total amount of hits, is was possible to attribute 99.4% of alerts with significances $\xi \leq 6.00$ to an increased appearance of atmospheric muons [161]. So far, the SMT8[2] (see Section 3.3) is the only one type of trigger that is used to identify triggered muons in this analysis.

It is part of the motivation for this thesis to improve this result by identifying and subtracting not only the hits associated to muons in any trigger channel but from all muons in the detector, triggered or subthreshold. The basis for studying this physics case is a dedicated new raw data stream called HITSPOOL which will be presented in the following chapters.

4.1.3 Supernova Alert Message

Once a supernova candidate is triggered by SNDAQ an alert message is formed and sent to the users via email through I3Live. I3Live [162] is the experimental control and monitoring system of the detector. Among other subsystems, it also has a connection to the supernova system

---

[2] SMT8 stands for Simple Multiplicity Trigger requiring eight HLC hits anywhere in the detector within 5 μs

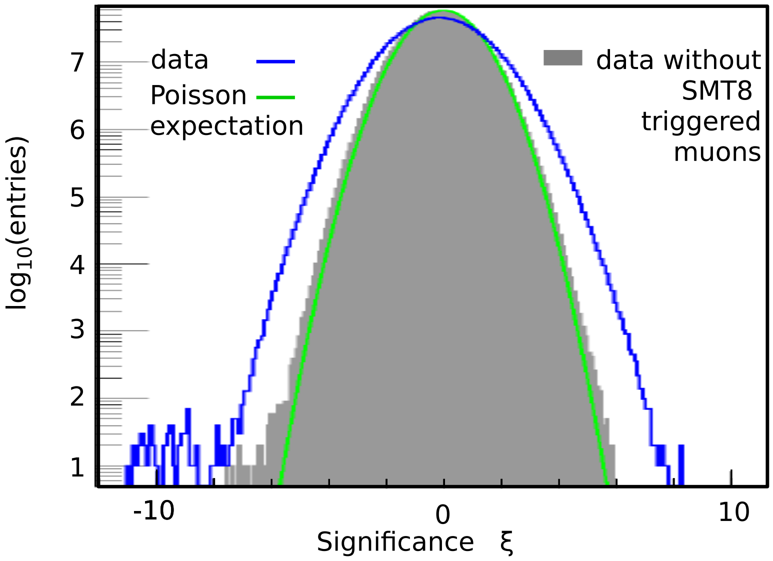

Figure 4.2: *Significance distribution as measured by SNDAQ without (blue line) and with (shaded gray) subtraction of triggered atmospheric muons for data taken from April 2008 to May 2011 (significances above 6 standard deviations are kept blind). The expectation from Poisson is given in green [159].*

which is based on the so-called Live Supernova DAQ (LSD) subcomponent of SNDAQ [63]. In this way, the user is able not only to control and monitor the supernova system entirely through the i3live webpage [163] but also to receive status and alert emails from the system. The threshold for sending alerts is set in SNDAQ internally to $\xi \geq 6.00$ which results in multiple alerts per day, depending on the season.

SNDAQ holds multiple trigger levels defining actions to be executed automatically by the system, see table 4.2.

Table 4.2: *SNDAQ trigger levels and associated action to be taken.*

Significance Level	(Additional) Action
$\xi \geq 6.00$	email to subscribed users
$\xi \geq 7.30$	2 ms datagram provided
$\xi \geq 7.65$	SNEWS alert & HitSpool data request (see Chapter 5)

IceCube is a member of the SuperNova Early Warning System (SNEWS) [164], an international network of neutrino experiments with the goal of providing an early alert for a galactic supernova. The unique advantage of the neutrino signal is that it is prompt, emerging on a timescale of seconds compared to the first electromagnetic signal that might arrive hours or days later at the observer's site. Hence a neutrino observation allows astronomers to detect a supernova lightcurve in its very early stage. With this consideration it is clear that a rapid analysis and alert message generation is desired with the shortest time delay possible. This leads to the question regarding the data processing latency of the SNDAQ system.

Figure 4.3 shows an exemplary snapshot of SNDAQ's latency as a function of time over a range of several days. Besides the inevitable latency of 5 min due to the real-time analysis, the remaining latency of roughly 150 s on average is partly due to the data reception frequency, SNDAQ is checking for new data once per minute, and pDAQ is sending data as soon as 200 MB new data are collected which can take few minutes. The spikes in plot are caused by the fact that IceCube 's standard run unit is 8 h which produces a short backlog at run transition.

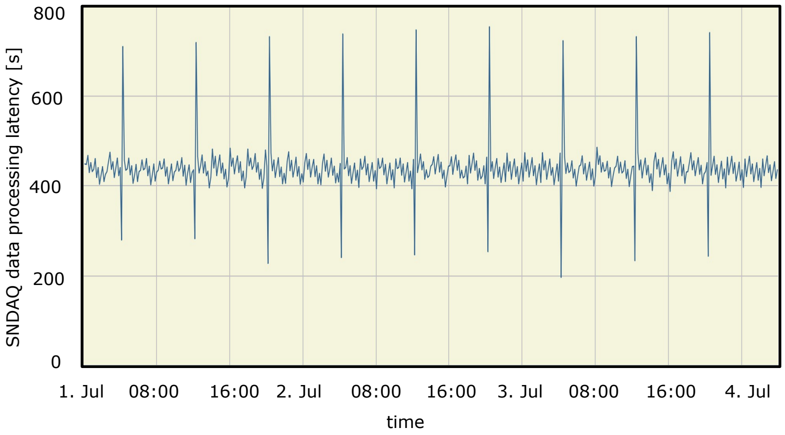

Figure 4.3: *Snapshot of SNDAQ latency taken from I3Live webpage. Clearly visible are the spikes at the start and end of one run unit (8 hr).*

4.2 Supernova Signal in IceCube

In order to quantify the detector response to a supernova neutrino signal in IceCube, one can use different approaches. The following section gives an overview of the necessary components and their various implementations.

The factors of the signal rate (equation 4.1) can be obtained by performing an independent simulation for neutrino interaction, Cherenkov photon creation and propagation in the ice as well as their final detection. The necessary neutrino cross-sections $\frac{d\sigma}{dE_e}(E_\nu, E_e)$ for the various interaction channels in ice are obtained by parameterizing the formulas given in Section 1.3. Here we will describe the remaining ingredients for estimating the signal rate. The effective photon volume $V_{\mathrm{eff}}^{\gamma}$ and the number of produced Cherenkov photons N_γ are the two factors that form the physical quantity of interest: the energy dependent effective volume for detecting a positron or electron $V_{\mathrm{eff}}^{e^\pm}$.

4.2.1 Effective Volume

The photon effective Volume,

$$V_{\mathrm{eff}}^{\gamma} = V_{\mathrm{gen}} \frac{N_{\mathrm{trig}}}{N_{\mathrm{gen}}} \quad , \tag{4.8}$$

quantifies in part the volume V_{gen} in which a number of photons N_{gen} need to be produced in order have N_{trig} photons detected by the DOM. Therefore, the photon effective volume is determined on the one hand by the optical properties of the ice and on the other by parameters describing the DOM response.

Ice Properties

Understanding the detection medium as well as possible is a natural requirement if one performs high precision measurements. Several models describing the Antarctic ice were developed in order to understand the properties of light propagation in the Antarctic ice in and around the detector. The Additionally Heterogeneous Absorption (AHA) model [165] was developed for ice layers where AMANDA was situated and extrapolated to depths of ICECUBE. The more recently developed South Pole Ice (Spice) models [166, 167] are based on in situ calibration measurements that were performed with flasher LEDs on-board of every DOM. In Figure 4.4 and Figure 4.5 the situation exemplary for photons of wavelength $\lambda = 400\,\mathrm{nm}$ is shown.

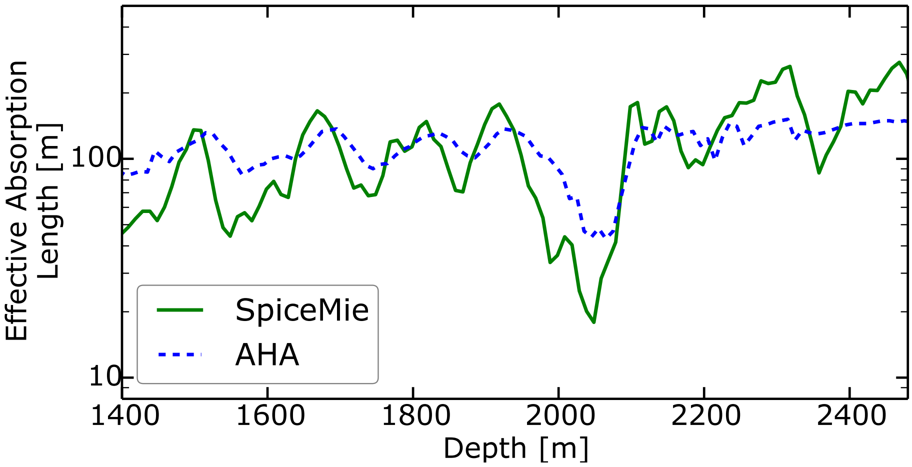

Figure 4.4: *Effective absorption length for photons of* $\lambda = 400\,\mathrm{nm}$ *as a function of depth in ice from AHA [165] and SpiceMie [166] model, respectively.*

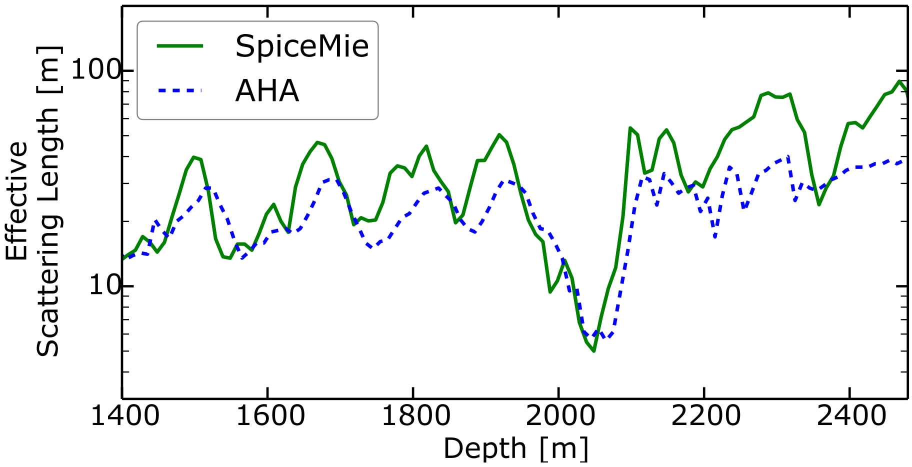

Figure 4.5: *Effective scattering length for photons of* $\lambda = 400\,\mathrm{nm}$ *as a function of depth in ice from AHA [165] and SpiceMie [166] model, respectively.*

The absorption length, defined as the distance after which the detection probability has dropped to e^{-1}, typically has values of $\mathcal{O}(100\,\mathrm{m})$. On the other hand the scattering lengths, usually lies in $\mathcal{O}(10\,\mathrm{m})$. Both parameters reflect well the fact that the glacial ice at the geographic South Pole is even cleaner than any manufactured optical material. At the depth of the detector, starting at 1450 m, the ice is already so old that the immense pressure of the upper layers forced out air bubbles, making the deep ice ultra-transparent. The depth dependent structure arises from dust particles that are present in all layers in the glacial ice cap coming from ashes of volcanic eruptions and atmospheric dust from different weather conditions in the past. Except for the dust peak between 1980 m and 2090 m which results from an increased volcanic activity, the absorption and scattering characteristics are not significantly disturbed by these contaminations. While this is a valid description of the 'bulk' ice, i.e. the unchanged part of the detection medium, the refrozen columns of ice surrounding the DOMs have to be considered as well. This is especially difficult to implement in any model because the fresh water/ice columns around the string are filled with air bubbles and a changed dust concentration compared to the bulk ice at the same depth. Secondary features of the ice cap are taken care of in the models as well. The most prominent aspects are the ice layer tilt [168] and the replacement of the asumption of a purely homogeneous bulk ice with a more anisotropic result by dust-logger measurement implemented in the Spice models.

DOM Properties

The second part for determining the effective volume is simulating the detector response. Basic calibration and characterization of the PMT are published in [143] and were partly discussed in Section 3.2. Quantities of interest are for example the single photon waveform and charge and the absolute efficiency of the PMT. These properties are collected in the DOMLauncher project, especially in the PMTResponseSimulator, both being part of the ICECUBE software framework ICETRAY which simulates the reaction of the DOM to the simulated light.

Result

In order to calculate the effective volume, one can use a statistical approach to simulate the light, as done with Photonics [169], or a direct propagation of the photon, performed with the simulation routines PPC [166] and CLSim [170]. Photonics represents the conventional method of sampling the arrival time distribution of photons on a photo-detector based on large, interpolated look-up tables. Although Photonics is able to perform reasonably well, the highly non-trivial challenges of generating these tables and finding robust interpolation methods leads to drawbacks like binning artifacts, large memory requirements etc. The new approach in ppc an clsim solves these problems by tracking each single photon generated by a given source in the detector. Each simulated particle in the detector is converted into a series of light-emitting partial tracks that are generated by a full Geant4 simulation and have constant speed and constant number of emitted photons over a given length [171]. A study comparing two ice models as well as using different photon propagation methods was performed by [172] to determine the effective volume, see Figure 4.6. In this analysis, 1.4×10^9 positrons with 10 MeV energy were simulated in a sphere of radius 250 m around each DOM on a standard string and a DeepCore string, respectively. By determining the number of detected leptons over the number of injected leptons one arrives directly at the effective positron volume $V_{\mathrm{eff}}^{e\pm}$ which is the product of the effective single photon volume and the number of generated Cherenkov photons per lepton energy. The difference in effective volume for DOMs on DeepCore string due to higher quantum efficiency of their PMTs is clearly visible. Assuming positrons that hold a mean energy of $\langle E_{e^+} \rangle = 20$ MeV, which is a reasonable choice according to Figure 1.5 and considering the SpiceMie model on an averaged InIce string, one encounters a effective

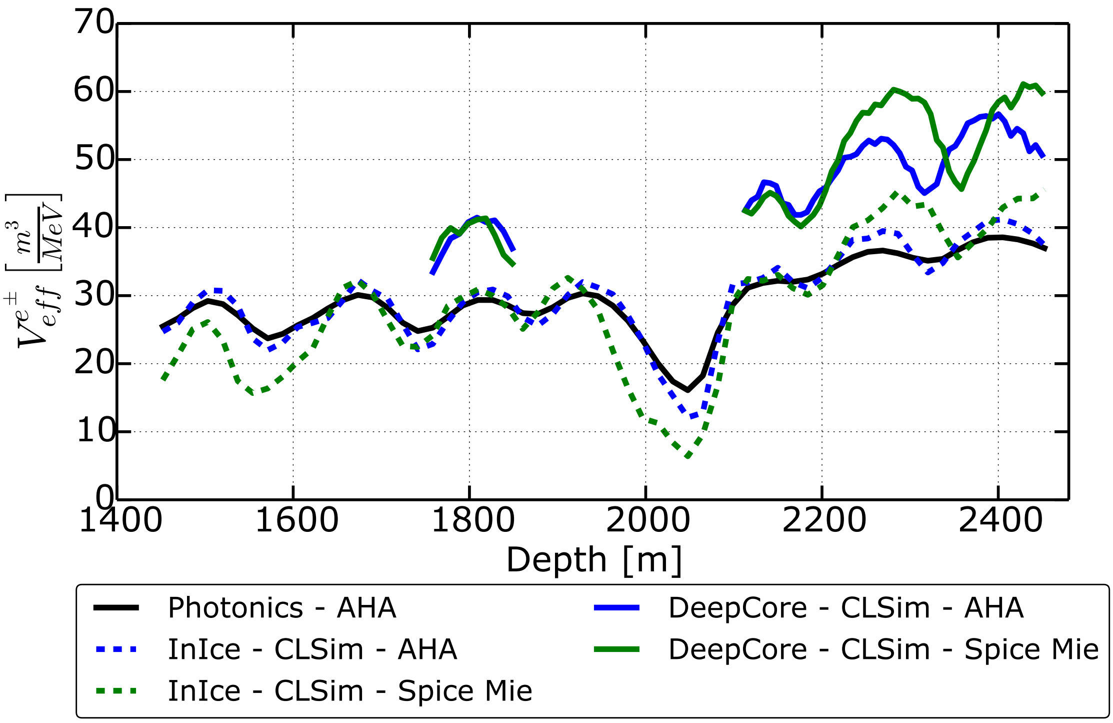

Figure 4.6: *Effective positron volume as a function of depth in ice from AHA [165] and SpiceMie [166] model, respectively. The notation 'InIce' stands for standard DOMs with qunatum efficiency* $\epsilon = 1$ *whereas DeepCore DOMs have high quantum efficiency of* $\epsilon = 1.35$ *on average. Credit: [172].*

positron volume of $V_{\text{eff}}^{e^+} = (28.6 \pm 10.1) \cdot \langle E_{e^+} \rangle \approx 560\,\text{m}^3$. This volume corresponds to a sphere centered at the DOM of 5.14 m radius with 100 % sensitivity inside and 0 % outside. Both ice models deliver similar results agreeing within 5 %.

4.2.2 Neutrino Flux

The final ingredient for estimating the signal rate (equation 4.1) is the model-dependent neutrino flux at detector level Φ_ν^{D} (equation 4.2). This quantity combines the three input parameters from theory: the time-dependent supernova neutrino luminosity L_{SN}^{ν}, the mean energy $\langle E_\nu \rangle$ and the energy spectrum 'pinching parameter' α (see equation 2.19.) Depending on the theoretical model, different results can be obtained for Φ_ν^{D}. The Lawrence-Livermore model (LL), see Section 2.6, is a conservative model based on the observations from SN1987A with a progenitor star of about 20 $\text{M}_\odot$. A more recent and advanced simulation performed by [105] is named *Garching* model and is based on a 8.8 $\text{M}_\odot$ star that consists of an O-Ne-Mg core at the time of its explosion, i.e. an electron capture supernova (see Section 2.2.1). Figure 4.7 shows the two models' determining parameters: neutrino luminosity $\mathcal{L}_\nu$, mean energy $\langle \text{E}_\nu \rangle$ and pinching parameter α, respectively. The first obvious difference is to be found in the neutrino emission lightcurve, whose feature were schematically shown in Figure 2.5. The Lawrence-Livermore scenario misses the pronounced dip in the luminosity curve of the electron neutrinos $L_{\text{SN}}^{\nu_e}$ at the time of neutrino trapping. Other differences are encountered in the $\langle E_\nu \rangle$ and α distribution which is flat throughout the simulated evolution of the supernova in the LL model. The modern Garching simulation in general tends to a little bit lower mean energies and allows stronger variations in α. One should keep in mind that neutrino oscillations effects due to the MSW effect in the Earth modify the neutrino flux at the detector, as presented in Chapter 1.2. This effects are summarized in a systematic uncertainty of 8 % at maximum [43], depending on the supernova model, the incident angle of the neutrinos and their properties.

4.2.3 Signal Hit Rate

Two distinguished simulation chains were used to process the factors influencing the expected signal rate [172]. The standard supernova signal estimation of IceCube, called Unified Supernova Simulation Routine (*USSR*), uses a parametric approach based on the steps explained above. Every factor of the signal hit rate is parametrized in independent simulations and mapped together at the end.

The newly developed *sni3sim* [172] approaches the task from an event based point of view. Single neutrino interactions are injected in the simulation and processed coherently in the programming framework IceTray. This brings several advantages compared to the standard simulation. Since the USSR produces an estimate of the response of SNDAQ to a given supernova model based on scalers stored in 500 ms bins, it is not possible to investigate for example the effect of atmospheric muons on shorter timescales. This problem is overcome by the fact that sni3sim simulates separately background and signal and furthermore performs not only the scaler simulation but also the standard data stream (pDAQ) response to an injected supernova model. Additionally, USSR produces an SNDAQ specific data type and hence makes it more difficult to include information gained from other systems, such as HitSpool , which are processed in the IceTray environment like sni3sim. Figures 4.8 and 4.9 show the results of both simulations for a detector response to a supernova according to the Lawrence-Livermore and the Garching model at 10 kpc distance, respectively. These

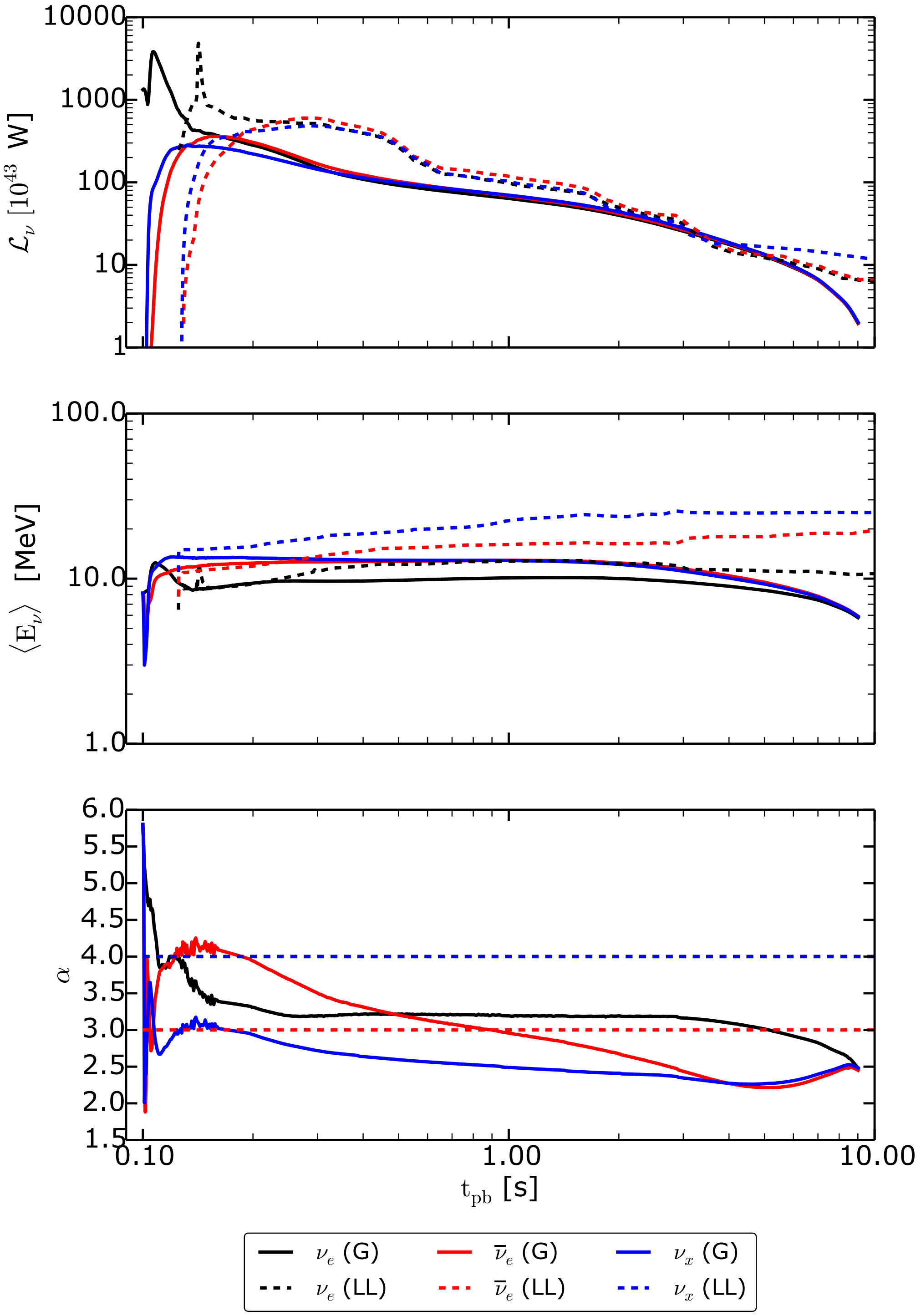

Figure 4.7: *Lawrence-Livermore (20 $\mathrm{M}_\odot$) and Garching O-Ne-Mg (8.8 $\mathrm{M}_\odot$) compared.*

two models were selected amongst the variety of possible supernova simulations because their evolution was run for comparatively long time scales of $\mathcal{O}(10s)$. Independent of the tested supernova model, the results of the simulations show a difference of 40% on average which is well understood [172]. The main differences arises from the fact that different neutrino energy spectra were used with a shift in the mean energies from 12.5 MeV (USSR) to 15 MeV (sni3sim). This is motivated by taking oscillation effects into account where for example ν_e will

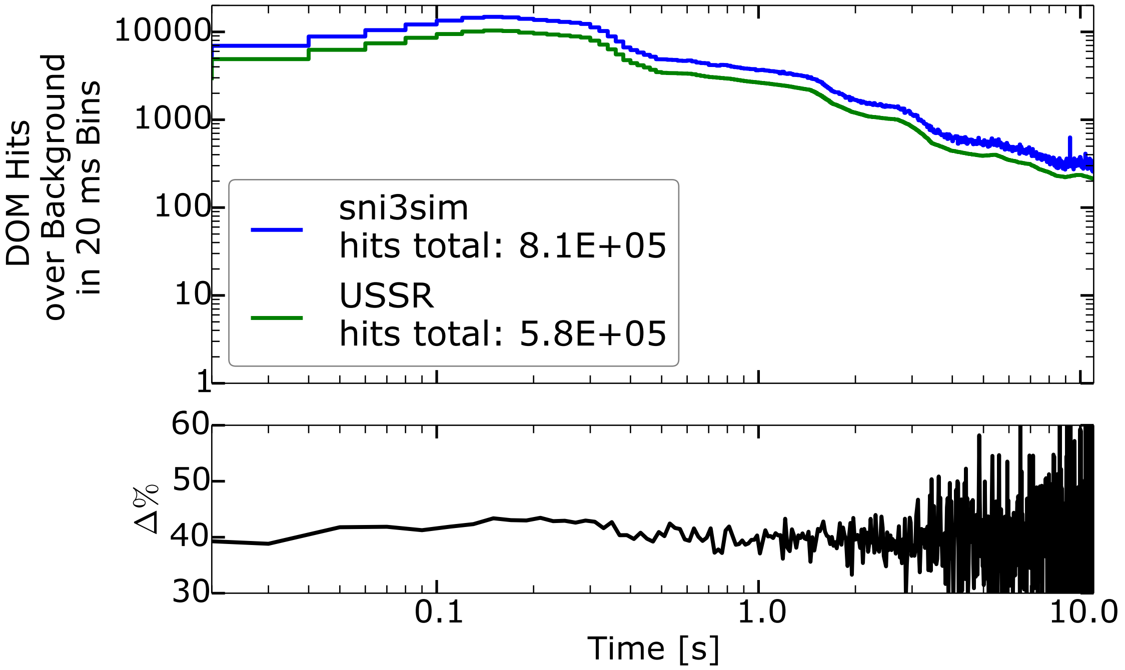

Figure 4.8: *Expected detector response of* IceCube *for a supernova according to the Lawrence-Livermore model [113]. The DOM hit rate in* 20 ms *is shown as a function of time in double logarithmic scale. The new simulation framework sni3sim gives on average a 40 % higher signal than the USSR. Credit: [172]*

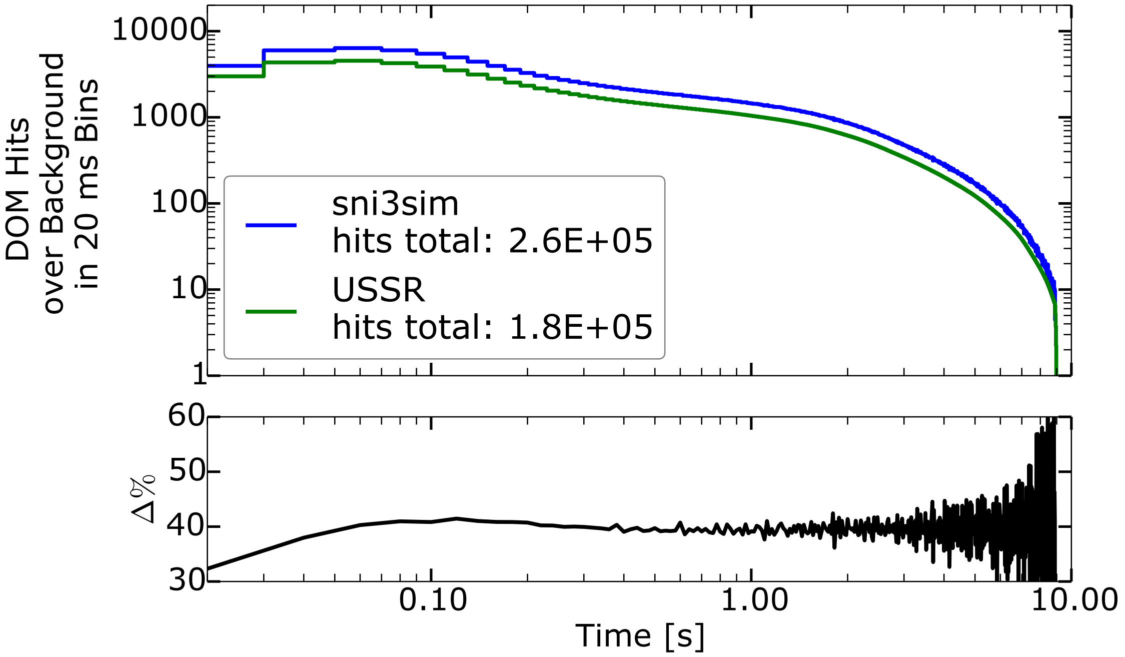

Figure 4.9: *Expected detector response of IceCube for a supernova according to the Garching O-Ne-Mg model [105]. The DOM hit rate in* 20 ms *is shown as a function of time in double logarithmic scale. The new simulation framework sni3sim gives on average a 40 % higher signal than the USSR. [172]*

have a higher mean energy when resulting from oscillation of ν_x rather than being produced as ν_e directly since $\langle E_{\nu_x} \rangle > \langle E_{\nu_e} \rangle$ (equation 2.18 and Figure 4.7). Higher energies result in more Cherenkov photons being produced in an interaction which increases the detection probability. This accounts for $\sim$ 20 % of the difference in the shown simulations according to [172]. Smaller contributions to the difference arise from the absence of a deadtime in the simulated scaler stream ($\sim$ 10 %), a different time binning ($\sim$ 5 %), new inverse β-decay cross-sections ($\sim$ 5 %) and changes in the detector geometry, the ice models used and the DOM sensitivity ($\sim$ 3 %). In general, and as already mentioned in Chapter 2, the detected signal naturally differs from the emitted neutrino luminosity at the source due to oscillation effects inside the star.

4.2.4 SNDAQ Signal: Physics Capabilities

The neutrino mass hierarchy problem could be answered as well from observing a galactic supernova in IceCube. As explained in Chapter 1.2, neutrinos oscillate and depending on the mass splitting one expects more oscillations into electron neutrinos which enhance the signal.

The detector response to the different mass hierarchy is shown in Figure 4.10 for supernova neutrino fluxes modeled after the LL and the Garching parametrization.

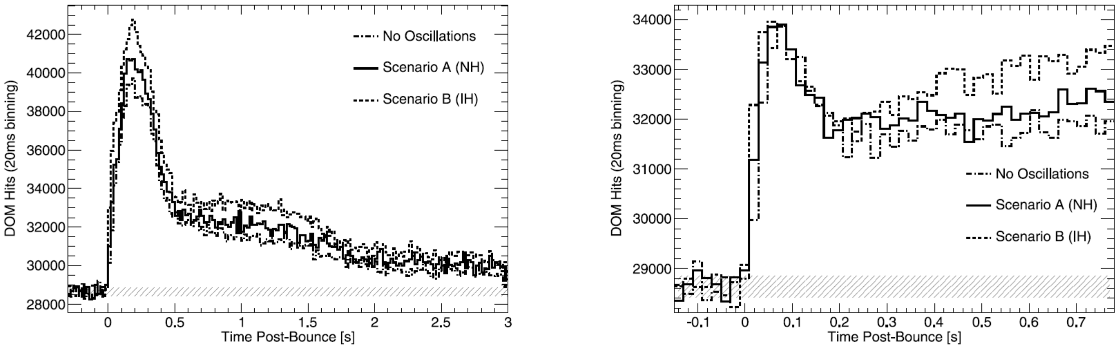

Figure 4.10: *Expected rate distribution at 10 kpc supernova distance for oscillation scenarios A (normal hierarchy) and B (inverted hierarchy). Fluxes and energies in the left panel are taken from the Lawrence-Livermore model and in the right panel from the Garching model [66].*

Of special interest is the investigation of the deleptonization peak since its time profile and magnitude are mostly independent mass of the of the progenitor or the nuclear equation of state. With a variation of $\sim 6\%$ [112] the peak in the lightcurve could be use to measure the distance to the supernova, i.e. establish it as a standard candle. This strong but very short lasting ν_e - burst, typically $\mathcal{O}$(10 ms), causes a strong induced signal, see figure 4.11. The standard SNDAQ data stream can record it in the finest available time binning of 2 ms. The signal would still be very difficult to extract due to its detection channel, the elastic scattering of electron neutrinos, which has a cross-section $\sim$ 50 times smaller than the dominant inverse β decay (IBD) in ice. The $\overline{\nu}_e$ flux grows rapidly after the collapse such that the deleptonization peak remains almost completely hidden in the combined signal, see right panel in Figure 4.11 [66]. Since IceCube currently cannot reconstruct individual supernova neutrino events, it is insensitive to directional information. Studies are under way that investigate how one can extract directionality from HitSpool data.

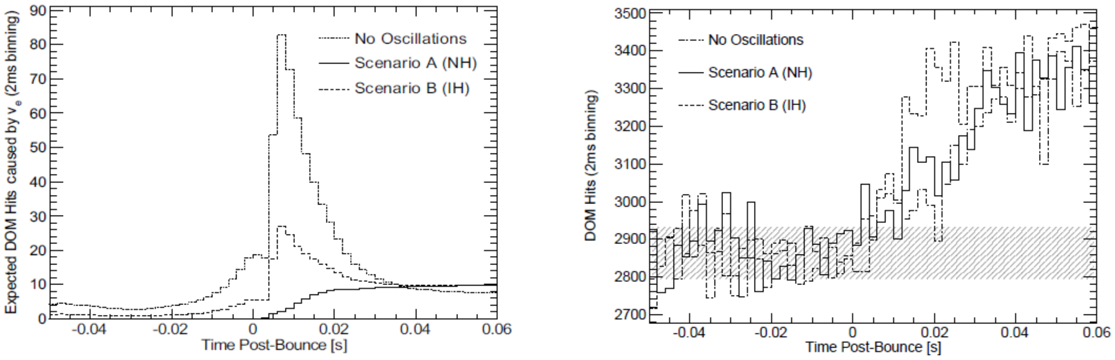

Figure 4.11: *The expected average signal hit rate for the Garching model [105] at* 10 kpc *distance in a time binning of* 2 ms*. The left panel shows the expected response to a purely* ν_e *signal as coming from the deleptonization burst. Adding DOM noise and the main detection channel, inverse* β*-decay, this signal is no longer visible, as shown in the right panel. Detector noise adds about* ±70 *counts in each* 2 ms *bin. [66].*

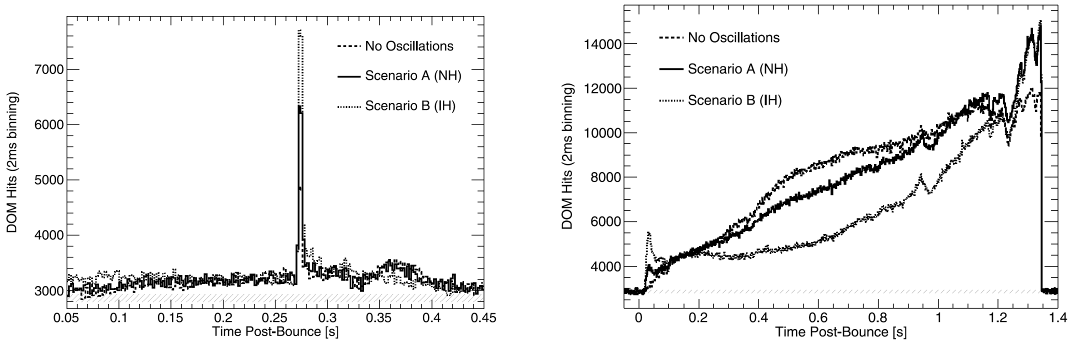

(a) *Quark star formation*

(b) *Black hole formation*

Figure 4.12: IceCube *signal response to quark star and black hole formation [66].*

Observing effects of instabilities like SASI or neutrino emission asymmetries like LESA in any signal response simulation needs to be investigated but it its success is doubtable because the 2 ms binning is very coarse for resolving such short signal oscillations. In Figure 4.13 is shown which event rates are expected in IceCube by the newest three dimensional simulations (as described in Chapter 2). New hopes for detecting these effects come from the HitSpool system which is expected to deliver more information about fine time structure because the only limiting factor is the DOM internal time resolution of 0.1 ns.

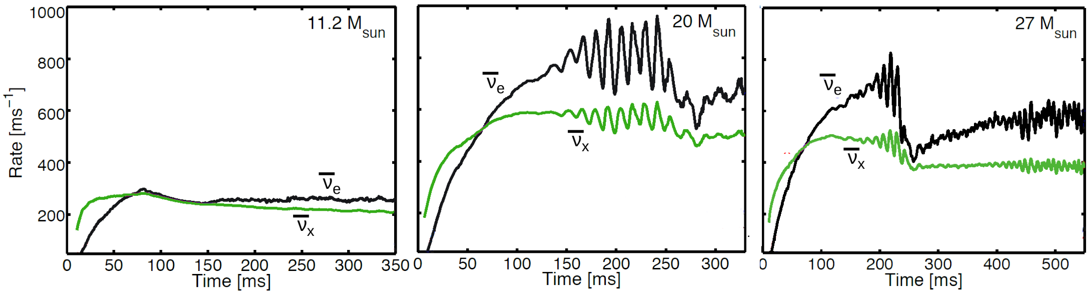

Figure 4.13: *Expected neutrino event rate for a 11.2, 20 and 27 $M_\odot$ progenitor SN model [54] flavor conversion. These models are (not yet) implemented in any signal response simulation of IceCube. These events rates have form the time dependent neutrino flux Φ_ν^{D} at the detector which has to be parametrized before being able to run the full simulation chain (USSR or sni3sim).*

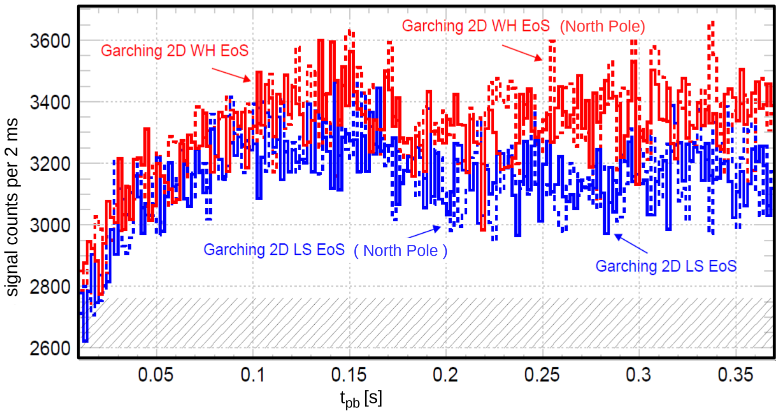

Figure 4.14: *Detector response to SASI excitations of the 2-dimensional Garching model [63]. Two different equations of state were used (LS EoS: Lattimer-Swesty [117] and WH EoS: Wolff-Hillebrandt [173]). Signals emitted from the stellar North Pole are shown for comparison to the total emitted signals.*

Earlier results derived by [63] from studying 2-dimensional SASI models came to the conclusion that at distance of 10 kpc the signal is almost indistinguishable from background, see Figure 4.14. Performing a Fourier-analysis of the signal spectrum yields a detection capability of IceCube with respect to SASI modes for supernova distances up to 5 kpc and SASI frequencies up to ∼ 250 Hz.

4.2.5 Detection Range

The overall detection range of IceCube with respect to core-collapse supernova is shown in Figure 4.15 based on the Lawrence-Livermore model. The expected significances decrease exponentially with distance. With respect to the no-oscillation scenario, neutrino flavor conversion inside the star given a normal mass hierarchy increases the signal by $\sim 15\%$ and as much as $\sim 40\%$ in the case of inverted hierarchy. IceCube will see a signal with $\xi \geq 12$ if the supernova happens inside our galaxy, i.e. at a maximum distance from us of $\sim$ 30 kpc. The closest sources for supernovae outside our galaxy, the Magellanic Clouds, are predicted to trigger IceCube with an average significance of $(5.7(15))$ in the LMC and (3.2 ± 1.1) significance in the Small Magellanic Cloud (SMC) [66] and thus are buried under the trigger level caused by atmospheric muons.

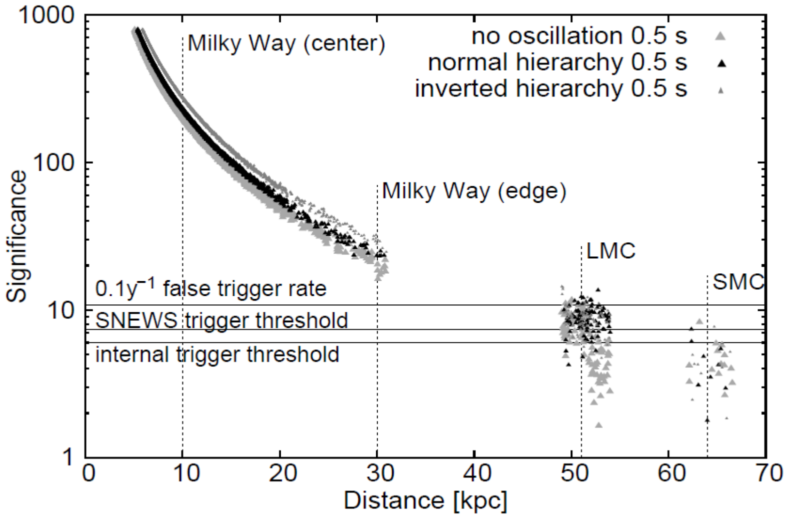

Figure 4.15: *IceCube's detection significance as a function of distance assuming the Lawrence-Livermore model [113] and a stellar distribution following [174] for three different oscillation scenarios [66].*

HitSpool data, explained in Chapter 5, can help to improve the detection range by identifying atmospheric muons in the data stream and lowering the overall noise threshold in this way.

4.3 Other Supernova Neutrino Detectors

This section is dedicated to present an overview of other detectors searching for supernova neutrinos that are currently running or being planned in the near future. Table 4.3 summarizes their basic characteristics. In general, the chosen detection method and material is what determines the measurable neutrino properties. Supernova search experiments can be grouped in four categories based on the technology they are using to detect neutrinos.

Water-Cherenkov Detectors

IceCube belongs to the group of experiments that use water as interacting medium. The other experiment currently running which also exploits the Cherenkov effect in water is Super-Kamiokande (Super-K) in Japan [176]. The detector consists of more than eleven thousand

Table 4.3: *Current supernova neutrino detectors and a selection of proposed and planned future experiments [35, 175]. Detector types are abbreviated: Water Cherenekov = WCh, Scintillator = Sc, Liquid Argon = LAr.*

Detector	Type	Location	Mass [10^6 kg]	Events 10 kpc	Status
MACRO	Scintillator	Italy	0.045		past
Amanda	WCh(long-string)	South Pole	120	65 000	past
SNO	Heavy WCh	Canada	1	780	past
IMB	WCh (tank)	USA	8	940	past
IceCube	WCh (long-string)	South Pole	3.000	8×10^5	Running
Super-K	WCh (tank)	Japan	32	8000	Running (SK IV)
LVD	Sc	Italy	1	300	Running
KamLAND	Sc	Japan	1	300	Running
Borexino	Sc	Italy	0.3	100	Running
Baksan	Sc	Russia	0.33	50	Running
Mini-BOONE	Sc	USA	0.7	200	Running
Daya Bay	Sc	China	0.33	100	Running
HALO	Lead	Canada	0.079	20	Running
NOνA	Sc	USA	15	3000	Starting
SNO+	Sc	Canada	1	300	Under Construction
Icarus	LAr	Italy	0.6	60	Near future
MicroBooNE	LAr	USA	0.17	17	Under construction
LENA	Sc	Europe	50	15.000	Future
Hyper-K	WCh	Japan	540	110.000	Future
LBNF	LAr ?	USA	40	?	2025

PMTs that are mounted on the mantel of a cylindrical stainless steel tank filled with purified water at about 1 km underground. Like IceCube, Super-K is not a dedicated supernova experiment but is used to study also neutrino oscillations, solar neutrinos, atmospheric neutrinos and proton decay [177]. The main difference to IceCube, which has inverse β-decay (IBD) as main detection channel, is the fact that Super-K is able to detect not only the $\overline{\nu}_e$ from IBD but also other flavors due to its low energy threshold of $\mathcal{O}(5\,\mathrm{MeV})$. To this effect, one can group these detectors in either *long-string* water Cherenkov detectors like IceCube or standard tank experiments. Super-K can directly measure the energy of the primary neutrino by determining the energy of the produced positron from the inverse β-decay ($E_{e^+} = E_{\overline{\nu}_e} - 1.3\,\mathrm{MeV}$)[3] with an energy resolution of $\sim 15\,\%$ at 10 MeV [178]. Exploiting the directionality of elastic scattering processes of electron neutrinos from the deleptonization peak ($\nu + e \longrightarrow \nu + e$) enables Super-K to determine the position of the supernova to $\sim 8°$ [64]. Radiative capture of neutrons on gadolinium helps identifying underlying near-isotropic events from inverse β-decay (with an estimated efficiency of $\sim$ 68 %) and improves the pointing accuracy to about 3° [64, 179]. Super-K searched for core-collapse Supernova bursts in their data sets taken between 1996 and 2007 without a discovery. From this result, given an effective lifetime of the detector of 2589 days, an upper limit on the supernova rate up to 100 kpc of $R_{SN} <$ 0.32 per year (90% C.L.) [176] was deduced.

---

[3] Results from the mass difference between the neutron being converted into a proton in the inverse β process: $m_n - m_p = 939.56\,\mathrm{MeV} - 938.27\,\mathrm{MeV} \approx 1.3\,\mathrm{MeV}$

The event rate in water Cherenkov detectors as a function of neutrino energy, for a specific supernova model and distance, can be seen in Figure 4.16 assuming a detector with 100 kt of water and covering 30 % of the volume with PMTs.

Scintillator Detectors

The second category consists of scintillator detectors that are composed of hydrocarbons. Charged particles passing though the medium deposit energy which can be observed via light emitted from relaxation of molecular energy levels. An example for such a detector type is the *Large Volume Detector* (LVD) [180], a dedicated supernova search experiment that consists of 1 kt of scintillator installed at the Gran Sasso Underground Laboratory. The nature of isotropic light emission from de-excitation of the scintillating material allows only little supernova direction information. For a supernova at 10 kpc distance, LVD expects to measure up to 400 events with a precision of $\mathcal{O}(1\,\mu\mathrm{s})$ and an energy resolution of $\sigma_E/E \approx 0.3/\sqrt{E[\mathrm{MeV}]}$ [181]. From 21 years, an effective lifetime of 7335 days, of data taking without a detection, LVD could place an upper limit on the supernova rate in our galaxy of $R_{SN} <$ 0.114 per year (90% C.L.) covering a distance up to 25 kpc [182].

Another scintillator based experiment is the Baksan Underground Scintillation Telescope (BUST) in Russia which went online in 1980. With no observation made in almost 25 years, BUST sets the most stringent upper bound on the frequency of galactic core-collapse supernovae to $R_{SN} <$ 0.093 per year (90% C.L.) [183].

A unique advantage of scintillator experiments is their ability to measure the low recoil energy protons from neutral current elastic scattering of neutrino. This is one of the very few possibilities to obtain information about the heavier neutrino flavors emitted in a supernova [184]. Event rates of possible interaction channels for this type of detector is shown in Figure 4.16. Further representatives of this detector class can be found in Table 4.3.

Lead Based Detectors

The unique representative of the third type of supernova neutrino detectors is the Helium and Lead Observatory (HALO) [185] using lead as target material. One of the advantages of using lead is the fact that the cross-section for charged and neutral current neutrino interaction is higher in lead than in water yielding comparably high rates. Anti neutrino interactions are suppressed by Pauli blocking due to the excess of neutrons in lead resulting in ν_e and ν_x being the predominantly sensitive interactions. Hence a lead based detector constitutes a new tool to probe other components of the neutrino flux from a core-collapse supernova [186]. Although it is not possible to extract energy information directly in a lead based detector, one can detect the ratio of single- and double-neutron ejections from excited nuclei by capturing them on $^3\mathrm{He}$ in order to retrieve a neutrino spectrum. Figure 4.16 summarizes the event rates assuming a detector with 1 kt lead.

Liquid Argon Detectors

At low energies ($E_\nu < 20$ MeV), charged current (CC) interaction of electron neutrinos with argon have high cross-sections. This motivates the last category of telescopes which use this element as their detection material. An example is the *Icarus* experiment that uses a large time projection chamber (TPC) filled with 600 kt of liquid argon to track the charged particles in the volume by measuring its ionization [187] via charge collection at the readout end-caps. Particle identification is obtained by measuring the energy loss along the track. As can be seen in Figure 4.16, the just mentioned CC interaction ($\nu_e +^{40} \mathrm{Ar} \longrightarrow e +^{40} \mathrm{Ar}^*$) is dominating over the possible interactions. This should enable Icarus to provide competitive information about the deleptonization bursts and neutrino trapping. Furthermore, pointing potential is given by determining the direction of the electron from elastic scattering processes [188].

Among all presented currently running supernova neutrino detectors, IceCube will provide the best statistics up to $\sim 8 \times 10^5$ events in the first 10 s after burst for a source at 10 kpc, as shown in figures 4.8 and 4.9. This is due to its unmatched large detection volume. With an average effective positron volume per DOM as derived in Section 4.2.1, IceCube roughly corresponds to a 3 Mton dedicated supernova search experiment which translates to a 0.45 Mton background free detector when taking into account the signal over background ratio as function of time and distance for a supernova at standard distance of 10 kpc [66].

Future Detectors

There are several detectors planned for the near future that either extend already existing experiments or are completely new facilities.

A promising proposal for a future neutrino detector based on the water Cherenkov technique is Hyper-Kamiokande (Hyper-K) [191]. With a planned detection volume of more than 500 kt, Hyper-K expects to detect more than 110.000 neutrino events of all flavors from a 10 kpc distant source. The timing resolution is believed to be in the order of a few milliseconds for the onset of the signal due to its high statistics. LENA [192] is a proposed concept for a next-generation scintillator based neutrino detector that would overtake the sensitivity of current scintillator or water based detectors by at least a factor of two.

Among the most auspicious detector upgrades is PINGU [193], planned for extending IceCube to lower energies by deploying optical modules on shorter distances in the ice. Based on the ratio of coincident hits to single events one can determine the average neutrino energy in IceCube with MeV resolution [194, 195]. The energy dependence on the hit ratio increases when the optical modules are closer together yielding a higher rate of coincidences. The energy resolution is expected to improve from $\sim 30\%$ for IceCube to better than $\sim 10\%$ in PINGU for a supernova at 10 kpc and an average energy of 12.5 MeV [193].

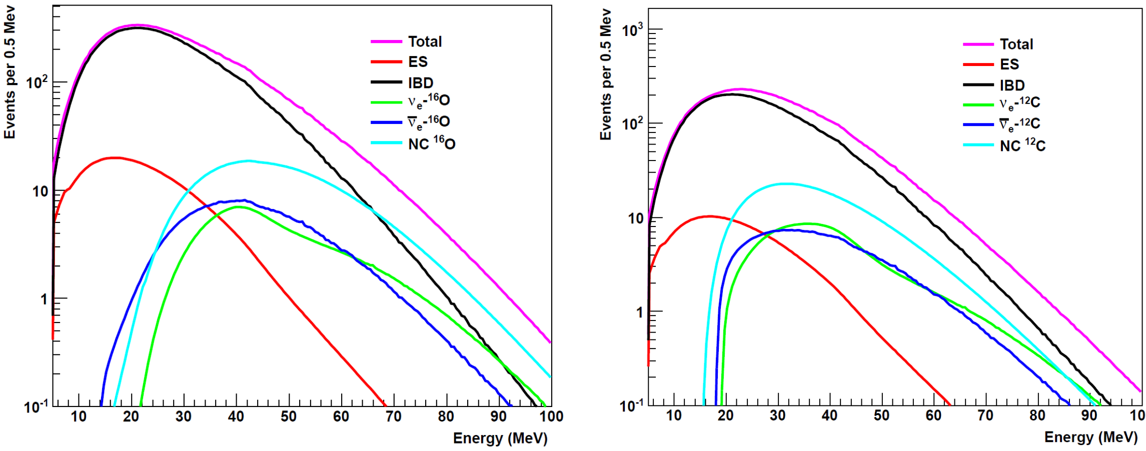

(a) 100 kt *of water.*

(b) 50 kt *of scintillator.*

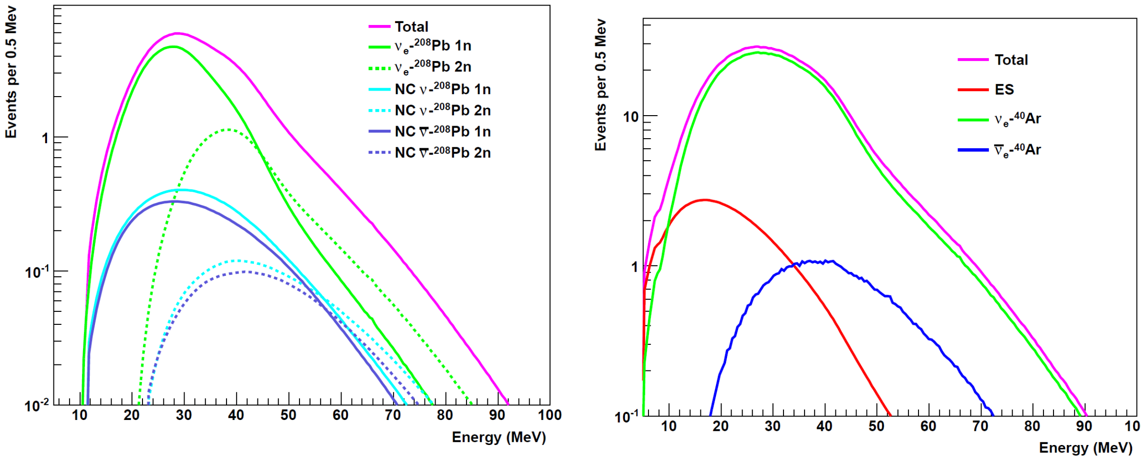

(c) 1 kt *of lead.*

(d) 17 kt *of liquid argon.*

Figure 4.16: *Relevant rates of neutrino interactions for four different detection materials, water (a), scintillator (b), lead (c) and liquid argon (d), as a function of true neutrino energy. The interactions were computed according to the SNOwGLoBES software package [189] and assuming a GKVM (Gava-Kneller-Volpe-McLaughlin) supernova model [190] for the neutrino fluxes. Elastic scattering (ES) processes are present in all materials but lead. Inverse β decay (IBD) dominates water and scintillator based interactions of neutrinos at these energies. Neutral current (NC) interactions can be observed in all detectors except those based on liquid argon.*

5

HitSpooling - A New Data Stream in IceCube

HitSpooling is a multi-purpose raw data buffer with the primary purpose to improve the data acquisition for supernova neutrino analysis. This chapter explains the basic concept and development of the system. A sphecial emphasis is given to the presentation of the interface developed for HitSpool *data taking. The details of* HitSpool *data processing for analysis are summarized in the last section.*

5.1 The HitSpool Concept

The implementation of HitSpool was started after working with raw data sets obtained with *Omicron*, a low-level interface to StringHub (see Section 3.3), which was used to solve dark noise related questions as presented in [196]. Omicron grasps all four data streams that are provided by the DataCollector. Although it is a good way for testing and debugging of single DOMs, Omicron was not designed to take data from the entire array at the same time. This is however necessary for a supernova analysis. Furthermore, the procedure is very complicated and accompanied by a high risk of disturbing normal data taking. This was the motivation for spooling the raw hits to disk of the DOMHub, shown as a dashed line in Figure 5.1, i.e. in addition to the hits in memory in the StringHub. The buffered data are organized by DAQ runs, as depicted in Figure 5.2, stored in one directory for the last run and one for the current run. The default data period per file is 15 s resulting in 1920 files per standard 8 h run. These values can easily be changed in the run configuration file provided with every run. At run transition, the files in the older directory are being overwritten. In theory, the available disk space allows for the storage of several days of data. Every string of IceCube generates about 1.8 MB/s of raw Hits data, see Figure 5.3. The data load reflects the summed hit rate of a string. For early deployed in-ice strings the data load is the lowest. DeepCore strings with high quantum efficiency modules have higher hit rates and thus a larger data volume. The strings implemented in the last deployment season of IceCube , which was in 2010, are recognizable by high data load, due to the still ongoing freezing process of the surrounding hole ice that causes higher hit rates.

As HitSpool is independent of any other surface DAQ element it also serves as a worst case scenario backup when IceCube's DOMHub memories could saturate due to the massive

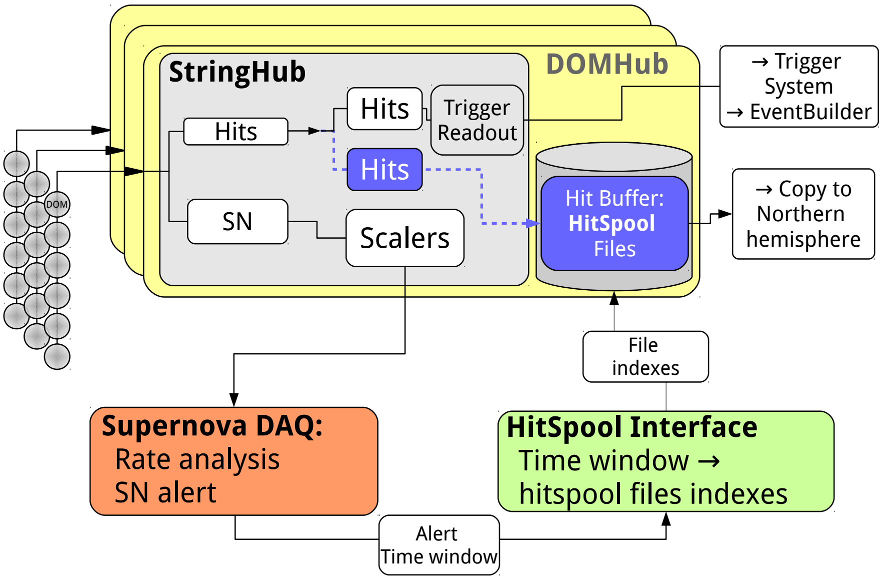
StringHub
DOMHub
Hits
Hits
Trigger Readout
Hits
SN
Scalers
DOM
Hit Buffer: HitSpool Files
→ Trigger System → EventBuilder
→ Copy to Northern hemisphere
File indexes
Supernova DAQ: Rate analysis SN alert
HitSpool Interface Time window → hitspool files indexes
Alert Time window

Figure 5.1: *Block diagram of surface DAQ components involved in the* HitSpool *data stream, shown by the blue dashed line. Hits are copied to the DOMHubs hard disk from where files can be picked up to be sent to the Northern hemisphere via satellite. The default service for requesting* HitSpool *data transfer is SNDAQ via the* HitSpool *interface.*

amount of hits from a nearby supernova. In order to keep track of the spooling process on a string, a `info.txt` file is written inside the buffer directory that holds the following information:

1. Time stamp of first hit on string at run start: t_{run}
2. Interval, e.g. length of each HitSpool file (default: 15 s): t_{ival}
3. Time stamp of first hit in current file: t_{cur}
4. File index of currently active HitSpool file: n_{cur}
5. Maximum number of files per HitSpool cycle (default: 1920): n_{max}

From these five values it is possible to calculate all necessary information about the hits contained in a HitSpool file without accessing the file itself and in this way avoiding any interference with the actual data taking. More details are given in Section 5.2.

5.1.1 HitSpool Raw Data Format

In contrast to the standard physics stream that deals with payloads, HitSpool uses the unprocessed binary data of Hits, so-called delta-compressed hits or engineering hits. The delta compressor [197] is a facility to read uncompressed fADC and ATWD data from the buffer on the DOM MainBoard. It produces a header for every hit followed by data, which is a peak sample of the fADC counts in case of SLC or fully sampled waveforms in case of an HLC hit. The data is compressed by only storing differences between successive samples instead of full ADC-counts and then losslessly compressing the entries. The compression header is

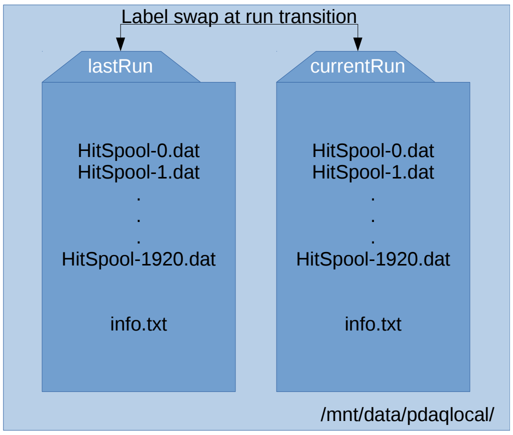
Label swap at run transition
lastRun
currentRun
HitSpool-0.dat
HitSpool-1.dat
HitSpool-1920.dat
info.txt
HitSpool-0.dat
HitSpool-1.dat
HitSpool-1920.dat
info.txt
/mnt/data/pdaqlocal/

Figure 5.2: *Diagram of HitSpool file buffer management on a DOMHubs hard disk.*

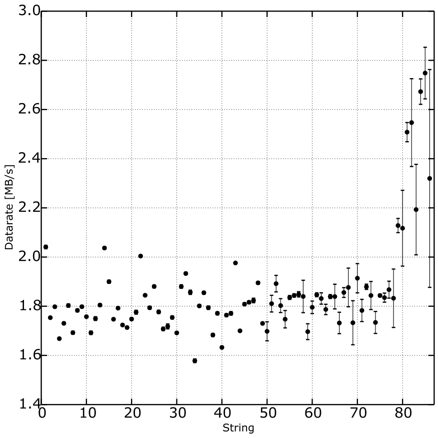

Figure 5.3: *Average data load and standard deviation of all in-ice strings with respect to the Hits data stream.*

packed as at least three 32-bit long words containing trigger conditions, readout channels, hit time stamp as well as waveform information. In case of an SLC, no waveforms are available and the header is stored without data. This implies a minimum size of a Hit of 12 bytes. More details can be found in Appendix A. For further processing, a binary file format is used for HitSpool data since it allows for a more efficient data storage and management compared to other formats.

5.2 HitSpool Interface

The HitSpool Interface has been developed in order to facilitate the collection of interesting HitSpool data from the DOMHubs and transfer the data to users in the Northern hemisphere. This section covers the design and operation of this system, which has partly been published in [159]. A detailed operations manual is given in Appendix B.

Figure 5.4 shows the main components involved in the interface. The *Publisher* service is the front-end that handles all incoming data requests. These data requests can derive from any DAQ subsystem but primarily are generated by SNDAQ. The HitSpool Interface itself does not trigger any data readout. The request message, containing a time window for the data in question, is sent to the *Workers* placed on each DOMHub. The Workers use the information stored in the monitoring `info.txt` file in their local HitSpool directories to calculate the HitSpool files integer indexes f_{start} and f_{stop} that contain data recorded between t_{start} and t_{stop}:

$$f_{start} = \frac{t_{start} - t_{run}}{t_{ival}} \mathrm{mod}(n_{max}) \tag{5.1}$$

$$f_{stop} = \frac{t_{stop} - t_{run}}{t_{ival}} \mathrm{mod}(n_{max}), \tag{5.2}$$

where $\mathrm{mod}(n_{max})$ accounts for the fact that HitSpooling overwrites existing files when the first loop is finished after time $t = n_{max} \cdot t_{ival}$. The data of all Hubs is collected and sent to data storage in the North by the *Sender* service.

5.2.1 Requirements and Solutions in the Interface

The following key points were crucial for the design of the interface:

Communication Thanks to the recent development of a multi-language network messaging tool, called ØMQ (ZeroMQ) [149], communication between the multiple HitSpool Interface services is taken care of by one single library. Reliable messaging is realized by using the *Transmission Control Protocol* (TCP) between the services running on different machines where data loss is automatically detected and solved. Sockets written in different languages can easily connect with each other thanks to the ZeroMQ library. Furthermore, the classical server-client structure for sockets is not obligatory anymore, i.e. clients can be launched even before the server has started. This eases the reconnection of lost services. The frequency and data volume of messages to be sent and received in the HitSpool Interface is low[1] compared to other detector operations and does not have any impact on the network performance.

Stability To ensure a stable performance of all components of the interface, several setups were tested. A version in which the interface would start up only for incoming requests and shut down afterwards, was not found to be reliable. ZeroMQ socket connections are very stable themselves and launched sockets lose connection only in case of the host machine shutting down. Therefore, the interface components connect and bind their sockets at system startup or via the command-line interface (next paragraph). Should

---

[1] A HitSpool data request generates a few hundred messages over a few seconds time with an average message size of 52 bytes. Monitoring messages are sent from each interface service once every hour.

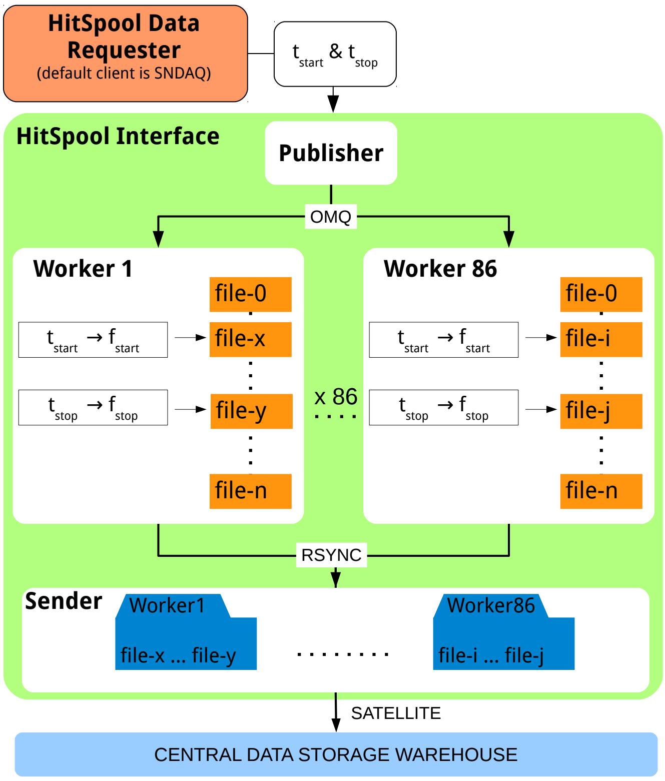
HitSpool Data Requester
(default client is SNDAQ)
t_{start} & t_{stop}
HitSpool Interface
Publisher
OMQ
Worker 1
file-0
$t_{start} \rightarrow f_{start}$
file-x
$t_{stop} \rightarrow f_{stop}$
file-y
file-n
x 86
Worker 86
file-0
$t_{start} \rightarrow f_{start}$
file-i
$t_{stop} \rightarrow f_{stop}$
file-j
file-n
RSYNC
Sender
Worker1
file-x ... file-y
Worker86
file-i ... file-j
SATELLITE
CENTRAL DATA STORAGE WAREHOUSE

Figure 5.4: *Data flow diagram of services involved in the interface. Messaging between components is handled by the network messaging library ZeroMQ whereas local data transfer is realized with the data synchronization software rsync. A dedicated satellite data stream is in place for transferring the data to the users in the Northern hemisphere.*

an unexpected shutdown of a component occur, a watchdog program running on the same machine restarts it automatically. A diagram of the messaging patterns used and the several components of the HitSpool interface is displayed in Figure 5.5.

Software deployment In order to facilitate the deployment and operation of the software to the surface DAQ system, a fabric script was developed. Fabric [198] is a Python library and command-line tool for streamlining the use of SSH[2] for application deployment or systems administration tasks.

Data transfer The way that the requested data are transferred from all DOMHubs to a central storage is based on *rsync*. That ensures a stable performance even on low bandwidth connections which were required to avoid interference with the normal data taking.

5.2.2 Messaging Architecture

Three basic messaging patterns are used in the HITSPOOL INTERFACE as shown in Figure 5.5. The sole bi-directional pattern is the *request-reply* (REQ-REP) pattern used for connecting any HITSPOOL data requester node with the central Publisher node of the interface. The Publisher returns a status message via its reply socket to the request socket. The default requesting node is SNDAQ that automatically sends a request if its online analysis system issues a trigger of significance $\xi \geq 7.65$, as mentioned in Chapter 4.1 and explained in more detail in the next section. If the Publisher is not responsive after several retries, the request is aborted and a failure report is sent out to experts via e-mail for further actions to be taken. The Publisher node hands over the request message internally to its *publisher* socket and sends its messages out to any number of connected *subscriber* sockets (PUB-SUB). With this messaging pattern, any subscriber socket can connect to or disconnect from the publisher socket without the need to reconfigure the network. This is in particular interesting as any change in the number of string participating in standard data taking will not affect the interface. The third messaging pattern used is the *push-pull* architecture. Any number of *push* sockets can connect to one *pull* socket. New connections or drop-outs are not reported and do not affect the network configuration. Additionally to the communications internally, the HITSPOOL INTERFACE is connected to the monitoring system I3Live that also uses ZeroMQ. The Worker nodes do not only push messages to the Sender service but also directly to a pull socket implemented in I3Live. The same pull socket is addressed by the Sender and a Watcher node is running in parallel to every Worker sending reports about a started, stopped or recovered Worker to I3Live.

5.2.3 SNDAQ HitSpool Data Requests

In order to meet the allocated data transfer limit per year, requested HITSPOOL data volumes depend on the SNDAQ trigger significance. In general, the supernova alarm rate is a function of the temperature-dependent atmospheric muon rate. Thus it is highest during Austral summer and averages to one alarm every two weeks of the entire year. The settings for data requests are summarized in Tab. 5.1. The basic request takes HITSPOOL data from 30 s before until 60 s after the SNDAQ trigger time stamp which is given in nanosecond precision. From supernova theories it is known that almost the entire neutrino signal is generated in the

---

[2] **S**ecure **SH**ell is a network protocol establishing a secure channel over an insecure network connection. It is widely used for remote command-line login and remote command execution.

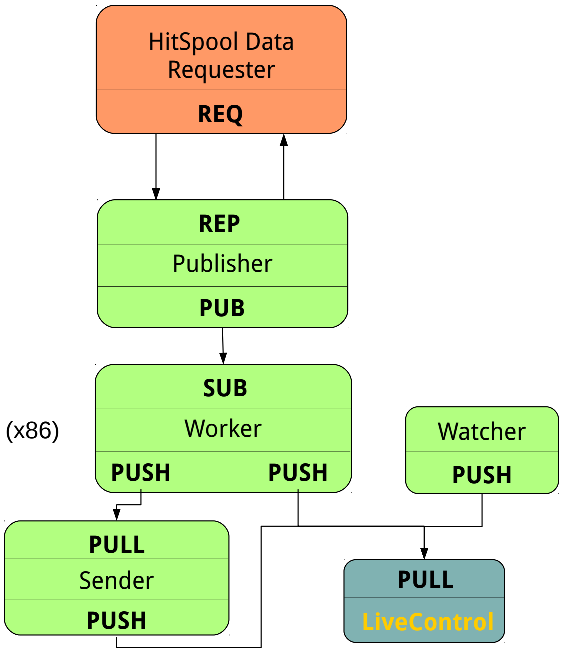
HitSpool Data Requester
REQ
REP
Publisher
PUB
SUB
Worker
PUSH
PUSH
(x86)
Watcher
PUSH
PULL
Sender
PUSH
PULL
LiveControl

Figure 5.5: *Messaging patterns in the interface. The bi-directional request-reply pattern (REQ-REP) connects any* HitSpool *data requester with the central publisher service of the interface. Any number of workers can connect to the latter via subscribing their socket to it (PUB-SUB). Monitoring messages from the Worker and Watcher components are pushed to I3Live (PUSH-PULL) or to the Sender node that is responsible for data compression and sending them to the Northern hemisphere.*

ten seconds following the core bounce, cf. Chapter 2.2. This time frame is covered in the request by including safety margins before and after the trigger time. For higher significant alarms, SNDAQ requests a larger period of data around the trigger time which is consistent with SNDAQ's internal time window used for the online significance calculation.

Table 5.1: HITSPOOL *data request settings from SNDAQ.*

SNDAQ Trigger [ξ]	Average Rate per Week	HITSPOOL Data Period	Data Volume, uncompressed	Data Volume, compressed
$\xi \geq 7.65$	0.5	$[-30\,\mathrm{s}, +60\,\mathrm{s}]$	18 GB	6 GB
$\xi \geq 10.00$	0.0006	$[-250\,\mathrm{s}, +250\,\mathrm{s}]$	90 GB	30 GB

5.3 HitSpool Data Processing in IceTray

Due to the fact that HITSPOOL data is separated from the standard surface DAQ at an early stage, all data processing is applied offline once the data have arrived in the Northern hemisphere. Besides the basic processing steps mentioned in Section 3.4, calibration and waveform feature extraction, the hits first have to be converted into IceTray objects, i.e. DOMLaunches. The data are divided into events, like standard data with the difference that the event size is not given by the triggers but is fixed, chosen to be 100 µs. Trigger algorithms are applied on the data afterwards. This is necessary in order to generate an event-by-event based relative timestamp for every hit in an event which is used by the following IceTray modules. After applying the waveform calibrations and feature extraction, the data are ready for higher level processing. The basic Hits are now transformed and possibly divided into multiple *RecoPulses* per Hit. Figure 5.6 shows a diagram of the following processing steps. The described processing chain was developed to identify atmospheric muons, see Chapter 6.1. The 100 µs long events are fed to two different event splitting algorithms in order to increase the chance to detect low energy muons.

The output of the two splitters is processed in slightly different ways, as shown in Figure 5.6. The data is separated into a muon sample, i.e. hits and RecoPulses caused by atmospheric muons, and a noise sample, containing hits related to detector dark noise. The purity of these samples has to be determined from simulation, explained in Chapter 7.

The modules used in the higher level processing are:

TopologicalSplitter This algorithm was developed in order to split events in individual sub-events by analyzing the time development of hit-clusters inside the detector. It constructs all possible subsets of input pulses that can be causally connected in terms of position and timing [200]. The possible range of these subsets is defined by a volume of fixed radius.

HiveSplitter This clustering algorithm, developed by Zoll and described in [199], is an advancement of TopologicalSplitter with respect to geometry settings defining the considered hit cluster. HiveSplitter describes the detector geometry in a more exact way than TopologicalSplitter, as shwon in Figure 5.7. Instead of using fixed radii like TopologicalSplitter, HiveSplitter uses hexagonal cylinders to construct the spatial limits over which hits can connect to a cluster. The cluster algorithm starts with defining an individual active volume (IAV), centered at the position of a hit DOM. The spatial limit of the IAV

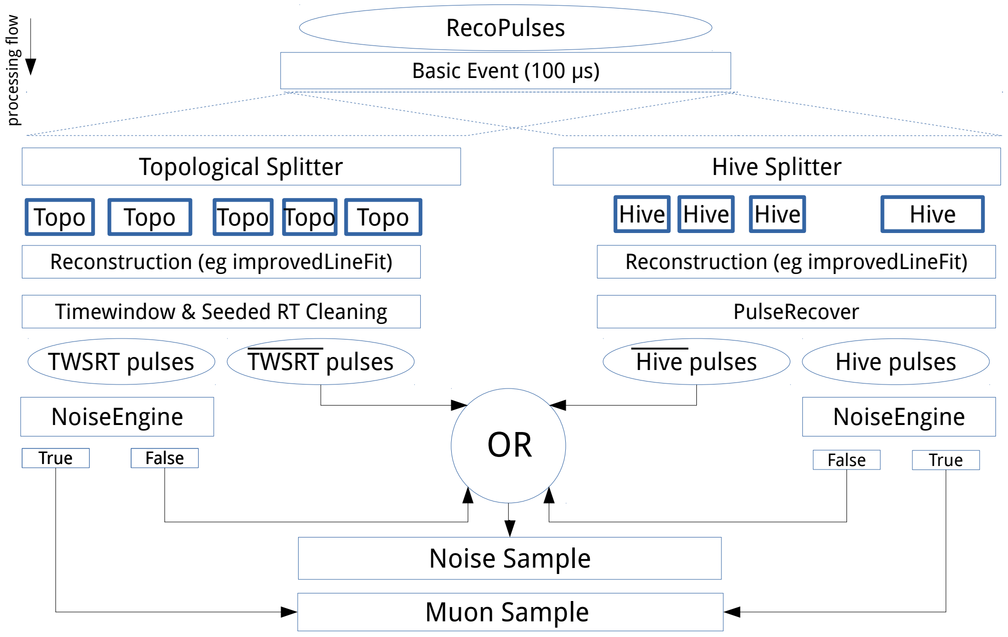
processing flow
RecoPulses
Basic Event (100 µs)
Topological Splitter
Topo
Topo
Topo
Topo
Topo
Reconstruction (eg improvedLineFit)
Timewindow & Seeded RT Cleaning
TWSRT pulses
$\overline{\text{TWSRT}}$ pulses
NoiseEngine
True
False
Hive Splitter
Hive
Hive
Hive
Hive
Reconstruction (eg improvedLineFit)
PulseRecover
$\overline{\text{Hive}}$ pulses
Hive pulses
NoiseEngine
False
True
OR
Noise Sample
Muon Sample

Figure 5.6: *Block-diagram of the higher-level processing steps for* HitSpool *data.*

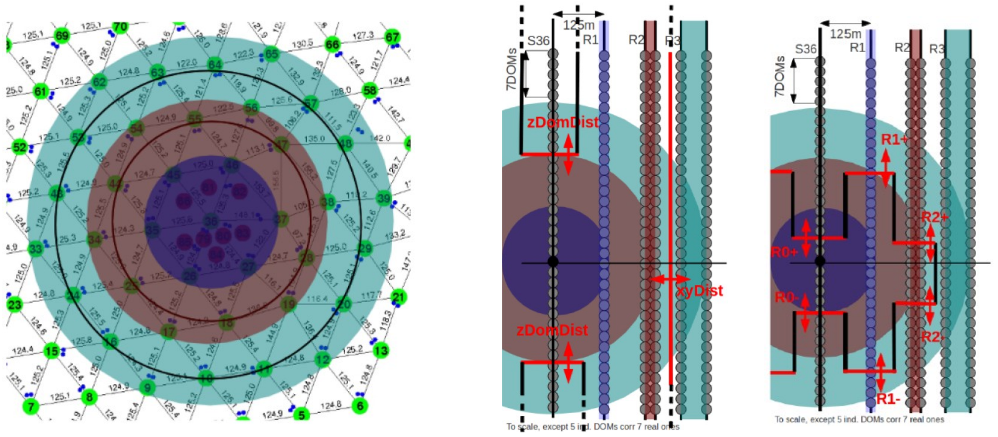
S36
125m
R1
R2
R3
7DOMs
zDomDist
xyDist
zDomDist
To scale, except 5 ind. DOMs corr 7 real ones
S36
125m
R1
R2
R3
7DOMs
R1+
R2+
R0+
R0-
R2-
R1-
To scale, except 5 ind. DOMs corr 7 real ones

a) top view

b) side view of TopologicalSplitter

c) side view of HiveSplitter

Figure 5.7: *Illustration of the spatial limits for hit clusters. Only hits inside these volumina can connect to one cluster [199]. The HiveSplitter settings, shown in c), are more advanced and tunable compared to the settings of TopologicalSplitter in b).*

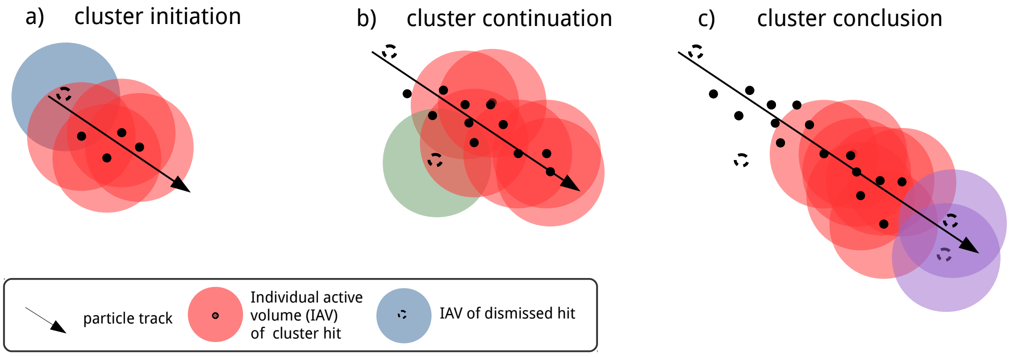

Figure 5.8: *Sketch of the initiation, continuation and conclusion of a hit cluster generated from Cherenkov photons of an incident particle to illustrate the working principle of cluster algorithms used in data processing [199].*

is defined by causality arguments, i.e. only hits are taken into account that lay within the time span that light could have traveled to reach them. If at least four of these IAV overlap, the minimum cluster size is found. This is shown in the right panel of Figure 5.8 by the red circled dots. The blue circle of the first hit in time is too isolated to contribute to the cluster seed created by the subsequent four hits. As the particle progresses through the detector, more hits are added to the cluster, if they fulfill the overlap criterion, as shown in the middle panel of the figure. When the particle leaves the detector or does not deposit enough energy to cause Cherenkov photons creating hits, the cluster is terminated, see the right panel. Noise hits (non-red circles in the figure) are usually not collected into the summed cluster since they do not fulfill the basic multiplicity requirement of four overlapping IAV. This technique empowers not only to separate physics related hits from noise hits but also to disentangle coincident events in the detector caused for instance by atmospheric muon bundles.

Reconstruction The events that are to be identified, namely sub-trigger atmospheric muons, are typically of low energy and thus low hit multiplicity which causes performance instabilities for any reconstruction algorithm. Therefore only a basic, fast and robust reconstruction was chosen, namely the improved linefit algorithm that was already mentioned in Section 3.4.

Hit Cleaning This is an extra step needed in the TopologicalSplitter stream. The first cleaning algorithm scans through the event with a sliding time window of a given length and keeps only the snapshot with the maximum number of hits in it. A second hit cleaning in space and time (*SeededRTCleaning*) [201] is performed that uses a similar hit cluster algorithm like HiveSplitter. A cluster seed is found if an HLC hit contains another hit within a radius $R = 125\,\text{m}$ and time $T = 1000\,\text{ns}$. SLC hits are successively added and are kept if lying inside the RT-volume.

PulseRecover This tool can be used to improve the performance of the HiveSplitter stream. It checks the event for lost pulses and adds them to the cluster if they fulfill the causality argument. This can improve the accuracy of the reconstruction applied to the hit cluster.

NoiseEngine In order to make a judgment about the nature of a pre-selected hit cluster, i.e. a selection of pulses, a module called *NoiseEngine*, developed by Michael Larson in [202], is used. Based on an idea formulated in [203], it decides if a cluster is rather noise-like or could be caused by an incident particle. This is achieved by examining the angular distribution of tracks formed by every possible hit pair. If the investigated hit pairs do not point in a preferred direction, the cluster is most probably of noise origin and the pulse series is collected to the noise sample. Otherwise it ends in the final sample of pulses possibly caused by atmospheric muons.

5.4 HitSpool Data Verification

5.4.1 Trigger Threshold

One of the main topics of this thesis is the detection of muons in IceCube which do not meet any trigger condition because they do not deposit enough light but still contaminate a possible supernova neutrino signal. In order to use HitSpool for this task it is necessary to ensure that triggers identify the same events in both data types, HitSpool and standard data, respectively. PFRaw data is used for this purpose since it is the raw standard data format of the detector after the event builder. This is the only stage in the standard DAQ where the raw data is still complete. A data sample of a few minutes was taken. For the same time period, a HitSpool data sample was collected, processed and triggered offline as mentioned in Section 5.3. The triggers are applied via a trigger simulation module of Icetray that is widely use for simulated data.

In figure 5.9 the four trigger types are shown for both data streams. The definitions of SMT3, SMT8, Volume and String trigger were given in chapter 3.3. As shown in the plots it appears that that the definition of trigger and sub-trigger muons agree in standard and HitSpool data. This verifies that the performance of triggers is the same for both data sets and the definitions of "sub-threshold" muons coincide. Another conclusion that can be drawn from these plots is the fact that the offline software trigger module reflects the online trigger system with satisfying agreement. The HitSpool concept works satisfying and HitSpool data collection and processing at high quality are achieved.

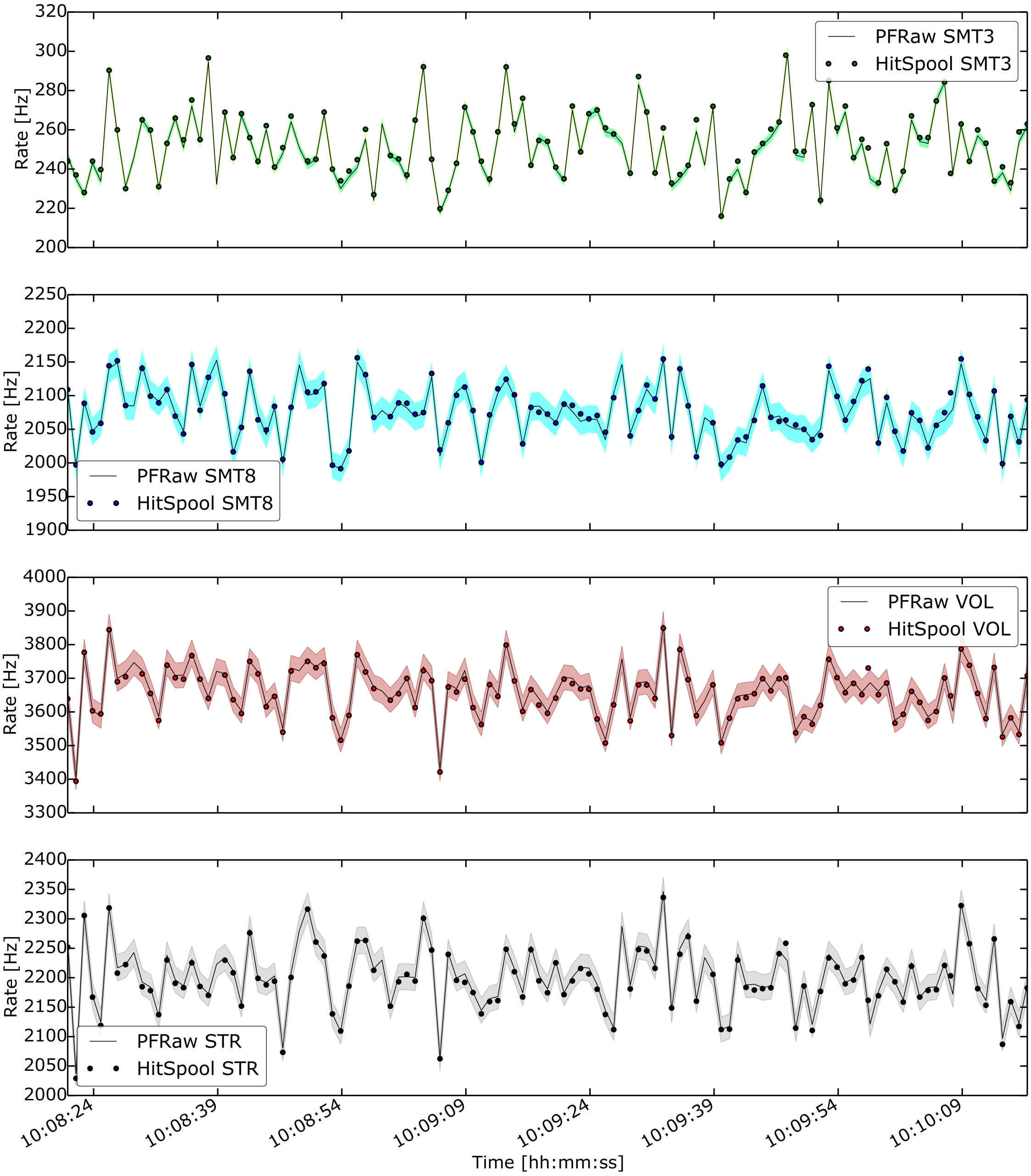

Figure 5.9: *Trigger rates for PFRaw, shown as lines and* HitSpool *data taken during the same time period, shown as dots. PFRaw data is the standard raw data type in IceCube after the online trigger system and before first processing and filtering. For* HitSpool *data, the triggers were applied offline. For all four trigger types, SMT3 in the top panel followed by SMT8, Volume and String trigger at the bottom, the* HitSpool *data offline trigger rates agree with the raw data in the* 1 % *deviation band of their trigger rates (colored bands).*

6

Backgrounds in IceCube

This chapter gives a summary of the state-of-the-art knowledge of backgrounds in the detector. The first section is dedicated to atmospheric muons that are produced in air showers of cosmic rays in our atmosphere. The second section deals with the instruments intrinsic dark noise and reviews the most important characteristics. A specific component of the dark noise, the non-thermal emission, is studied in detail using HitSpool *data, presented in the last section.*

6.1 Atmospheric Muons

Muons produced by cosmic rays in interactions in the Earth's atmosphere are five orders of magnitude more abundant in the detector than muons generated from cosmic neutrinos, the primary science goal of IceCube. Additionally, and of particular interest for this thesis, atmospheric muons influence the scalers rates that are the basis for the supernova analysis. Identifying these background contributions is an essential task for any analysis as mentioned in Section 4.1. To achieve this goal, the production of atmospheric muons and their signal in the detector have to be understood as much as possible.

6.1.1 Cosmic Rays

Charged particles that are generated outside our atmosphere are generally called *cosmic rays*. Since their discovery more than a hundred years ago, a lot of progress has been made towards revealing their composition and their origin, with IceCube taking part in these efforts. Although the sources of cosmic rays are still undiscovered, their composition is determined to consist mostly of free protons (79%) and helium nuclei (15 %) [39]. Figure 6.1 summarizes the major components measured as a function of the energy per primary particle. The physics of air showers, see next section, allows also the determination of the energy spectrum of cosmic rays, as shown in Figure 6.2. It extends over several orders of magnitude in energy and shows characteristic features such as the steepening around 10^{15} eV, called the *knee*, and the flattening starting at 4×10^{18} eV, called the *ankle* of the spectrum. Whenever a cosmic ray hits the Earth's atmosphere, it produces a cascade of secondary particles that can be detected at the ground as so called air showers.

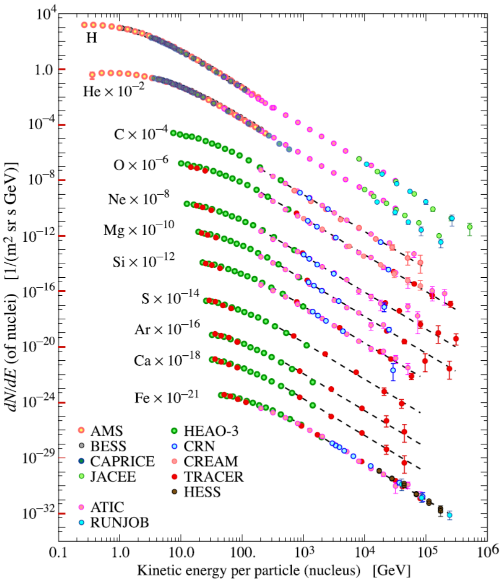

Figure 6.1: *Fluxes of nuclei of the primary cosmic radiation in particles per energy-per-nucleus [39].*

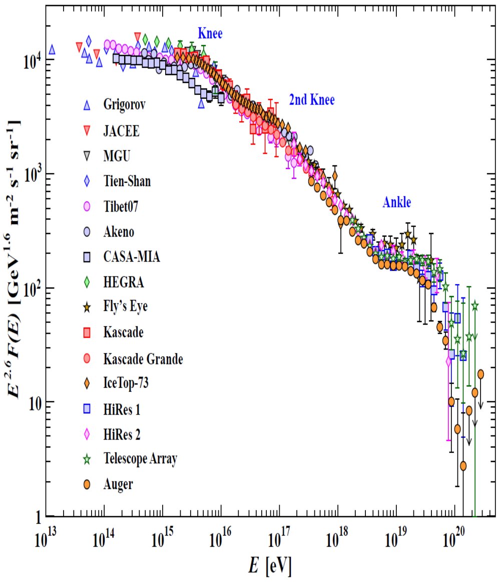

Figure 6.2: *The all-particle spectrum as a function of E (energy-per-nucleus) from air shower measurements [39].*

6.1.2 Air Showers

The collision of the primary cosmic ray particle with an air molecule produces a pion ($\pi^{\pm}$, π^0) in most of the cases but also other mesons like kaons ($K^{\pm}$, K^0) or baryons. The hadronic core of the shower, consisting of nuclear fragments from the collision, initiates electromagnetic sub-showers originating mostly from the two-photon decay of the neutral pion π^0, as shown in the right part of Figure 6.3. The electrons and positrons originating from pair-production processes are the most abundant charged particles of the shower. On the other hand, and one order of magnitude less abundant, muons are produced by decaying pions or kaons accompanied by neutrinos:

$$\begin{aligned} \pi^+ &\longrightarrow \mu^+ + \nu_\mu \\ \pi^- &\longrightarrow \mu^- + \overline{\nu}_\mu \qquad , \end{aligned} \tag{6.1}$$

as shown in the left part of Figure 6.3. Due to the high energy of their mother particle, the produced muons are highly relativistic. Their mean life time $\tau \sim 2.2 \times 10^{-6}$ s [39] is therefore extended by relativistic time dilation. For instance, a muon created in the upper atmosphere with a velocity of 0.999 c results in a Lorentz factor $\gamma \sim 70$ which enables the muon to travel more than 40 km in the rest frame of the Earth before decaying. Unlike electrons and positrons that are created in the shower and will be absorbed when reaching the Earth's surface, neutrinos and muons can (depending on their energy) penetrate far enough through the Antarctic ice cap to produce a signal in the detector.

6.1.3 Consequences of In-Ice Atmospheric Muons

The number of muon events triggering the detector is shown in Figure 6.4. This plot is a result of simulations using CORSIKA [204] and assuming a cosmic ray flux given in Reference [205].

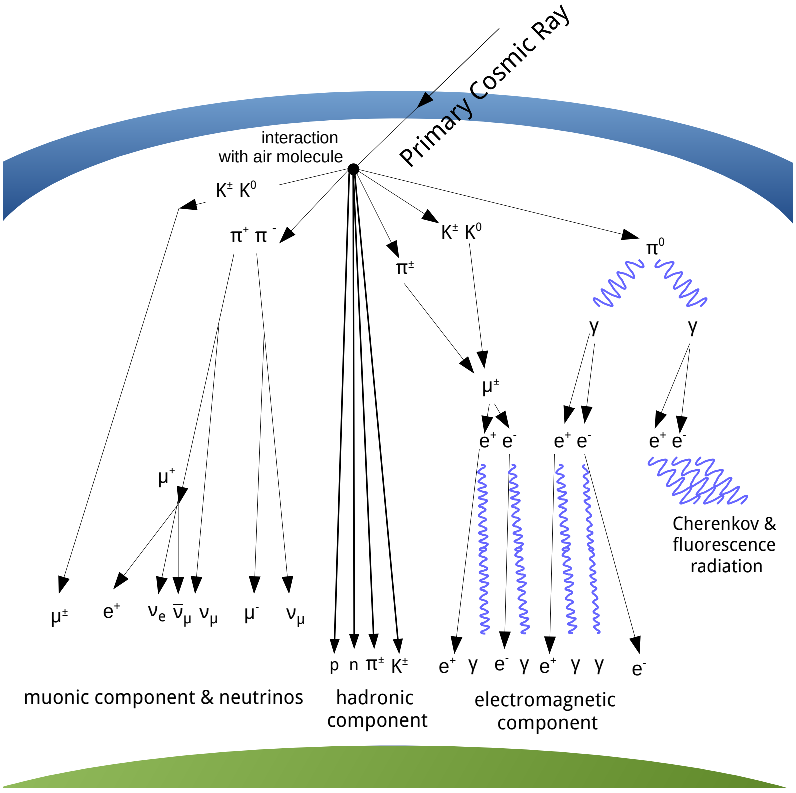
Primary Cosmic Ray
interaction with air molecule
K± K0
π+ π-
K± K0
π±
π0
γ
γ
μ±
e+ e-
e+ e-
e+ e-
μ+
Cherenkov & fluorescence radiation
μ± e+ νe ν̄μ νμ μ- νμ
p n π± K±
e+ γ e- γ e+ γ γ e-
muonic component & neutrinos
hadronic component
electromagnetic component

Figure 6.3: *Diagram of the possible evolutions of a cosmic ray air shower.*

This figure reflects the fact that most cosmic rays are protons, as well as the fact that the energy threshold for primary cosmic rays to trigger the detector is approximately 400 GeV.

In fact, the event rate in IceCube due to atmospheric muons is between 2.6 kHz and 3.0 kHz. This not only causes difficulties for any search where atmospheric muons mimic the sought-after signal with their track-like events but also the supernova channel is affected by atmospheric muons. Given the average muon rate of $R_\mu \sim 2.8\,\mathrm{kHz}$, we expect about 6 muons to contribute to every 2 ms supernova scaler sample which is the basis for SNDAQ's online analysis and trigger calculation. Later we will see that a large fraction of muons does not trigger but still produce hits in the detector. How to identify these muons is addressed in detail in Chapter 7.

In Figure 6.5 the average hit rate caused by muons per DOM is shown as a function of depth in the ice. The number of HLC hits is a valid representation of the triggered atmospheric muon hit rate per DOM since HLC hits are unlikely to be caused by intrinsic dark noise of the DOMs[1]. The effect of the dust layer is visible in the plot as the sudden dip in the hit rate around 2000 m depth.

---

[1] A single HLC hit pair consists of two hits in near-by DOMs in a time period of 1 μs(see Section 3.2.2). The condition is fulfilled by pure noise hits with a probability of 1.51×10^{-7}, assuming a pure Poissonian noise rate of 550 Hz and neglecting any internal dead time of the DOM, which translates to an accidental noise HLC rate of 0.15 Hz per DOM compared to the 2 Hz − 16 Hz observed in data.

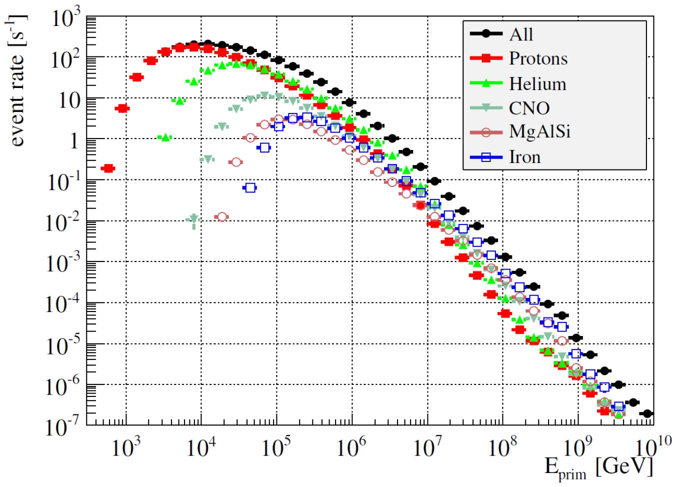

Figure 6.4: *Simulated atmospheric muon event rate in* IceCube *by primary cosmic ray component [206].*

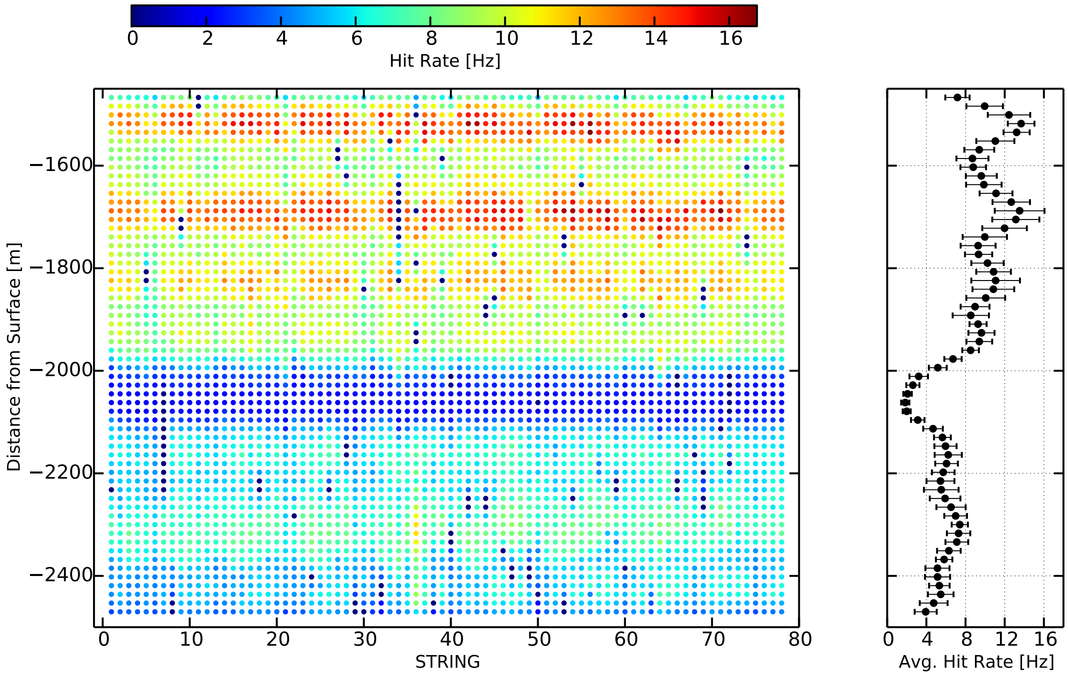

Figure 6.5: *Average HLC hit rate from experimental data of each DOM representing the component of triggering atmospheric muons (DeepCore strings are excluded). On the left, the hit rate is shown as a function of depth for the individual DOMs whereas the average values per layer are shown on the right.*

6.1.4 Temperature Effects

The fact that the temperature profile of the Earth's atmosphere changes, affects the atmospheric muon production directly. In Figure 6.6 we can see how widely the profile can vary between two different days in a year. In summer, the atmosphere is warmer and hence more expanded to higher altitudes and less dense. Pions and kaons are produced by cosmic ray interactions in higher altitudes and collide less often with molecule in the atmosphere. This results in more particles being able to decay into muons. The opposite is true in winter when the atmosphere is colder, shallower and denser. The produced pions and kaons interact more often, lose on average more energy and are less likely to decay into muons [207]. This explains the seasonal variations in Figure 6.7. The temperature deviation shown is for an effective atmospheric temperature that is a weighted average which takes into account temperature and pressure values at all levels of the atmosphere, as well as the attenuation lengths of pions and kaons [207]. In order to visualize the muon rate in the detector, the SMT8 trigger rate (see Section 3.3.2) is used as an estimator. This is preferred over extracting the simple event rate since muons tend to arrive in bundles that cannot be resolved by the online DAQ system. It is remarkable how accurately the trigger curve follows the temperature deviation throughout the season. As mentioned earlier, muons also affect the supernova system as it is obvious from Figure 6.7 where the number of reported significant supernova triggers (blue line) follows the seasonal variations of atmospheric muons (dots in the figure). As already presented in References [160, 161], atmospheric muons increase the abundance of supernova candidate triggers with a significance ξ greater than 6.0. With the help of trigger information, SNDAQ is able to subtract hits that are caused by triggering muons and can correct for that in the significance statement. A complete discussion of the relation between triggered atmospheric muons and SNDAQ trigger candidates can be found in Reference [172].

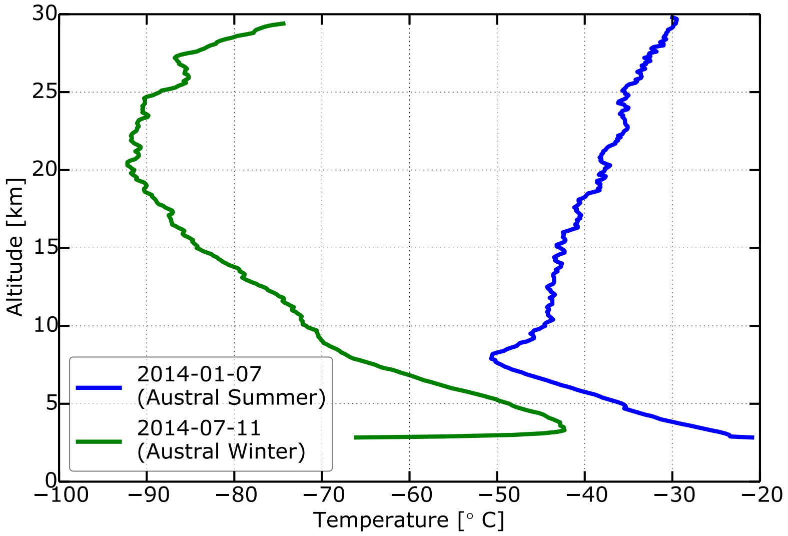

Figure 6.6: *Atmospheric temperature profile at South Pole from two arbitrary days in the year 2014 [208].*

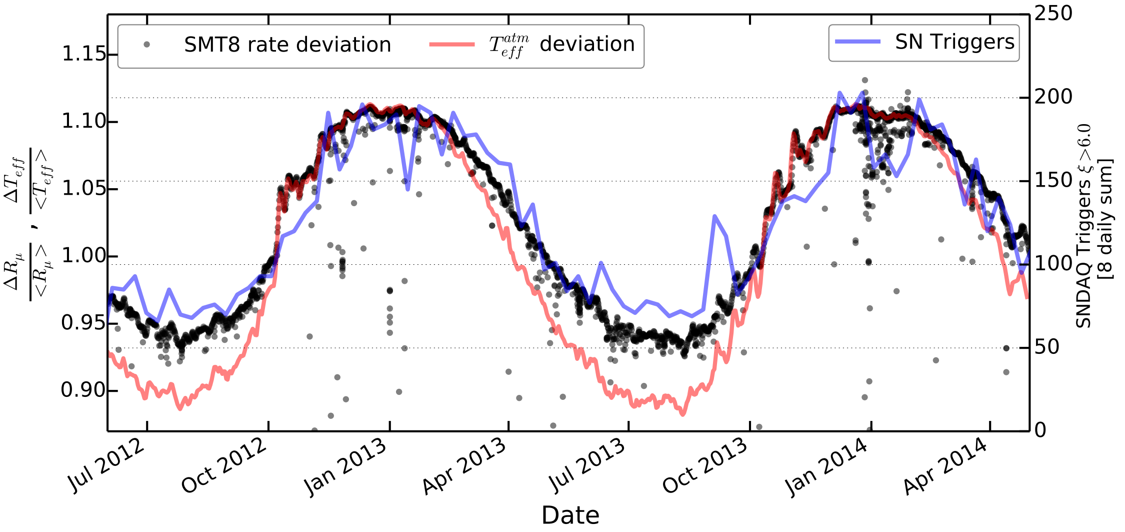

Figure 6.7: *SMT8 trigger rate deviation from average $\Delta R_{\mu}/ < R_{\mu} >$, (left y-axis and black dots) which correlates to the detection of atmospheric muons. The same oscillating behavior is also visible in the deviation of the effective temperature $\Delta T_{eff}/ < T_{eff} >$, shown by the red line, as well as in SNDAQ's trigger rate, given by the blue line and the y-axis on the right. The temperature data was extracted following a method explained in Reference [207] on the basis of data from an instrument on NASA's AQUA satellite [209].*

6.2 DOM Noise

While atmospheric muons, triggered and non-triggered, produce only a small fraction of the total amount of background hits in the detector, the vast majority result from dark noise. In this term we collect all effects that lead to the emission of an electron from the cathode of the PMT in the absence of an external photon, i.e pulses that are not directly caused by Cherenkov photons emitted from an ice-traversing charged particle. As shown in Figure 6.8, the total hit rate of DOMs with normal quantum efficiency PMTs is on average 560 Hz, and 780 Hz for high QE DOMs.

Several components contribute to the total amount of dark noise in a DOM. PMT induced pre- and afterpulses are responsible for approximately 30 Hz of DOM noise whereas thermal emission from the photocathode produces less than 10 Hz [66]. The vast majority of hits originate from radioactive decays in the glass with a large fraction of them introducing bursts of hits which last over several milliseconds. The physical nature of these bursts is not yet fully understood and recent investigations are presented in Section 6.2.3 and 6.3. Table 6.1 summarizes the characteristics of each of these noise components which are also illustrated in Figure 6.9. The individual noise sources are addressed in detail in the following.

6.2.1 Prepulses and Afterpulses

The PMT signal can be accompanied by *prepulses* when a photon bypasses the photocathode and hits one of the early dynodes directly to eject photoelectrons. A common feature of PMTs, and more prominent than prepulses, is *afterpulsing* which is attributed to ionization of residual gases by electrons that were accelerated in between the dynodes. The resulting ions are attracted to the photocathode and cause the liberation of electrons which follow

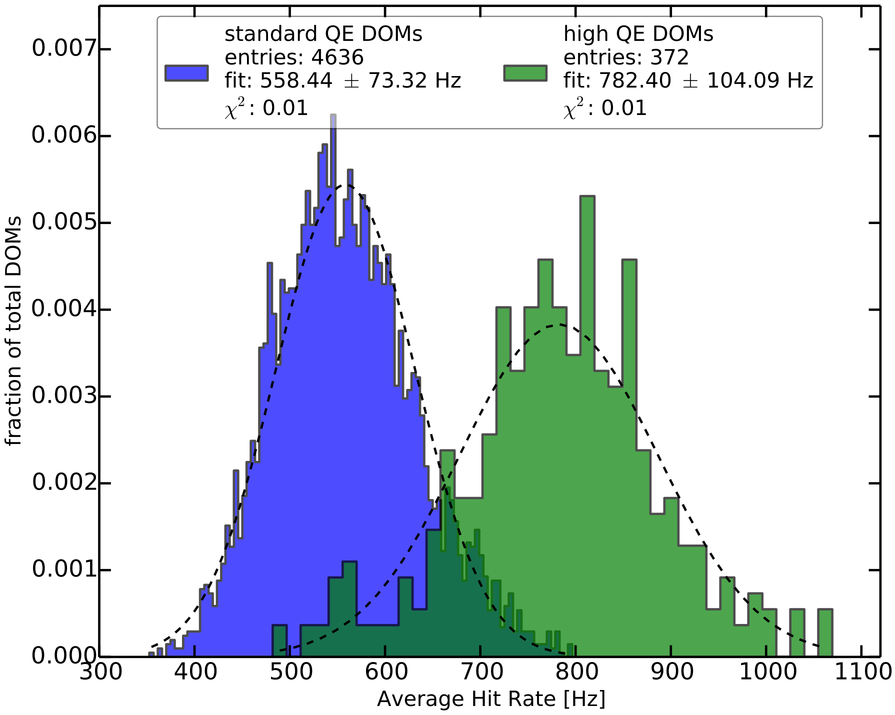

Figure 6.8: *Average noise rates for normal and high quantum efficiency DOMs in* IceCube *histogrammed and normalized.*

Table 6.1: *Characteristics of noise components in* IceCube *DOMs, adapted from [210].*

Noise Component	Origin	Distribution	Parameters
Afterpulses	PMT	Gaussian	$\mu = 6\,\mu s$ $\sigma = 2\,\mu s$
Uncorrelated	Thermal noise Radioactive Decay	Poissonian	$\lambda =\sim 250\,Hz$
Correlated	Luminescence (?)	Log-normal	$\mu = -6[\log_{10}(\frac{\Delta T}{s})]$ $\sigma = 0.85[\log_{10}(\frac{\Delta T}{s})]$

the same amplification process like the original photoelectrons [143]. Measurements of PMTs performed in the laboratory show that afterpulses arise most likely at 6 µs after the main peak, believed to be caused by ions of certain mass.

6.2.2 Uncorrelated Noise

Noise pulses of Poissonian nature (right peak and red line in Figure 6.9) are caused by noise of the electronics in the DOM as well as decay of radioactive elements in the PMT and the pressure sphere glass[2] such as Potassium (^{40}K) and decays from Uranium to Thorium [66].

These noise components are temperature dependent following Richardson's law for thermal emission. To confirm this assumption, the slope of the time interval distribution of hits

---

[2] In the case of Potassium, the electrons emitted from the predominant $\beta^{-}\tilde{-}$decay produce Cherenkov photons along their mean free path of 3.5 mm. On average, one photoelectron per ^{40}K decay is produced with a 63 % detection probability [211].

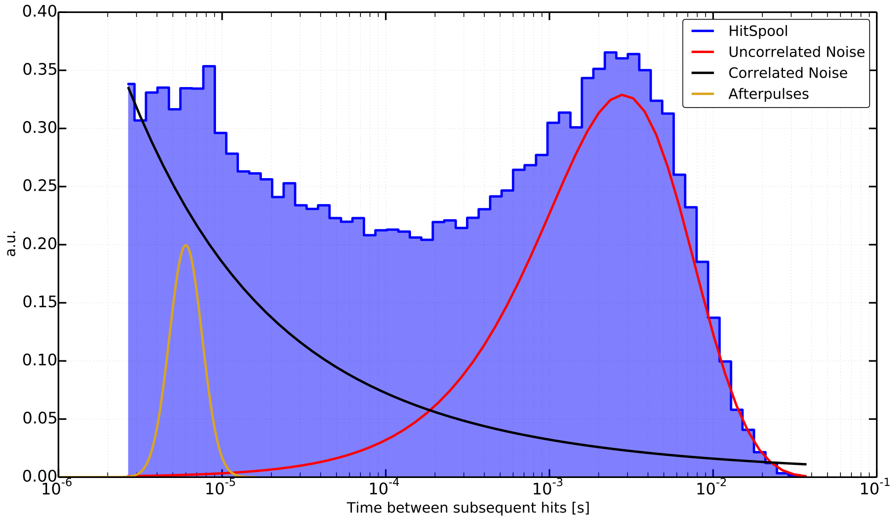

Figure 6.9: *Histogram of time differences between successive hits from* HitSpool *data of DOM 15-27 (blue) on a logarithmic scale in order to visualize the different noise components (without prepulses which are comparatively insignificant).*

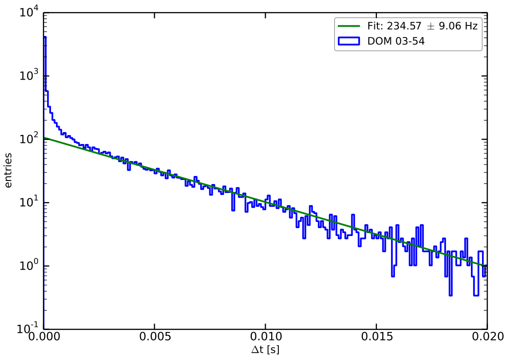

Figure 6.10: *Distribution of time differences between Hits in a DOM (blue line) and the exponential expectation for a Poissonian process fitted in the range* 15 ms $<$ Δt $<$ 70 ms *(green line).*

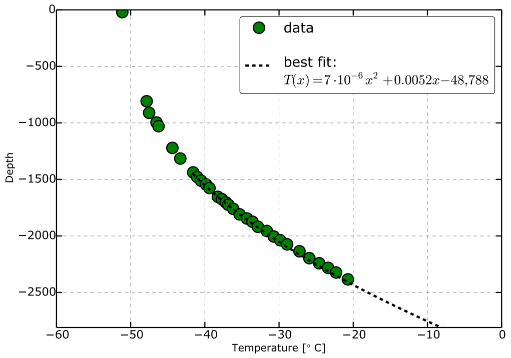

Figure 6.11: *Temperature profile of the ice cap at the South Pole [212].*

for every DOM is fitted, as shown in Figure 6.10, in order to estimate the rate of random arrivals [66]. Furthermore, the temperature of the DOM has to be determined. As shown in Figure 6.11, the temperature of the ice surrounding the DOMs increases with depth from about $-42\,^\circ$C at the top layer of the in-ice detector to $-20\,^\circ$C at the bottom [212]. The temperature of the DOMs is measured on the mainboards and is biased by approximately $10\,^\circ$C due to energy dissipation by the readout electronics, making it difficult to determine the temperature of the DOM glass and PMT itself [66]. With this in mind, a temperature dependent noise rate ($r(T)$) profile was made as shown in Figure 6.12. The fitting function for Poissonian noise follows the Richardson law for thermal emission [66, 213]:

$$r(T) = A \cdot T^2 e^{-\frac{W}{kT}} + C \quad , \tag{6.2}$$

where k is the Boltzmann constant and W is the work function[3]. The remaining variables are free fit parameters, determined to be $A = 8 \times 10^{-3}$ and $C = 230\,$Hz.

The fact that the Poissonian part of the noise deviates from the Richardson fit in figure 6.12 (green data point and green dashed line) is a result of the contribution of the non-thermal component, explained in detail here after, which is difficult to separate and contaminates the data sample. Atmospheric muons cannot be an explanation for that behavior since they are already subtracted. Although the fit is not optimal, it demonstrates well the dominance of the non-thermal component over the thermal noise.

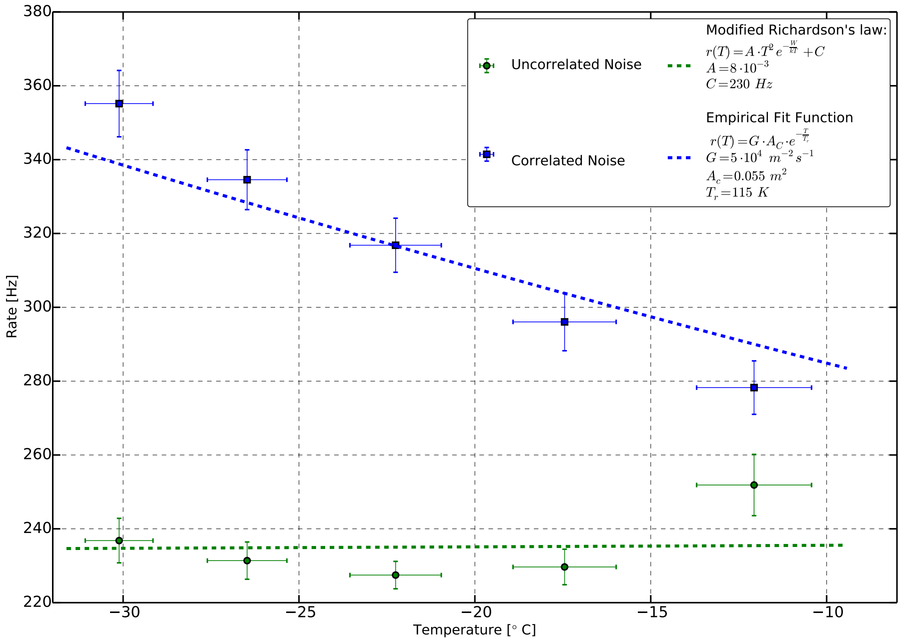

Figure 6.12: *Noise rate in* IceCube *as a function of temperature, obtained from* HitSpool *data. Each data point represents the average of 12 DOM layers from 78 strings (DeepCore excluded). Atmospheric muon hits, see Figure 6.5, are subtracted.*

---

[3] The minimum energy needed to liberate an electron from the material. $W \approx 0.5\,$eV for photocathodes made of Bialkali.

6.2.3 Correlated Noise

The high abundance of short time intervals (see left peak in Figure 6.9) cannot be explained by afterpulses alone. Meyer et al point out in their study of dark noise emission in cold photomultipliers [213, 214] that another noise component dominates over thermal emission at temperatures below 200 K. The temperature dependence of the non-thermal dark noise rate then follows an exponential distribution [214]:

$$r(T) = G \cdot A_C \cdot e^{-\frac{T}{T_r}} \quad , \tag{6.3}$$

where T is the temperature, $A_C = 0.055\,\mathrm{m}^2$ denotes the cathode area pf the PMT and $G = 5 \times 10^4\,\mathrm{m}^{-2}\,\mathrm{s}^{-1}$ is a free fit parameter. The non-Poissonian noise component is in good agreement with this empirical fit function, as can be seen in Figure 6.12.

Although the measurements by Meyer are performed with bare PMTs and at lower temperatures, this noise component is enhanced by the surrounding glass sphere of the DOMs and thus dominates over thermal noise in the temperature range of IceCube as well.

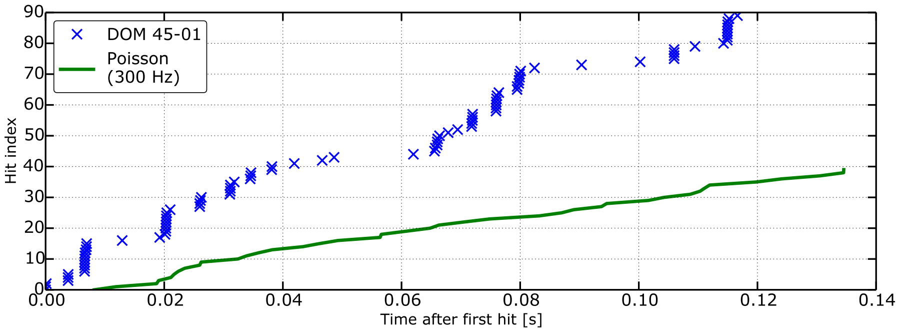

Figure 6.13: *Time sequence of hits on DOM 45-01. A number of noise clusters, caused by statistically correlated hits, are visible (blue corsses on top of each other). The Poisson expectation from a random* 300 Hz *noise rate is shown as green line.*

As it is obvious from Figure 6.13 the noise events do not occur randomly but in sequences of short intervals. This behavior coined the term *noise bursts* or correlated noise hit clusters.

Several attempts to characterize the non-thermal noise rate and identify its source have been made [211, 213, 214]. Recent efforts in the simulation of noise hits in IceCube confirm that the time interval distribution of correlated hits can be fitted by a log-normal distribution [202, 210], see Figure 6.9. Although the behavior of correlated noise can be simulated satisfactorily, a detailed understanding of the underlying process is still missing. So far, luminescence is suggested as an explanation. It can arise in the glass pressure sphere and the PMT glass, triggered by decaying elements in the material such as Potassium (^{40}K) and decays from Uranium to Thorium [211]. In general, a process that increases when lowering the temperature is very unusual [214]. The next section is dedicated to a study of noise bursts with HitSpool data in order to learn more about this fascinating process.

6.3 Correlated Noise Studies with HitSpool Data

Before we discuss the possible physical explanations further, we need to quantify and parametrize the characteristics of non-thermal noise in IceCube.

6.3.1 Definitions

The following studies are undertaken with HitSpool data from all in-ice DOMs with standard quantum efficiency PMTs. On average 70 s of data was used from every DOM. The data are grouped into layers of DOMs deployed at equal depth in order to guarantee a measurement at approximately the same temperature and to increase the statistics. Since the biggest impact of correlated noise is expected at the lowest temperatures, layers of DOMs towards the top of the detector, i.e. at depth around 1500 m and corresponding to a temperature of roughly −35° in the DOMs, were used for temperature independent measures. In order to put the results in the right context, definitions and terms are used in parallel to Meyer's [213, 214]:

Burst Cutoff Time after which a burst is considered to be finished. Here we chose 3 ms as the cutoff value, justified by Figure 6.14 where the deviation from the exponential expectation converges at 3 ms.

Burst In parallel to Meyer's definition, a burst is a sequence of hits whose time intervals are short (< 3 ms).

Burst Size L The number of hits present in a burst.

Burst Frequency F_L The total number of bursts of size L in the data set.

Burst Duration D_L The duration of a burst of size L, i.e. the time between the last and the first hit in a burst and averaged over all bursts of this size.

A data set of DOMs from the next-to-top layer contains over three million intervals in total of which over 90 % are shorter than 3 ms, see Figure 6.14. Compared to earlier studies, the data set at hand provides an increase of over three orders of magnitude in statistics. With the definitions given above and using the number from Figure 6.14, our next-to-top layer data contains 883 499 bursts which results in an average burst size of $< L >= 3.84$.

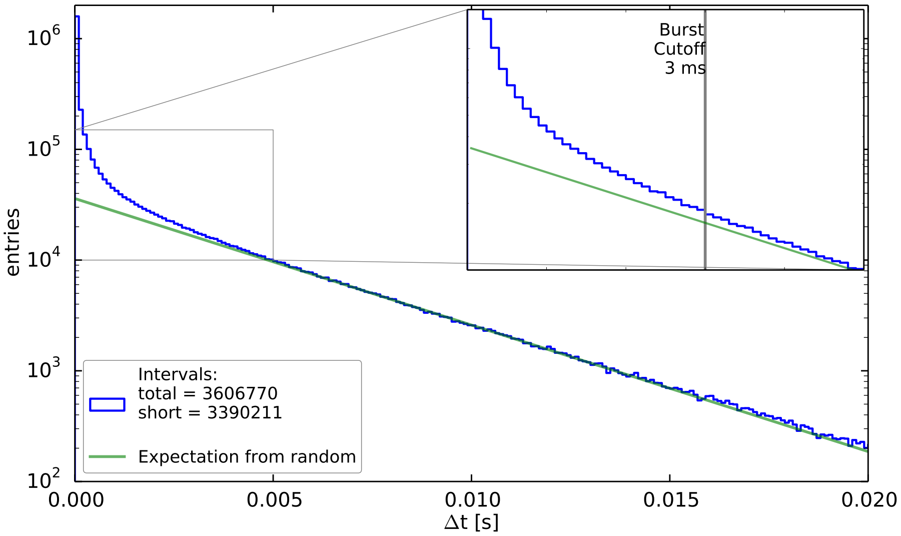

Figure 6.14: *Time interval between successive hits for all next-to-top layer DOMs (DeepCore excluded).*

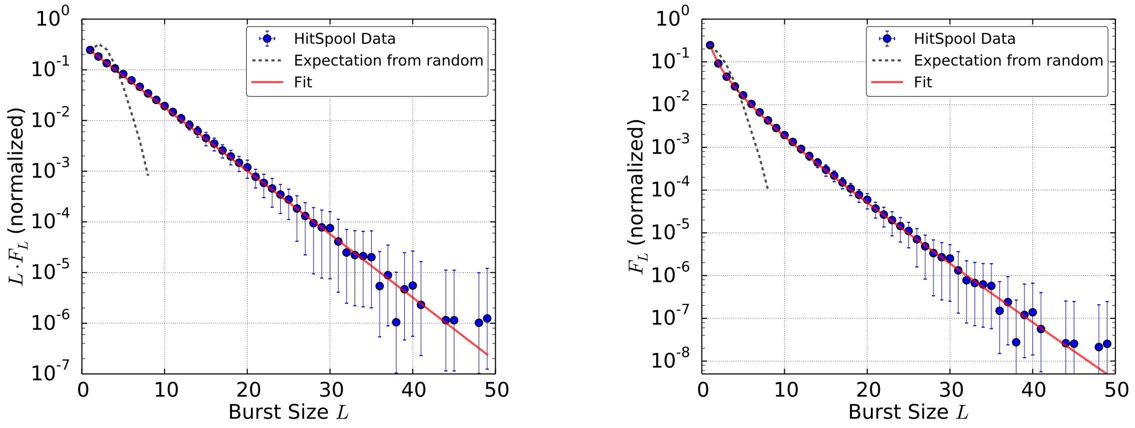

Figure 6.15: *Total number of hits, $L \cdot F_L$, as a function of burst size L.*

Figure 6.16: *Total number of bursts F_L, i.e. the burst size distribution.*

6.3.2 Burst Size Distribution

It was found earlier that the abundance of bursts in PMTs, denoted with F_L, can be expressed by the average burst size $< L >$ and the total number of bursts M [213]. This is also true for IceCube DOMs as demonstrated in the following. The fit function follows Meyer's Ansatz:

$$L \cdot F_L = N_s \frac{1-q}{q} q^L \tag{6.4}$$

which expresses the total number of hits in bursts of given size, $L \cdot F_L$, as being dependent on the number of short intervals N_s and burst size L. The parameter q is a free fit value. Figure 6.15 shows the distribution which is in good agreement with the fit function (red line). The abundance of bursts of a given size is presented in Figure 6.16, obtained by dividing the total hits distribution by L. The dashed line in both plots shows the expectation for burst in the case of randomly distributed short time intervals between hits. Its deviation from the data illustrates that the short intervals are in fact correlated. The parameter q in Equation 6.4 can be written in terms of $< L >$ due to the fact that $\sum_L L \cdot F_L = N_s$ and $\sum_L F_L = M$:

$$< L >= -q \cdot [(1-q)ln(1-q)]^{-1} \quad . \tag{6.5}$$

6.3.3 Burst Rate

The burst rate can be estimated by studying the time difference Δt of first events in subsequent bursts. Figure 6.17 gives an example of such a distribution on a logarithmic scale. The minimum Δt results naturally from our burst definition of 3 ms. Since this is an exponential distribution, one can conclude that bursts occur independently of each other. From the fit, which is proportional to $e^{-\Delta t \cdot \lambda}$, the burst rate λ can be directly deduced and was found to be 150 ± 5 Hz in the example given in Figure 6.17.

In order to find the rate for a given size of bursts, the same procedure is applied to the corresponding subsets where Δt denotes the time between first events in bursts of same size. The result is given in Figure 6.18 with data from all next-to-top layer DOMs. Again, the distribution follows an exponential decrease with bursts of the smallest size ($L = 2$) holding

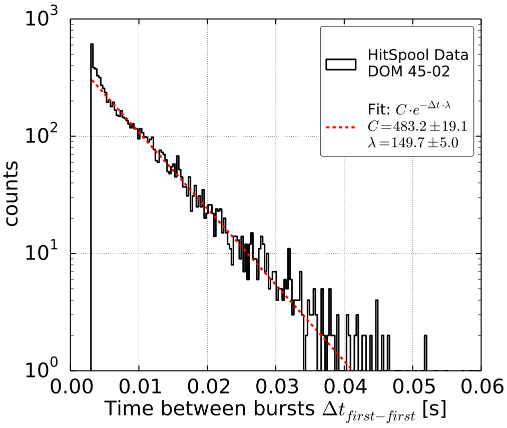

Figure 6.17: *Time between first hits in successive bursts.*

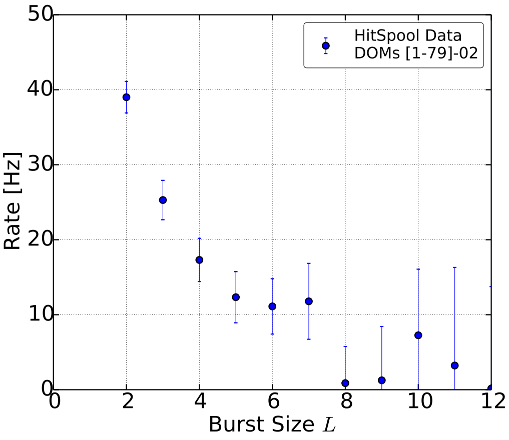

Figure 6.18: *Burst Rate as a function of burst size L.*

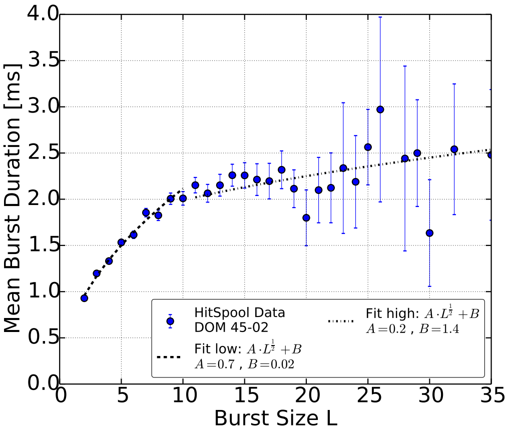

Figure 6.19: *Average burst duration as a function of burst size L, burst cutoff value is* 3 ms.

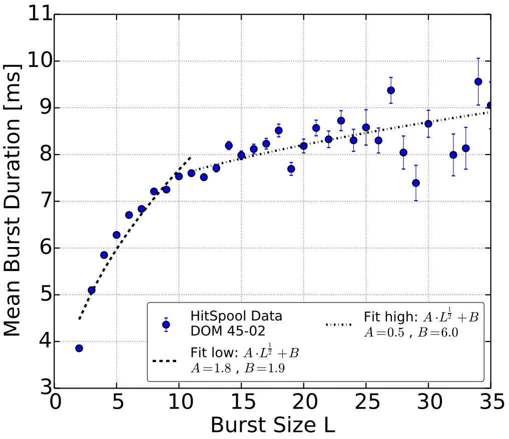

Figure 6.20: *Average burst duration as a function of burst size L, burst cutoff value is* 10 ms.

the highest rate of $\sim$ 40 Hz. For burst of size $L > 12$ the fits on the individual Δt distributions of the included DOMs do not converge any more due to low statistics.

6.3.4 Burst Duration

The burst size duration D_L follows a power law as shown in Figure 6.19. The distribution is described best by dividing it into a low and high burst size region. For burst sizes $L < 10$, the distribution rises steeply and levels off at greater values. This behavior was not observed by earlier studies. An explanation for that might be the burst size cutoff at 3 ms. By increasing the burst cutoff value to 10 ms, see Figure 6.20, the shape of the distribution remains unchanged and leads to the conclusion that this is a new observation which is probably caused by at least two overlaying emission processes.

6.3.5 Inner Interval Distribution

Meyer found that the time between hits in bursts of fixed size increases as the burst progresses. This remarkable behavior can be confirmed with IceCube DOMs, as demonstrated in Figure 6.21. Shown are inner interval distributions for bursts with 6 and 16 hits, respectively. Both histograms show a pronounced diagonal area from short intervals between early hits to larger intervals between later hits. The shortest interval between hits, 2.45 µs, is defined by the minimum internal dead time for successive hits within a DOM, as presented in Table 3.2.

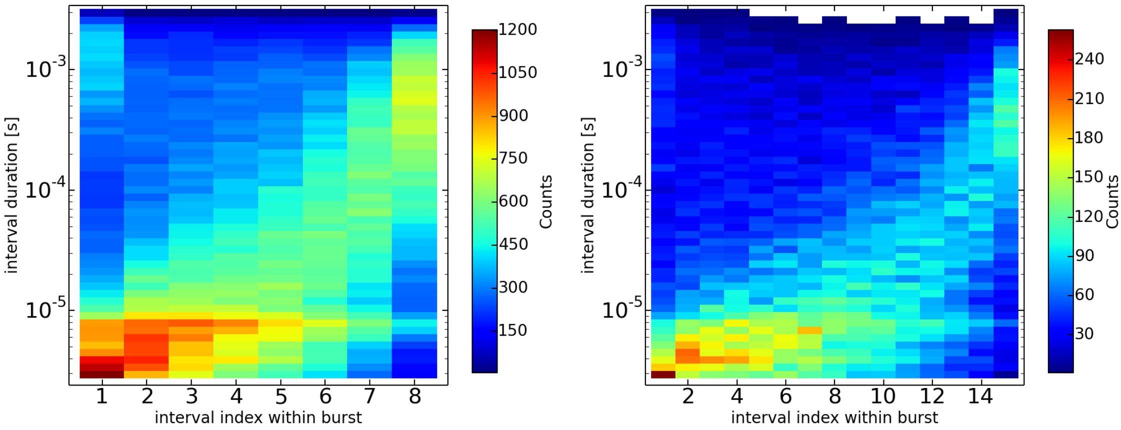

Figure 6.21: *Inner interval duration distribution for burst of size $L = 9$ (left) and $L = 16$ (right).*

6.3.6 Temperature Dependence

Not only the total correlated noise rate (Figure 6.12) is a function of temperature. Other quantities internal to the noise also show a temperature dependence. In agreement with [213], we find a decreasing average burst size $< L >$ with increasing temperature (Figure 6.22). For this measurement, HitSpool data from four equidistant DOM layers was evaluated. The behavior of the average burst rate, on the other hand, is harder to interpret (Figure 6.23). Assuming the same temperature dependence as before (Equation 6.3) one would expect a monotonic decrease. Since we operate in a temperature regime where Meyer's results are ambiguous, we cannot draw a final conclusion whether this is an abnormal behavior or has already been seen in studies before.

6.3.7 Discussion of Physical Explanations

Motivated by the highly non-stochastic time distribution of correlated dark noise events, an empirical trap model was proposed [213]. The cryogenic dark rate of electrons in PMTs is then described by the combination of emission and recombination in a trap filled with k electrons:

$$r(T,k) = \underbrace{k \cdot \epsilon \cdot \left(1 + \gamma \left(\frac{k}{k_0}\right)^4\right)}_{\text{emission}} + \underbrace{k \cdot \alpha \cdot \exp\left(\frac{T}{T_0}\right)}_{\text{recombination}} \quad , \tag{6.6}$$

where k_0 is the initial number of electrons in the trap and α, γ, ϵ and T_0 are adjustable

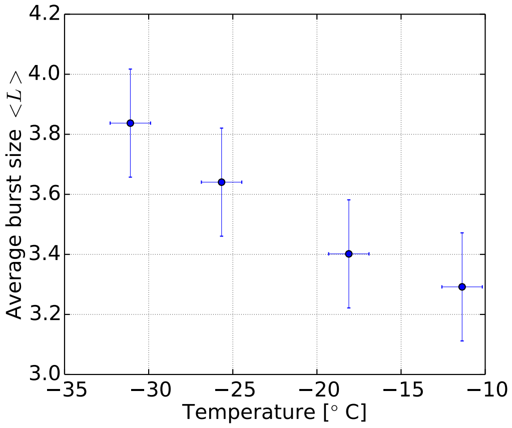

Figure 6.22: *Average burst size by temperature.*

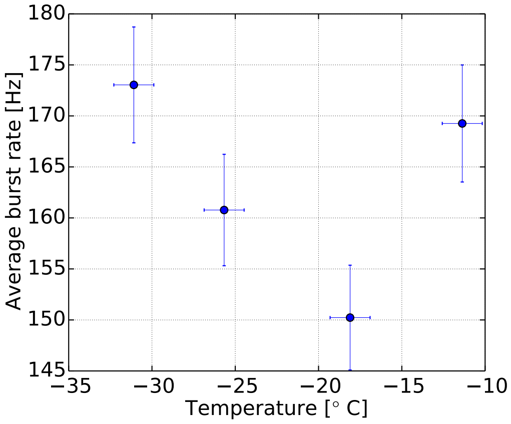

Figure 6.23: *Average burst rate by temperature.*

parameters of the model. In this model, the increasing rate with decreasing temperature is then a consequence of a less abundant recombination.

We suggest that some sort of luminescence is the driving force behind the correlated noise where an initial photon is absorbed by an atom of the material surrounding the PMT. The absorption of the photon excites the atom, from a singlet ground state S_0 to a singlet excited state S_1. Instead of returning radiatively to the ground state S_0 directly, also called *fluorescence*, the system can also undergo a non-radiative crossing to a triplet state T_1. Relaxation from a triplet state to the ground state via radiation is forbidden due to spin conservation. Thus it can only de-excite with the help of a new molecular vibrational excitation, setting it back to a singlet state and returning to the ground state from there via radiation. This triplet-singlet process, or *phosphorescence* is slow compared to fluorescence and happens on timescales of $\mathcal{O}(\mu\text{s})$ and longer which makes it the favorite process for correlated noise, likewise happening in this time regime. Another point is the issue of the initiation of the noise bursts, i.e. the energy that excites the molecules in the first place. One possibility is radioactive decay of $^{40}\mathrm{K}$ in the glass which occurs with less than 100 Bq. Other possibilities are ionization or ultra-violet light. The fact that the correlated noise is enhanced in DOMs compared to bare PMTs gives rise to the assumption that the glass of the pressure sphere plays an important, if not leading role in this process as it was already suggested by the results of investigations of optical modules from AMANDA in Reference [211].

Part III

Analysis

7

Identification of Subthreshold Atmospheric Muons in IceCube

In this chapter we investigate low energy atmospheric muons that pass IceCube *without being noticed by the trigger system. Such subthreshold muons are of particular interest for the supernova detection since they contaminate or even mimic a possible signal. In the first section, the detector response to simulated atmospheric muons is studied using untriggered simulation data. The influence and characteristics of subthreshold muons compared to triggering muons is quantified. Simulations also help to interpret the results from techniques developed to identify these muons in experimental data which is presented in the second section. The final part of this chapter presents the results of atmospheric muon identification in* HitSpool *data.*

7.1 Subthreshold Atmospheric Muons in Simulation

The HitSpool data stream was developed to improve the supernova data acquisition in the first place by subtracting atmospheric muons from the data in order to obtain a data set that contains only the supernova neutrino signal and instrumental noise. Since not all atmospheric muons that pass the detector also cause a trigger, one needs to develop techniques to identify the remaining subthreshold muons. For quantifying the result of such identification tools one relies on simulation where the injected signal is known a priori. The steps involved to produce a simulation data set that is as close to HitSpool data as possible are explained in the following section.

7.1.1 Simulation Framework: IceSim

BaseProcessing

From the generation of the primary cosmic ray until the final hit in the detector, the simulation has to include the propagation of the particle in air, the Cherenkov photons resulting from the propagation in ice, the DOM performance and the data acquisition. The individual simulation modules are integrated in the software framework of IceCube, namely IceSim, which is an extension to the basic software environment, IceTray. The data used in the following investigation were produced for supernova studies, presented in [172], where more details can be found. Here we focus on the steps involved to produce the unfiltered and untriggered data of the detector that contains generated noise with only atmospheric muons injected as signal. The generation of atmospheric or astrophysical neutrinos can be omitted in this study since their flux is two orders of magnitude lower compared to the muon flux.

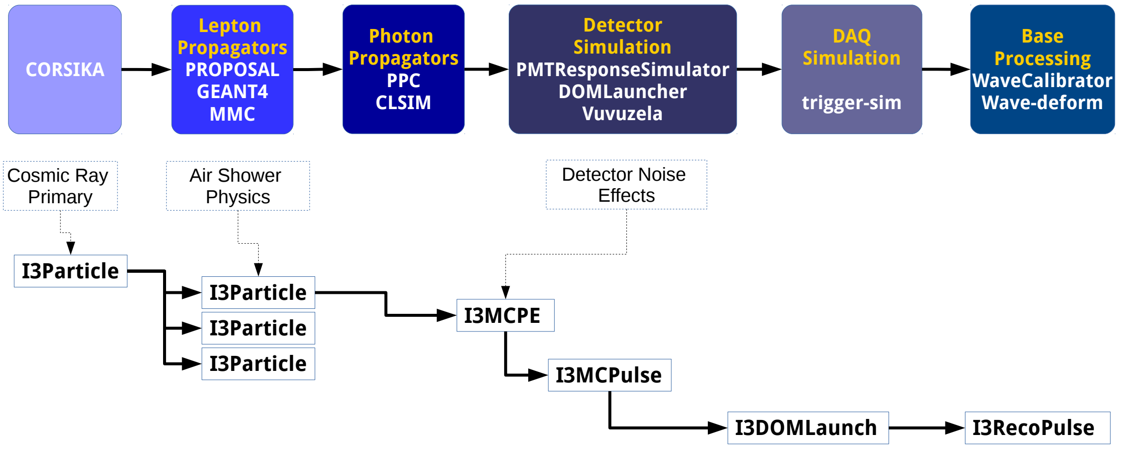
CORSIKA
Lepton Propagators
PROPOSAL
GEANT4
MMC
Photon Propagators
PPC
CLSIM
Detector Simulation
PMTResponseSimulator
DOMLauncher
Vuvuzela
DAQ Simulation
trigger-sim
Base Processing
WaveCalibrator
Wave-deform
Cosmic Ray Primary
Air Shower Physics
Detector Noise Effects
I3Particle
I3Particle
I3Particle
I3Particle
I3MCPE
I3MCPulse
I3DOMLaunch
I3RecoPulse

Figure 7.1: *Diagram of the IceTray's simulation modules in the top part and their corresponding datatypes in the bottom part used to produce the studied data set (adapted from [172]).*

The standard chain of simulation production is given in Figure 7.1. Several tools are available for producing background events like atmospheric muons in IceSim. For our purposes, CORSIKA [204] is used to simulate a cosmic ray interaction in the upper atmosphere and to propagate the air shower to the Earth's surface. The simulation data set used in the following was produced with a modified version of CORSIKA for IceCube [215]. The atmosphere was simulated corresponding to the composition and typical parameters in December, i.e. in austral summer when the atmospheric muon rate is highest at the location of the detector. Once the simulated air shower reaches the ice surface, further propagation of the particles is handled by various tools, depending on energy and type of the leptons. For interaction products of neutrinos from supernovae or other low energy sources, GEANT4 provides the particle propagation and Cherenkov photon production [65, 79]. Particle propagation and light production for all other cases is handled by either *Muon Monte Carlo* (MMC) [216], or PROPOSAL[1] [217]. The propagation of the Cherenkov photons is calculated by either Photonics, with a stochastic approach, or clsim and ppc using a direct propagation code, as explained in Section 4.2. At the point where the light reaches the DOM, the detector performance is simulated in multiple steps, starting with the response of the PMT. This is simulated by the *PMTResponseSimulator* module that reads in the simulated number of photoelectrons ejected from the photocathode. After the module generates pulses in units of photoelectrons representing the data after passage through the photomultiplier, including pre- and afterpulsing effects. The launching and digitization of the DOM mainboard is simulated with *DOMLauncher* [218]. The instrumental noise is included at this stage which is realized with *Vuvuzela* [202]. As mentioned in Section 6.2, this module simulates the thermal and non-thermal components of the dark noise. The data produced by elements explained so far represents the counterpart of HitSpool data in simulation since it contains a complete picture of the raw data before triggers and filters are applied.

---

[1] Propagator with Optimized Precision and Optimized Speed for All Leptons

The following steps are needed to simulate the DAQ and the basic online processing. The *trigger-sim* module applies triggers, namely the SMT, Volume and String trigger conditions to the data and forms events, imitating the online trigger system (see Section 3.3). The final treatment of the simulation data, before higher-level tools can be used, is the application of base processing like calibration and feature extraction of the waveforms (see also Section 3.4).

Pulse Mapping

In order to identify the contribution of hits from atmospheric muons, multiple steps have to be taken, as shwon in Figure 7.2. The first challenge lies in the fact that the information about the MonteCarlo object, i.e. the simulated primary cosmic ray particle, is not carried throughout the entire processing chain. In particular, the final observables *DOMLaunches* and *RecoPulses* which are produced in the detector simulation (Figure 7.1) do not contain that information. In order to regain information about the origin of every RecoPulse, the *MCPulseSeparator* module in IceSim is used. This tool investigates each hit in the event and re-discovers its source being either noise or caused by a primary particle [219].

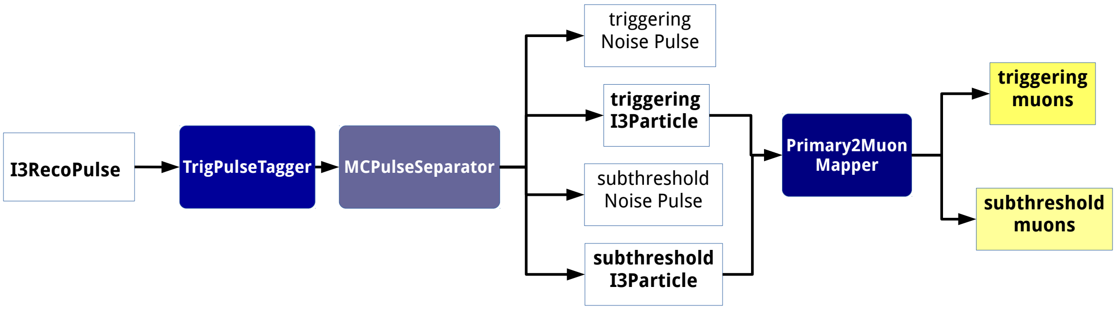

Figure 7.2: *Diagram of subthreshold and triggering muon identification via pulse mapping by recovering a priori knowledge from simulation, starting from the basic observable, the reconstructed pulse.*

Although the MCPulseSeparator connects cosmic ray primary particles to the hits in the detector, deducing the actual secondary particle that created the hit is nontrivial. Cosmic ray primaries can create multiple secondary muons that pass the detector simultaneously in so-called muon bundles, making a one-to-one mapping of hits to light producing particle more difficult. Nonetheless, whenever hits can be mapped to a primary the hits are surely caused by Cherenkov radiation from at least one atmospheric muon since no other charged particle from the air shower propagates to these depths. These muons are then traced back to the original primary in the CORSIKA production tree of particles which finally maps the muons to their hits. Therefore, we will use the term *detected primaries* and *detected muons* interchangeably.

7.1.2 Atmospheric Muons in Simulation

The duration of an event in the simulation data is fixed[2] to 2 ms. During this period every DOM should on average see at least one dark noise hit and about six atmospheric muons are expected to trigger in the detector. Figure 7.3 shows such an event display. The following presentation summarizes the differences found between these triggering muons and the undiscovered ones beneath the trigger threshold.

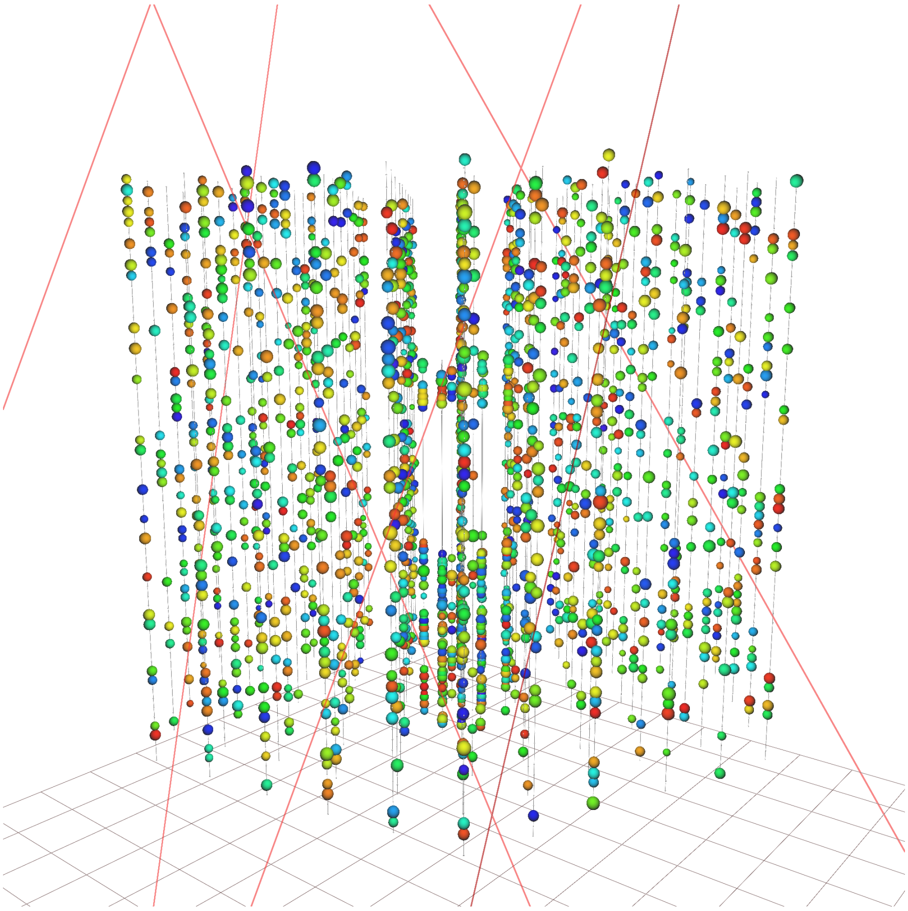

Figure 7.3: *Event display of* 2 ms *accumulated time in* ICECUBE *from simulation. The red lines indicate the tracks of injected muons. The hit DOMs are visualized by spheres where their color indicates the time of the hit (red=early, blue=late) and their size the amount of charge deposited. The hits caused by atmospheric muons are buried under the majority of hits caused by noise.*

Primary Multiplicity

Not all simulated primaries actually produce secondary muons that pass through the detector, as Figure 7.4a demonstrates. Only 88 % of the 2.5×10^5 cosmic ray particles generated with CORSIKA produce secondaries with hits in the detector. Although the plot indicates a mean multiplicity of 10 detected muons in 2 ms, the number of particles *triggering* the detector is

---

[2] Due to the fact that the simulation was produced for supernova simulation studies [172], the event size was chosen to match the minimal bin size of SNDAQ's scalers.

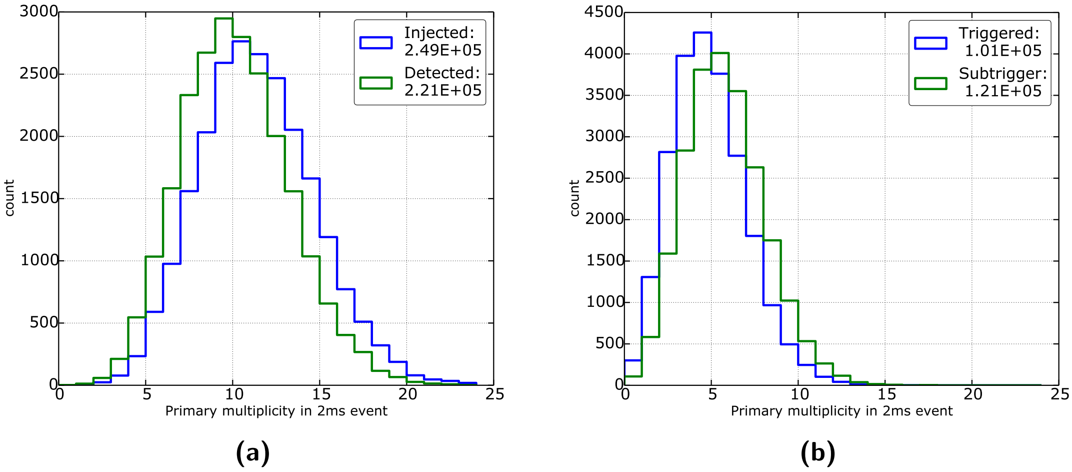

Figure 7.4: *The number of injected and detected primaries per* 2 ms *of data in simulation is shown in* **(a)***. The latter can be separated into triggering primaries and primaries under the trigger threshold which is shown in* **(b)***.*

significantly lower, as presented in Figure 7.4b. Only 45 % of the total detected secondaries cause a trigger whereas the majority remains unidentified by the online DAQ system.

The reason for that can be found in the number of pulses created per primary. Figure 7.5 shows the distribution of pulses for both triggered and subtrigger primaries, respectively. Compared to the average number of pulses per muon for secondary muons below the trigger threshold, $< N_{Pulses} >=$ 4.1, a triggering particle contains seven times more pulses with $< N_{Pulses} >=$ 28.8. Special attention has to be given to the amount of particles leaving less than 4 hits since this is the minimum number of hits needed for software tools to possibly tag an atmospheric muon, as will be explained in detail in Section 7.2. More than half of all subthreshold atmospheric muons produce only three hits or less in the detector while this is the case for only 6 % of all triggering muons.

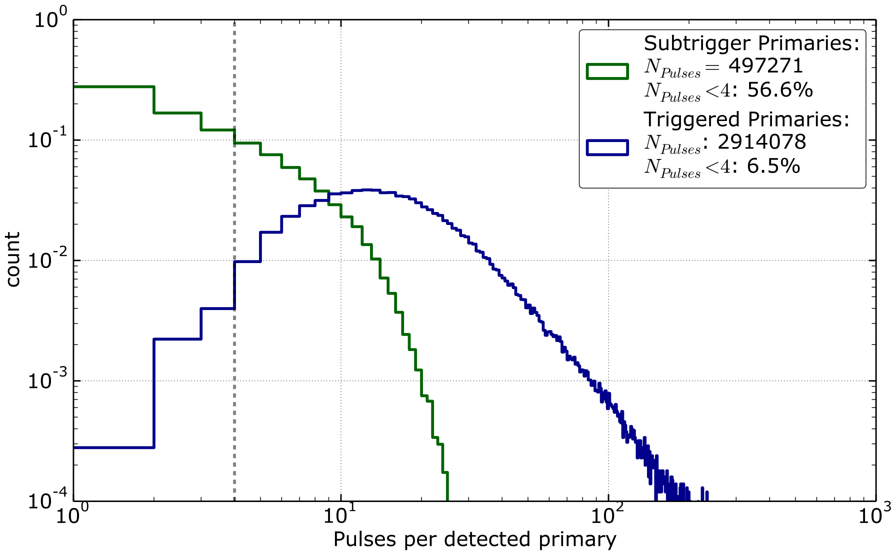

Figure 7.5: *Number of pulses produced by atmospheric muons in the detector.*

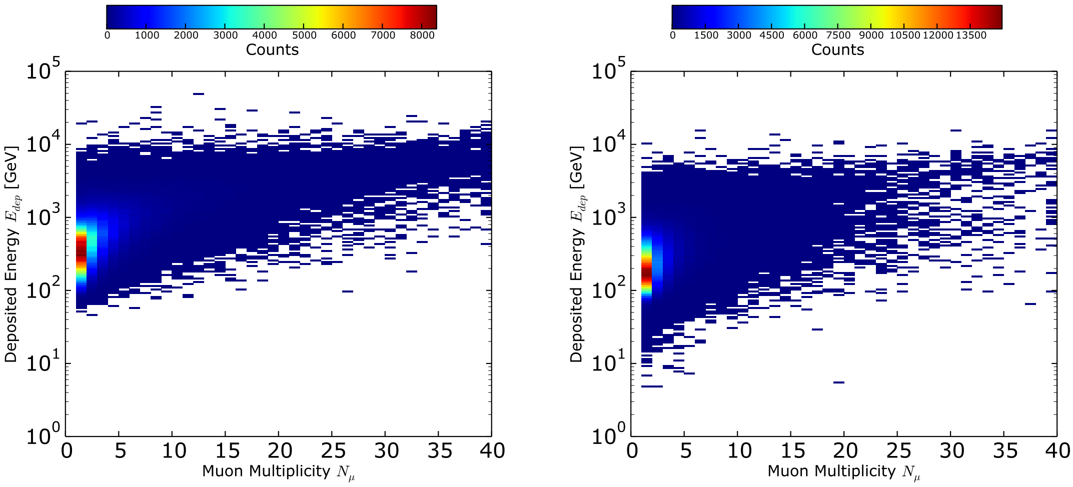

(a) **(b)**

Figure 7.6: *Deposited energy of triggered* **(a)** *and subthreshold* **(b)** *muon bundles as a function of their muon multiplicity* N_μ.

Muon Multiplicity

As discussed in Section 6.1, multiple atmospheric muons can emerge from a cosmic ray induced air-shower. Primary cosmic rays can produce multiple secondary muons, that will be pass the IceCube detector in bundles. These bundles are more probable to trigger the detector since their summed deposited energy is on average higher, resulting in brighter events in the detector. This can be seen in both plots of Figure 7.6 where the lower limit of deposited energy E_{dep} increases with muon multiplicity N_μ for triggering and subtrigger particles. The muon multiplicity per primary for triggered and subthreshold events is shown in Figure 7.7. In the total data set, 59 % of the detected primaries produce single muons. When splitting the data into subthreshold and triggering particles, the former subset contains 66 % single muons, which is above the 51 % resulting from the triggering primaries. This result tells us that subtrigger primaries tend to be lower in energy and produce less muon bundles than triggering primaries.

Energy Profile

The two previously presented figures already gave us an idea about the energies of subtrigger and triggering particles deduced from their muon multiplicity. Especially, the hot spots visible in Figure 7.6 indicate already where the main peak of the primary energy distribution is located. This is supported by Figure 7.8 for both triggered and subthreshold particles. On average, triggering primaries have higher energies than the ones that pass the detector unnoticed. This observation translates directly to the situation of generated muons, as shown in Figure 7.8b. The particle flux follows an energy dependence proportional to E^{-2} (see Chapter 6.1) which becomes visible for triggering muons above 500 GeV (see also Figure 6.2). The fact that the distribution does not follow the flux expectations for lower energies is due to the triggers working fully efficient only for energies starting at that range which is connected to the relation between deposited energy and Cherenkov photon yield, elaborated in Chapter 1.

The correlation of energies of primary cosmic rays with the deposited energy by resulting muons is shown in Figure 7.9. No primaries with less than 600 GeV produce muons that

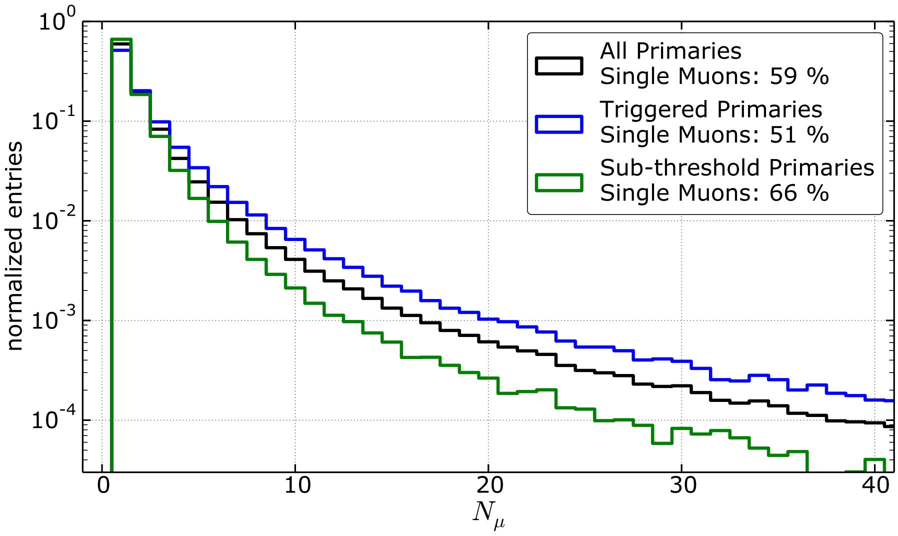

Figure 7.7: *The number of secondary muons from detected primaries that triggered the detector (blue line) and for those which passed the detector under the trigger threshold (green line). The total is given by the black line.*

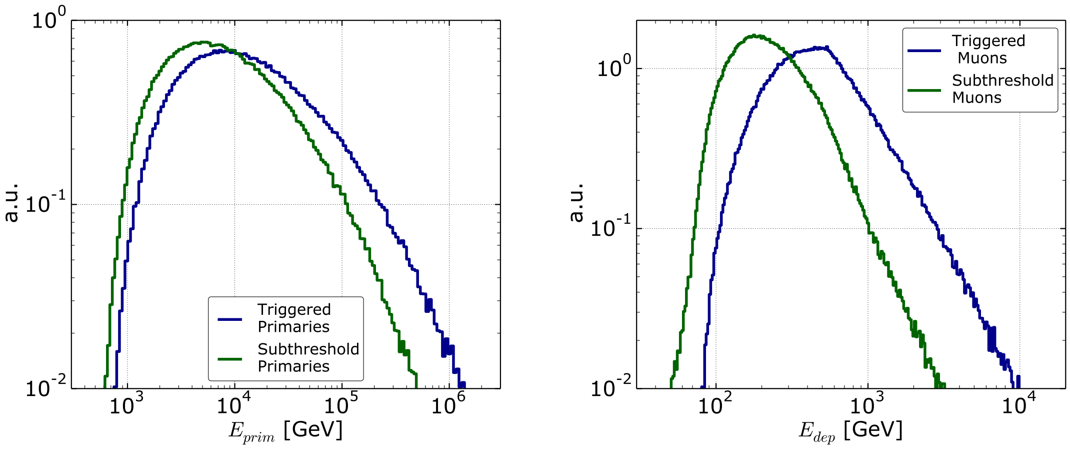

(a) **(b)**

Figure 7.8: *The true energy of detected primaries is shown in* **(a)***. The deposited energy by the resulting muons in the detector is given in* **(b)***.*

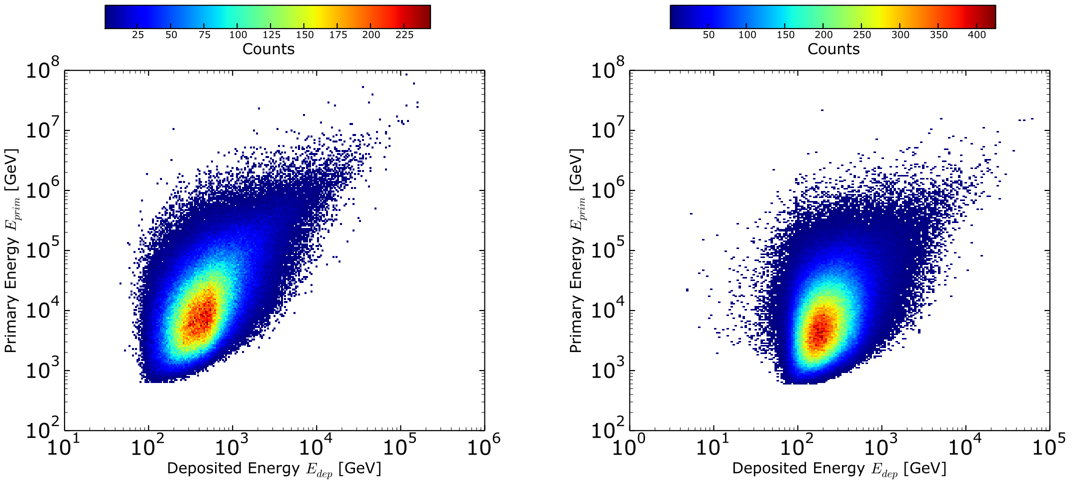

(a) **(b)**

Figure 7.9: *Energy of triggered primary cosmic ray in relation to their deposited energy* **(a)**. *The situation for subthreshold primaries is given in* **(b)**.

would be detectable. The fact that the deposited energies increase on average with higher primary energies is expected and reflects a proper simulation chain.

Local Coincidence Profile

IceCube's DAQ system is only triggered by HLC hits, i.e. the presence of two neighboring DOMs registering hits within ±1 µs. The reasons why single SLC hits are not considered for triggering are manifold with the obvious one being limited processing resources. Since IceCube was primarily built with the intention to detect cosmic neutrinos with energies above a few hundred GeV, the triggers are set up in such a way that they select events that fulfill this criterion. Particles that pass the detector below the trigger threshold are not interesting for standard analyses and are usually rejected from the data stream in order to keep the data transfer at a reasonable amount[3]. The fact that only HLC hits are considered by the triggers are justified by the local coincidence profile of the atmospheric muons, i.e. the fraction of SLC and HLC hits produced by their Cherenkov light, as given in Figure 7.10. The major part of triggering muons generates up to 15 HLC hits accompanied by less than 5 SLC hits (Figure 7.10a) with the HLC fraction being always higher than the SLC hit component. Whereas triggering muons can produce up to several hundreds hits, or even a few thousand in rare cases, this is by definition different for subthreshold muons (Figure 7.10b). The majority (27 %) of subtrigger muons leaves exactly one SLC hit in the detector. Such a hit is indistinguishable from any noise hit when it comes to the identification of the hits without prior knowledge, i.e. in experimental data. Furthermore, almost half of the these muons (46 %) create only SLC hits whereas 16 % leave a pure HLC hit footprint. The maximum number of hits caused by a subthreshold muon is of $\mathcal{O}(10)$ regarding SLC as well as HLC hits. Since both triggering and subtrigger profiles do not show more characteristics, they are unfortunately not conclusive enough to be exploited as a muon identification tool by themselves.

---

[3] This is the reason why we use HitSpool data and untriggered simulation to investigate the subtrigger muon content and its impact on the supernova detection

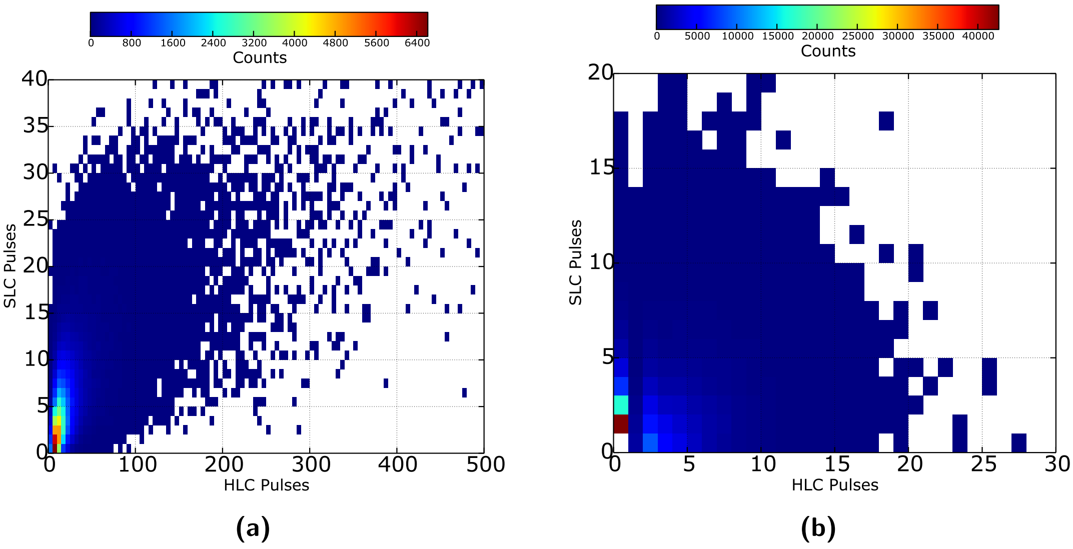

(a) (b)

Figure 7.10: *HLC and SLC pulses of triggered muons in* **(a)** *and subtrigger muons in* **(b)**.

Hit Location

Investigating the local distribution of triggering and subthreshold muon hits in the detector starts with recalling Figure 6.5 that shows the depth dependent muon trigger rate in experimental data. A minimum of 3 Hz in the main dust layer and a maximum of 16 Hz in the detector is observed. Simulation data gives us the possibility not only to compare the muon hit rate to the experimental result for triggering muon hits but also to extent it to subthreshold muons. Figure 7.11 shows hit maps for both cases, trigger and subtrigger muon hits, respectively. The overall hit pattern is comparable to the one in experimental data. The simulation data set from which these figures were extracted has a lifetime of 8 s. By taking this lifetime into account one derives at a maximum muon trigger hit rate in the most exposed DOMs of 30 Hz which is a factor 2 above the experimental maximal value. Due to the limited statistics of this data set, it is most likely that the difference between data and simulation is a fluctuation rather than a severe simulation issue. The actual geometrical distribution of muon hits in cylindrical coordinates of the detector can be seen in Figure 7.12. In the case of triggering muons (Figure 7.12a), this presentation confirms that they generate hits anywhere in the detector with less abundance in places of higher dust concentration and naturally decreasing towards the bottom of the detector. Subthreshold muons are concentrated at the mantle of the detector, i.e. in the top layers and the outer strings as visible from Figure 7.12b. This picture suggests that subtrigger muons, with their on average lower energy, do not traverse the entire detector. The subtrigger particles are rather stopped in the upper part, only touching the corner of the detector or passing in the vicinity with their Cherenkov photons still being detected due to the long attenuation length in ice.

Hit Rates

In view of supernova neutrino detection with IceCube, the detector intrinsic dark noise rate is an important parameter. Figure 7.13 shows the histogrammed hit rates per 2 ms in simulation. The data is kept in its natural bin size of 2 ms instead of summing them to 1 s bins because the limited lifetime of the data set does not provide a reasonable statistic that allows for a representation in broader bins. Nonetheless, a quantitative statement about triggering and

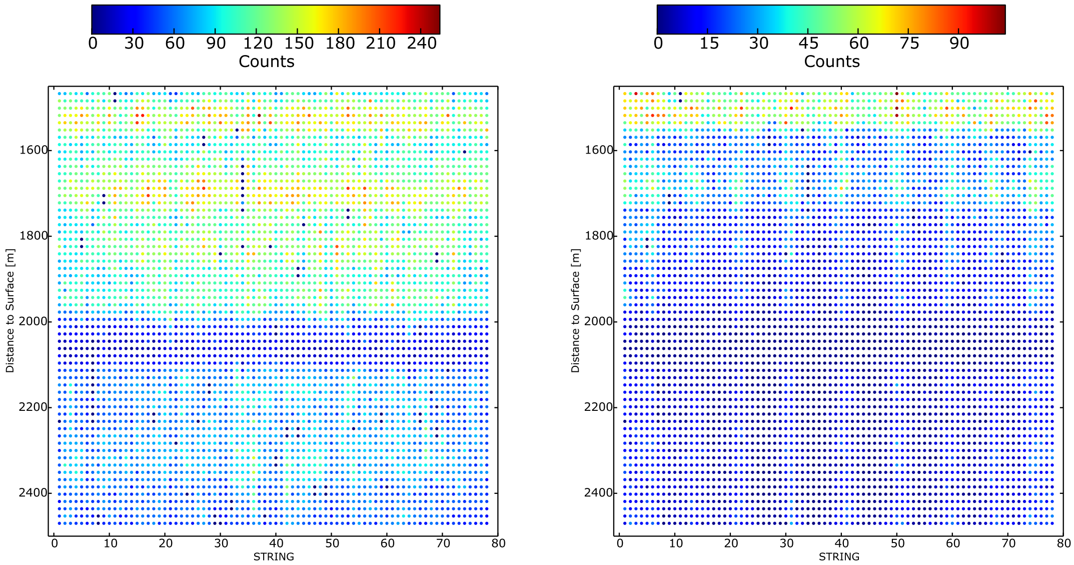

(a) **(b)**

Figure 7.11: *Hit map of* 8 s *of simulation data for triggered (***a***) and subtrigger (***b***) muon hits for each DOM on in-ice strings as a function of depth. DeepCore strings are excluded.*

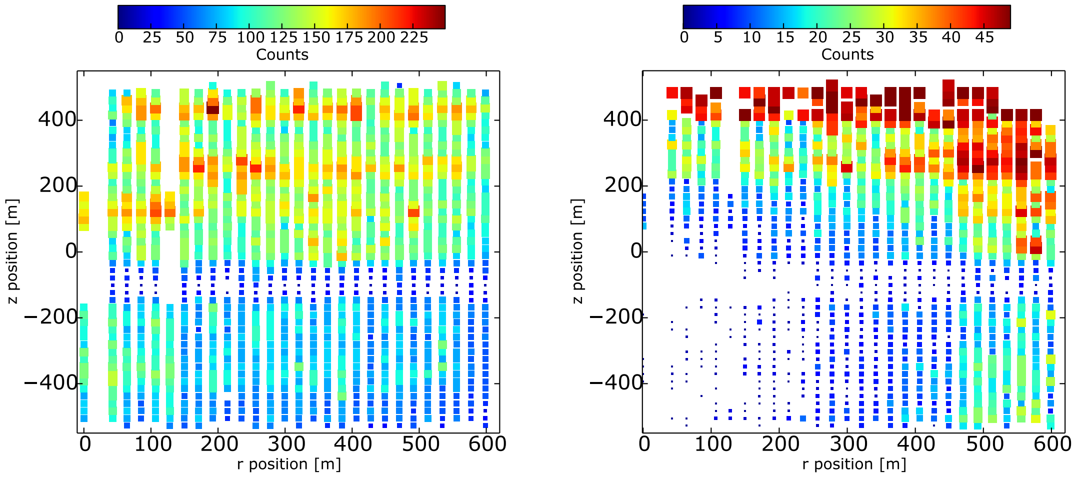

(a) **(b)**

Figure 7.12: *Pulse distribution of triggering muons in* **(a)** *and subtrigger muons in* **(b)** *in cylindrical detector coordinates accumulated over* 8 s *of simulated data (same data as in Figure 7.11). Size and color of the tiles indicate the amount of pulses in the corresponding area.*

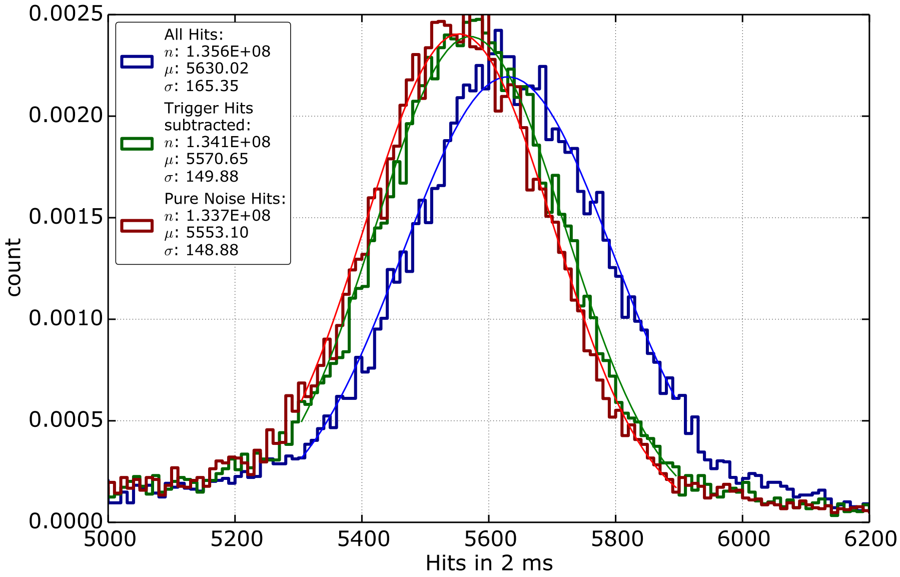

Figure 7.13: *Hit rate per* 2 ms *from simulation. By subtracting triggering muon hits from the total hit rate (blue histogram and blue fit line) one derives the untriggered hit rate (green histogram and green fit line) where the hits from subthreshold muons are still contained. Subtracting the latter uncovers the real noise rate (red histogram and fit line).*

subthreshold muon hits can be made from the total number of hits in each category. The hits from triggering muons contribute about 1.1 % to the total rate, deduced by the difference between the red and blue histograms in the figure. Subtracting the hits caused by subthreshold muon reduces that rate by another 0.3 %. Thus the pure dark noise rate of IceCube is about 98.6 % of the total hit rate and atmospheric muons account for $\sim$ 1.4 %.

7.2 Potential of Identification of Subthreshold Muons via Splitter Algorithms

Algorithms that identify hit clusters are widely use within IceCube in order to locate and separate possible sub-events. In this sense, these tools are developed primarily in order to split coincident events like an atmospheric muon traversing the detector simultaneously with a neutrino. This is the reason why they are mainly known as *event splitter* rather than *hit clusterer* which would be more natural due to their working principle, as explained in Section 5.3. Splitters are in this analysis not only applied to events reported by the online DAQ system, i.e. triggered events, but on all hits.

The processing chain for muon identification is shown in Figure 7.14. In a first step, general performance tests and hit cluster characterizations are carried out by applying the two splitters, namely *HiveSplitter* and *TopologicalSplitter*, on the simulation data sample used in the previous section and with the help of the developed primary hit mapping tools. A closer look to the splitters' identification potential with respect to triggering versus subthreshold muons is provided in the second step. As a last step in the process of muon identification, the *NoiseEngine* module of IceTray is employed, which classifies the hit clusters as being generated by a muon[4] or consistent with noise.

---

[4] this corresponds to NoiseEngine's return value being **True**.

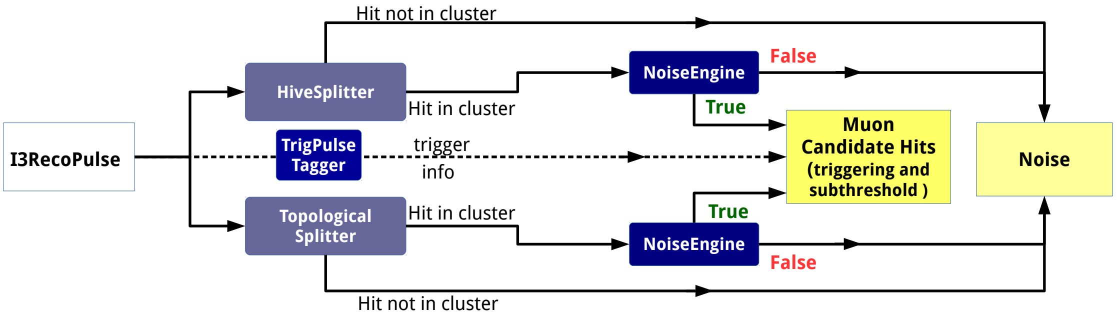

Figure 7.14: *Diagram of muon identification via splitter algorithms as performed in higher level processing of simulation data and* HitSpool *data.*

7.2.1 Overall Performance

In order to evaluate the accuracy of the splitter algorithms with respect to finding hits caused by atmospheric muons, a series of tests are performed and compared to the true values available in the simulation when possible.

Primary Mapping

Due to the similar but not identical working principle of the two splitters HiveSplitter and TopologicalSplitter, as discussed in Section 5.3, slight differences in their results are expected. We use the a priori knowledge about muon hits from the simulation in order to determine how accurately the hit clusters match their corresponding primaries.

In Figure 7.15, we compare the total number of hits with the number of primary-matching hits in each cluster formed by the splitters. HiveSplitter performs very satisfyingly when identifying clusters caused by primaries that contain up to 200 hits. The deviation from an optimal performance, indicated by the dashed line in the figure, increases from 20 % to 40 % for clusters containing more than 500 hits. A similar observation can be made for the primary-matching hits in clusters from TopologicalSplitter, see Figure 7.16. When considering the width of the distribution of both splitters, HiveSplitter is preferred over TopologicalSplitter since its clusters contain on average slightly more primary-matching hits. Especially for the region between 100 and 200 primary hits, HiveSplitters performs better than TopologicalSplitter where the latter shows more entries in the lower off-diagonal region.

Cluster Purity

The slight advantage of HiveSplitter over TopologicalSplitter is manifested in the purity of the clusters. As Figure 7.17a presents, hive-split clusters that contain physics hits, i.e. hits from muons, are contaminated by up to 20 noise hits in general. For clusters with low hit multiplicity, $N \leq 20$, noise contributes maximal 10 % in most cases and seldom more than 15 hits in total, as can be seen from the hot spot in Figure 7.17b. The purity of hit clusters from TopologicalSplitter is shown in Figure 7.18. Compared to HiveSplitter, a higher fraction of noise hits present in primary associated clusters is visible (note the enlarged scale for noise pulses compared to Figure 7.17). Low multiplicity hit clusters show a cumulation between 2 and 4 noise hits contributing to the cluster. By definition, the upper left region of Figure 7.17b and Figure 7.18b is empty since a physics associated hit cluster can hold at most 50 %

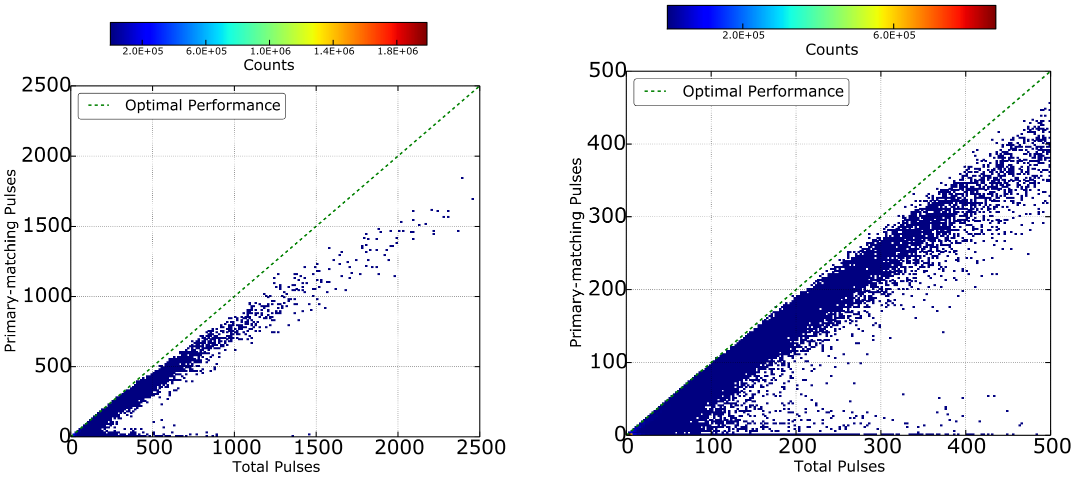

(a) **(b)**

Figure 7.15: *Fraction of pulses in hit cluster from HiveSplitter that are generated by associated primary cosmic ray, i.e. are caused by the corresponding atmospheric muons. Figure (**b**) shows a zoom in the low pulse region.*

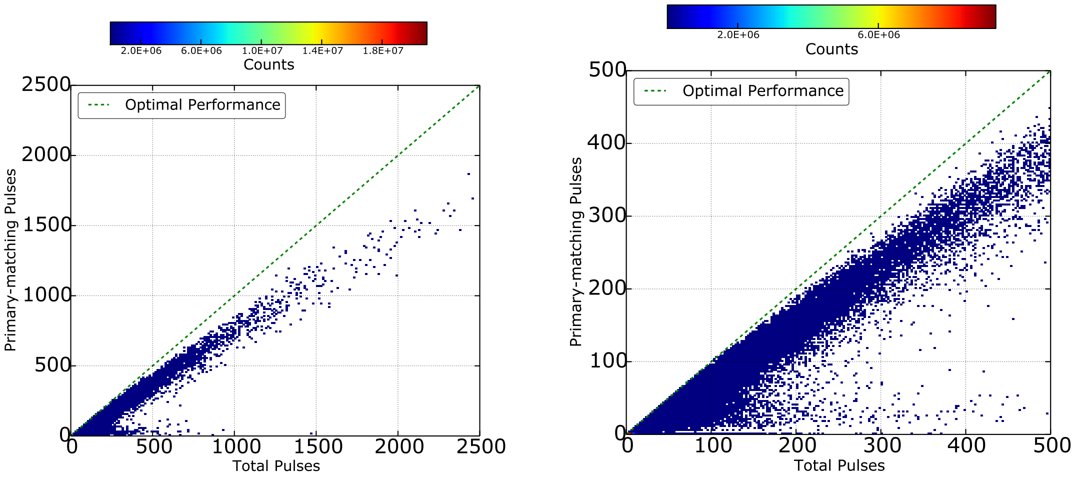

(a) **(b)**

Figure 7.16: *Same as Figure 7.15 for TopologicalSplitter: Fraction of pulses in hit cluster from TopologicalSplitter that are generated by associated primary cosmic ray, i.e. are caused by the corresponding atmospheric muons. Figure (**b**) shows a zoom in the low pulse region.*

of its hits originating from noise.

Split Multiplicity

When determining the number of hit clusters associated to physics events, the split multiplicity per primary has to be taken into account in order to provide a fair comparison of the splitters. This is defined by the number of clusters a splitter identifies from a single primary, i.e. the number of splits performed on a single hit source. Figure 7.19 shows that hive-split clusters originate more often from the same primary than topological-split hits. Where TopologicalSplitter identifies at most four different hit clusters, HiveSplitter cuts the events in up to nine different sub-groups. Since we aim for identifying single hits (and not events) from muons for improving the supernova detection system, the split multiplicity does not have further consequences. Nonetheless, it might have to be considered for other channels that rely on an event based analysis. The behavior of HiveSplitter is actually desired as individual primaries produce in almost 50 % of the cases not only one but multiple muons in the detector. Although TopologicalSplitter splits less often on the same event, it splits in general ten times more frequently than HiveSplitter (see Figure 7.20) which basically translates to an order of magnitude more hit clusters caused by pure noise.

Local Coincidence Profile

Similar to the SLC-HLC hit map made for true primary hits in Section 7.1, a local coincidence profile for hit clusters identified by splitters is shown in Figure 7.21 and Figure 7.22. Compared to the true fraction of SLC hits in primaries, the hit clusters from the splitters have in general a higher contribution of single hits, being twice or three times in the case of Hive- and TopologicalSplitter, respectively. The zoom-in into the low region (Figure 7.21a and Figure 7.22b) shows that a majority of clusters is composed of four single hits. The unpopulated lower left corner of the histograms represents the lower limit on the number of hits for the splitter to form a cluster.

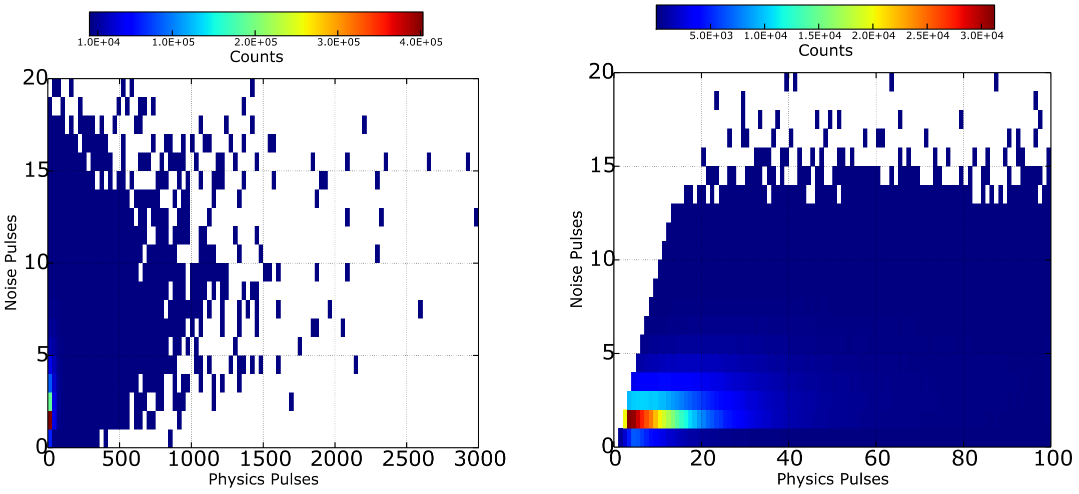

(a) **(b)**

Figure 7.17: *Cluster purity, i.e. the fraction of pulses originating from noise versus the components generated by muons, for pulses grouped by HiveSplitter in* **(a)** *and a zoom-in into the low region in* **(b)**.

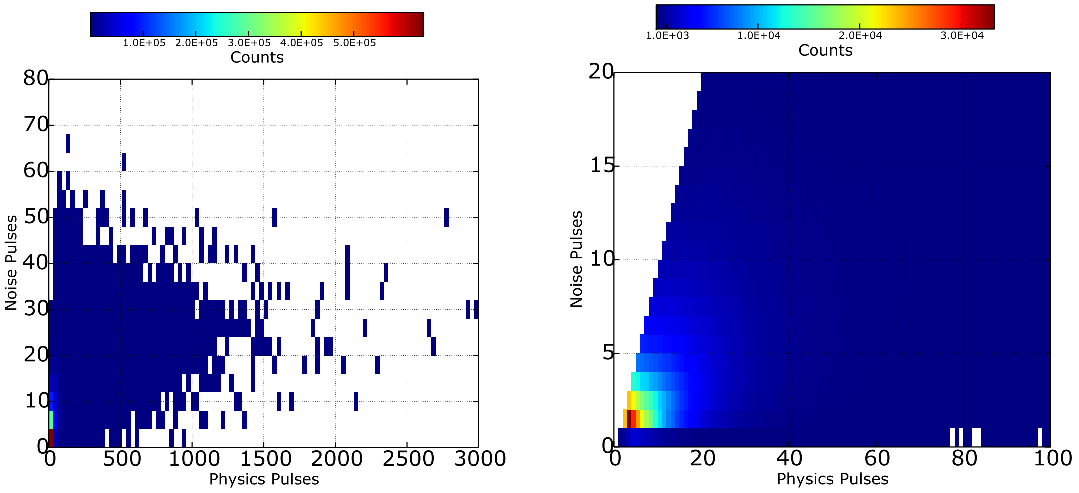

(a) **(b)**

Figure 7.18: *Same as Figure 7.17 for TopologicalSplitter.*

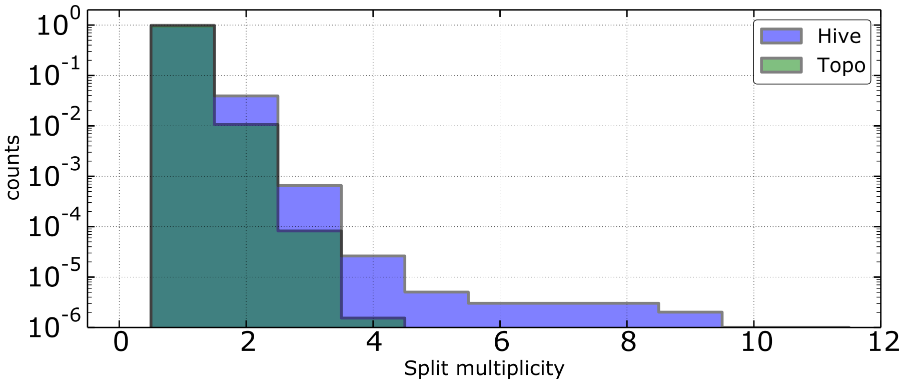

Figure 7.19: *Multiplicity of primaries represented in HiveSplitter's and TopologicalSplitter's hit clusters.*

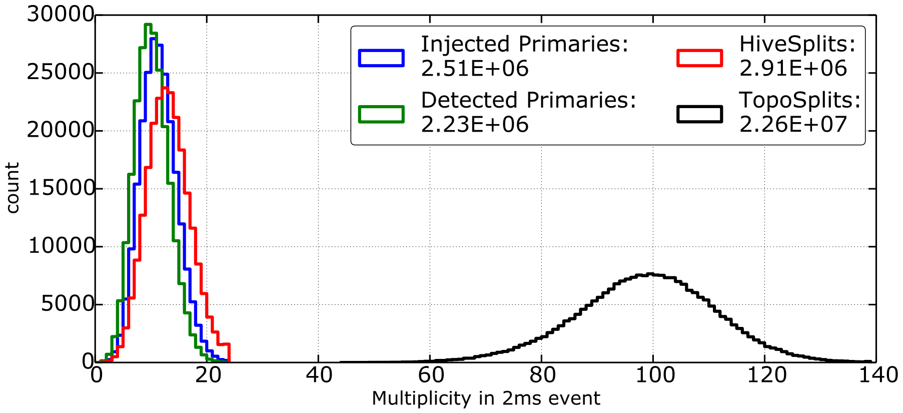

Figure 7.20: *The number of total splits, i.e. hit clusters formed, per* 2 ms *by HiveSplitter (red) and TopologicalSplitter (black). The number of injected and detected primaries per* 2 ms *of data from Figure 7.4a are given as reference.*

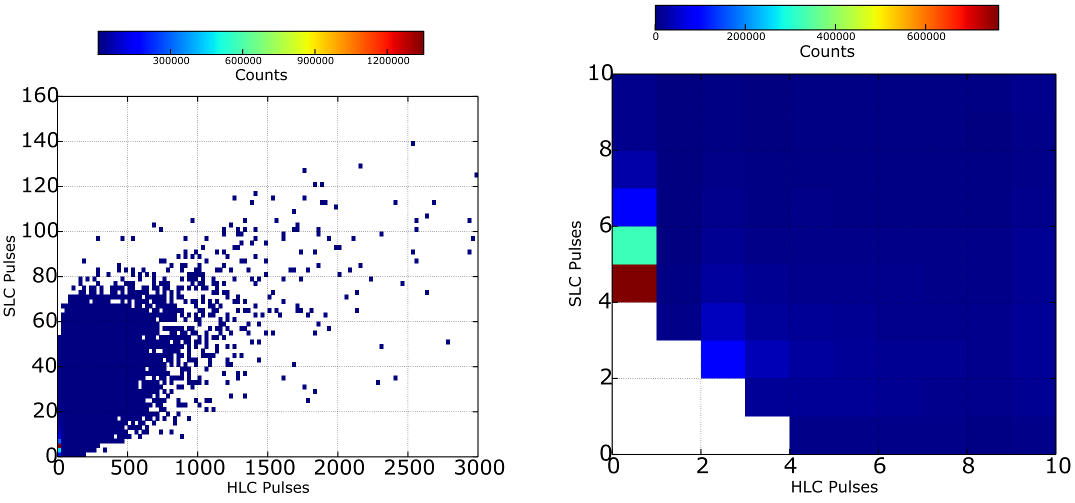

(a) **(b)**

Figure 7.21: *HLC versus SLC pulse contribution in hit clusters formed by HiveSplitter in* **(a)** *and a zoom into the low pulse region in* **(b)***.*

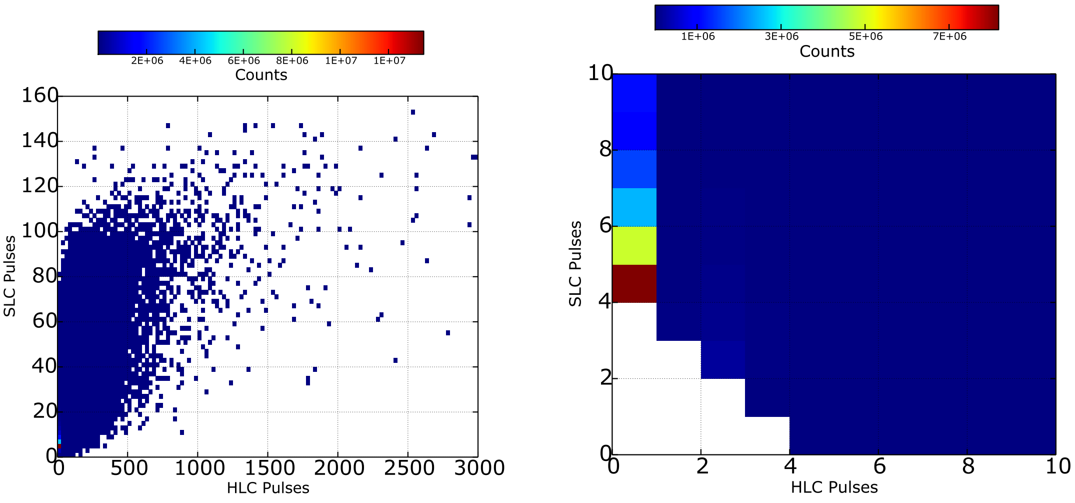

(a) **(b)**

Figure 7.22: *HLC versus SLC pulse contribution in hit clusters formed by TopologicalSplitter in* **(a)** *and a zoom into the low pulse region in* **(b)***.*

7.2.2 Muons in Hit Clusters

The simulation data set used has an intrinsic minimal event size of 2 ms and hence holds multiple primaries as explained in Section 7.1. We also learned that the splitter algorithms tend to divide physical hits caused by a single cosmic ray primary into several sub-events. Therefore, whenever a splitter builds a new hit cluster that is based on an already identified primary, the new cluster should not be counted with respect to new identified primaries. The result of this counting experiment is given in Figures 7.23 and 7.24 for both splitting algorithms with a division into triggering and subtrigger primaries, respectively.

The first pair of plots, Figure 7.23, shows the behavior of HiveSplitter. The most entries for triggering primaries in hive-split clusters, in Figure 7.23a, are obtained in four to six primaries being present in 2 ms. This fits to the result from experimental data with an atmospheric event rate in the detector between 2.6 kHz and 3.0 kHz depending on the season, as presented in Section 6.1. Therefore, the hot spot can be seen as an indication for an accurate simulation of the real situation. In the case of primaries that did not cause a trigger, the splitter has difficulties to identify them all, as Figure 7.23b shows. This is not astonishing as we learned earlier in Section 7.1 that 57 % of all subtrigger primaries leave less than 4 hits in the detector which is under the threshold for cluster formation by any splitter algorithm. These low hit multiplicity primaries can still be identified if the splitters adds one, or several, noise hits to a cluster. From the cluster purity, which is not 100 % (see also Section 7.2.1), we know that this happens. Nonetheless, there is a fraction of almost 20 % in subthreshold muons that form exactly one single SLC hit leaving no chance of being identified as a hit with physical origin since at least two such hits need to be present in a cluster in order to count it as muon candidate.

All these arguments also hold for the case of TopologicalSplitter, presented in Figure 7.24 with the same division into trigger and subtrigger primaries, respectively. TopologicalSplitter performs slightly better in the case of subthreshold muons which can be realized by comparing the hot spots in the corresponding histograms. Figure 7.25 summarizes these results by giving the abundance of a certain fraction for identified primaries. The higher the bins are to the right of the histograms the better is the performance of the splitter. For triggering muons, both splitter perform equally satisfying. The greater difference between the two splitting tools arises in the case of subtrigger muon hits. HiveSplitter has a higher representation in low fractions of identified subtrigger primaries and is underrepresented above 50 %.

The identification potential of the splitter algorithms for muon identification is presented Table 7.1. More than two million primaries are present in the data set of which about 44.4 % are identified by HiveSplitter and 58.3 % find representations in topological-split hit groups. Although TopologicalSplitter creates ten times more clusters from the same data, HiveSplitter identifies about 15 % less of subthreshold primaries. On the other hand, HiveSplitter creates a lot less noise clusters, only 64.3 % of all its clusters, whereas TopologicalSplitter has a noise-based output of over 94 %. In the following, we discuss the behavior of NoiseEngine for both splitters.

7.2.3 Noise Engine Agreement

In a final step in the processing chain of muon identification via splitters (see also Figure 7.14), NoiseEngine is applied in order to judge if a hit cluster is noise-like or possibly has a physical origin, i.e. induced by a traversing particle. Figure 7.26 shows the angreement of NoiseEngine with the true origin of the hit clusters formed by HiveSplitter and TopologicalSplitter. In

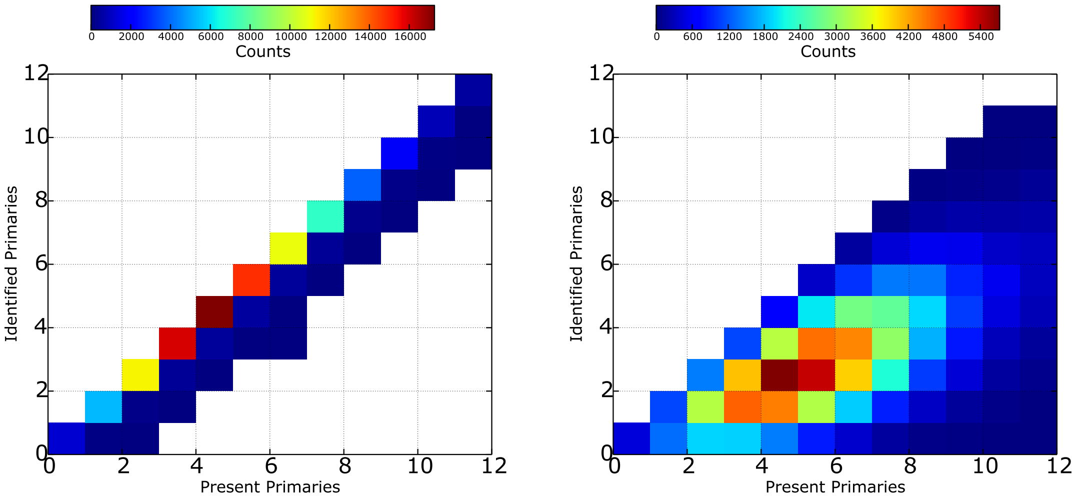

(a) *Triggered* **(b)** *Subthreshold*

Figure 7.23: *The number of detected primaries per* 2 ms *of simulation data versus their representation in HiveSplitter's hit clusters.*

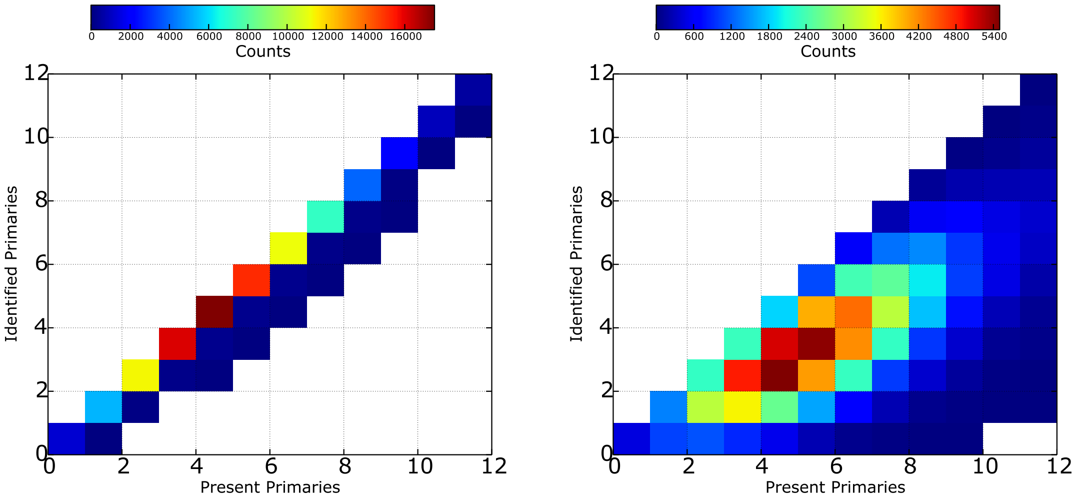

(a) *Triggered* **(b)** *Subthreshold*

Figure 7.24: *The number of detected primaries per* 2 ms *of simulation data versus their representation in topological-split hit clusters.*

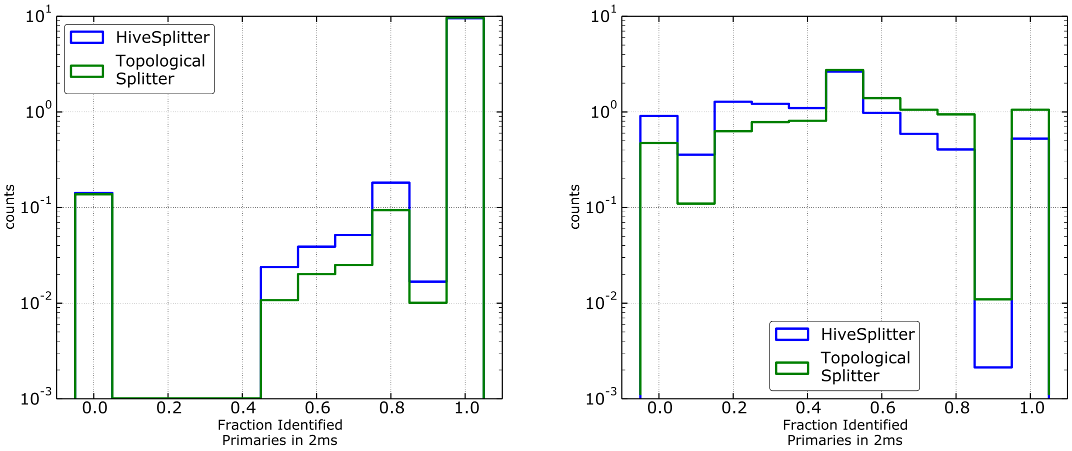

(a) *Triggered* **(b)** *Subthreshold*

Figure 7.25: *Fraction of identified primaries per* 2 ms

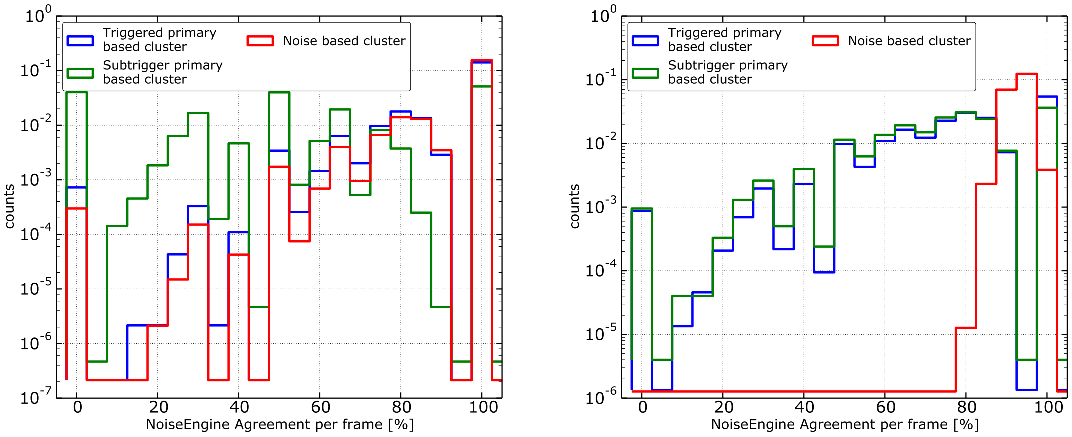

(a) *HiveSplitter* **(b)** *TopologicalSplitter*

Figure 7.26: *Fraction of NoiseEngine results in agreement with simulation truth of the hit cluster being caused by noise or atmospheric muon.*

Table 7.1: *Identification of detected (triggered or subthreshold) primaries via HiveSplitter and TopologicalSplitter in simulation.*

Splitter	Total Primaries	Identified Primaries			Total Clusters	Noise Clusters
		Total	Triggered	Subtrigger		
Hive	2.23×10^6	44.4 %	99.3 %	46.1 %	2.91×10^6	64.3 %
Topological	2.23×10^6	58.3 %	99.6 %	58.2 %	2.26×10^7	94.3 %

this representation, high bins to the right of the plot stand for a good agreement. The fact that the bin of 100 % agreement in Figure 7.26a is higher than in Figure 7.26b tells us that NoiseEngine comes more often to the right conclusion for all clusters in a 2 ms when evaluating HiveSplitter's hit clusters than for TopologicalSplitter. Considering only hit clusters that are due to noise (red lines in both histogramms of Figure 7.26), we see that there are no events in which NoiseEngine has identified less than 80 % of the hit clusters correctly if they are formed by TopologicalSplitter. The agreement of NoiseEngine for triggered and subtrigger primary based hit clusters is more subtle (blue and green histograms). From the bin of 0 % agreement we learn, on the one hand, that NoiseEngine misjudges more often primary based hive-split clusters and, on the other hand, among the misjudged clusters the majority are clusters based on subtrigger primaries. A quantitative overview of NoiseEngine's performance is given in Table 7.2. The simulation data set used for this evaluation has a lifetime of roughly 200 s which is enough to provide high statistics as can be seen from the total number of identified primary based hit clusters for both splitters. About 80 % percent of all represented primaries in clusters formed by either HiveSplitter or TopologicalSplitter have a positive NoiseEngine result. The agreement of NoiseEngine on topological-split events is worse than for HiveSplitter regarding triggering primaries. An overall yield of 80 % of all topological-split physics clusters being categorized correctly by NoiseEngine versus 92 % for hive-split clusters reflects the fact that HiveSplitter's clusters associated to a trigger primary are less contaminated with noise (see also Figures 7.17 and 7.18) and therefore easier to categorized correctly by NoiseEngine. The situation is turned to the opposite for the case of subthreshold primaries where NoiseEngine judges physics cluster correctly in 77 % of the cases of topological-split clusters and only 53 % of HiveSplitter's clustered hits. NoiseEngine is in more than 95 % of the cases in agreement with hit clusters that are based on noise for both splitters. This leads to the conclusion that NoiseEngine is in general trustworthy, preferably run on hive-split clusters containing hits reported in the trigger system and topological-split clusters based on subtrigger muons. This result suggest that the use of both splitters is recommended for an optimal result.

Table 7.2: *NoiseEngine's result for hit clusters by HiveSplitter and TopologicalSplitter*

Splitter	Primary Clusters	NE Agreement			Noise Clusters	NE Agreement
		Total	Triggered	Subtrigger		
Hive	6.8×10^5	79.3 %	92.6 %	53.7 %	5.1×10^5	95.3 %
Topological	6.4×10^5	79.7 %	80.4 %	77.2 %	8.6×10^6	95.6 %

7.3 Application of Muon Identification to HitSpool Data

Sections 7.1 and 7.2 showed that subthreshold muon identification via splitters is feasible. The very same methods are applied to real experimental HitSpool data with results presented in the following.

7.3.1 Resulting Hit Rates

The information we obtained from the a-priori knowledge about simulated muons in the detector suggested a hit contribution to the total detector hit rate of about 1 % by triggering muons and about 0.3 % by subthreshold muons (see Figure 7.13). The statistic provided by a standard HitSpool data set is one order of magnitude higher than the simulation data investigated. This allows for a wider binning compared to simulation. Figure 7.27 shows the overall hit rate compared to the corrections applied to a HitSpool data set with a lifetime of 60 s. The IceCube detector reveals a total hit rate of 2.93 MHz for all 5160 in-ice DOMs combined. Subtracting the triggering muon candidate hits results in an 1.8 % hit rate reduction, as given by the green histogram. The hits subtracted are the ones that were tagged by NoiseEngine to be muon candidates from hit clusters formed by HiveSplitter. In the case of subtreshold muons, topological-split cluster are the source for candidates. Subtracting these hits from the already trigger-corrected hit rate results in the final pure noise rate of 2.83 MHz which is more than 3 % lower than the total detector rate. This result deviates from the expectation from simulation by a factor of two. The reason for that can be understood by reviewing the local coincidence hit profile, presented in Section 7.2, it was shown that hit clusters identified by the event splitting tools contain two to three times more SLC hits compared to simulated atmospheric muons, regardless of being below or above the trigger threshold of the detector. Since the probability for an SLC hit to be caused by noise over its chances to originate from a subthreshold muon are almost 99/1, it is likely that a fraction of SLC hits present in clusters are noise. Although our hit selection for subthreshold muons obviously cuts into the noise level, it does so to a still acceptable amount.

A closer look at the individual atmospheric muon related hit rates is taken in in Figure 7.28. The red histogram shows the hit rate from subtrigger muon candidates. Compared to the muon candidates that have triggered the detectors (blue), we find a relation for subtrigger to triggering hits of 2/3. From simulation, we expect a 1/3 ratio. The absolute amount of subthreshold muon hits among all subtrigger muon candidates can be estimated as follows. From Table 7.1 and 7.2 we know that not less than 60 % of subthreshold muons are identified by splitters of which maximal 77 % are categorized correctly by NoiseEngine. This results in a maximum of about 45 % of all subtrigger muons being identified which corresponds to a fraction of the total detector hit rate of approximately 0.15 %. Figure 7.28 also shows the trigger hit rate of IceCube [5]. The hit rate from the in-ice simple multiplicity trigger (SMT8) is given as a reference in order to illustrate that most triggering hits (92 %) are accompanied by at least 7 HLC hits within ±1 μs. The amount of hits that cause any of IceCube's in-ice triggers to launch (black) are recovered to 99 % in hit clusters formed by the muon identification processing. The evaluation presented in this chapter about the resulting rates after the successful identification of triggering and subthreshold hits in the detector via the tools, concludes the investigations regarding atmospheric muons in IceCube.

---

[5] The trigger hit rate should not be confused with the *event* rate of IceCube which is in the order of 3 kHz. The latter is formed by merging overlapping triggers into global events possibly caused by the same particle(s) crossing the detector, as explained in Chapter 3.3.

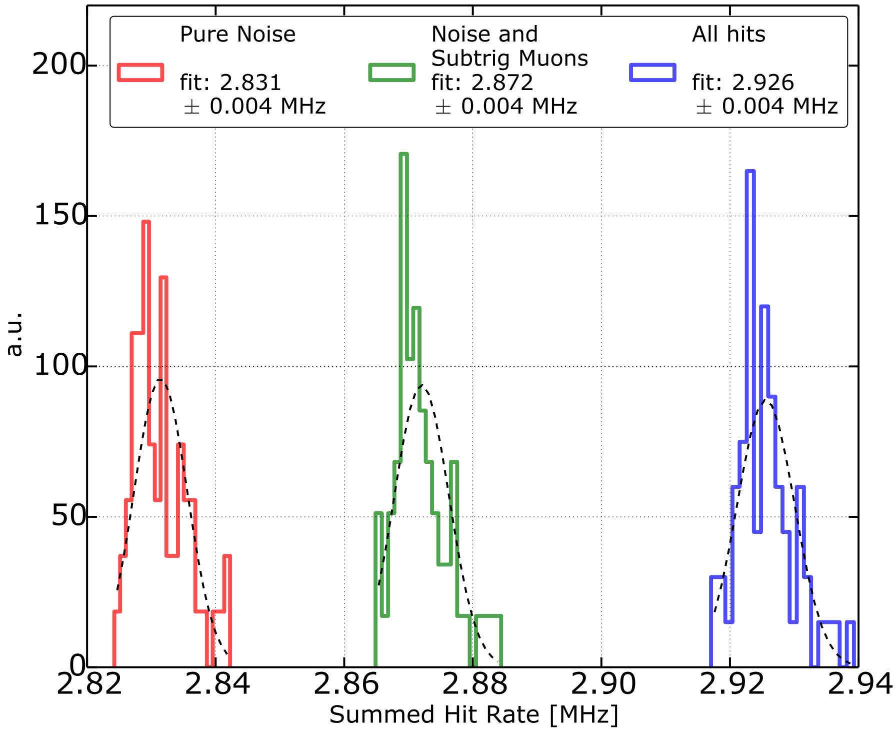

Figure 7.27: *Histogram of hit rate of all* 5160 *in-ice DOMs from* 60 s *of* HitSpool *data. The overall hit rate with corrections for muon tagged hits that have representations in triggers (green), those identified to possibly originate from subthreshold muons (red) and the total hit rate (blue).*

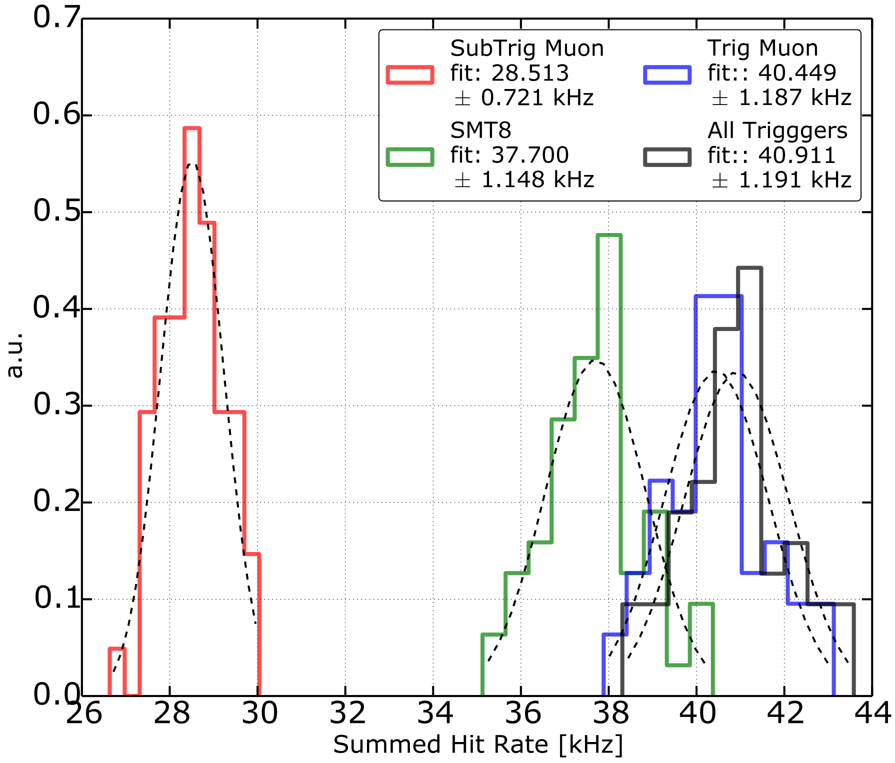

Figure 7.28: *Muon candidate hit rates, triggered (blue) and subtrigger (red), compared to the Simple Multiplicity Trigger hit rate (green) as well as all in-ice trigger hits (black).*

8

HitSpooling for Supernova Detection

In the development of this thesis, multiple data sets of high significant supernova candidate triggers were collected via the HitSpool Interface. *The additional information provided by* HitSpool *raw data enables us to produce scaler data in which hits caused by triggering muons can be identified as well as to some extent those hits originating from subthreshold muons. This chapter demonstrates the feasibility of producing lightcurves as well as significances for supernova candidates from* HitSpool *data. The processing of* HitSpool *data to scalers is presented in the first section. The significances of the supernova candidate triggers are calculated from* HitSpool *data with a comparison to the corresponding results from SNDAQ in the second section. The resulting lightcurves of the various scaler types of one exemplary data set are the topic of the third section. Finally, the last section presents an outlook of possible causes for the outstanding high significant data set.*

8.1 Scaler Production from HitSpool data

As soon as SNDAQ's online analysis reports a significance ξ above 7.65 in one of its four analysis channels, the HitSpool Interface collects the corresponding HitSpool data, see also Chapter 4 and Equation 4.7. Once the data arrives in the data warehouse in the northern hemisphere, it is unpacked and processed as presented in Chapters 5 and 7. After processing, all hits are categorized to belong to at least one of the following groups described in Table 8.1.

The calculation of the significance is performed with single DOM scalers in binning of SNDAQ's analysis channels. While SNDAQ performs the analysis of the significance with the consideration of a total time-window of ±300 s around the current bin at t_0, the available time span of HitSpool data is 90 s ($[-30\,\mathrm{s}, +60\,\mathrm{s}]$) for all data sets. This arises from the fact that non of the reported triggers exceeded the minimum significance $\xi \geq 10$ that would launch a HitSpool data request of ±250 s around the trigger time, see Section 5.2.

The basis for the calculation of the significance ξ are the individual DOM's mean hit rates $\langle r_i \rangle$, where index i covers all in-ice DOMs ($N_{DOM} = 5160$). Their deviations from the mean $\langle \sigma_i \rangle$, obtained from the background region, and the hit rate in the corresponding analysis bin r_i are also included in the calculation. The total mean $\Delta\mu$ of all rates is given by

Table 8.1: *Summary of hit categories produced from* HitSpool *data.*

Group Name	Details
All	All hits are present.
Deadtime	Hits that survive the artificial deadtime of 247.5 µs applied to every DOM. In order to account for the intrinsic deadtime of SNDAQ scalers which is motivated by the efficient reduction of correlated noise hits in this way, we apply this to produce comparable results.
Trigger	Hits that contribute to the formation of any in-ice trigger, SMT3, SMT8, Volume or String (Section 3.3).
Subthreshold	Hits that are identified to be candidates for subtrigger muons (Chapter 7).

$$\Delta\mu = \sigma^2_{\Delta\mu} \sum_{i=1}^{N_{DOM}} \frac{\epsilon_i (r_i - \langle r_i \rangle)}{\langle \sigma_i \rangle^2} \tag{8.1}$$

where ϵ_i is the DOM's efficiency and the squared standard deviation of the total mean is given by

$$\sigma^2_{\Delta\mu} = \left(\sum_{i=1}^{N_{DOM}} \frac{\epsilon_i^2}{\langle \sigma_i \rangle} \right)^{-1} \tag{8.2}$$

resulting in the known significance expression

$$\xi = \frac{\Delta\mu}{\sigma_{\Delta\mu}} = \sigma_{\Delta\mu} \cdot \sum_{i=1}^{N_{DOM}} \frac{\epsilon_i (r_i - \langle r_i \rangle)}{\langle \sigma_i \rangle^2} = \frac{\sum_{i=1}^{N_{DOM}} \frac{\epsilon_i (r_i - \langle r_i \rangle)}{\langle \sigma_i \rangle^2}}{\left(\sum_{i=1}^{N_{DOM}} \frac{\epsilon_i^2}{\langle \sigma_i \rangle} \right)^{1/2}} \tag{8.3}$$

The numbers of available background bins from wich $\langle r_i \rangle$ is calculated are summarized in Figure 8.1 for each analysis channel.

In order to investigate the effect of the amount of included background on the resulting significance of the analysis bin, two separate analysis chains are performed with HitSpool data. The *symmetrical* analysis takes only the first 60 s of the data set into account whereas the *asymmetrical* uses the full data range from $[-30\,\mathrm{s}, +60\,\mathrm{s}]$ around the trigger time reported by SNDAQ.

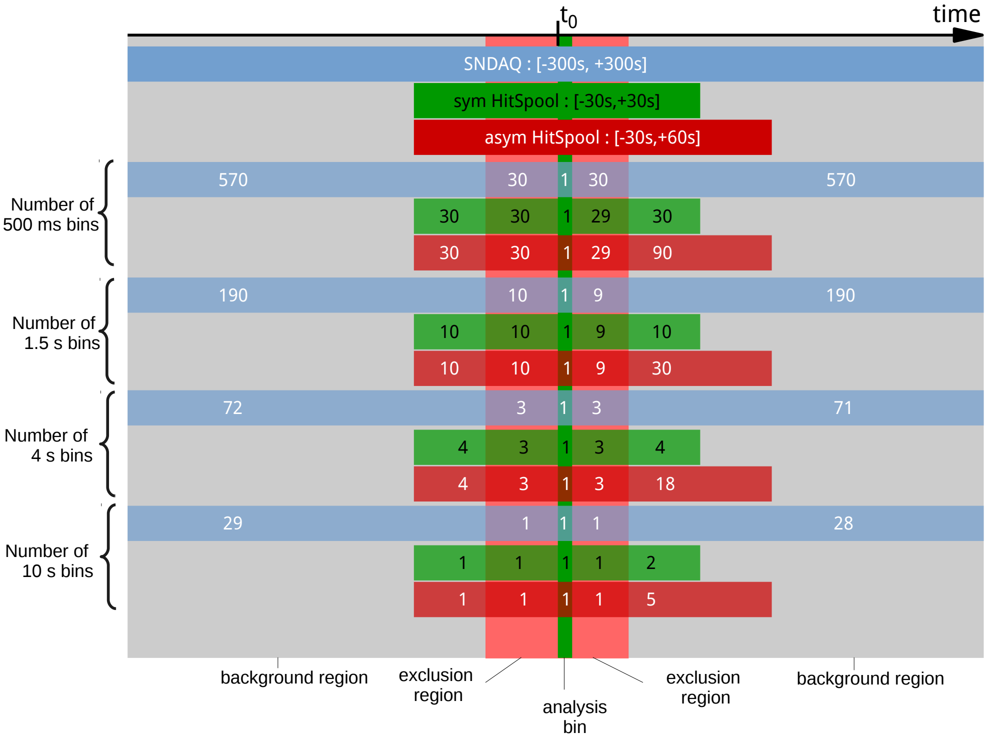
t0
time
SNDAQ : [-300s, +300s]
sym HitSpool : [-30s,+30s]
asym HitSpool : [-30s,+60s]
Number of 500 ms bins
570
30
1
30
570
30
30
1
29
30
30
30
1
29
90
Number of 1.5 s bins
190
10
1
9
190
10
10
1
9
10
10
10
1
9
30
Number of 4 s bins
72
3
1
3
71
4
3
1
3
4
4
3
1
3
18
Number of 10 s bins
29
1
1
1
28
1
1
1
1
2
1
1
1
1
5
background region
exclusion region
analysis bin
exclusion region
background region

Figure 8.1: *Comparison of data binnings for the calculation of the significance for a certain analysis bin at time t_0. SNDAQ takes a total time-window of $\pm 300\,\mathrm{s}$ into account (blue) whereas for* HitSpool *data a symmetrical timewindow of $\pm 30\,\mathrm{s}$ (green) and an asymmetrical timewindow of $[-30\,\mathrm{s}, +60\,\mathrm{s}]$ (red) are constructed.*

8.2 Supernova Candidate Significance

We concentrate here on the results of the application of the likelihood method to HitSpool data, outlined in Section 4.1 and recalled in Section 8.1. The following investigation does not only verify the likelihood method in an independent way but also demonstrates the feasibility of producing and extracting single DOM scalers from HitSpool data. In total, 28 HitSpool data sets are used in this analysis, covering a period from April 2013 until December 2014. All of the supernova triggers reported by SNDAQ in this period are below the threshold of $\xi \leq 10$ so that 90 s of HitSpool data were collected for each trigger.

In order to estimate the statistical error of the significance resulting from the limited time range available for the estimation of the background rates (see Figure 8.1), a toy MonteCarlo simulation was performed. We calculate an error of the derived significance by running 1000 pseudo-experiments with

$$\mu_i^{MC} = < r_i > \tag{8.4}$$

$$\sigma_{\mu_i^{MC}} = \frac{<\sigma_i>}{N_{bkg}} \quad , \tag{8.5}$$

where N_{bkg} is the number of background bins of the corresponding analysis channel [1]. This results in 1000 slightly different values for ξ for each analysis channel with a mean value ξ_{MC} and a standard deviation $\sigma_{\xi_{MC}}$. The standard deviation is taken as the error on the stated significance from HitSpool data.

8.2.1 Scalers with Deadtime

In order to compare the HitSpool significance to the value from SNDAQ, we select the ξ value from the analysis channel in which the trigger happened. Figure 8.2 gives the results of that comparison for both the symmetrical as well as the asymmetrical analysis window.

From the 28 HitSpool data sets, only 21 are displayed in the upper plot and 25 in the lower plot of Figure 8.2, respectively. This is justified by the fact that the missing data points are far away from any reasonable result, as can be reviewed in table 8.4. Most of these deviating significance values arise in 4 s and 10 s binning of the data where we have at least 3 and maximal 22 bins for the background estimation available (see Figure 8.1). Compared to a minimum of 57 bins of background in the case of SNDAQ, that provides in any analysis channel at least one order of magnitude more background bins than the analysis bin and the exclusion region contain, it is easy to understand that the limited statistic of the HitSpool data in coarse binnings can lead to such deviations. The remaining displayed significances from supernova triggers reported in 4 s and 10 s binnings are more distant from the identity line (dashed blue line) than smaller time bins. When using all available HitSpool data, i.e. the asymmetrical analysis in the lower plot of Figure 8.2, more data points populate the picture since more background bins are considered for the significance calculation and hence reducing its statistical randomness.

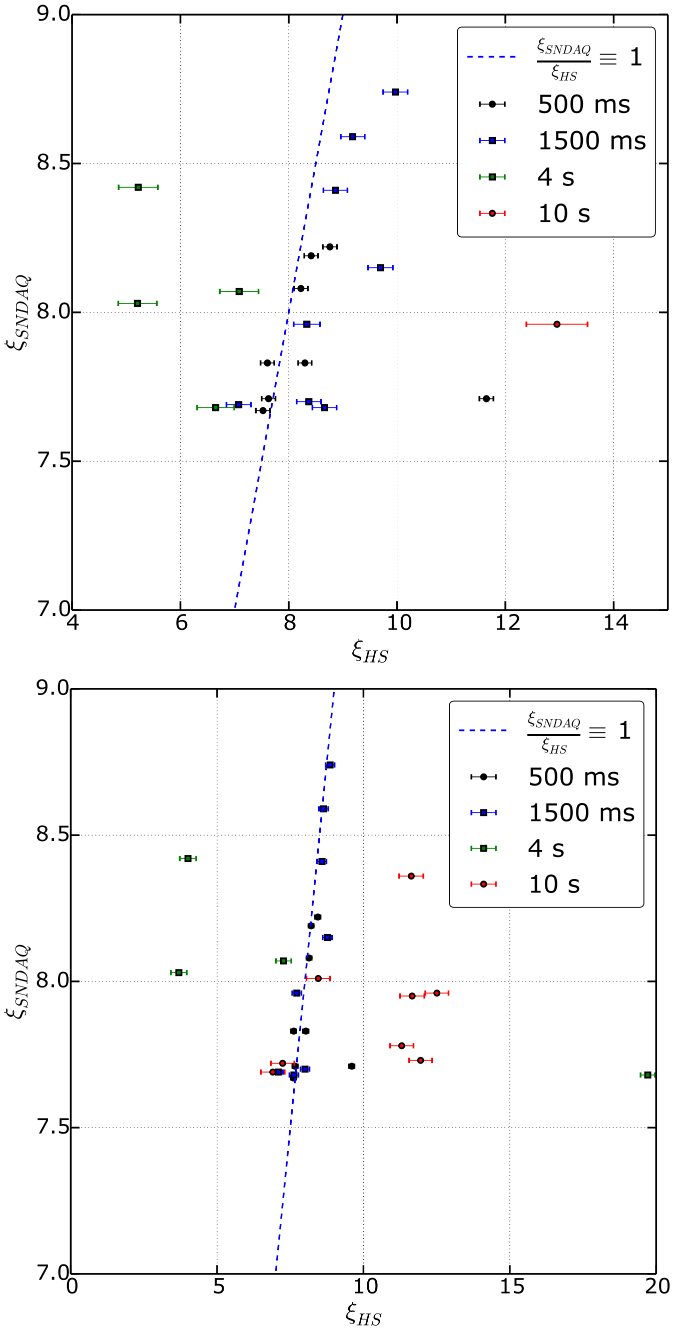

Figure 8.2: *Comparison of trigger candidate significances reported by SNDAQ versus* HitSpool *results with symmetric analysis window (above)and asymmetric (below).*

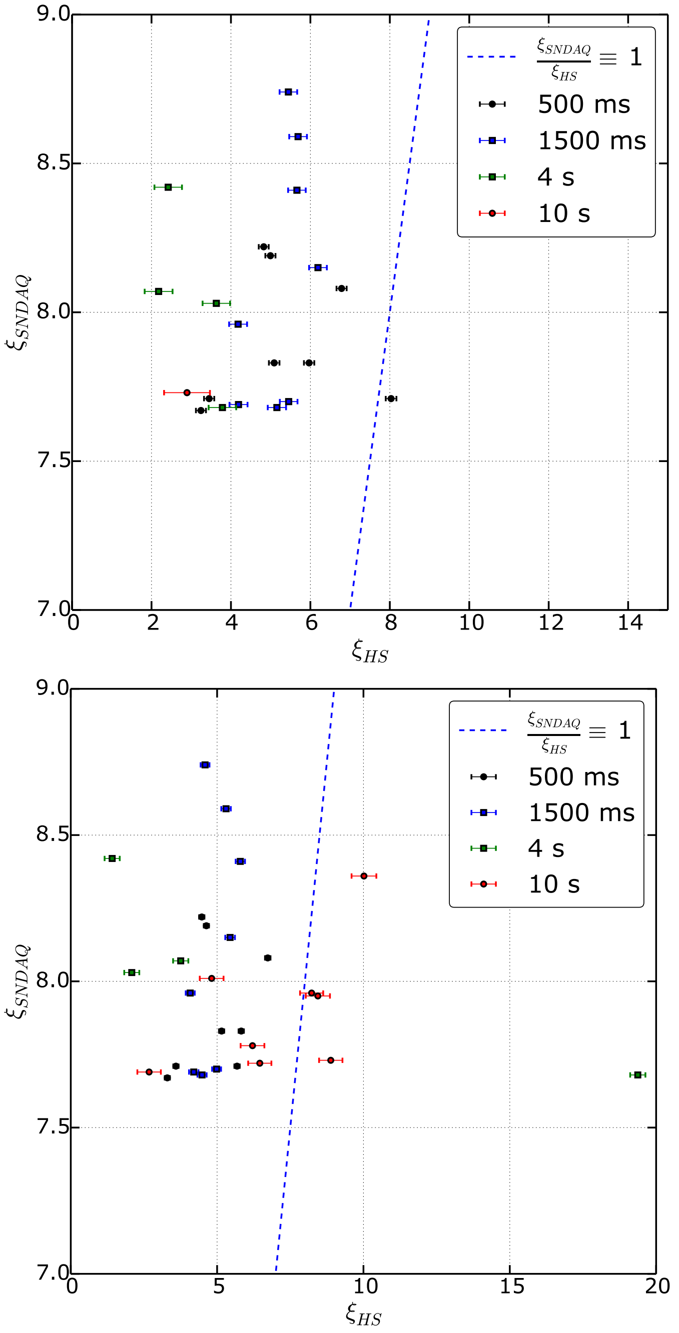

Figure 8.3: *Comparison of trigger candidate significances reported by SNDAQ versus* HitSpool *results with symmetrical analysis window (above) and asymmetrical (below). The values from* HitSpool *data,* ξ_{HS} *are corrected for triggering muon hits.*

Table 8.2: *Average reduction of* HitSpool *significance from scalers with deadtime to trigger hits correction per analysis timebase and timewindow .*

Analysis Timewindow	500 ms Binning	1.5 s Binning	4 s Binning	10 s Binning
Symmetrical	36.6 %	40.0 %	53.2 %	25.9 %
Asymmetrical	38.4 %	29.6 %	51.6 %	17.6 %

Table 8.3: *Average reduction of* HitSpool *significance from scalers with deadtime and trigger hits correction to subthreshold hits correction per analysis timebase and timewindow .*

Analysis Timewindow	500 ms Binning	1.5 s Binning	4 s Binning	10 s Binning
Symmetrical	42.1 %	47.4 %	66.7 %	-
Asymmetrical	45.3 %	29.6 %	69.6 %	9.4 %

8.2.2 Triggering Muon Correction

The correction for triggering muon hits is a big step towards the desired aim of a clean significance statement without any contribution of atmospheric muons that might have caused the significant signal in the first place. As we can see in Figure 8.3, the same set of data points is present in the displayed range of both analyses, symmetrical and asymmetrical. In the case of the symmetrical timewindow calculations, all data points except one are located to the left of the identity line, reporting a decreased HitSpool significance compared to SNDAQs results. The asymmetrical analysis, shown in the lower plot in Figure 8.3 shows a less drastic decrease but still the same effect as the symmetrical analysis. The averaged significance over all data sets that produce reasonable values is reduced by 45 % in symmetrical and 35 % in asymmetrical timewindow analysis compared to scalers with only deadtime. The individual decrease in significance per analysis timebase and timewindow is summarized in Table 8.2.

8.2.3 Subthreshold Muon Correction

In Figure 8.4 we can see that the trigger corrected ξ-values decrease by another notable fraction when subtracting the remaining, subthreshold, muon candidate hits. For the analysis performed with the limited symmetrical timewindow ($\pm$30 s around trigger) non of the triggers reported in 10 s bins enters the displayed region in the upper plot of Figure 8.4 since they are either negative or at least 50 % above the meaningful range. All remaining data points show a significance $\xi_{HS}^{subtrig}$ that is at least decreased by 40 % in comparison to the significance ξ_{HS}^{trig} that was obtained after trigger correction (see Table 8.3). Only two candidates remain high significant with $\xi_{HS}^{subtrig} > 5$ namely the already familiar supernova candidate triggers from August 16th 2014 whose lightcurves were presented in Section 8.3 and another from May 10th 2014. After applying the asymmetrical analysis, result are shown in the lower plot of Figure 8.4, the latter candidate decreased to an insignificant event whereas the former remains stable above the threshold of 5. A dedicated investigation of that candidate is performed in Section 8.4.1. Besides this interesting candidate from the trustworthy 500 ms analysis,

---

[1] We perform eight different analyses by taking two time ranges (symmetrical and asymmetrical) and four re-binnings (500 ms, 1500 ms, 4 s and 10 s).

multiple supernova triggers from the most coarse binning enter the picture when considering the entire available range of 90 s HitSpool data. Due to the direct proportionality of hit rates involved in the likelihood method (see Equation 8.3) one expects a sequential decrease of the significance resulting from the various muon corrections that reflects the ratio of the triggering muon hits to their subthreshold component. In other words, given the subtrigger-to-trigger hit ratio of $3/4$ presented in Section 7.3, the decrease in significance from trigger to subtrigger correction should not be more than 75 % of the decrease when adding trigger correction to the significance extracted from scaler with deadtime. In that sense all significance values that either change sign or decrease by one order of magnitude after one of the corrections are doubtable. Thus all of the 10 s-candidates are withdrawn from further investigations and the only remaining significant candidate is the trigger from 2014-08-16. The averaged decrease in significance per analysis timebase and timewindow is summarized in Table 8.3. All significance calculation results are summarized in Table 8.4. This concludes our discussion of the application of muon identification and subtraction for a corrected significance statement from HitSpool data for the supernova candidates under investigation. In the next section, we use the data sets of the interesting trigger from 2014-08-16 as an example for presenting the production of lightcurves from HitSpool data.

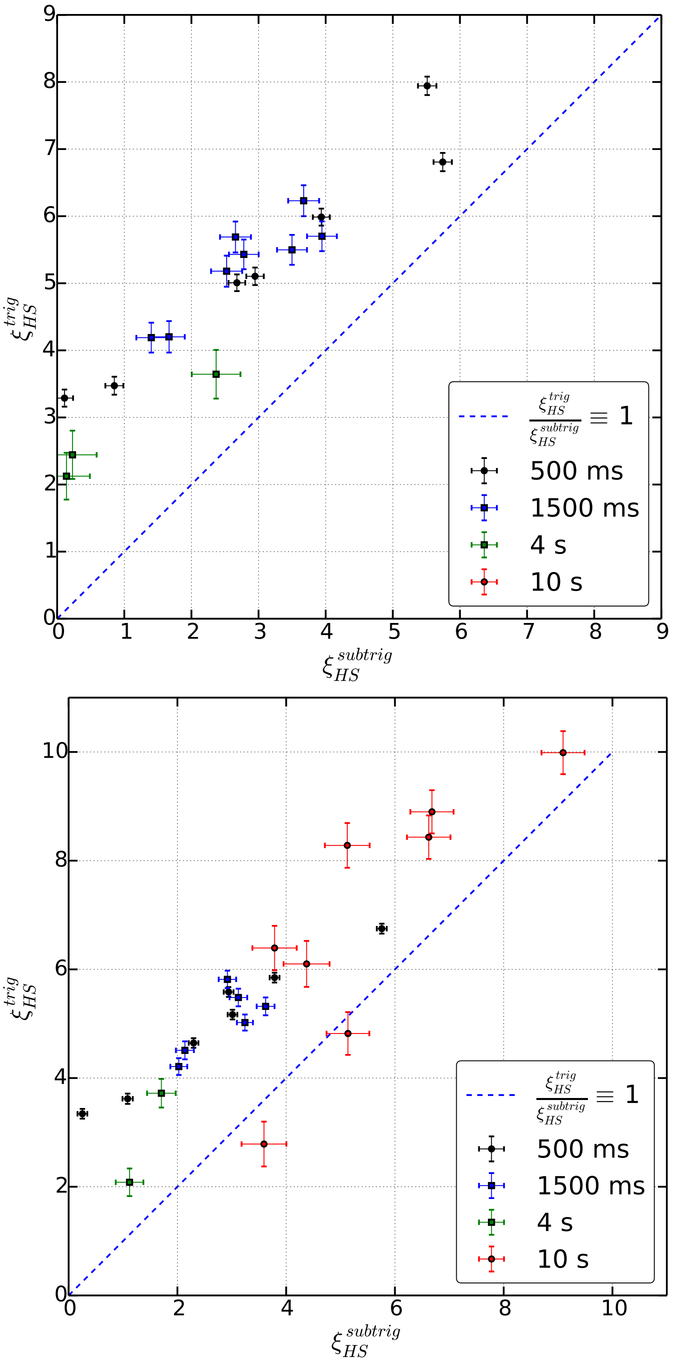

Figure 8.4: *Comparison of significances of* HitSpool *data sets with triggering muon corrections versus subthreshold correction in symmetrical (above) and asymmetrical (below) analysis time windows.*

Table 8.4: *Summary of supernova candidate triggers and their significances calculated by SNDAQ (its basic value and muon corrected if available) as well as retrieved from* HitSpool *data (in six different analyses).*

Trigger Time	Binning [ms]	SNDAQ		HitSpool					
		basic	corr	sym, D	asym, D	sym, DT	asym, DT	sym, DTS	asym, DTS
2013-04-03 06:11:13	4000	8.07	-	7.06	7.24	2.12	3.72	0.14	1.71
2013-05-08 01:58:39	4000	8.42	-	5.26	4.03	2.44	1.44	0.23	−0.62
2013-08-03 14:11:21	1500	8.41	-	8.87	8.60	5.69	5.82	2.66	2.92
2013-12-13 18:34:27	1500	8.15	-	9.70	8.78	6.23	5.48	3.67	3.12
2013-12-21 07:33:13	1500	8.74	-	9.96	14.73	5.43	11.50	2.78	9.53
2014-01-14 20:18:39	10 000	7.96	-	27.27	12.51	−140	8.28	15.44	5.12
2014-01-24 21:37:53	1500	7.68	-	8.67	7.63	5.18	4.51	2.52	2.14
2014-01-27 10:21:58	4000	8.03	-	5.23	3.71	3.64	2.08	2.37	1.12
2014-02-03 11:17:50	10 000	8.01	-	26.23	8.47	7.03	4.82	−2.76	5.14
2014-02-05 15:32:23	500	7.67	-	7.53	7.61	3.29	3.34	0.11	0.25
2014-02-14 16:16:36	1500	7.69	-	7.09	7.10	4.20	4.21	1.67	2.03
2014-02-15 19:05:39	1500	7.96	-	8.34	15.42	4.19	13.74	1.40	12.52
2014-03-03 14:59:31	10 000	7.95	-	−88.18	11.65	−34.39	8.43	−2.15	6.62
2014-04-07 07:17:28	500	7.83	-	8.31	8.04	5.99	5.85	3.94	3.79
2014-04-27 08:04:18	500	7.71	-	7.63	7.67	3.47	3.62	0.85	1.09
2014-05-04 09:30:08	500	7.83	-	7.61	7.62	5.10	5.17	2.95	3.01
2014-05-10 16:05:00	500	7.71	-	11.56	9.51	7.94	5.58	5.51	2.94
2014-08-15 06:25:50	10 000	8.36	7.41	98.78	11.70	42.44	9.99	98.73	9.09
2014-08-16 16:07:59	500	8.08	6.28	8.23	8.15	6.81	6.75	5.74	5.76
2014-08-22 15:28:19	10 000	7.82	7.28	−134	32.40	133.75	32.12	41.02	31.96
2014-10-31 15:14:12	10 000	8.17	-	150	35.19	153.01	35.11	146.04	35.06
2014-11-01 23:57:14	10 000	7.73	-	60.23	11.98	−4.51	8.90	−29.55	6.68
2014-11-13 04:19:22	10 000	7.69	-	−2.90	6.88	−7.94	2.79	99.81	3.59
2014-11-14 05:38:34	1500	8.59	-	9.20	8.65	5.70	5.32	3.94	3.62
2014-11-22 20:40:30	10 000	7.72	-	8.47	7.23	−0.48	6.39	99.02	3.79
2014-11-24 12:01:51	500	8.19	-	8.42	8.22	5.01	4.65	2.68	2.30
2014-12-02 23:53:25	1500	7.70	-	8.38	8.01	5.50	5.02	3.50	3.24
2014-12-04 16:42:03	10 000	7.78	-	21.88	11.28	−26.68	6.10	94.61	4.38

basic: as reported by SNDAQ using untreated scalers
corr: SNDAQs scalers correction for hits from SMT8 triggers
sym: HitSpool symmetrical analysis timewindow, $\pm 30\,\mathrm{s}$ around trigger time
asym: HitSpool asymmetrical analysis timewindow, $[-30\,\mathrm{s}, 60\,\mathrm{s}]$ around trigger time
D: Deadtime of $247.5\,\mu\mathrm{s}$ applied
DT: Deadtime applied, hits from any trigger subtracted
DTS: Deadtime applied, trigger hits subtracted, subthreshold muon candidate hits subtracted

8.3 Supernova Candidate Lightcurves

In order to arrive at the histogrammed time distribution of hits, the so-called lightcurve, and to calculate the corresponding significance for the relevant hit groups, the data is processed to SNDAQ-like scalers. For the lightcurve, the hits of all in-ice modules are summed in 1 ms bins overcoming the limitations of SNDAQ that is bound to a minimum bin size of 2 ms. Since SNDAQ is reporting the lightcurve not only in its four significance analysis channels (500 ms, 1.5 s, 4 s and 10 s) but also in the basic 2 ms stream, HitSpool data is re-binned to these five formats on order to be comparable. Results of these lightcurves are given in Section 8.3.

The HitSpool data set used in the series of lightcurve plots throughout this section was chosen because it is the only candidate for which SNDAQ triggered in the 500 ms binning, reported a muon corrected ξ value and that also remains rather significant in HitSpool data after corrections, as demonstrated in Section 8.2. A possible explanation for that specific supernova candidate trigger is discussed in Section 8.4.1. In the following, we use the corresponding data set to cover general aspects of the various lightcurves.

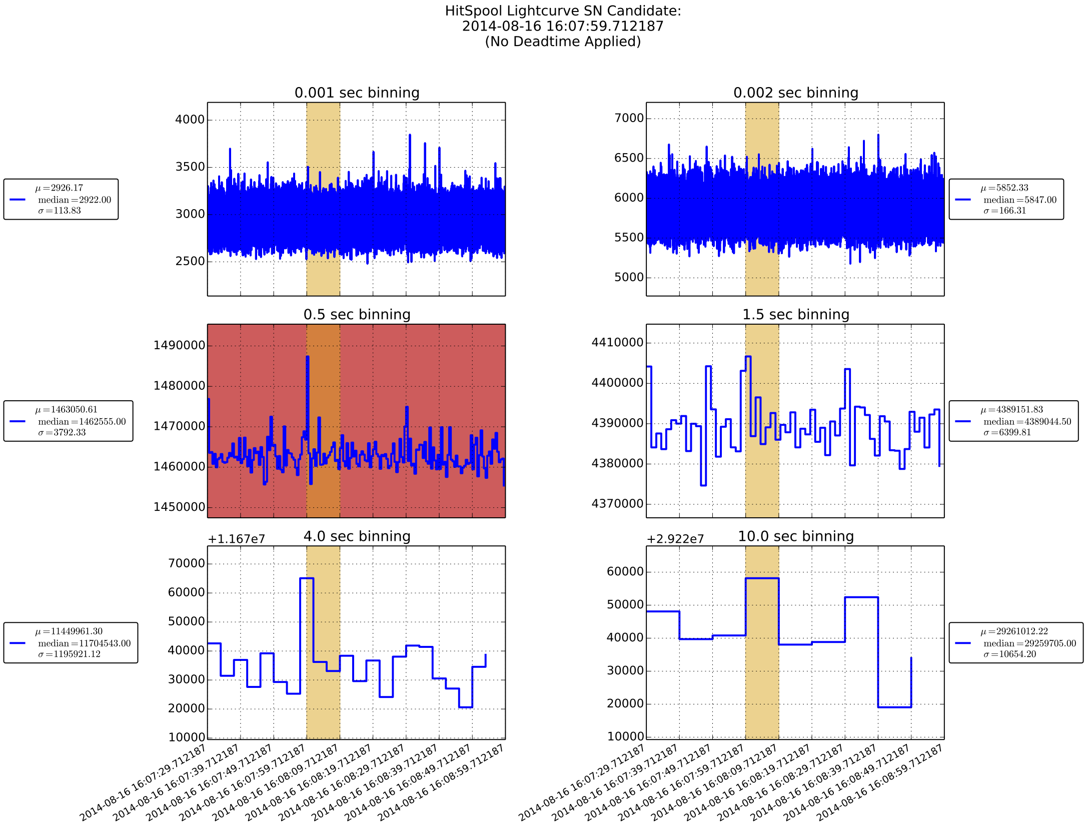

Figure 8.5: *HitSpool data lightcurve for candidate trigger from August 16th 2014 in bins of* 1 ms, 2 ms, 0.5 s, 1.5 s, 4 s *and* 10 s. *The binning in which SNDAQ reports the trigger is highlighted in red.*

8.3.1 All Hits

Lightcurves are produced from entries in the *All* hits group. Exemplary shown in Figure 8.5 are the lightcurves of a data set that was collected around a trigger candidate reported by SNDAQ in its 500 ms analysis channel. We show 6 different binnings of which the triggering binning can be identified by the red background. Since this candidate had a reported significance of $\xi_{SNDAQ} < 10$, HitSpool data is collected between 30 s before until 60 second after the trigger timestamp. Most of the interesting physics is expected to happen up to 10 s following the trigger time (see Chapter 2), this period is highlighted in the panel plots. The triggering bin is easily visible in Figure 8.5 as the high peak in the plot underlaid in red. Figure 8.5 is a unique representation of the data since all available hits are provided. In contrast, SNDAQ uses the scaler stream that collects only hits surviving an internal deadtime on every DOM, as we see in the following.

8.3.2 Deadtime Application

As we have seen in Chapter 4, the scalers fed to SNDAQ have an intrinsic deadtime of 250 µs applied to every hit in each DOM in order to reduce effects from correlated noise. In contrast, the hits in the HitSpool stream come from a different processing line in the DOM (see Section 3.2.2) and have passed at least one digitization step, i.e. the fADC in the DOM mainboard. A minimal deadtime of 2.5 µs is already intrinsic to every HitSpool hit. This is artificially increased by adding 247.5 µs in post-processing to produce a comparable value of HitSpool to SNDAQ. The value chosen for an artificial deadtime in HitSpool data was found to produce the smallest discrepancy in the lightcurves among various values tested. Figure 8.6 shows a comparison of SNDAQs lightcurve to the distributions produced by HitSpool hits from the *Deadtime* class. As can be seen from Figure 8.6, all HitSpool lightcurves, for which SNDAQ provides data as well, agree well in shape but are offset by 0.5 %. The offset has its origin in the impossibility of reproducing the intrinsic deadtime of SNDAQ's scalers and the DOM internal binning of 1.6384 ms (see also Section 4.1) to full extent in HitSpool data.

8.3.3 Triggering Muon Correction

Recent developments in SNDAQ enable us to receive information from the trigger system of the separated standard surface DAQ system of IceCube. An online correction of the reported scalers with respect to hits caused by triggering muons is now possible which was previously only available through an offline analysis [160]. This muon correction is based on SMT8 hits only and does not take into account other triggers. However such a corrected significance ξ_{corr}^{sndaq} is calculated on-the-fly in SNDAQ and the lightcurve of that data is not stored. Therefore, we use solely HitSpool data to compare the effect of SMT8 trigger corrections with the resulting lightcurve when subtracting all hits from any trigger type. The result is presented in Figure 8.7. Comparing to the lightcurves that include only deadtime, given in Figure 8.6, the distribution now becomes obviously more stable in the fine bins of 1 ms and 2 ms. The standard deviation of the distribution is lowered by approximately 30 %. The overall hit count is reduced by 1 % when subtracting all trigger hits from the deadtime surviving distribution as expected, see Chapter 7. The differences between lightcurves cleaned from SMT8 to all trigger hits is more subtle. As we can see in Figure 8.7, the two lightcurves are barely distinguishable in the fine binnings. The 2 ms binned histogram shows exactly one

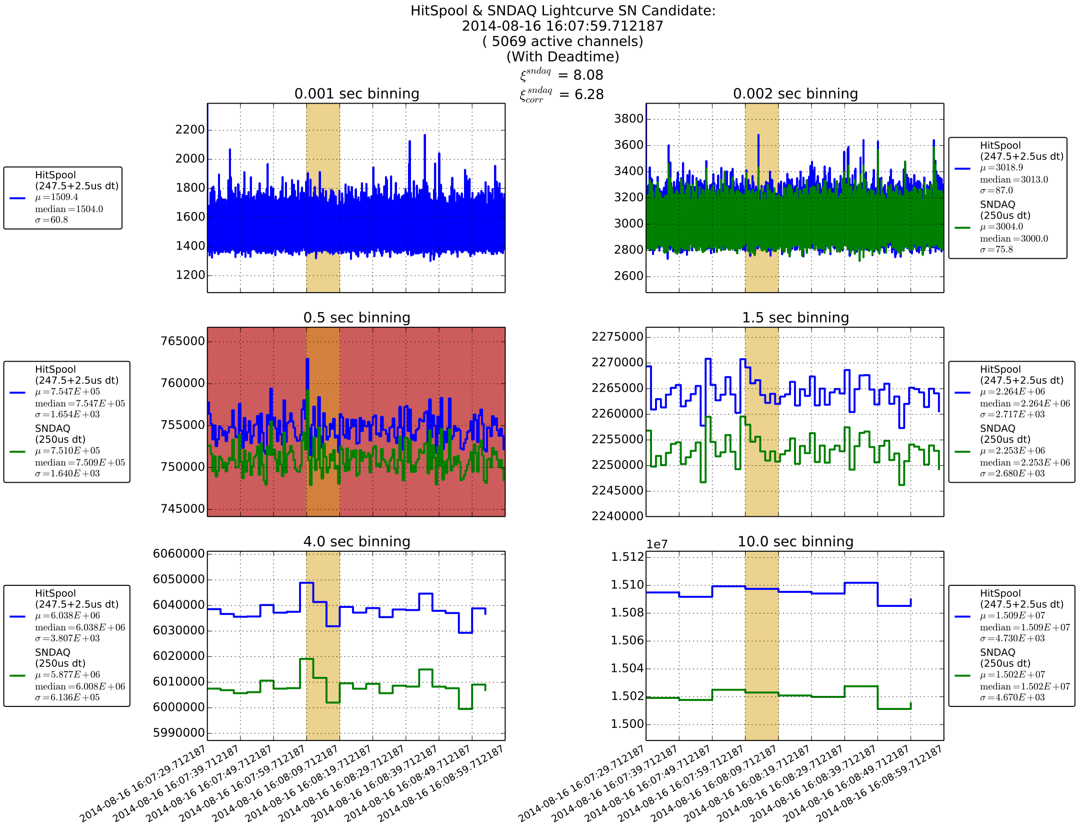

Figure 8.6: *HitSpool data lightcurve (blue) for candidate trigger from 2014-08-16 in bins of* 1 ms, 2 ms, 0.5 s, 1.5 s, 4 s *and* 10 s *with an artificial deadtime applied to each hit in* HITSPOOL *data in order to be comparable with SNDAQ (green). The binning in which SNDAQ reports the trigger is highlighted in red.*

hit count difference in the standard deviation between the two distributions. The mean hit count per bin decreases by 0.5 % when taking hits from all trigger types into account compared to solely using information from SMT8.

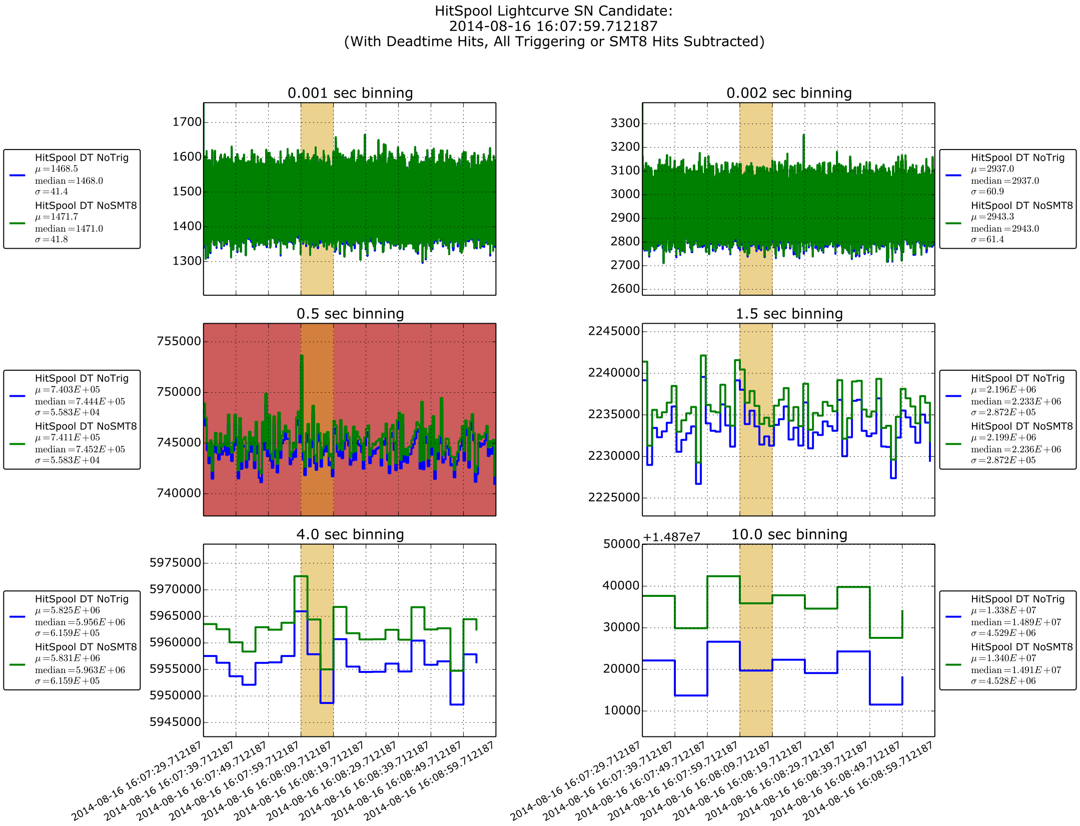

Figure 8.7: *HitSpool data lightcurve for candidate trigger from 2014-08-06 in bins of* 1 ms, 2 ms, 0.5 s, 1.5 s, 4 s *and* 10 s *with an artificial deadtime applied to each hit. Hits forming SMT8 triggers (green) and hits from all in-ice trigger types (blue) hits are subtracted. The binning in which SNDAQ reports the trigger is highlighted in red.*

8.3.4 Subthreshold Muon Correction

We now incorporate the results from Chapter 7 where we developed a technique to identify and subtract subthreshold muons from the data. The result is shown in the series of plots in Figure 8.8. From comparing the standard deviations of the lightcurves in the 2 ms binning, we can see that the width of the distribution decreases by more than 3 % when we subtract the subtrigger muon hits from the already trigger-cleaned lightcurve. This is in good agreement with the results from Section 7.3.

For this particular data set, the triggering bin (left flank of the yellow highlighted ten seconds in Figure 8.8) stays pronounced throughout all shown lightcurves, especially well recognizable in the 500 ms binning. A possible explanation for that enhancement is discussed in the following section.

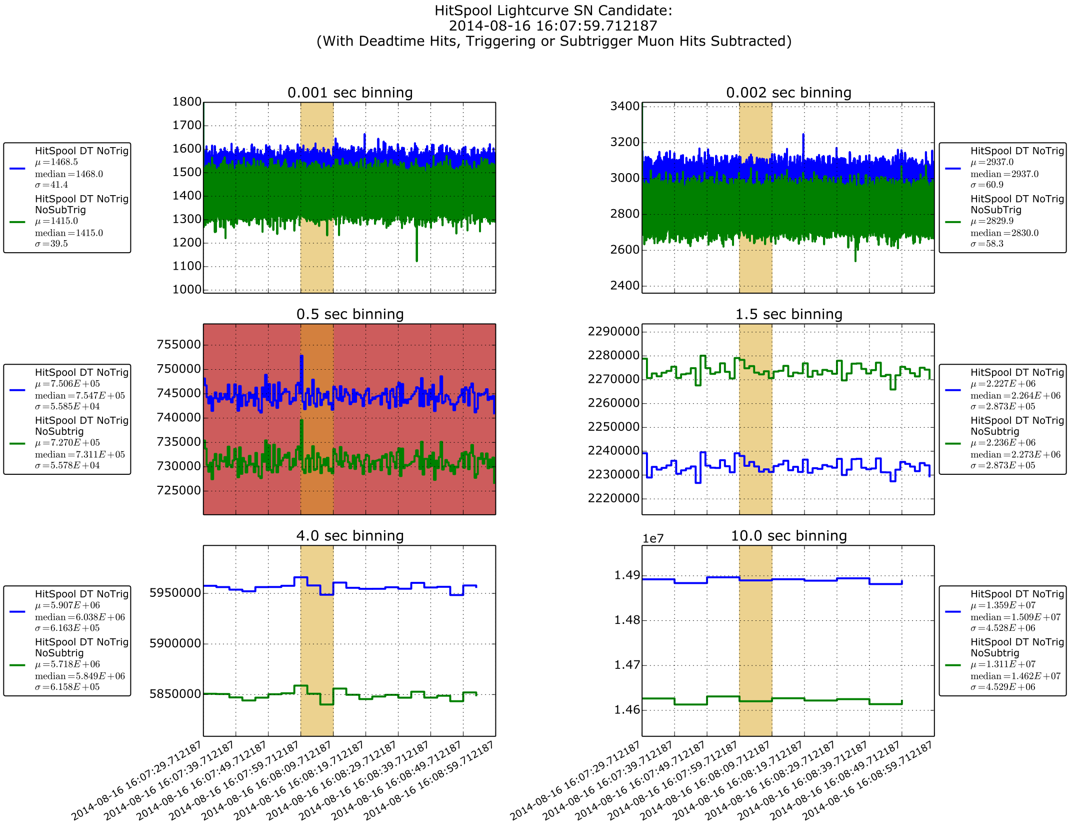

Figure 8.8: *HitSpool data lightcurve for candidate trigger from August 16th 2014 in bins of* 1 ms, 2 ms, 0.5 s, 1.5 s, 4 s *and* 10 s *with an artificial deadtime applied to each hit. Triggering hits are identified and subtracted (blue line) as well as all subthreshold muon candidate hits (green line).*

8.4 Outlook

Almost all of the HitSpool data sets recorded for high significant SNDAQ triggers were found to be reduced to an insignificant level after muon subtraction. This underlines the fact that atmospheric muons are the most prominent external source of background for a supernova detection in IceCube. The following section investigates solar activity as possible origin of the candidate trigger from 2014-08-16, the only candidate with a significant ξ-value after all possible atmospheric muon corrections and whose lightcurves were presented in Section 8.3.

8.4.1 Investigation of Supernova Candidate Trigger from 2014-08-16

Although this candidate shows a remaining high significance, $\xi > 5$, after subtraction of all possibly identifiable contributions from atmospheric muons, as shown in the previous sections, the fact that SNEWS[2] did not receive an alarm for that timestamp from any other experiment rises the doubt that this trigger is caused by neutrinos from a galactic supernova. Hence an investigation of possible other explanations for the high significance after corrections is desirable.

When considering extra-terrestrial neutrino sources that could cause a low energy signal in IceCube it is not surprising to look at our closest neutrino generator, the Sun. However, it is not the standard nuclear fusion channels in the Sun that should be considered here as neutrino sources but rather neutrinos generated by sudden and burst like solar activity like solar flares and coronal mass ejections (CMEs). The flare onset produces signals in different energy bands from radio waves through visible light to x-rays and γ-rays, and are often associated with CMEs [220]. However, the connection between the flare and the CME is theoretically not yet established. Intense solar flares, originating from the sudden release of concentrated magnetic energy that has built up in the solar atmosphere[3], produce high energy particles like protons and ions that are well observable by satellites and ground-based detectors [220]. When colliding with the solar atmosphere, these accelerated protons generate mesons which decay into neutrinos [221]:

$$\pi^+ \longrightarrow \mu^+ + \nu_\mu \tag{8.6}$$

$$\mu^+ \longrightarrow e^+ + \nu_e + \overline{\nu}_\mu \tag{8.7}$$

$$\pi^- \longrightarrow \mu^- + \overline{\nu}_\mu \tag{8.8}$$

$$\mu^- \longrightarrow e^- + \overline{\nu}_e + \nu_\mu \tag{8.9}$$

With a proton spectrum ranging from 30 MeV to 5 GeV, we expect a neutrino flux on Earth of $\mathcal{O}(100\,\mathrm{cm}^{-2})$ with energies between 10 MeV and 10×10^3 MeV, depending on the model used for the spectral index of the protons [222]. Furthermore, high energy γ-rays produced by the decay of neutral pions:

$$\pi^0 \longrightarrow \gamma + \gamma \tag{8.10}$$

play an important role in the search for neutrinos from solar flares which is primarily motivated by results from the Chlorine experiment in the Homestake mine in the 1980's that detected an increase in the total solar neutrino flux in a possible coincidence with large solar flares

---

[2] The Supernova Early Warning System, mentioned in Section 4.1.3

[3] visible as *sunspots*

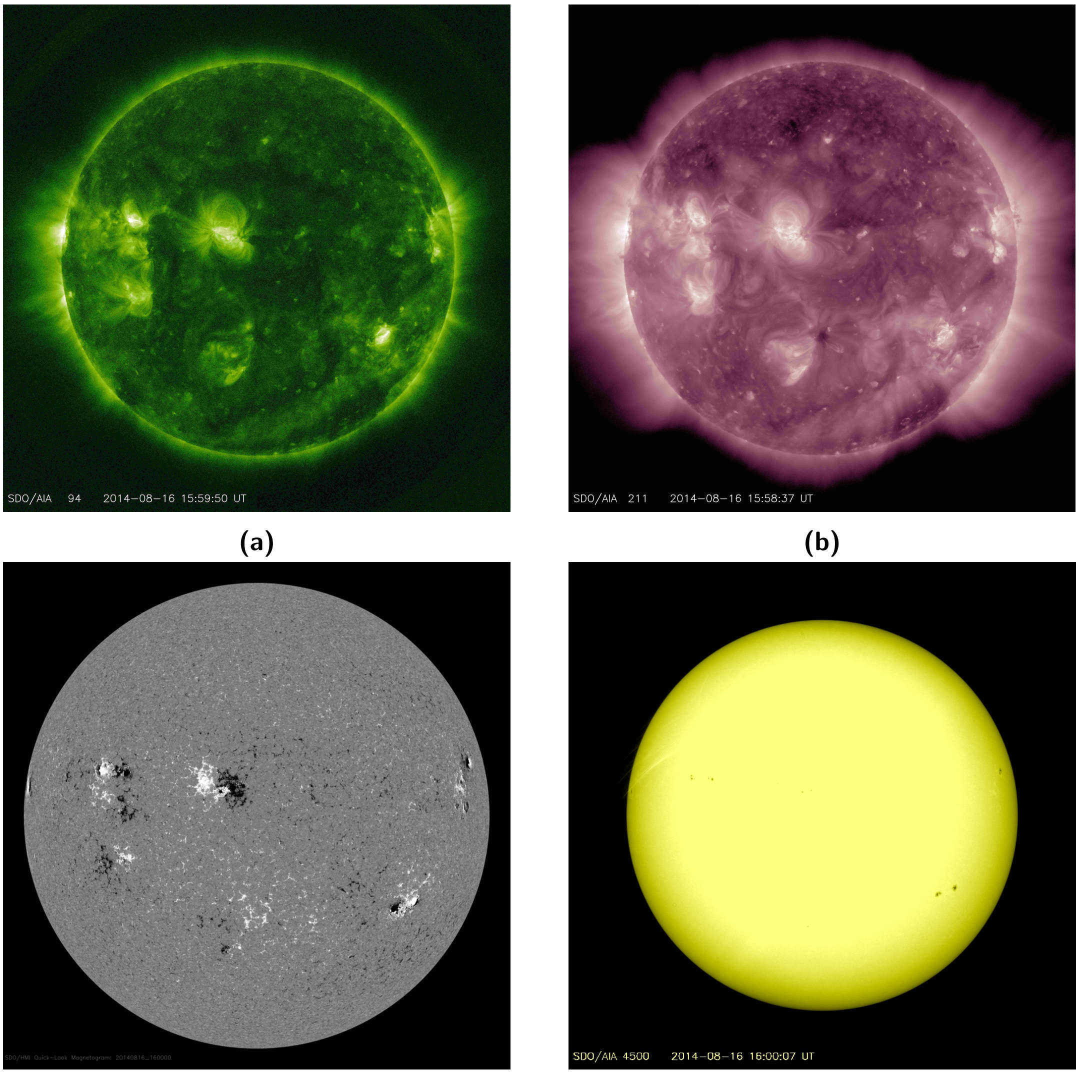
SDO/AIA 94 2014-08-16 15:59:50 UT
SDO/AIA 211 2014-08-16 15:58:37 UT
SDO/HMI Quick-Look Magnetogram: 20140816_160000
SDO/AIA 4500 2014-08-16 16:00:07 UT

(a) **(b)**

(c) **(d)**

Figure 8.9: *Images of the Earth facing side of the Sun taken by SDO in various optical filter band, shown in* **(a)** *and* **(b)** *as well as magnetic intensity in* **(c)** *and* **(d)** *around ten minutes prior to the supernova candidate trigger.*

[223, 224]. The model of chromospheric flare regions [225] suggests the emission of these photons on time scales of order $\mathcal{O}(4\,\mathrm{min})$ [226] which is well in the time frame of SNDAQ's online analysis and thus justifies solar flare activity to be categorized as possible background in IceCube's supernova candidate triggers.

A dedicated analysis and feasibility study to detect these neutrinos in IceCube is under preparation [222, 227]. In a stacking approach, the authors look for neutrinos from solar flares data samples that contain γ-rays from pion-decays (see Equation 8.10). Several space-based mission study the Sun, among which NASA's Solar Dynamics Observatory (SDO) takes an important role by observing the solar atmosphere on small scales of space and time and in many wavelengths simultaneously [228]. Information provided by SDO that show the part of the Sun pointing toward Earth at the trigger time do not show significant activity in any filter.

Another space-based observatories that monitor the Sun's activity at all times is *STEREO*[4]. In this mission, two spacecrafts are orbiting the Sun taking images from separate positions and thus providing a stereoscopic picture of the Sun's activity at the moment. For the time under investigation, i.e. the SNDAQ trigger time at 2014-08-16 16:07:59, both spacecrafts were behind the Sun and taking data, as Figure 8.10 indicates.

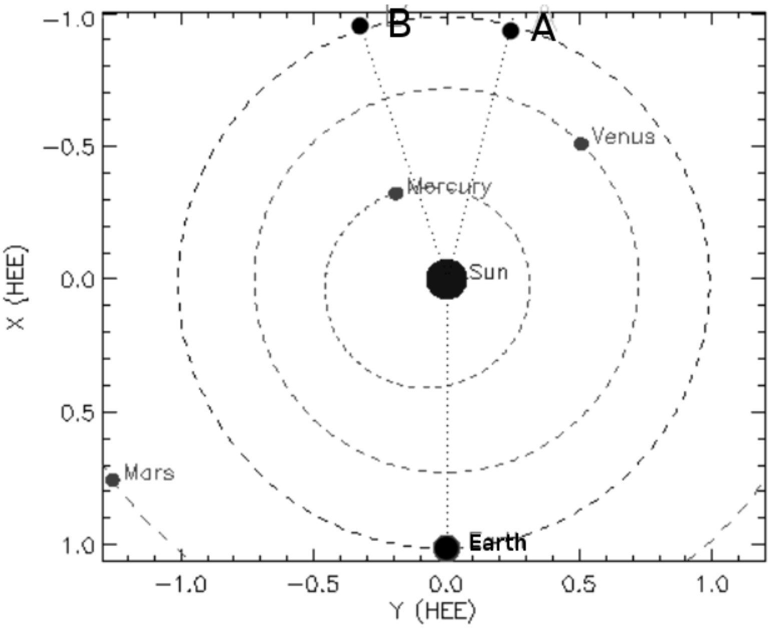

Figure 8.10: *Position of the STEREO spacecrafts A and B during 2014-08-16 [230].*

On August 16th 2014, there was no obvious flare activity observed by STEREO on the backside of the Sun. Nonetheless, coronal mass ejections are visible at the backside of the Sun, as shown in Figures 8.11 and 8.12. Since light emitted from the Sun takes about 8 min to reach Earth we focus our investigations of solar activity to time window prior to the supernova candidate trigger.

The hard γ-rays from the neutral pion-decay can be detected by the *Fermi* space mission especially its large area telescope (Fermi-LAT) [231]. A compiled list of events observed by Fermi-LAT is provided by the *Fermi Solar Flare Observations facility* [232]. This list is basis for tagging solar flares accompanied by gamma rays that are considered for analysis carried out by the authors of References [222, 227]. For the time of the supernova candidate trigger, no significant event was recorded by Fermi-LAT. The last remaining indication for solar flare activity, the detection of x-rays from the Sun, can be tested by investigating data from satellite systems like GOES[5]. The fact that solar flaring remained low during that day, as indicated by SDO, is supported by the x-ray flux measured by GOES that does not list any significant events during the time period in question [234], as shown in Figure 8.13.

All these investigations of solar activity around the time period of the supernova candidate trigger of August 16th 2014 support the statement that the trigger is unlikely to be caused by a solar flare. Although there was a CME happening it was located at the backside of the Sun and thus unlikely to produce a signal pointing towards us and triggering the supernova system. In the scope of an ongoing search for solar flare neutrinos in IceCube [222, 227] it will be proven if solar flare neutrinos are detectable in IceCube in general and if they are

---

[4] Solar TEresstrial RElations Observatory [229]

[5] Geostationary Operational Environmental Satellite [233]

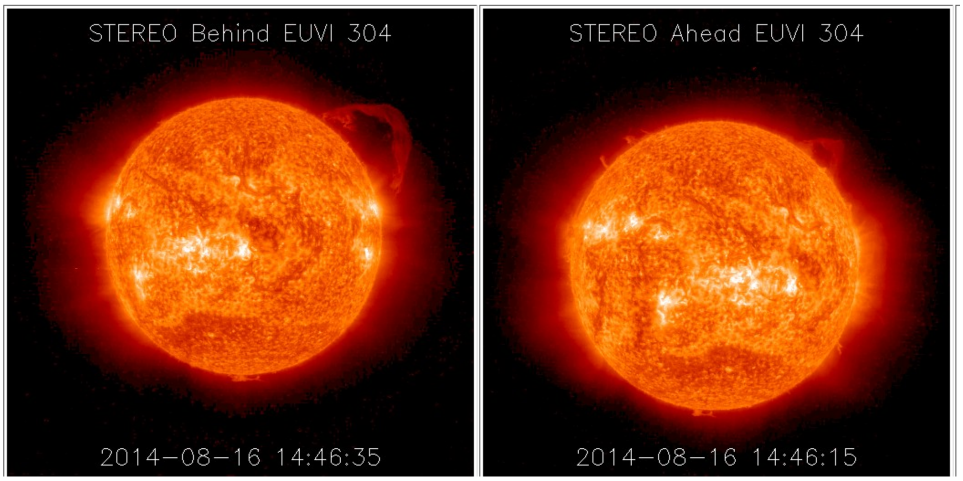
STEREO Behind EUVI 304
2014–08–16 14:46:35
STEREO Ahead EUVI 304
2014–08–16 14:46:15

Figure 8.11: *Pictures of the Sun taken by STEREO spacecrafts A and B more than one hour before our candidate [230].*

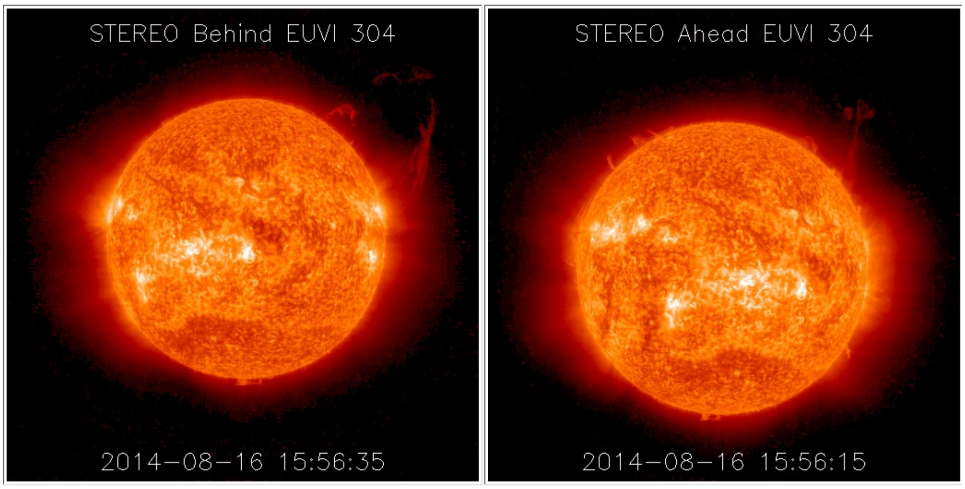
STEREO Behind EUVI 304
2014–08–16 15:56:35
STEREO Ahead EUVI 304
2014–08–16 15:56:15

Figure 8.12: *Pictures of the Sun taken by STEREO spacecrafts A and B eleven minutes prior to our supernova candidate trigger [230]. The CME is visible in the upper right corner of all pictures.*

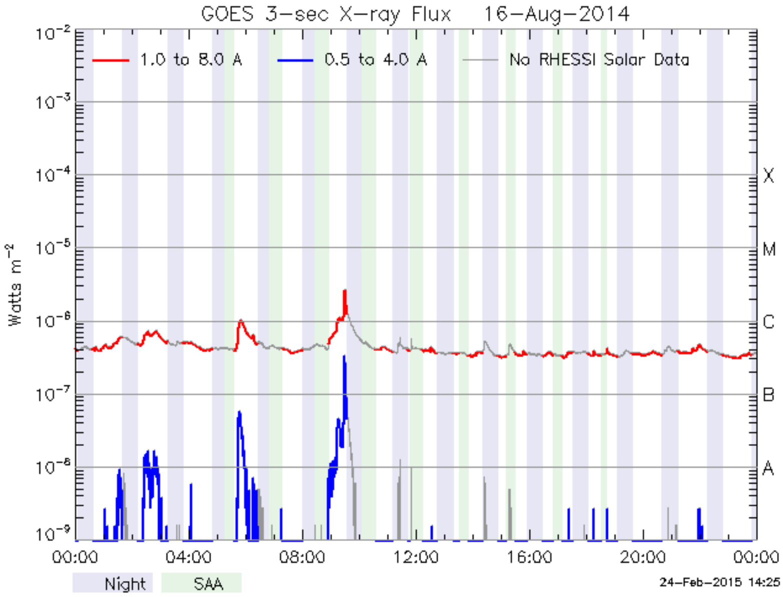

Figure 8.13: *X-ray flus observed by GOES [235].*

able to produce false positive triggers in the supernova system in particular.

9

Conclusions and Outlook

The aim of this work was to introduce the new raw data stream of IceCube, *called* HitSpool, *and to present various studies performed with this new data that are of relevance for the detection of neutrino from galactic core-collapse supernovae. A* HitSpool Interface *was designed, tested and implemented in order to collect* HitSpool *data from all DOMs by receiving requests from any DAQ subsystem, with the supernova system being the primary client.* HitSpool *data was used to investigate the noise characteristics of the detector as well as to identify triggering and subthreshold hits from atmospheric muons which is of particular interest for the supernova search in* IceCube. *The first part of this chapter summarizes the work presented in this thesis whereas the second section is dedicated to introduce ideas for analyses where* HitSpool *data can be of benefit and the role of* HitSpool *in future experiments.*

9.1 Summary of Results

The first part of this thesis introduced the theoretical background of neutrinos in particle physics in its first chapter and the astrophysical phenomenon of supernovae in the second chapter. The interaction of low energy neutrinos in ice and their detection were followed by an extensive review of the state-of-the-art knowledge about the mechanism of core-collapse supernovae in order to explain the interest in detecting neutrinos from this most violent and spectacular events in the universe. In the second part of this work, we have described in detail the working principle of the IceCube detector in general and its supernova data acquisition system in particular to demonstrate the physics capabilities resulting from an observation of a supernova signal. A special emphasis was given to the explanation of the various DAQ system to prepare the ground for the introduction of HitSpool data and the HitSpool Interface. Motivated by the goal to gain as much information as possible from the detector in case of a galactic supernova, raw data is continuously buffered. The mechanism of the interface is explained to show the reliability of the system. Additionally, we discussed the developed data processing in various data formats in order to provide the proof of concept for HitSpool data being available for higher level analysis. Due to the supernova detection principle in IceCube, a profound understanding of the detector's background is essential. HitSpool data helps in many ways to improve our knowledge about the instruments' noise. The detailed study of a high statistics data sample confirmed that the hits of the non-thermal dark noise component in a DOM appear in bursts with an average rate of $\sim 150\,\mathrm{Hz}$ containing on average 4 hits. A special characteristic of the burst is the inner-interval time distribution which shows that later hits in the bursts are further apart in time. This could be the key for finally understanding the underlying processes of this mysterious noise component that is thought to be originating from radioactive decay but a final proof is still missing. Furthermore, the influence of atmospheric muons which contaminate a possible supernova signal was investigated under various aspects. With the help of simulation data, we were able to quantify and characterize the contribution of subthreshold atmospheric muons which do not create enough hits in the detector to cause a trigger. We learned that although only 45 % of the atmospheric muons passing the detector actually cause a trigger, they are responsible for the majority of hits with physical origin (1.1 %) and are distributed all over the detector. The remaining 55 % of muons passes the detector without being noticed by the trigger system and contribute 0.3 % to the total hit rate. This is due to the fact that the majority (27 %) of subthreshold muons creates exactly one SLC hit in the detector. Subtrigger muon hits are mostly distributed at the outer layers the detector. This gave rise to the assumption that the subtrigger muons consist of a combination of muons stopping in the mantle of the detector and of those passing by in the vicinity of the detector whose Cherenkov light is still being caught by the DOMs due to the long attenuation length.

In order to identify subthreshold muons without a-priori information from simulation, we identified and developed data processing tools that categorize hit clusters in the detector to be either caused by subtrigger atmospheric muons or rather originating from random noise. The event splitting algorithms, on which the tool chain is based, have the potential to identify hits from $\sim 58\,\%$ of all subtrigger muons while registering over 99 % of the triggering muons at the same time. The final efficiency of identifying atmospheric muons, without a-priori knowledge about the origin of the hit cluster, is $\sim 80\,\%$ in total whereas hit clusters with representations in triggers have a higher efficiency ($\sim 93\,\%$) than clusters containing subtrigger muon hits ($\sim 77\,\%$). The contribution from pure noise hit clusters to the final muon candidate hit sample is less than 5 %. The effect of the application of muon identification to HitSpool data was studied with respect to the resulting hit rates in IceCube. Hit clusters that are not only categorized to be potential muon candidates but also include trigger forming hits represent 1.8 % of the total hit rate. The subtraction of all subtrigger muon hit candidates results in an additional reduction of the hit rate of about 1.4 %. The resulting ratio of subtrigger to triggering muon hits is a factor two above the expectation from simulations which was identified to be caused by the cluster purity that cuts into the noise level but is still acceptable when considering the fact that maximal 45 % of all subtrigger muons can be identified in this way.

The benefit of the knowledge about subthreshold muons in IceCube with respect to the supernova neutrino detection was presented in the final chapter of this thesis. We were able to demonstrate the feasibility of processing HitSpool data to SNDAQ type data by presenting various lightcurves, i.e. the hit distribution in various binnings for an exemplary supernova candidate trigger. HitSpool data provides a unique look at the lightcurve since the limitation of SNDAQ's 2 ms is overcome. Including all information from tagging trigger as well as subthreshold muon hits, we learned that the standard deviation of the lightcurve of a supernova candidate trigger decreases by 30 % when subtracting trigger hits compared to the lightcurve of scalers to which only an internal deadtime has been applied. Furthermore, the expansion from considering only SMT8 trigger hits to including any in-ice trigger type hit, does not have a huge impact on the lightcurves since only a 0.5 % decrease in the standard deviation is visible. Not only the processing of HitSpool data to global scalers was provided but also the extraction of scalers for each individual DOM was developed in order to perform the corresponding likelihood analysis with HitSpool data as it is done with SNDAQ scalers. From a total of 28 sets of HitSpool data around supernova candidate triggers collected with the HitSpool Interface during almost two years we calculated the significance in various binnings and using different amounts of available HitSpool data. Due to the limited amount of data collected, $[-30\,\mathrm{s}, +60\,\mathrm{s}]$ around the trigger time, the standard 4 s and 10 s re-binnings of the data doe not provide reliable results. Only one supernova candidate, reported in 500 ms, remained significant after applying all described correction regarding atmospheric muon subtraction. Due to the fact that no other supernova neutrino experiment registered a similar event at the trigger time reported we investigated solar activity as a potential explanation for the enhanced hit rate. Although there was visible activity close to the supernova trigger, it happened at the back of the sun and is not conclusive enough to link any solar flare neutrino production to the event seen. Future investigations have to show if solar flares at all produce a detectable neutrino signal in the IceCube detector.

9.2 Outlook

The HitSpool concept is not only useful for the studies presented in this thesis. The following is a summary of possible fields of research that could benefit from HitSpool data in the future or are already exploiting information provided by HitSpool.

9.2.1 Supernova Characteristics

The analyses presented in this thesis regarding an improvement to IceCube's supernova detection system are only the beginning of possible studies with HitSpool data in this field of research. The following presents a short overview of potential topics.

Short Time Scale Phenomena

We have seen in Chapter 2 that modern simulations of core-collapse supernovae predict phenomena like *SASI* and *LESA* that result in effects lasting on time scales of $\mathcal{O}(100\,\mathrm{ms})$. Studying signals from these supernova internal properties (as done in Chapter 4) is predestined to happen with HitSpool data due to its unlimited fine time-structure. However, in order to predict such a signal in IceCube the corresponding models still need to be implemented in the simulation framework. Due to recent progress in the development of supernova related simulation [172] we are optimistic that this can be feasible in the near future.

Supernova Neutrino Energy Estimation

The track length and thus the probability to detect a photon from a supernova neutrino interaction in the ice increases with the energy. Therefore the probability to detect light from a single interaction in multiple DOMs also rises with the neutrino energy. A recently developed method [236] takes advantage of the HitSpool data stream by investigating coincident hits in one, two and three DOMs in a time-window of 150 ns and a spatial distance up to next-to-next neighboring DOMs on next-to-nearby strings[1]. The various hit patterns are sensitive to different regions of the energy spectrum depending on the patterns geometry [237]. Evaluating the ratio of, e.g. the two-fold nearest-neighbor DOM hit rate over the single DOM hit rate, one obtains an energy dependent observable. Assuming a specific shape of the neutrino spectrum, this observable can be used to determine the absolute energy scale of the spectrum, i.e. determine the mean neutrino energy [238]. It is expected that this method puts a lower bound of 30 % on the energy resolution for a core-collapse supernova at 10 kpc. For other models with heavier stars and harder neutrino spectra this resolution will improve. It is planned for the near future to test this algorithm on HitSpool data.

9.2.2 Fast Radio Bursts

A fast radio burst (FRBs) is a recent discovery that reveals itself in a short transient radio pulse, lasting only a few milliseconds at any given frequency with a large dispersion measurements, i.e. declining in frequency in a characteristic fashion [239]. FRB were seen in data by the Parkes radio telescope [239] and the Arecibo observatory [240]. In total, eleven FRBs have been detected so far whose physical nature and progenitors are still a mystery. Among the possible explanations for this phenomenon are collapsing neutron stars [241, 242] or evaporating black holes [243] which could produce neutrinos along with the radio burst. Given the case that energy and spectrum of the neutrinos are within detection range of IceCube we would be able to see a signal. The efforts undertaken so far in IceCube to search for low energy neutrinos from FRBs include the SNDAQ scaler data stream in its 500 ms binning and using the same likelihood method as performed for the supernova candidate significance calculation. Due to the estimated rate of FRBs, $1 \times 10^5\,\mathrm{d}^{-1}$, a background window of 10 s is chosen. HitSpool data is predestined for such an analysis since the required data is very short lasting and substructure might be lost in the SNDAQ data that can be recovered from HitSpool data that has the additional benefit of subtrigger atmospheric muon tagging.

9.2.3 Dark Matter

Boosted Dark Matter

Triggered by the recent discovery of astrophysical neutrino in IceCube [8, 244], lots of different theoretical explanations for the observed excess were given by the scientific community. An outstanding scenario is the concept of *boosted dark matter* [245] to explain the events in IceCube by the recoil of dark decay products of heavy ($\mathcal{O}(4\,\mathrm{PeV})$) dark matter particles that scatter off nuclei in the detector resulting in a purely hadronic shower. The track-like signature of events is also covered in the model by predicting a secondary population of events in the regime $\mathcal{O}(100\,\mathrm{TeV})$ originating from a 3-body decay of the primary scalar dark matter particle which also produces neutrinos. The analysis methods that resulted in IceCube's discovery are now implemented in the online data stream in the framework of a standard data filter. Combining this filter with HitSpool data requests in order to access all information available in the case of a next event should help us in finally uncovering the sources of these unique observations.

---

[1] These hits are not available in the standard supernova data stream due to the internal deadtime of 250 µs on each DOM

Molecular Excitations by Dark Matter

Using HitSpool data for dark matter searches is not only motivated by the above described scenario of heavy dark matter particles but also by light weakly interacting massive particles (WIMPs). The basis for this assumption is the fact that light WIMPs excite hydroxide molecules while traversing the Antarctic ice [246]. With a minimal energy for excitation of 2 eV and a well understood absorption spectrum of molecular hydroxide, the relaxation of these absorption peaks can be detected by photomultipliers sensitive in a wavelength range from ~ 400 nm to ~ 740 nm. Since we do not expect these light WIMPs do interact more than once, a counting experiment as it is performed for the supernova detection could be established based on HitSpool data. Motivated by a seasonal depending WIMP flux (e.g. [247]), investigating the variations of the resulting WIMP significance would be an exciting analysis.

Part IV

Appendix

A

HitSpool Data Format

This is a description of the several HitSpool *data formats used in the analysis part of the thesis. The first section gives an overview of the* HitSpool *data treatment in* IceTray *where the main processing takes place and on which the muon analysis is based (see Chapter 7). The second part describes the data structure of scalers from* HitSpool *data which is the basis of the analysis performed for supernova neutrino detection in Chapter 8.*

IceTray Format

During the course of this thesis a HitSpool data processing chain was identified and developed that allows the production of high level analysis data. Data treatment is performed in the order presented in Table A.1. The naming scheme for the processing levels is chosen according to the standard data processing chain where level 0 denotes the triggered and filtered data coming from the detector and level 2 is usually the starting point for all analysis working groups for their specified analysis goals.

Table A.1: HitSpool *data processing from raw data to final level*

Level	Details
L−2	HitSpool raw data
L−1	Transforms raw binary data in IceTray objects (I3DOMLaunches)
L0	Waveform calibration, waveform feature extraction, trigger application
L 1	trigger hit tagging
L2	Muon Identification as described in Section 5.3
L2’	Primary mapping, only applied in simulation data
L3	Results extraction to hit tables

Level -2

The easiest way to visualize a raw data binary hit is by dumping the content of its delta compressed header to ASCII format. A basic script for producing this output is `dumpiva.py` [248]. By providing a HitSpool data file as input, one retrieves a human readable output of which each line holds a hit with several fields of information that are explained in table A.2 and more details can be found in [197].

Table A.2: *Basic hit output of* HitSpool *data. The field names are listed in order of output.*

Field Name	Details
domid	Position of DOM in which the hit occurred. Example: $23-34$, for DOM 34 on string 23.
timestamp	Timestamp of the hit in 0.1 ns from beginning of current year.
LC flag	Information about hit being SLC or HLC. Values: $0 =$ SLC, $1 =$ HLC hit with partner hit below, $2 =$ HLC hit with partner hit above, $2 =$ HLC hit with partner hit above and below
MinBias	Hit is present in Minimum Bias trigger (1) or not (0).
Trigger word	The lower 12 bits of the 16 bit raw data Trigger Word.
DigInfo	Digitization information: $F =$ fADC, $A =$ATWD A, $B =$ATWD B, $- =$ no digitization nor readout
Charge	sample of entries in fADC around peak value and the peak position (pos, peak-1, peak, peak+1)
size	data size of the hit in bits. Size is 12 bit if its a SLC hit and only the delta compressed header is stored

Level -1

The basic module for transforming raw HitSpool data to IceTray objects is `hitspool-reader` as documented in [249]. Since HitSpool data is recorded before online triggers are applied, there is no default sub-structure, i.e. events in the data. Several options are available to split the raw data stream into short, usually $mathcalO(10\,\mu s)$, data packets in order to be easily processed by the following modules. The module converts raw hits into *DOMLaunches* that have basically the same attributes as shown in Table A.2. The `hitspool-reader` module is embedded in the `HitSpoolReader.py` script [250] that was developed for this first processing step. In order to ensure a reliable and fast processing, a HitSpool data set is divided into multiple sub-sets of maximal /(10 s) per file.

Level 0 and Level 1

In this level of processing, the basic waveform treatments are applied, see Section 3.4. Since HitSpool data is untriggered data, we also need to apply trigger conditions in order to retrieve the correct data format (*RecoPulses*) for further processing by standard modules. Recopulses have additional attributes compared to DOMLaunches, as the reconstructed charge and width of the waveform resulting from the hit. Since in the standard module for offline trigger application (`trigger-sim`), no bookkeeping for trigger causing hits is performed, we need to re-apply the trigger conditions for doing so. All this is done in `HitSpoolTrigger.py` in [250].

Level 2

The processing details for mun identification are already covered in detail in Section 5.3. The production script `HitSpoolSubTrigger.py` is provided in [250].

Level 2'

Simulation data has the additional advantage over experimental data in the fact that we can access the a-priori information about the origin of a hit via pulse mapping (see Chapter 7). Production scripts for that are deposited in [251].

Level 3

After using the benefits of ICETRAY to process the data, we extract the needed information and store the result in hit tables which are based on the *hierarchical data format* (HDF5) and are independent of ICETRAY. This data format is convenient since it supports large data samples and allows fast and parallel access. The attributes of every hit stored in the hit tables are summarized in Table A.3. The output is produced with `HsHitTableH5WriterSorter.py`, documented in [252].

Table A.3: *Final hit information after muon identification stored in HDF5 hit tables.*

Field Name	Details
domstring	String number of the DOM
dompos	DOM position on string
timestamp	Timestamp of the hit in 1 ns from beginning of current year.
lc	Boolean value for hit being HLC (True) or SLC (False).
hive	Boolean value for hit being part of a hit cluster by HiveSplitter.
hive_ne	Boolean value of NoiseEngine if hit being part of a hit cluster by HiveSplitter.
srttopo	Boolean value for hit being part of a hit cluster by TopologicalSplitter.
srttopo_ne	Boolean value of NoiseEngine if hit being part of a hit cluster by TopologicalSplitter.
muon	Boolean value representing: (hive is True AND hive_ne is True) OR (srttopo is True AND srttopo_ne is True).
smt3	Boolean value for hit being part of an SMT3 trigger.
smt8	Boolean value for hit being part of an SMT8 trigger.
voltrig	Boolean value for hit being part of a Volume trigger.
strtrig	Boolean value for hit being part of a String trigger.

This information is the basis of the results reported in Section 7.3.

Scaler Format

Scalers are extracted from HITSPOOL data that is processed in the way described above (level −2 until level 3). They are structure in two groups defined by the purpose they serve. Again, we chose the HDF5 data structure to store all values. In order to produce lightcurves, we need the summed hit rates of the detector of the various scaler groups (similar to Table 8.1). The

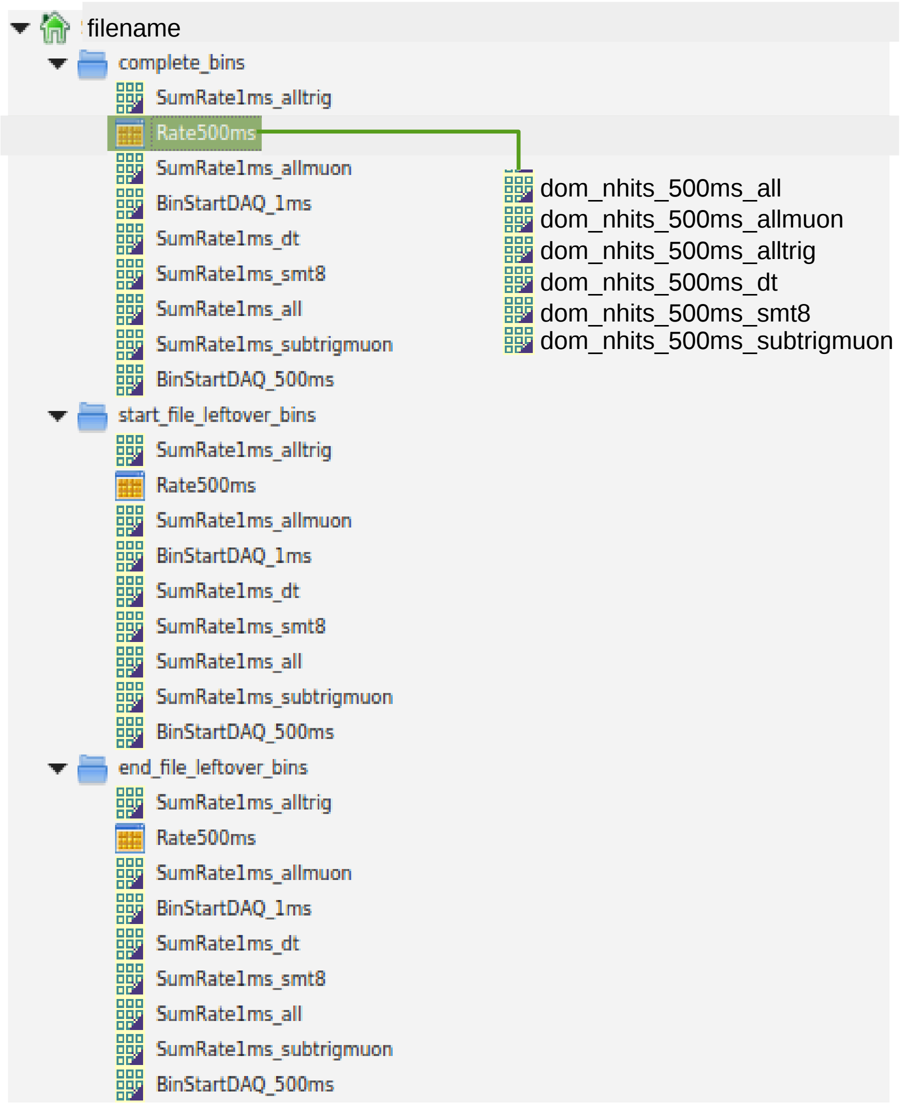

- filename
  - complete_bins
    - SumRate1ms_alltrig
    - Rate500ms
      - dom_nhits_500ms_all
      - dom_nhits_500ms_allmuon
      - dom_nhits_500ms_alltrig
      - dom_nhits_500ms_dt
      - dom_nhits_500ms_smt8
      - dom_nhits_500ms_subtrigmuon
    - SumRate1ms_allmuon
    - BinStartDAQ_1ms
    - SumRate1ms_dt
    - SumRate1ms_smt8
    - SumRate1ms_all
    - SumRate1ms_subtrigmuon
    - BinStartDAQ_500ms
  - start_file_leftover_bins
    - SumRate1ms_alltrig
    - Rate500ms
    - SumRate1ms_allmuon
    - BinStartDAQ_1ms
    - SumRate1ms_dt
    - SumRate1ms_smt8
    - SumRate1ms_all
    - SumRate1ms_subtrigmuon
    - BinStartDAQ_500ms
  - end_file_leftover_bins
    - SumRate1ms_alltrig
    - Rate500ms
    - SumRate1ms_allmuon
    - BinStartDAQ_1ms
    - SumRate1ms_dt
    - SumRate1ms_smt8
    - SumRate1ms_all
    - SumRate1ms_subtrigmuon
    - BinStartDAQ_500ms

Figure A.1: *Display of the data tree of scalers extracted from* HITSPOOL *data and stored in HDF5 tables.*

summed scalers are stores in a resolution of 1 ms from which all re-binnings (2 ms, 500 ms, 1.5 s, 4 s, 10 s) are obtained. The individual rates of each DOM needed for the significance calculation are stored in a separate group in 500 ms bin size and are the basis for all further re-binnings. Since a HITSPOOL data set from supernova candidate trigger is processed in multiple sub-sets, fractional bins from the file start and file end have to be accounted for in separate groups. Figure A.1 shows a the data structure of such a data file with the individual fields explained in Table A.4.

Table A.4: *Explanations for field names of scaler tables extracted form* HitSpool *data.*

Field Name	Details
complete_bins	Group of complete bin of 500 ms individual DOM scalers and 2 ms summed scalers in file.
start_file_leftover_bins	Group of fraction bin from file start of 500 ms individual DOM scalers and 2 ms summed scalers in file.
end_file_left_over_bins	Group of fraction bin from file end of 500 ms individual DOM scalers and 2 ms summed scalers in file.
Rate500ms	Group of 500 ms scalers.
dom_nhits_500ms_all	Data set of all individual (5160 entries) 500 ms hits.
dom_nhits_500ms_allmuon	Data set of all individual (5160 entries) 500 ms hits that are muon candidates.
dom_nhits_500ms_alltrig	Data set of all individual (5160 entries) 500 ms hits from triggers.
dom_nhits_500ms_dt	Data set of all individual (5160 entries) 500 ms hits that passed the 247.5 µs deadtime.
dom_nhits_500ms_smt8	Data set of all individual (5160 entries) 500 ms hits from SMT8 triggers.
dom_nhits_500ms_subtrigmuon	Data set of all individual (5160 entries) 500 ms hits that are subtrigger muon candidates.
SumRate1ms_all	Data set of all summed 1 ms hits.
SumRate1ms_allmuon	Data set of summed 1 ms hits that are muon candidates.
SumRate1ms_alltrig	Data set of summed 1 ms hits from triggers.
SumRate1ms_dt	Data set of summed 1 ms hits that passed the 247.5 µs deadtime.
SumRate1ms_smt8	Data set of summed 1 ms hits from SMT8 triggers.
SumRate1ms_subtrigmuon	Data set of summed 1 ms hits that are subtrigger muon candidates.
BinStartDAQ_1ms	timestamp of bin start.
BinStartDAQ_500ms	timestamp of bin start.

B

HitSpool Interface Operation Manual

Installation

The HitSpool Interface is a project in the software repository of IceCube dedicated to DAQ `http://code.icecube.wisc.edu/daq/projects/hitspool/`. Although the primary installation location is foreseen to be at the South Pole System (SPS), it also tuns on any local host or the dedicated test system (SPTS). Besides ZeroMQ (version ≥ 4.0) and Fabric (≥ 1.4) no extra libraries need to be installed since all others are standard modules in python ($\geq 1.7.3$).

The following describes the installation and operation on SPS. The code should be checked out on the sps-access machine:

```
$ cd /home/pdaq/HsInterface/
$ svn co http://code.icecube.wisc.edu/daq/projects/hitspool/trunk
    trunk/
```

Operation

Fabric Script

The projects contains a `fabfile` that controls all sub-function of the individual components of the interface. A listing of all available function of the fabric script is displayed on the command line via:

```
$ cd /home/pdaq/HsInterface/trunk/
$ fab -l
```

The most important command are explained in the following.

Deploy & Start the Interface

The most common scenario is the deployment of the software to the system and to (re-)start the interface for any changes made in the code to become effective:

```
$ fab hs_deploy
$ fab hs_start
```

In the first step, the interface is deployd to all inice and icetop DOMHubs, as well as to the machines hosting the SecondaryBuilder (2ndbuild) and the ExperimentControl (expcont). The installation directory of the interface on these machines is `/mnt/data/pdaqlocal/HsInterface/trunk/`.

The `fab hs_start` command stops any possible running components before initiating the restart. After that, the crontabs for the HsWatcher as initialized.

Interface components can be starting individually as well by providing the hostname `<host>` with the following commands:

```
$ hs_start_pub_bkg:<host>
$ hs_start_sender_bkg:<host>
$ hs_start_worker_bkg:<host>
```

Check Status

The status of the interface, running and stopped components, can be queried by issuing:

```
$ fab hs_status
```

which returns a summary of stopped and running components at the time. This command is also issued periodically in a cronjob with the results reported to I3Live. It can be checked on the monitoring webpage, as shown in Figure B.1.

Stop Components

Stopping the interface can be done via :

```
$ fab hs_stopf
```

In order to stop the entire interface. Components can be stopped depending on the service by the following commands :

```
$ hs_stop_all_workers
$ hs_stop_pub
$ hs_stop_sender
```

or individually, e.g. for services on string 21:

```
$ hs_stop_watcher_on_host:ichub21
$ hs_stop_worker_on_host:ichub21
```

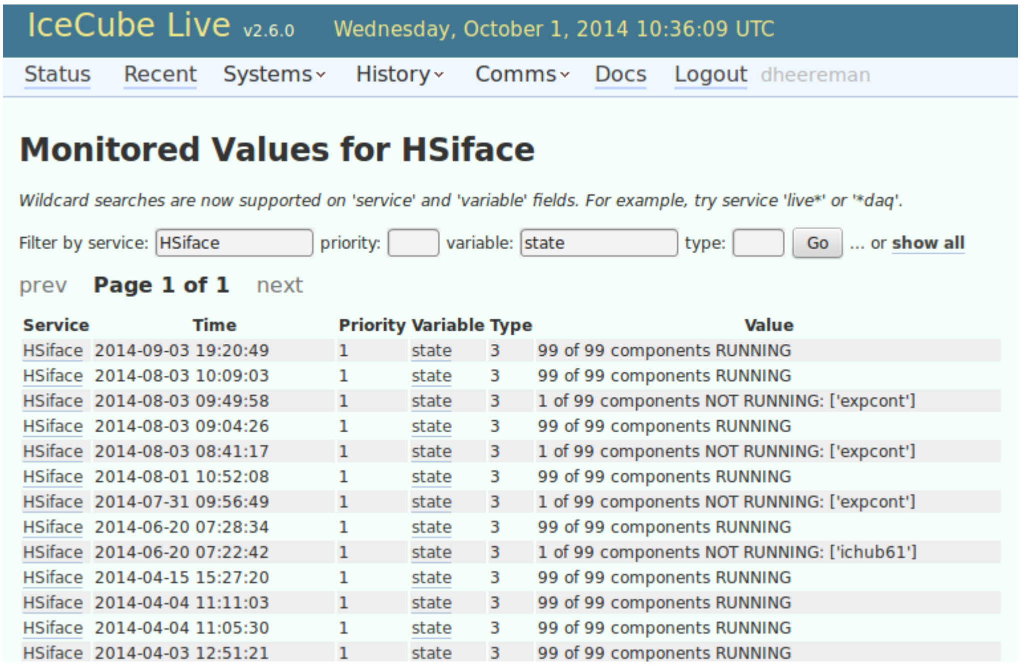

IceCube Live v2.6.0 Wednesday, October 1, 2014 10:36:09 UTC

Monitored Values for HSiface

Wildcard searches are now supported on 'service' and 'variable' fields. For example, try service 'live' or '*daq'.*

Filter by service: HSiface priority: variable: state type: ... or **show all**

Page 1 of 1

Service	Time	Priority	Variable	Type	Value
HSiface	2014-09-03 19:20:49	1	state	3	99 of 99 components RUNNING
HSiface	2014-08-03 10:09:03	1	state	3	99 of 99 components RUNNING
HSiface	2014-08-03 09:49:58	1	state	3	1 of 99 components NOT RUNNING: ['expcont']
HSiface	2014-08-03 09:04:26	1	state	3	99 of 99 components RUNNING
HSiface	2014-08-03 08:41:17	1	state	3	1 of 99 components NOT RUNNING: ['expcont']
HSiface	2014-08-01 10:52:08	1	state	3	99 of 99 components RUNNING
HSiface	2014-07-31 09:56:49	1	state	3	1 of 99 components NOT RUNNING: ['expcont']
HSiface	2014-06-20 07:28:34	1	state	3	99 of 99 components RUNNING
HSiface	2014-06-20 07:22:42	1	state	3	1 of 99 components NOT RUNNING: ['ichub61']
HSiface	2014-04-15 15:27:20	1	state	3	99 of 99 components RUNNING
HSiface	2014-04-04 11:11:03	1	state	3	99 of 99 components RUNNING
HSiface	2014-04-04 11:05:30	1	state	3	99 of 99 components RUNNING
HSiface	2014-04-03 12:51:21	1	state	3	99 of 99 components RUNNING

Figure B.1: *Snapshot of the I3Live monitoring webpage displaying status reports of the* HITSPOOL INTERFACE .

Primary Programs

Details of the ZeroMQ structure is given in Figure B.2.

HsPublisher

The `HsPublisher` can be started locally:

```
$ python HsPublisher.py
```

or via the fabric script as explained above. On SPS, the HsPublisher runs on `expcont` and binds a *REP* socket on port 55 557 and waits for arriving JSON messages. The messages can be send from anywhere via the HsGrabber or from the an SNDAQ internal client which is the default. The messages are handed over internally to a `PUB` socket, bind to port 55 561.

HsWorker

This is the work horse of the interface. It is running on every DOMHub, waiting from messages to be published by the HsPublisher. For now and because the only active HitSpool data requester is SNDAQ at the moment, the requested HitSpool files are store per hubs in folder by the following naming convention: `SNALERT_<trigger-timestamp>_<stringhubname>`

HsSender

This program collects service messages from HsWorkers. It is running on SecondaryBuilder with an option foreseen to be implemented in order to make it less independent from the host. Furthermore, it is responsible for sending the HitSpool data over satellite to the data warehouse in the northern hemisphere.

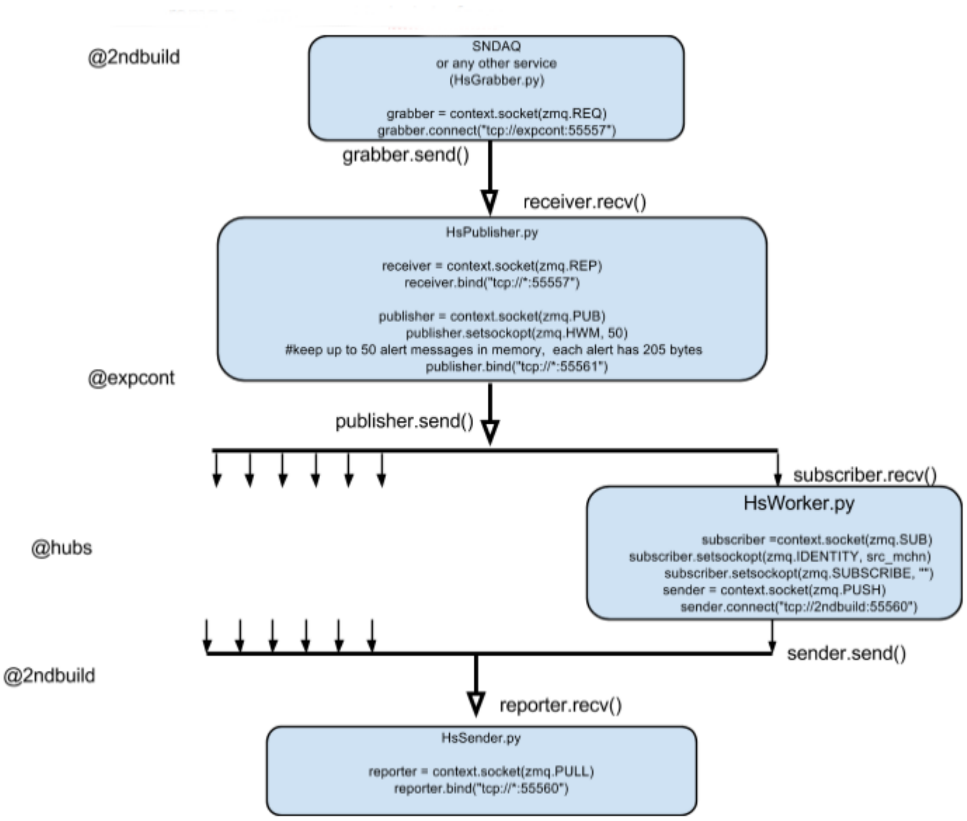

@2ndbuild
SNDAQ
or any other service
(HsGrabber.py)
grabber.send()
receiver.recv()
HsPublisher.py
@expcont
publisher.send()
subscriber.recv()
HsWorker.py
@hubs
sender.send()
@2ndbuild
reporter.recv()
HsSender.py

```
grabber = context.socket(zmq.REQ)
grabber.connect("tcp://expcont:55557")
```

```
receiver = context.socket(zmq.REP)
receiver.bind("tcp://*:55557")

publisher = context.socket(zmq.PUB)
publisher.setsockopt(zmq.HWM, 50)
#keep up to 50 alert messages in memory,  each alert has 205 bytes
publisher.bind("tcp://*:55561")
```

```
subscriber =context.socket(zmq.SUB)
subscriber.setsockopt(zmq.IDENTITY, src_mchn)
subscriber.setsockopt(zmq.SUBSCRIBE, "")
sender = context.socket(zmq.PUSH)
sender.connect("tcp://2ndbuild:55560")
```

```
reporter = context.socket(zmq.PULL)
reporter.bind("tcp://*:55560")
```

Figure B.2: *Details of the ZeroMQ patterns used in the* HITSPOOL INTERFACE .

Secondary Programs

Besides the `HsWorker`, `HsPublisher` and `HsSender` code was developed that ensures the stable operation of the interface and eases the handling of HitSpool data requests received from other systems than SNDAQ.

HsWatcher

Cronjobs execute the `HsWatcher` script once every hour. Depending on the machine on which the `HsWatcher` is executed, it looks for running instances of `HsWorker` (on hubs), `HsPublisher` (on expcont) or `HsSender` programs and will restart them if necessary. For any change in the status of the watched program, either from *stopped* to *running* or vice-versa, the `HsWatcher` send out emails to the interface maintainer as well as to the SNDAQ developers mailinglist.

Individual HitSpool Data Requests: HsGrabber

A powerful and easy to use tool is the `HsGrabber` that can be issued from every machine, preferably on access:

```
 $ python HsGrabber -h
   usage :: HsGrabber.py [options]
           -b         | begin of data: YYYY-mm-dd HH:MM:SS.[us] OR
              SNDAQ timestamp [ns from Jan 1st]
           -e         | end of data YYYY-mm-dd HH:MM:SS.[us]    OR
              SNDAQ timestamp [ns from Jan 1st]
           -c         | copydir e.g. "pdaq@2ndbuild:/mnt/data/
              pdaqlocal/HsDataCopy/"
           HsGrabber reads UTC timestamps or SNDAQ timestamps.
           It sends SNDAQ timestamps to HsInterface (HsPublisher).
```

With providing the necessary flags, the HsGrabber send a HitSpool data request to the Publisher service, just like the SNDAQ integrated request, and forwards it to all running hubs. The HsGrabber accepts timestamps in UTC format and in SNDAQ format, i.e. nanoseconds from the beginning of the year. The desired destination for the HitSpool data has to be a directory on 2ndbuild.

HsSpader

If your HitSpool data was requested to be stored not i the default directory but anywhere else on 2ndbuild, it might not transferred over satellite automatically. The `HsSpader` python script takes care of that:

```
$ python HsSpader.py -h
  usage :: HsSpader.py [options]
           -i         | Input dir where hs data is located, e.g. /mnt
              /data/pdaqlocal/HsDataCopy/
           -p         | time pattern of HS data alert:<yyyymmdd>_<
              hhmmss> e.g. 20131101_045126
           -o         | Output directory: default is /mnt/data/
              HitSpool/
```

```
        -l          | logfile, e.g. to path HsSenders log: /mnt/
            data/pdaqlocal/HsInterface/logs/hssender_2ndbuild.sps.
            log
```

The timestamp of the HitSpool data request is carried on the directory naming scheme in the destination folder. So providing that timestamp in the form `yyyymmdd_hhmmss` is enough for the HsSpader to find that data and to put in the satellite transfer queue.

Monitoring and Logging

Individual Logging Log files are generated by every service and are stored a corresponding logfile directory on every host at
`/mnt/data/pdaqlocal/HsInterface/logs/`. Additionally, every HsWorker sends its log file report to `2ndbuild` after a HitSpool data transfer is completed. The logfiles are summarizes in
`/mnt/data/pdaqlocal/HsInterface/logs/workers/`.

List of Figures

1.1 Feynman diagrams for charged current (CC, left) and neutral current (NC, right) neutrino interactions [14]. 8

1.2 Combined measurement of the hadronic production cross section around Z^0 mass as obtained by the LEP experiments OPAL, DELPHI, L3 and ALEPH. The data is best fit by the prediction arising from three (light) neutrino species [15]. 9

1.3 Illustration of the configurations of neutrino mass splitting in the case of normal mass hierarchy and inverted mass hierarchy [14]. 12

1.4 Average energy $\langle E_{e^+} \rangle$ (blue and left axis) and cosine of the scattering angle $\langle \cos\theta_\mathrm{s} \rangle$ (red and right axis) for the resulting positron in the inverse β process of an anti-electron neutrino with energy $E_{\overline{\nu}_e}$ [52, 53]. 17

1.5 Normalized distributions for energies of $\overline{\nu}_e$ (black solid line) with mean energy $\langle E_\nu \rangle = 13\,\mathrm{MeV}$ and resulting positron (solid blue line) from inverse β-decay interactions [54]. Approximating the positron spectrum with a Gamma distribution gives the red dashed line. Assuming a naive IBD cross-section, ignoring recoil effects and the proton-neutron mass difference results in the black dashed line. 18

1.6 Total cross-section as a function of energy for most relevant interaction of low energy neutrinos in ice [52, 60, 61]. 19

1.7 Energy loss of positrons in ice normalized to the inverted density ($\mathrm{cm}^2\,\mathrm{g}^{-1}$) over the energy range of a few tens of MeV [74]. 22

1.8 Spherical wavelets (blue circles) of the diploe field created by a charged particle traveling with a velocity less (left panel) or greater (right panel) than the speed of light in that medium. An electromagnetic "shock" wave appears for $\beta c > c'$. Since in ice the index of refraction is almost independent of the wavelength, Cherenkov photons are emitted perpendicular to the wave front [75]. 23

1.9 Positron track length vs positron energy [65]. 24

1.10 Cherenkov photons vs positron energy [65]. 24

2.1 The Hertzsprung-Russell diagram on the left [87] shows stars with their luminosity (in units of solar luminosity) as a function of theirs surface temperature. The right plot shows a sub-region of the Hertzsprung-Russel diagram with evolutionary tracks for a selected set of initial masses of stars after their main sequence period [63, 87, 88]. The colored dashed lines show from the main sequence for different stellar mass regimes. 27

2.2 Shell-structure of a massive star. Transition regions between the layers are left out for simplicity. 29

2.3 Final fate of non-rotating stars depending on their initial mass (horizontal axis) and initial metallicity (vertical axis) [89]. As opposed to the straight limit at $9M_{\odot}$, more recent calculations [104] define the minimum mass of stars for ending in a CCSN to be about $8.3M_{\odot}$ and depending slightly on its metallicity. 32

2.4 Schematics of the evolution steps in a core-collapse supernova via the neutrino-driven delayed explosion mechanism. Nuclear composition and processes are indicated in the lower half of each panel whereas the upper half shows the direction of matter flow, indicated by arrows [94]. Detailed explanation is to be found in the text. 33

2.5 Schematic drawing of the neutrino light curve during the development of the stars core from collapse to neutron star [110]. Neutrino luminosity and time are shown in logarithmic scales. See text for details. 37

2.6 Expected supernova neutrino energy spectra associated to the supernova neutrino burst as modeled in [113], averaged in the time interval for shock-wave effects ($t > 2s$) with shape parameter $\alpha = 3$ as defined in the parametrization in equation 2.19 40

2.7 Expansion and contraction of the shock until the start of the explosion of a 15 $M_{\odot}$ star progenitor simulation. Radial position of the shock near the north and south poles as a function of post-bounce time. The color scheme reflects the entropy per nucleon of the stellar plasma, i.e. hotter region due to neutrino heating. Clearly visible are amplitudes of the quasi-periodic and bi-polar (i.e. g-mode) vibration of the matter due to the SASI [120]. 41

2.8 Snapshots from the evolution of supernova explosions in simulations from [120] for a non-rotating 11.2 $M_{\odot}$ in **(a)** and a rotating 15 $M_{\odot}$ model in **(b)**, respectively. The color coding represents the entropy of the stellar gas (where blue means less and red means stronger heated gas). The times displayed are post-bounce time stamps. 42

2.9 Illustration of the self-sustained lepton-emission asymmetry. See text for explanations. Taken from [122]. 44

2.10 Luminosity variations of a 11.2 $M_{\odot}$ progenitor for ν_e (black line), $\overline{\nu}_e$ (blue line) and ν_x ($x = \mu, \tau$) (red line) relative to the time-dependent average over all directions $\langle L \rangle$ [54]. The observer location is chosen such that the flux variation is largest. The strong dipole pattern of the ν_e and $\overline{\nu}_e$ is clearly visible. There is no SASI in this simulation. 46

2.11 Luminosity variations of a 27 $M_{\odot}$ progenitor for ν_e (black line), $\overline{\nu}_e$ (blue line) and ν_x ($x = \mu, \tau$) (red line) relative to the time-dependent average over all directions $\langle L \rangle$ [54]. The observer location is chosen to be approximately in the plane where SASI develops. LESA activity is clearly visible although the line of sight does not coincide with the LESA axis. 46

2.12 Supernova rate depending on the morphology of the galaxy [124]. Values of core-collapse SN for elliptic galaxy types (E/S0) are particularly small and not plotted. For type Ib/c: $SnM <$ 0.0093 and type II $SnM <$ 0.013, respectively. S0a/b and Sbc/s stands for spiral galaxy types and Irr for irregular morphology , following Hubbles classification. 47

2.13 Theoretical estimations of the rate of core-collapse supernovae in the Milky-way per century. References are partly mentioned in the text or can be find in [9] . . . 47

2.14 This Hubble Space Telescope image, taken in February 1994, shows the full system of three rings of glowing gas surrounding supernova 1987A [132]. . . 48

2.15 Energies of all events detected at 7:35 UT on February 23, 1987 versus time. $t = 0.0$ is set as the time of the first event of each signal observed. 49

2.16 First one-dimensional simulation of a supernova explosion from the onset of the collapse to 18 seconds after the core bounce. Neutrino luminosities and average energies are based on results from SN1987A whose progenitor is a main-sequence star of about $20M_\odot$ [113]. . . . 50

3.1 The IceCube Neutrino Observatory with its sub-array DeepCore and the air shower array IceTop. . . . 54

3.2 IceCube's top and side view. The origin of the x-y plane is set to the position of string 86. The vertical DOM position is shown on the right. DeepCore DOMs (black dots) are instrumented denser than DOMs on standard strings (blue dots) and elude the dust layer (gray band). . . . 54

3.3 Technical drawing of the DOM and its main hardware components on the left. The picture on the right shows the final of 5160 deployed DOMs. 55

3.4 Block-diagram of the DOM mainboard components [142]. A photon hits the photomultiplier, which is in the upper left. This signal is split to the ATWD and fADC. The entire readout is controlled by the FPGA. Details about the waveform digitization are given in the text. . . . 56

3.5 ATWD and fADC digitized waveforms of a PMT hit. The ATWD provides 3 amplification channels with the bin content being either 16×, 2× or 0.25× the original. . . . 58

3.6 IceCube Hit data flow diagram. Secondary data streams are omitted for simplicity. Thin lines indicate unidirectional data flow and thick lines stand for bi-directional communication. . . . 59

3.7 Diagram of the StringHub internals. . . . 60

3.8 Merge and Sort algorithm. . . . 61

3.9 The trigger system. Triggers and GloablTrigger. . . . 62

3.10 Schematic representations of the geometry settings used for triggering in IceCube. Based on the fundamental hit pair, i.e. a hit within $\pm 1\,\mu s$ in (at least) one next or next-to-next neighbor around a hit DOM (left panel), the volume trigger (central panel) looks for four HLC hits in a given volume whereas the string trigger is fulfilled in case of five HLC hits on a single string. 63

3.11 Secondary Builder and EventBuilder diagrams. . . . 64

3.12 Diagram of the control flow and its main components. The CnC server manages all control communications between the surface DAQ components and I3Live's control back end. Other sub-systems are directly connected to LiveControl and visualized via LiveView for the user. . . . 65

3.13 Examples of waveform unfolding for both simple and complex waveforms. The lines marked Best-fit are predictions of the various digitizer read-outs given the reconstructed PMT hits. For a perfect reconstruction, and with no noise in the data, these lines would exactly match within the digitizer step. The vertical lines with crosses at the top represent the times and amplitudes of the unfolded pulses relative to the right-hand axis [153]. 68

3.14 Sketch of an event with track-like topology on the left and the recorded light of a track-like event on the right with a reconstructed energy of ∼ 31 TeV and an angular resolution better than 1.2° [8]. 69

3.15 Sketch of an event with cascade-like topology on the left and the recorded light of a cascade-like event on the right with a reconstructed energy of ∼ 130 TeV and an angular resolution of ∼ 8° [8]. 69

4.1 Time range in the SNDAQ real-time analysis. A time-window of ±5 min around the analysis bin at t_0, surrounded by two exclusion zones of maximum 15 s, moves in steps of the smallest bin size (500 ms) and independently of the analysis bin size (0.5 s, 1.5 s, 4 s and 10 s). 73

4.2 Significance distribution as measured by SNDAQ without (blue line) and with (shaded gray) subtraction of triggered atmospheric muons for data taken from April 2008 to May 2011 (significances above 6 standard deviations are kept blind). The expectation from Poisson is given in green [159]. 75

4.3 Snapshot of SNDAQ latency taken from I3Live webpage. Clearly visible are the spikes at the start and end of one run unit (8 hr). 76

4.4 Effective absorption length for photons of $\lambda = 400$ nm as a function of depth in ice from AHA [165] and SpiceMie [166] model, respectively. 77

4.5 Effective scattering length for photons of $\lambda = 400$ nm as a function of depth in ice from AHA [165] and SpiceMie [166] model, respectively. 77

4.6 Effective positron volume as a function of depth in ice from AHA [165] and SpiceMie [166] model, respectively. The notation 'InIce' stands for standard DOMs with qunatum efficiency $\epsilon = 1$ whereas DeepCore DOMs have high quantum efficiency of $\epsilon = 1.35$ on average. Credit: [172]. 79

4.7 Lawrence-Livermore (20 $\mathrm{M}_\odot$) and Garching O-Ne-Mg (8.8 $\mathrm{M}_\odot$) compared. . 81

4.8 Expected detector response of IceCube for a supernova according to the Lawrence-Livermore model [113]. The DOM hit rate in 20 ms is shown as a function of time in double logarithmic scale. The new simulation framework *sni3sim* gives on average a 40 % higher signal than the *USSR*. Credit: [172] . 82

4.9 Expected detector response of IceCube for a supernova according to the Garching O-Ne-Mg model [105]. The DOM hit rate in 20 ms is shown as a function of time in double logarithmic scale. The new simulation framework *sni3sim* gives on average a 40 % higher signal than the *USSR*. [172] 82

4.10 Expected rate distribution at 10 kpc supernova distance for oscillation scenarios A (normal hierarchy) and B (inverted hierarchy). Fluxes and energies in the left panel are taken from the Lawrence-Livermore model and in the right panel from the Garching model [66]. 83

4.11 The expected average signal hit rate for the Garching model [105] at 10 kpc distance in a time binning of 2 ms. The left panel shows the expected response to a purely ν_e signal as coming from the deleptonization burst. Adding DOM noise and the main detection channel, inverse β-decay, this signal is no longer visible, as shown in the right panel. Detector noise adds about ±70 counts in each 2 ms bin. [66]. 84

4.12 ICECUBE signal response to quark star and black hole formation [66]. 84

4.13 Expected neutrino event rate for a 11.2, 20 and 27 $M_\odot$ progenitor SN model [54] flavor conversion. These models are (not yet) implemented in any signal response simulation of IceCube. These events rates have form the time dependent neutrino flux Φ_ν^{D} at the detector which has to be parametrized before being able to run the full simulation chain (USSR or sni3sim). 85

4.14 Detector response to SASI excitations of the 2-dimensional Garching model [63]. Two different equations of state were used (LS EoS: Lattimer-Swesty [117] and WH EoS: Wolff-Hillebrandt [173]). Signals emitted from the stellar North Pole are shown for comparison to the total emitted signals. 85

4.15 IceCube's detection significance as a function of distance assuming the Lawrence-Livermore model [113] and a stellar distribution following [174] for three different oscillation scenarios [66]. 86

4.16 Relevant rates of neutrino interactions for four different detection materials, water (a), scintillator (b), lead (c) and liquid argon (d), as a function of true neutrino energy. The interactions were computed according to the *SNOwGLoBES* software package [189] and assuming a GKVM (Gava-Kneller-Volpe-McLaughlin) supernova model [190] for the neutrino fluxes. Elastic scattering (ES) processes are present in all materials but lead. Inverse β decay (IBD) dominates water and scintillator based interactions of neutrinos at these energies. Neutral current (NC) interactions can be observed in all detectors except those based on liquid argon. 90

5.1 Block diagram of surface DAQ components involved in the HITSPOOL data stream, shown by the blue dashed line. Hits are copied to the DOMHubs hard disk from where files can be picked up to be sent to the Northern hemisphere via satellite. The default service for requesting HITSPOOL data transfer is SNDAQ via the HITSPOOL interface. 92

5.2 Diagram of HitSpool file buffer management on a DOMHubs hard disk. . . . 93

5.3 Average data load and standard deviation of all in-ice strings with respect to the Hits data stream. 93

5.4 Data flow diagram of services involved in the interface. Messaging between components is handled by the network messaging library ZeroMQ whereas local data transfer is realized with the data synchronization software rsync. A dedicated satellite data stream is in place for transferring the data to the users in the Northern hemisphere. 95

5.5 Messaging patterns in the interface. The bi-directional request-reply pattern (REQ-REP) connects any HitSpool data requester with the central publisher service of the interface. Any number of workers can connect to the latter via subscribing their socket to it (PUB-SUB). Monitoring messages from the Worker and Watcher components are pushed to I3Live (PUSH-PULL) or to the Sender node that is responsible for data compression and sending them to the Northern hemisphere. 97

5.6 Block-diagram of the higher-level processing steps for HitSpool data. . . . 99

5.7 Illustration of the spatial limits for hit clusters. Only hits inside these volumina can connect to one cluster [199]. The HiveSplitter settings, shown in c), are more advanced and tunable compared to the settings of TopologicalSplitter in b). 99

5.8 Sketch of the initiation, continuation and conclusion of a hit cluster generated from Cherenkov photons of an incident particle to illustrate the working principle of cluster algorithms used in data processing [199]. 100

5.9 Trigger rates for PFRaw, shown as lines and HitSpool data taken during the same time period, shown as dots. PFRaw data is the standard raw data type in IceCube after the online trigger system and before first processing and filtering. For HitSpool data, the triggers were applied offline. For all four trigger types, SMT3 in the top panel followed by SMT8, Volume and String trigger at the bottom, the HitSpool data offline trigger rates agree with the raw data in the 1 % deviation band of their trigger rates (colored bands). . . 102

6.1 Fluxes of nuclei of the primary cosmic radiation in particles per energy-per-nucleus [39]. 104

6.2 The all-particle spectrum as a function of E (energy-per-nucleus) from air shower measurements [39]. 104

6.3 Diagram of the possible evolutions of a cosmic ray air shower. 105

6.4 Simulated atmospheric muon event rate in IceCube by primary cosmic ray component [206]. 106

6.5 Average HLC hit rate from experimental data of each DOM representing the component of triggering atmospheric muons (DeepCore strings are excluded). On the left, the hit rate is shown as a function of depth for the individual DOMs whereas the average values per layer are shown on the right. 106

6.6 Atmospheric temperature profile at South Pole from two arbitrary days in the year 2014 [208]. 107

6.7 SMT8 trigger rate deviation from average $\Delta R_\mu / < R_\mu >$, (left y-axis and black dots) which correlates to the detection of atmospheric muons. The same oscillating behavior is also visible in the deviation of the effective temperature $\Delta T_{eff} / < T_{eff} >$, shown by the red line, as well as in SNDAQ's trigger rate, given by the blue line and the y-axis on the right. The temperature data was extracted following a method explained in Reference [207] on the basis of data from an instrument on NASA's AQUA satellite [209]. 108

6.8 Average noise rates for normal and high quantum efficiency DOMs in IceCube histogrammed and normalized. 109

6.9 Histogram of time differences between successive hits from HitSpool data of DOM 15-27 (blue) on a logarithmic scale in order to visualize the different noise components (without prepulses which are comparatively insignificant). . 110

6.10 Distribution of time differences between Hits in a DOM (blue line) and the exponential expectation for a Poissonian process fitted in the range 15 ms $<$ $\Delta t <$ 70 ms (green line). 110

6.11 Temperature profile of the ice cap at the South Pole [212]. 110

6.12 Noise rate in IceCube as a function of temperature, obtained from HitSpool data. Each data point represents the average of 12 DOM layers from 78 strings (DeepCore excluded). Atmospheric muon hits, see Figure 6.5, are subtracted. 111

6.13 Time sequence of hits on DOM 45-01. A number of noise clusters, caused by statistically correlated hits, are visible (blue corsses on top of each other). The Poisson expectation from a random 300 Hz noise rate is shown as green line. 112

6.14 Time interval between successive hits for all next-to-top layer DOMs (DeepCre excluded). 113

6.15 Total number of hits, $L \cdot F_L$, as a function of burst size L. 114

6.16 Total number of bursts F_L, i.e. the burst size distribution. 114

6.17 Time between first hits in successive bursts. 115

6.18 Burst Rate as a function of burst size L. 115

6.19 Average burst duration as a function of burst size L, burst cutoff value is 3 ms. 115

6.20 Average burst duration as a function of burst size L, burst cutoff value is 10 ms. 115

6.21 Inner interval duration distribution for burst of size $L = 9$ (left) and $L = 16$ (right). 116

6.22 Average burst size by temperature. 117

6.23 Average burst rate by temperature. 117

7.1 Diagram of the IceTray's simulation modules in the top part and their corresponding datatypes in the bottom part used to produce the studied data set (adapted from [172]). 122

7.2 Diagram of subthreshold and triggering muon identification via pulse mapping by recovering a priori knowledge from simulation, starting from the basic observable, the reconstructed pulse. 123

7.3 Event display of 2 ms accumulated time in IceCube from simulation. The red lines indicate the tracks of injected muons. The hit DOMs are visualized by spheres where their color indicates the time of the hit (red=early, blue=late) and their size the amount of charge deposited. The hits caused by atmospheric muons are buried under the majority of hits caused by noise. 124

7.4 The number of injected and detected primaries per 2 ms of data in simulation is shown in **(a)**. The latter can be separated into triggering primaries and primaries under the trigger threshold which is shown in **(b)**. 125

7.5 Number of pulses produced by atmospheric muons in the detector. 125

7.6 Deposited energy of triggered **(a)** and subthreshold **(b)** muon bundles as a function of their muon multiplicity N_μ. 126

7.7 The number of secondary muons from detected primaries that triggered the detector (blue line) and for those which passed the detector under the trigger threshold (green line). The total is given by the black line. 127

7.8 The true energy of detected primaries is shown in **(a)**. The deposited energy by the resulting muons in the detector is given in **(b)**. 127

7.9 Energy of triggered primary cosmic ray in relation to their deposited energy **(a)**. The situation for subthreshold primaries is given in **(b)**. 128

7.10 HLC and SLC pulses of triggered muons in**(a)** and subtrigger muons in **(b)**. . 129

7.11 Hit map of 8 s of simulation data for triggered (**a**) and subtrigger (**b**) muon hits for each DOM on in-ice strings as a function of depth. DeepCore strings are excluded. 130

7.12 Pulse distribution of triggering muons in **(a)** and subtrigger muons in **(b)** in cylindrical detector coordinates accumulated over 8 s of simulated data (same data as in Figure 7.11). Size and color of the tiles indicate the amount of pulses in the corresponding area. 130

7.13 Hit rate per 2 ms from simulation. By subtracting triggering muon hits from the total hit rate (blue histogram and blue fit line) one derives the untriggered hit rate (green histogram and green fit line) where the hits from subthreshold muons are still contained. Subtracting the latter uncovers the real noise rate (red histogram and fit line). 131

7.14 Diagram of muon identification via splitter algorithms as performed in higher level processing of simulation data and HitSpool data. 132

7.15 Fraction of pulses in hit cluster from HiveSplitter that are generated by associated primary cosmic ray, i.e. are caused by the corresponding atmospheric muons. Figure (**b**) shows a zoom in the low pulse region. 133

7.16 Same as Figure 7.15 for TopologicalSplitter: Fraction of pulses in hit cluster from TopologicalSplitter that are generated by associated primary cosmic ray, i.e. are caused by the corresponding atmospheric muons. Figure (**b**) shows a zoom in the low pulse region. 133

7.17 Cluster purity, i.e. the fraction of pulses originating from noise versus the components generated by muons, for pulses grouped by HiveSplitter in **(a)** and a zoom-in into the low region in **(b)**. 135

7.18 Same as Figure 7.17 for TopologicalSplitter. 135

7.19 Multiplicity of primaries represented in HiveSplitter's and TopologicalSplitter's hit clusters. 135

7.20 The number of total splits, i.e. hit clusters formed, per 2 ms by HiveSplitter (red) and TopologicalSplitter (black). The number of injected and detected primaries per 2 ms of data from Figure 7.4a are given as reference. 136

7.21 HLC versus SLC pulse contribution in hit clusters formed by HiveSplitter in **(a)** and a zoom into the low pulse region in **(b)**. 137

7.22 HLC versus SLC pulse contribution in hit clusters formed by TopologicalSplitter in **(a)** and a zoom into the low pulse region in **(b)**. 137

7.23 The number of detected primaries per 2 ms of simulation data versus their representation in HiveSplitter's hit clusters. 139

7.24 The number of detected primaries per 2 ms of simulation data versus their representation in topological-split hit clusters. 139

7.25 Fraction of identified primaries per 2 ms 140

7.26 Fraction of NoiseEngine results in agreement with simulation truth of the hit cluster being caused by noise or atmospheric muon. 140

7.27 Histogram of hit rate of all 5160 in-ice DOMs from 60 s of HitSpool data. The overall hit rate with corrections for muon tagged hits that have representations in triggers (green), those identified to possibly originate from subthreshold muons (red) and the total hit rate (blue). 143

7.28 Muon candidate hit rates, triggered (blue) and subtrigger (red), compared to the Simple Multiplicity Trigger hit rate (green) as well as all in-ice trigger hits (black). 144

8.1 Comparison of data binnings for the calculation of the significance for a certain analysis bin at time t_0. SNDAQ takes a total time-window of $\pm$300 s into account (blue) whereas for HitSpool data a symmetrical timewindow of $\pm$30 s (green) and an asymmetrical timewindow of $[-30\,\mathrm{s}, +60\,\mathrm{s}]$ (red) are constructed. 147

8.2 Comparison of trigger candidate significances reported by SNDAQ versus HitSpool results with symmetric analysis window (above)and asymmetric (below). . . . 149

8.3 Comparison of trigger candidate significances reported by SNDAQ versus HitSpool results with symmetrical analysis window (above) and asymmetrical (below). The values from HitSpool data, ξ_{HS} are corrected for triggering muon hits. 150

8.4 Comparison of significances of HitSpool data sets with triggering muon corrections versus subthreshold correction in symmetrical (above) and asymmetrical (below) analysis time windows. 153

8.5 HitSpool data lightcurve for candidate trigger from August 16th 2014 in bins of 1 ms, 2 ms, 0.5 s, 1.5 s, 4 s and 10 s. The binning in which SNDAQ reports the trigger is highlighted in red. 155

8.6 HitSpool data lightcurve (blue) for candidate trigger from 2014-08-16 in bins of 1 ms, 2 ms, 0.5 s, 1.5 s, 4 s and 10 s with an artificial deadtime applied to each hit in HitSpool data in order to be comparable with SNDAQ (green). The binning in which SNDAQ reports the trigger is highlighted in red. 157

8.7 HitSpool data lightcurve for candidate trigger from 2014-08-06 in bins of 1 ms, 2 ms, 0.5 s, 1.5 s, 4 s and 10 s with an artificial deadtime applied to each hit. Hits forming SMT8 triggers (green) and hits from all in-ice trigger types (blue) hits are subtracted. The binning in which SNDAQ reports the trigger is highlighted in red. 158

8.8 HitSpool data lightcurve for candidate trigger from August 16th 2014 in bins of 1 ms, 2 ms, 0.5 s, 1.5 s, 4 s and 10 s with an artificial deadtime applied to each hit. Triggering hits are identified and subtracted (blue line) as well as all subthreshold muon candidate hits (green line). 159

8.9 Images of the Earth facing side of the Sun taken by SDO in various optical filter band, shown in **(a)** and **(b)** as well as magnetic intensity in **(c)** and **(d)** around ten minutes prior to the supernova candidate trigger. 161

8.10 Position of the STEREO spacecrafts A and B during 2014-08-16 [230]. . . . 162

8.11 Pictures of the Sun taken by STEREO spacecrafts A and B more than one hour before our candidate [230]. 163

8.12 Pictures of the Sun taken by STEREO spacecrafts A and B eleven minutes prior to our supernova candidate trigger [230]. The CME is visible in the upper right corner of all pictures. 163

8.13 X-ray flus observed by GOES [235]. 164

A.1 Display of the data tree of scalers extracted from HitSpool data and stored in HDF5 tables. 176

B.1 Snapshot of the I3Live monitoring webpage displaying status reports of the HitSpool Interface 181

B.2 Details of the ZeroMQ patterns used in the HitSpool Interface 183

List of Tables

1.1 Best fit values (assuming a normal mass hierarchy) with 3σ band for neutrino oscillation parameters resulting from a global analysis of data from multiple experiments [14, 38, 39]. 12

1.2 Parameters A,B,C, and D from the total cross-section of relevant neutrino interaction with oxygen resulting from fits [64, 65] 20

1.3 Relevant reactions for low energy neutrinos in ice via inverse β-decay [52], electron scattering [60] and reaction on oxygen [61, 67, 68] with their signal fraction and corresponding uncertainty [66] assuming a normal mass hierarchy. 21

2.1 The various fusion stages of a massive star. With every next burning stage (from top down) the process becomes faster, hotter, denser and brighter [90] 28

2.2 Overview of main differences of thermonuclear and core-collapse supernovae. 31

2.3 Summary of spherical symmetry breaking instability processes in a core-collapse supernova ([122] and references therein). The convection-based instabilities are divided further by their region of appearance. 45

3.1 Readout modes of the IceCube Digital Optical Module [14]. 57

3.2 Minimum time differences between successive launches, i.e. deadtime, on a DOM Mainboard for all four possible readout sequences [145, 146]. 58

3.3 Trigger parameters and typical trigger rates [148]. 63

4.1 SNDAQ's rebinning and their physics motivation. 73

4.2 SNDAQ trigger levels and associated action to be taken. 75

4.3 Current supernova neutrino detectors and a selection of proposed and planned future experiments [35,175]. Detector types are abbreviated: Water Cherenekov = WCh, Scintillator = Sc, Liquid Argon = LAr. 87

5.1 HitSpool data request settings from SNDAQ. 98

6.1 Characteristics of noise components in IceCube DOMs, adapted from [210]. 109

7.1 Identification of detected (triggered or subthreshold) primaries via HiveSplitter and TopologicalSplitter in simulation. 141

7.2 NoiseEngine's result for hit clusters by HiveSplitter and TopologicalSplitter . 141

8.1 Summary of hit categories produced from HitSpool data. 146

8.2 Average reduction of HitSpool significance from scalers with deadtime to trigger hits correction per analysis timebase and timewindow 151

8.3 Average reduction of HitSpool significance from scalers with deadtime and trigger hits correction to subthreshold hits correction per analysis timebase and timewindow 151

8.4 Summary of supernova candidate triggers and their significances calculated by SNDAQ (its basic value and muon corrected if available) as well as retrieved from HitSpool data (in six different analyses). 154

A.1 HitSpool data processing from raw data to final level 173

A.2 Basic hit output of HitSpool data. The field names are listed in order of output. 174

A.3 Final hit information after muon identification stored in HDF5 hit tables. . . 175

A.4 Explanations for field names of scaler tables extracted form HitSpool data. 177

Bibliography

[1] Walter Baade and Fritz Zwicky. On super-novae. *Proceedings of the National Academy of Sciences of the United States of America*, 20(5):254, 1934.

[2] Walter Baade and Fritz Zwicky. Cosmic rays from super-novae. *Proceedings of the National Academy of Sciences of the United States of America*, 20(5):259, 1934.

[3] Adam S Burrows. Baade and zwicky:super-novae, neutron stars, and cosmic rays. *Proceedings of the National Academy of Sciences*, 112(5):1241–1242, 2015.

[4] A. Hewish and S. E. Okoye. Evidence for an Unusual Source of High Radio Brightness Temperature in the Crab Nebula. *Nature*, 207:59–60, July 1965.

[5] Markus Ackermann, M Ajello, A Allafort, L Baldini, J Ballet, G Barbiellini, MG Baring, D Bastieri, K Bechtol, R Bellazzini, et al. Detection of the characteristic pion-decay signature in supernova remnants. *Science*, 339(6121):807–811, 2013.

[6] BS Meyer, GJ Mathews, WM Howard, SE Woosley, and RD Hoffman. R-process nucleosynthesis in the high-entropy supernova bubble. *The Astrophysical Journal*, 399:656–664, 1992.

[7] The IceCube Collaboration. Evidence for high-energy extraterrestrial neutrinos at the icecube detector. *Science*, 342(6161):1242856, 2013.

[8] The IceCube Collaboration. Observation of high-energy astrophysical neutrinos in three years of icecube data. *Physical review letters*, 113(10):101101, 2014.

[9] Carlo Giunti and Chung W. Kim. *Fundamentals of Neutrino Physics and Astrophysics*. Oxford University Press, 2007.

[10] David Griffiths. *Introduction to elementary particles*. John Wiley & Sons, 2008.

[11] Kai Zuber. *Neutrino physics*. CRC Press, 2011.

[12] P. Hernandez. Neutrino physics. 2010.

[13] Vernon Barger, Danny Marfatia, and Kerry Lewis Whisnant. *The physics of neutrinos*. Princeton University Press, 2012.

[14] Juan Pablo Yáñez Garza. *Measurement of neutrino oscillations in atmospheric neutrinos with the IceCube DeepCore detector*. PhD thesis, 2014.

[15] ALEPH Collaboration, DELPHI Collaboration, L3 Collaboration, OPAL Collaboration, SID Collaboration, LEP Electroweak Working Group, et al. Precision electroweak measurements on the z resonance. *Physics Reports*, 427:257–454, 2006.

[16] Maurice Goldhaber, L Grodzins, and AW Sunyar. Helicity of neutrinos. *Physical review*, 109(3):1015, 1958.

[17] VN Aseev, AI Belesev, AI Berlev, EV Geraskin, AA Golubev, NA Likhovid, VM Lobashev, AA Nozik, VS Pantuev, VI Parfenov, et al. Upper limit on the electron antineutrino mass from the troitsk experiment. *Physical Review D*, 84(11):112003, 2011.

[18] Ch Kraus, B Bornschein, L Bornschein, J Bonn, B Flatt, A Kovalik, B Ostrick, EW Otten, JP Schall, Th Thümmler, et al. Final results from phase ii of the mainz neutrino mass searchin tritium decay. *The European Physical Journal C-Particles and Fields*, 40(4):447–468, 2005.

[19] Ch Weinheimer. Katrin, a next generation tritium β decay experiment in search for the absolute neutrino mass scale. *Progress in Particle and Nuclear Physics*, 48(1):141–150, 2002.

[20] Bruno Pontecorvo. Mesonium and antimesonium. *Zhur. Eksptl'. i Teoret. Fiz.*, 33, 1957.

[21] Y Fukuda, T Hayakawa, K Inoue, K Ishihara, H Ishino, S Joukou, T Kajita, S Kasuga, Y Koshio, T Kumita, et al. Solar neutrino data covering solar cycle 22. *Physical Review Letters*, 77(9):1683, 1996.

[22] M Altmann, M Balata, P Belli, E Bellotti, R Bernabei, E Burkert, C Cattadori, G Cerichelli, M Chiarini, M Cribier, et al. Gno solar neutrino observations: Results for gno i. *Physics Letters B*, 490(1):16–26, 2000.

[23] S Fukuda, Y Fukuda, M Ishitsuka, Y Itow, T Kajita, J Kameda, K Kaneyuki, K Kobayashi, Y Koshio, M Miura, et al. Determination of solar neutrino oscillation parameters using 1496 days of super-kamiokande-i data. *Physics Letters B*, 539(3):179–187, 2002.

[24] QR Ahmad, RC Allen, TC Andersen, JD Anglin, JC Barton, EW Beier, M Bercovitch, J Bigu, SD Biller, RA Black, et al. Direct evidence for neutrino flavor transformation from neutral-current interactions in the sudbury neutrino observatory. *Physical Review Letters*, 89(1):011301, 2002.

[25] Y Fukuda, T Hayakawa, E Ichihara, K Inoue, K Ishihara, H Ishino, Y Itow, T Kajita, J Kameda, S Kasuga, et al. Evidence for oscillation of atmospheric neutrinos. *Physical Review Letters*, 81(8):1562, 1998.

[26] Y Ashie, J Hosaka, K Ishihara, Y Itow, J Kameda, Y Koshio, A Minamino, C Mitsuda, M Miura, S Moriyama, et al. Evidence for an oscillatory signature in atmospheric neutrino oscillations. *Physical review letters*, 93(10):101801, 2004.

[27] MH Ahn, S Aoki, H Bhang, S Boyd, D Casper, JH Choi, S Fukuda, Y Fukuda, W Gajewski, T Hara, et al. Indications of neutrino oscillation in a 250 km long-baseline experiment. *Physical Review Letters*, 90(4):041801, 2003.

[28] P Adamson, DJ Auty, DS Ayres, C Backhouse, G Barr, M Betancourt, M Bishai, A Blake, GJ Bock, DJ Boehnlein, et al. Improved search for muon-neutrino to electron-neutrino oscillations in minos. *Physical Review Letters*, 107(18):181802, 2011.

[29] FP An, JZ Bai, AB Balantekin, HR Band, D Beavis, W Beriguete, M Bishai, S Blyth, K Boddy, RL Brown, et al. Observation of electron-antineutrino disappearance at daya bay. *Physical Review Letters*, 108(17):171803, 2012.

[30] JK Ahn, S Chebotaryov, JH Choi, S Choi, W Choi, Y Choi, HI Jang, JS Jang, EJ Jeon, IS Jeong, et al. Observation of reactor electron antineutrinos disappearance in the reno experiment. *Physical Review Letters*, 108(19):191802, 2012.

[31] KN Abazajian, E Calabrese, A Cooray, F De Bernardis, S Dodelson, A Friedland, GM Fuller, Steen Hannestad, BG Keating, EV Linder, et al. Cosmological and astrophysical neutrino mass measurements. *Astroparticle Physics*, 35(4):177–184, 2011.

[32] PAR Ade, N Aghanim, C Armitage-Caplan, M Arnaud, M Ashdown, F Atrio-Barandela, J Aumont, C Baccigalupi, AJ Banday, RB Barreiro, et al. Planck 2013 results. xxv. searches for cosmic strings and other topological defects. *arXiv preprint arXiv:1303.5085*, 2013.

[33] Paul AM Dirac. The quantum theory of the electron. *Proceedings of the Royal Society of London. Series A, Containing Papers of a Mathematical and Physical Character*, pages 610–624, 1928.

[34] Ettore Majorana. A symmetric theory of electrons and positrons. *Nuovo Cimento*, 14:171–184, 1937.

[35] Alexander Piégsa. *Supernova-Detektion mit dem IceCube-Neutrinoteleskop*. PhD thesis, Johannes Gutenberg-Universität Mainz, 2009.

[36] Ziro Maki, Masami Nakagawa, and Shoichi Sakata. Remarks on the unified model of elementary particles. *Progress of Theoretical Physics*, 28(5):870–880, 1962.

[37] J. Beringer et al. Review of particle physics. *Phys. Rev. D*, 86:010001, Jul 2012.

[38] Gian Luigi Fogli, E Lisi, A Marrone, D Montanino, A Palazzo, and AM Rotunno. Global analysis of neutrino masses, mixings, and phases: Entering the era of leptonic c p violation searches. *Physical Review D*, 86(1):013012, 2012.

[39] K.A. Olive et al. (Particle Data Group). The review of particle physics. *Chin. Phys. C , 38, 090001 (2014)*, 2014.

[40] L. Wolfenstein. Neutrino oscillations in matter. *Physical Review Letters D, 17:2369-2374*, 1978.

[41] SP Mikheev and A Yu Smirnov. Resonance amplification of oscillations in matter and spectroscopy of solar neutrinos. *Sov. J. Nucl. Phys.*, 42:1441–1448, 1986.

[42] Amol S Dighe, Mathias Th Keil, and Georg G Raffelt. Detecting the neutrino mass hierarchy with a supernova at icecube. *Journal of Cosmology and Astroparticle Physics*, 2003(06):005, 2003.

[43] AS Dighe, M Kachelriess, GG Raffelt, and R Tomas. Signatures of supernova neutrino oscillations in the earth mantle and core. *Journal of Cosmology and Astroparticle Physics*, 2004(01):004, 2004.

[44] P Reinartz and L Stodolsky. Neutrino masses and mixings in supernova bursts. *Zeitschrift für Physik C Particles and Fields*, 27(4):507–513, 1985.

[45] Amol S Dighe and Alexei Yu Smirnov. Identifying the neutrino mass spectrum from a supernova neutrino burst. *Physical Review D*, 62(3):033007, 2000.

[46] Huaiyu Duan, George M Fuller, J Carlson, and Yong-Zhong Qian. Simulation of coherent nonlinear neutrino flavor transformation in the supernova environment: Correlated neutrino trajectories. *Physical Review D*, 74(10):105014, 2006.

[47] GL Fogli, E Lisi, A Marrone, and A Mirizzi. Collective neutrino flavor transitions in supernovae: analytical and numerical aspects. In *Journal of Physics: Conference Series*, volume 120, page 052019. IOP Publishing, 2008.

[48] Huaiyu Duan, George M Fuller, J Carlson, and Yong-Zhong Qian. Coherent development of neutrino flavor in the supernova environment. *Physical review letters*, 97(24):241101, 2006.

[49] Huaiyu Duan, George M Fuller, J Carlson, and Yong-Zhong Qian. Neutrino mass hierarchy and stepwise spectral swapping of supernova neutrino flavors. *Physical review letters*, 99(24):241802, 2007.

[50] Huaiyu Duan, George M Fuller, J Carlson, and Yong-Zhong Qian. Analysis of collective neutrino flavor transformation in supernovae. *Physical Review D*, 75(12):125005, 2007.

[51] Gianluigi Fogli, Eligio Lisi, Antonio Marrone, and Alessandro Mirizzi. Collective neutrino flavor transitions in supernovae and the role of trajectory averaging. *Journal of Cosmology and Astroparticle Physics*, 2007(12):010, 2007.

[52] Alessandro Strumia and Francesco Vissani. Precise quasielastic neutrino/nucleon cross-section. *Physics Letters B*, 564(1):42–54, 2003.

[53] P Vogel and John F Beacom. Angular distribution of neutron inverse beta decay, $\nu_e + p \longrightarrow e^+ + n$. *Physical Review D*, 60(5):053003, 1999.

[54] I. Tamborra, G. Raffelt, F. Hanke, H.-T. Janka, and B. Mueller. Neutrino emission characteristics and detection opportunities based on three-dimensional supernova simulations. *ArXiv e-prints*, May 2014.

[55] Carlo Bemporad, Giorgio Gratta, and Petr Vogel. Reactor-based neutrino oscillation experiments. *Reviews of Modern Physics*, 74(2):297, 2002.

[56] Varley F Sears. Neutron scattering lengths and cross sections. *Neutron news*, 3(3):26–37, 1992.

[57] Hideki Watanabe, Haibing Zhang, K Abe, Y Hayato, T Iida, M Ikeda, J Kameda, K Kobayashi, Y Koshio, M Miura, et al. First study of neutron tagging with a water cherenkov detector. *Astroparticle Physics*, 31(4):320–328, 2009.

[58] Thomas Kowarik. *Supernova Neutrinos in AMANDA and IceCube - Monte Carlo Development and Data Analysis*. PhD thesis, Johannes Gutenberg-Universität Mainz, 2010.

[59] H. M. Childers and J. D. Graves. Bipartition angles for compton scattering by free electrons. *Phys. Rev.*, 99:343–345, Jul 1955.

[60] William J Marciano and Zohreh Parsa. Neutrino–electron scattering theory. *Journal of Physics G: Nuclear and Particle Physics*, 29(11):2629, 2003.

[61] E Kolbe, Karlheinz Langanke, and P Vogel. Estimates of weak and electromagnetic nuclear decay signatures for neutrino reactions in super-kamiokande. *Physical Review D*, 66(1):013007, 2002.

[62] WC Haxton and RGH Robertson. Solar neutrino interactions with 18 o in the superkamiokande water cerenkov detector. *Physical Review C*, 59(1):515, 1999.

[63] T. Griesel. *Optimierung des Nachweises von Supernovae in IceCube*. PhD thesis, Johannes-Gutenberg-Universität Mainz, 2010.

[64] Ricard Tomas, D Semikoz, Georg G Raffelt, M Kachelriess, and AS Dighe. Supernova pointing with low-and high-energy neutrino detectors. *Physical Review D*, 68(9):093013, 2003.

[65] Lukas Schulte. Supernova detection in a future extension of the icecube neutrino telescope. Master's thesis, JGU Mainz, 2011.

[66] The IceCube Collaboration. Icecube sensitivity for low-energy neutrinos from nearby supernovae. *Astronomy and Astrophysics*, 535:109, July 2011.

[67] WC Haxton and RGH Robertson. Solar neutrino interactions with 18 o in the superkamiokande water cerenkov detector. *Physical Review C*, 59(1):515, 1999.

[68] WC Haxton. Nuclear response of water cherenkov detectors to supernova and solar neutrinos. *Physical Review D*, 36(8):2283, 1987.

[69] Felix Bloch. Zur bremsung rasch bewegter teilchen beim durchgang durch materie. *Annalen der Physik*, 408(3):285–320, 1933.

[70] Hans Bethe. Bremsformel für elektronen relativistischer geschwindigkeit. *Zeitschrift für Physik*, 76(5-6):293–299, 1932.

[71] Stephen M Seltzer and Martin J Berger. Improved procedure for calculating the collision stopping power of elements and compounds for electrons and positrons. *The International Journal of Applied Radiation and Isotopes*, 35(7):665–676, 1984.

[72] Claus Grupen and Boris Shwartz. Particle detectors. *Particle Detectors, by Claus Grupen, Boris Shwartz, Cambridge, UK: Cambridge University Press, 2011*, 1, 2011.

[73] Edwin A Uehling. Penetration of heavy charged particles in matter. *Annual review of nuclear science*, 4(1):315–350, 1954.

[74] National Institute for Standards and Technology. Stopping power and range tables for electrons. http://physics.nist.gov/PhysRefData/Star/Text/ESTAR.html.

[75] John David Jackson. *Classical electrodynamics*, volume 3. Wiley, 1998.

[76] Boris Mikhailovich Bolotovskii. Vavilov-cherenkov radiation: its discovery and application. *Physics-Uspekhi*, 52(11):1099–1110, 2009.

[77] P. A. Cherenkov. Visible radiation produced by electrons moving in a medium with velocities exceeding that of light. *Phys. Rev.*, 52:378–379, Aug 1937.

[78] IETIM Frank and Ig Tamm. Coherent visible radiation from fast electrons passing through matter. *CR Acad. Sci. USSR*, 14:109–114, 1937.

[79] S Agostinelli, John Allison, K al Amako, J Apostolakis, H Araujo, P Arce, M Asai, D Axen, S Banerjee, G Barrand, et al. Geant4 -a simulation toolkit. *Nuclear instruments and methods in physics research section A: Accelerators, Spectrometers, Detectors and Associated Equipment*, 506(3):250–303, 2003.

[80] John Allison, K Amako, J Apostolakis, HAAH Araujo, P Arce Dubois, MAAM Asai, GABG Barrand, RACR Capra, SACS Chauvie, RACR Chytracek, et al. Geant4 developments and applications. *Nuclear Science, IEEE Transactions on*, 53(1):270–278, 2006.

[81] A. Unsöld and B. Baschek. *Der Neue Kosmos*. Springer verlag, Heidelberg-berlin, seventh edition edition, 2005.

[82] Hans-Thomas Janka. *Supernovae und kosmische Gammablitze*. Spektrum akademischer Verlag Heidelberg, 2011.

[83] Norbert S. Schulz. *The Formation and Early Evolution of Stars*. Springer-Verlag Berlin Heidelberg, 2012.

[84] Rudolf Kippenhahn, Alfred Weigert, and Achim Weiss. *Stellar structure and evolution*, volume 282. Springer, 1990.

[85] Donald D Clayton. *Principles of stellar evolution and nucleosynthesis*. University of Chicago press, 1968.

[86] M Schwarschild. *Structure and Evolution of the Stars*. Dover Publications, 1955.

[87] Wolfgang Demtröder. *Experimentalphysik 4*. Springer-Verlag Berlin Heidelberg New York, 2 edition, 2005.

[88] Hannu Karttunen, PEKKA KR, Heikki Oja, et al. *Fundamental astronomy*. Springer, 2007.

[89] Alexander Heger, C.L. Fryer, S.E. Woosley, N. Langer, and D.H. Hartmann. How massive single stars end their life. *Astrophys.J.*, 591:288–300, 2003.

[90] Stan Woosley and Thomas Janka. The physics of core-collapse supernovae. *Nature Physics*, 2006.

[91] S.E Woosley, A. Heger, and T. A. Weaver. The evolution and explosion of massive stars. *Review of Modern Physics*, 74:1015–1071, 2002.

[92] Hans Albrecht Bethe. Supernova mechanisms. *Reviews of Modern Physics*, 62(4):801, 1990.

[93] Evan O'Connor and Christian D. Ott. Black hole formation in failing core-collapse supernovae. *The Astrophysical Journal*, 730(2):70, 2011.

[94] H.-T. Janka, K. Langanke, A. Marek, G. Martínez-Pinedo, and B. Müller. Theory of core-collapse supernovae. 442:38–74, April 2007.

[95] Alexei V Filippenko. Optical spectra of supernovae. *Annual Review of Astronomy and Astrophysics*, 35(1):309–355, 1997.

[96] Bruno Leibundgut. Type ia supernovae. *The Astronomy and Astrophysics Review*, 10(3):179–209, 2000.

[97] Paolo A. Mazzali, Friedrich K. Ropke, Stefano Benetti, and Wolfgang Hillebrandt. A Common Explosion Mechanism for Type Ia Supernovae. *Science*, 315:825, 2007.

[98] Wolfgang Hillebrandt and Jens C. Niemeyer. Type Ia supernova explosion models. *Ann.Rev.Astron.Astrophys.*, 38:191–230, 2000.

[99] Friedrich Konrad Ropke and W. Hillebrandt. The Case against the progenitor's carbon - to - oxygen ratio as a source of peak luminosity variations in Type Ia supernovae. *Astron.Astrophys.*, 420:L1–L4, 2004.

[100] Vadim N Gamezo, Alexei M Khokhlov, and Elaine S Oran. Three-dimensional delayed-detonation model of type ia supernovae. *The Astrophysical Journal*, 623(1):337, 2005.

[101] S. Perlmutter and The Supernova Cosmology Project. Measurements of $omega$ and $lambda$ from 42 high-redshift supernovae. *The Astrophysical Journal*, 517(2):565, 1999.

[102] The Royal Swedish academy of Sciences. Scientific background on the nobel prize in physics 2011: The accelerating universe.

[103] S Wanajo, K Nomoto, H-T Janka, FS Kitaura, and B Müller. Nucleosynthesis in electron capture supernovae of asymptotic giant branch stars. *The Astrophysical Journal*, 695(1):208, 2009.

[104] Duligur Ibeling and Alexander Heger. The metallicity dependence of the minimum mass for core-collapse supernovae. *The Astrophysical Journal Letters*, 765(2):L43, 2013.

[105] L Hüdepohl, B Müller, H-T Janka, A Marek, and GG Raffelt. Neutrino signal of electron-capture supernovae from core collapse to cooling. *Physical review letters*, 104(25):251101, 2010.

[106] H.-T. Janka. Conditions for shock revival by neutrino heating in core-collapse supernovae. *Astronomy & Astrophysics*, 368:527–560, March 2001.

[107] H. A. Bethe and J. R. Wilson. Revival of a stalled supernova shock by neutrino heating. *Astrophysical Journal*, 295:14–23, August 1985.

[108] S. A. Colgate and R. H. White. The Hydrodynamic Behavior of Supernovae Explosions. *Astrophysical Joouranal*, 143:626, March 1966.

[109] S. E. Woosley, J. R. Wilson, G. J. Mathews, R. D. Hoffman, and B. S. Meyer. The r-process and neutrino-heated supernova ejecta. *Astrophysical Journal*, 433:229–246, September 1994.

[110] H.T. Janka, A. Burkert, H. Lesch, N. Heckmann, and H. Hetznecker. *Supernovae und kosmische Gammablitze: Ursachen und Folgen von Sternexplosionen*. Astrophysik aktuell. Spektrum Akademischer Verlag, 2011.

[111] M. Kachelriess, R. Tomàs, R. Buras, H.-Th. Janka, A. Marek, and M. Rampp. Exploiting the neutronization burst of a galactic supernova. *Phys. Rev. D*, 71:063003, Mar 2005.

[112] Mathias Th Keil, Georg G Raffelt, and Hans-Thomas Janka. Monte carlo study of supernova neutrino spectra formation. *The Astrophysical Journal*, 590(2):971, 2003.

[113] Totani. Future detection of supernova neutrino burst and explosion mechanism. *ApJ 496 216*, 1998.

[114] Ron Mayle and James R Wilson. Supernovae from collapse of oxygen-magnesium-neon cores. *The Astrophysical Journal*, 334:909–926, 1988.

[115] Stephen W Bruenn and Tamara Dineva. The role of doubly diffusive instabilities in the core-collapse supernova mechanism. *The Astrophysical Journal Letters*, 458(2):L71, 1996.

[116] R Buras, M Rampp, H-Th Janka, and K Kifonidis. Improved models of stellar core collapse and still no explosions: What is missing? *Physical Review Letters*, 90(24):241101, 2003.

[117] James M Lattimer and Douglas F Swesty. A generalized equation of state for hot, dense matter. *Nuclear Physics A*, 535(2):331–376, 1991.

[118] A Mezzacappa, AC Calder, SW Bruenn, JM Blondin, MW Guidry, MR Strayer, and AS Umar. An investigation of neutrino-driven convection and the core collapse supernova mechanism using multigroup neutrino transport. *The Astrophysical Journal*, 495(2):911, 1998.

[119] John M Blondin, Anthony Mezzacappa, and Christine DeMarino. Stability of standing accretion shocks, with an eye toward core-collapse supernovae. *The Astrophysical Journal*, 584(2):971, 2003.

[120] A Marek and H-Th Janka. Delayed neutrino-driven supernova explosions aided by the standing accretion-shock instability. *The Astrophysical Journal*, 694(1):664, 2009.

[121] Adam Burrows, Eli Livne, Luc Dessart, CD Ott, and Jeremiah Murphy. A new mechanism for core-collapse supernova explosions. *The Astrophysical Journal*, 640(2):878, 2006.

[122] Irene Tamborra, Florian Hanke, Hans-Thomas Janka, Bernhard Mueller, Georg G Raffelt, and Andreas Marek. Self-sustained asymmetry of lepton-number emission: A new phenomenon during the supernova shock-accretion phase in three dimensions. *arXiv preprint arXiv:1402.5418*, 2014.

[123] Wolfgang Keil, H-Thomas Janka, and Ewald Müller. Ledoux convection in protoneutron stars - a clue to supernova nucleosynthesis? *The Astrophysical Journal Letters*, 473(2):L111, 1996.

[124] Filippo Mannucci, M. Della Valle, N. Panagia, E. Cappellaro, G. Cresci, et al. The Supernova rate per unit mass. *Astron.Astrophys.*, 433:807–814, 2005.

[125] E CAPPELLARO, R EVANS, and M TURATTO. A new determination of supernova rates and a comparison with indicators for galactic star formation. *Astronomy and astrophysics*, 351(2):459–466, 1999.

[126] Claude-André Faucher-Giguere and Victoria M Kaspi. Birth and evolution of isolated radio pulsars. *The Astrophysical Journal*, 643(1):332, 2006.

[127] Roland Diehl, Hubert Halloin, Karsten Kretschmer, Giselher G Lichti, Volker Schönfelder, Andrew W Strong, Andreas Von Kienlin, Wei Wang, Pierre Jean, Jürgen Knödlseder, et al. Radioactive 26al from massive stars in the galaxy. *Nature*, 439(7072):45–47, 2006.

[128] L-S The, DD Clayton, R Diehl, DH Hartmann, AF Iyudin, MD Leising, BS Meyer, Y Motizuki, and V Schönfelder. Are 44ti-producing supernovae exceptional? *A&A*, 450:1037–1050, 2006.

[129] RM Bionta, G Blewitt, CB Bratton, D Casper, A Ciocio, R Claus, B Cortez, M Crouch, ST Dye, S Errede, et al. Observation of a neutrino burst in coincidence with supernova 1987a in the large magellanic cloud. *Physical Review Letters*, 58(14):1494, 1987.

[130] KS Hirata, T Kajita, M Koshiba, M Nakahata, Y Oyama, N Sato, A Suzuki, M Takita, Y Totsuka, T Kifune, et al. Observation in the kamiokande-ii detector of the neutrino burst from supernova sn1987a. *Physical Review D*, 38(2):448, 1988.

[131] EN Alexeyev, LN Alexeyeva, IV Krivosheina, and VI Volchenko. Detection of the neutrino signal from sn 1987a in the lmc using the inr baksan underground scintillation telescope. *Physics Letters B*, 205(2):209–214, 1988.

[132] P Challis. Esa/hubble archive. http:==www:spacetelescope:org=images=opo9808g=.

[133] H-T Janka and W Hillebrandt. Neutrino emission from type ii supernovae-an analysis of the spectra. *Astronomy and Astrophysics*, 224:49–56, 1989.

[134] Kei Kotake, Katsuhiko Sato, and Keitaro Takahashi. Explosion mechanism, neutrino burst and gravitational wave in core-collapse supernovae. *Reports on Progress in Physics*, 69(4):971, 2006.

[135] Ron Mayle, James R Wilson, and David N Schramm. Neutrinos from gravitational collapse. *The Astrophysical Journal*, 318(1):288–306, 1987.

[136] The IceCube Collaboration. Icecube preliminary design document. *URL http://www. icecube. wisc. edu/science/publications/pdd*, 2001.

[137] The IceCube Collaboration. Status of the icecube neutrino observatory. *New Astronomy Reviews*, 48(5):519–525, 2004.

[138] The IceCube Collaboration. The design and performance of icecube deepcore. *Astroparticle physics*, 35(10):615–624, 2012.

[139] The IceCube Collaboration. Measurement of the atmospheric neutrino energy spectrum from 100 gev to 400 tev with icecube. *Physical Review D*, 83(1):012001, 2011.

[140] The IceCube Collaboration. Icetop: The surface component of icecube. *Nuclear Instruments and Methods in Physics Research Section A: Accelerators, Spectrometers, Detectors and Associated Equipment*, 700:188–220, 2013.

[141] The IceCube Collaboration. Observation of cosmic-ray anisotropy with the icetop air shower array. *The Astrophysical Journal*, 765(1):55, 2013.

[142] The IceCube Collaboration. The icecube data acquisition system: Signal capture, digitization, and timestamping. *Nuclear Instruments and Methods in Physics Research Section A: Accelerators, Spectrometers, Detectors and Associated Equipment*, 601(3):294 – 316, 2009.

[143] The IceCube Collaboration. Calibration and characterization of the icecube photomultiplier tube. *Nucl. Instrum. Meth.*, A618:139–152, 2010.

[144] K. J. Ma, W. G. Kang, J. K. Ahn, S. Choi, Y. Choi, M. J. Hwang, J. S. Jang, E. J. Jeon, K. K. Joo, H. S. Kim, J. Y. Kim, S. B. Kim, S. H. Kim, W. Kim, Y. D. Kim, J. Lee, I. T. Lim, Y. D. Oh, M. Y. Pac, C. W. Park, I. G. Park, K. S. Park, S. S. Stepanyan, and I. Yu. Time and amplitude of afterpulse measured with a large size photomultiplier

tube. *Nuclear Instruments and Methods in Physics Research A*, 629:93–100, February 2011.

[145] Thorsten Stezelberger. Icecube domapp firmware timing. `https://docushare.icecube.wisc.edu/dsweb//Get/Document-28424/DOMAPPtiming.pdf`, April 2007.

[146] The IceCube Collaboration. Internal Documentation on DOM MainBoard Release 443. `https://wiki.icecube.wisc.edu/index.php/Effects_of_DOM_Mainboard_Release_443`.

[147] The IceCube DAQ Group. Icecube DAQ Review (icecube internal documentation). https://docushare.icecube.wisc.edu/dsweb/View/Collection-9045, 2010.

[148] John Kelley for the IceCube Collaboration. Event triggering in the icecube data acquisition system 1. In *IProceedings of the VLVnT Workshop (Stockholm, Sweden)*, 2013.

[149] Pieter Hintjens. *ZeroMQ: Messaging for Many Applications*. " O'Reilly Media, Inc.", 2013.

[150] M. Casier. *Study of short Gamma Ray Bursts with the IceCube Neutrino Observatory*. PhD thesis, Vrije Universiteit Brussel, 2015.

[151] The Icecube Collaboration. Internal documentation on the IceTray module "WaveCalibrator". *http://code.icecube.wisc.edu/svn/projects/WaveCalibrator/*.

[152] Nathan Whitehorn. *A Search for High-Energy Neutrino Emission from Gamma-Ray Bursts*. PhD thesis, 2012.

[153] The IceCube Collaboration. Energy Reconstruction Methods in the IceCube Neutrino Telescope. *JINST*, 9:P03009, 2014.

[154] VJ Stenger. Track fitting for dumand-ii octagon array. *University of Hawaii at Manoa*, 1990.

[155] The IceCube Collaboration. Muon track reconstruction and data selection techniques in amanda. *Nuclear Instruments and Methods in Physics Research Section A: Accelerators, Spectrometers, Detectors and Associated Equipment*, 524(1):169–194, 2004.

[156] The IceCube Collaboration. Improvement in fast particle track reconstruction with robust statistics. *Nuclear Instruments and Methods in Physics Research Section A: Accelerators, Spectrometers, Detectors and Associated Equipment*, 736:143–149, 2014.

[157] The IceCube Collaboration. Observation of the cosmic-ray shadow of the moon with icecube. *Physical Review D*, 89(10):102004, 2014.

[158] The IceCube Collaboration. Search for supernova neutrino bursts with the amanda detector. *Astroparticle Physics*, 16(4):345–359, 2002.

[159] The IceCube Collaboration. An improved data acquisition system for supernova detection with IceCube. *Proceedings of the 33rd Internation Cosmic Ray Conference*, September 2013.

[160] Volker Baum. The icecube data acquisition system for galactic core collapse supernova searches. *Proceedings of the VLVnT 2013*, 2014.

[161] Volker Baum. Verbesserung der supernova-detektion mit dem icecube-neutrinoteleskop. Master's thesis, Johannes Gutenberg-Universität Mainz, 2011.

[162] NPX-Designs John Jacobsen. A vision for an integrated icecube live system. IceCube Internal Document, march 2008.

[163] NPX-Designs John Jacobsen. http://live.icecube.wisc.edu, 2014.

[164] Pietro Antonioli, Richard Tresch Fienberg, Fabrice Fleurot, Yoshiyuki Fukuda, Walter Fulgione, Alec Habig, Jaret Heise, Arthur B McDonald, Corrinne Mills, Toshio Namba, et al. Snews: The supernova early warning system. *New Journal of Physics*, 6(1):114, 2004.

[165] The IceCube Collaboration. Optical properties of deep glacial ice at the south pole. *Journal of Geophysical Research: Atmospheres (1984–2012)*, 111(D13), 2006.

[166] IceCube Collaboration, M. G. Aartsen, R. Abbasi, Y. Abdou, M. Ackermann, J. Adams, J. A. Aguilar, M. Ahlers, D. Altmann, J. Auffenberg, and et al. Measurement of South Pole ice transparency with the IceCube LED calibration system. 2013.

[167] The IceCube Collaboration. The IceCube Neutrino Observatory Part VI: Ice Properties, Reconstruction and Future Developments. 2013.

[168] RC Bay, RA Rohde, PB Price, and NE Bramall. South pole paleowind from automated synthesis of ice core records. *Journal of Geophysical Research: Atmospheres (1984–2012)*, 115(D14), 2010.

[169] Johan Lundberg, P Miočinović, K Woschnagg, T Burgess, J Adams, S Hundertmark, P Desiati, and P Niessen. Light tracking through ice and water: Scattering and absorption in heterogeneous media with photonics. *Nuclear Instruments and Methods in Physics Research Section A: Accelerators, Spectrometers, Detectors and Associated Equipment*, 581(3):619–631, 2007.

[170] Claudio Kopper. Performance studies for the km3net neutrino telescope. *Nuclear Instruments and Methods in Physics Research Section A: Accelerators, Spectrometers, Detectors and Associated Equipment*, 692:188–191, 2012.

[171] Claudio Kopper. clsim. https://github.com/claudiok/clsim, January 2015.

[172] Benedikt Riedel. *Modeling and Understanding Supernova Signals in the IceCube Neutrino Observatory*. PhD thesis, University of Wisconsin - Madison, 2014.

[173] Wolfgang Hillebrandt, K Nomoto, and RG Wolff. Supernova explosions of massive stars-the mass range 8 to 10 solar masses. *Astronomy and Astrophysics*, 133:175–184, 1984.

[174] John N Bahcall and Tsvi Piran. Stellar collapses in the galaxy. *The Astrophysical Journal*, 267:L77–L81, 1983.

[175] K. Scholberg. Supernova Neutrino Detection. *Annual Review of Nuclear and Particle Science*, 62:81–103, November 2012.

[176] Motoyasu Ikeda, Atsushi Takeda, Y Fukuda, MR Vagins, K Abe, T Iida, K Ishihara, J Kameda, Y Koshio, A Minamino, et al. Search for supernova neutrino bursts at super-kamiokande. *The Astrophysical Journal*, 669(1):519, 2007.

[177] S Fukuda, Y Fukuda, T Hayakawa, E Ichihara, M Ishitsuka, Y Itow, T Kajita, J Kameda, K Kaneyuki, S Kasuga, et al. The super-kamiokande detector. *Nuclear Instruments and Methods in Physics Research Section A: Accelerators, Spectrometers, Detectors and Associated Equipment*, 501(2):418–462, 2003.

[178] Kirk Bays, Super-Kamiokande Collaboration, et al. Supernova relic neutrinos at super-kamiokande. In *Journal of Physics: Conference Series*, volume 375, page 042037. IOP Publishing, 2012.

[179] Ranjan Laha and John F Beacom. Gadolinium in water cherenkov detectors improves detection of supernova ν e. *Physical Review D*, 89(6):063007, 2014.

[180] N Yu Agafonova, M Aglietta, P Antonioli, G Bari, A Bonardi, VV Boyarkin, G Bruno, W Fulgione, P Galeotti, M Garbini, et al. On-line recognition of supernova neutrino bursts in the lvd. *Astroparticle Physics*, 28(6):516–522, 2008.

[181] M Aglietta, P Antonioli, G Bari, C Castagnoli, W Fulgione, P Galeotti, PL Ghia, P Giusti, E Kemp, AS Malguin, et al. Effects of neutrino oscillations on the supernova signal in lvd. *Nuclear Physics B-Proceedings Supplements*, 110:410–413, 2002.

[182] N.Y. Agafonova, M. Aglietta, P. Antonioli, V.V. Ashikhmin, G. Bari, et al. Implication on the core collapse supernova rate from 21 years of data of the Large Volume Detector. 2014.

[183] R. V. Novoseltseva, M. M. Boliev, I. M. Dzaparova, M. M. Kochkarov, S. P. Mikheyev, Y. F. Novoseltsev, V. B. Petkov, P. S. Striganov, G. V. Volchenko, V. I. Volchenko, and A. F. Yanin. Search for neutrino bursts from core collapse supernovae at the Baksan Underground Scintillation Telescope. *ArXiv e-prints*, October 2009.

[184] Basudeb Dasgupta and John F Beacom. Reconstruction of supernova ν_μ, ν_τ, $\overline{\nu}_\mu$, and $\overline{\nu}_\tau$ neutrino spectra at scintillator detectors. *Physical Review D*, 83(11):113006, 2011.

[185] CA Duba, F Duncan, J Farine, A Habig, A Hime, RGH Robertson, K Scholberg, T Shantz, CJ Virtue, JF Wilkerson, et al. Halo–the helium and lead observatory for supernova neutrinos. In *Journal of Physics: Conference Series*, volume 136, page 042077. IOP Publishing, 2008.

[186] D. Väänänen and C. Volpe. The neutrino signal at HALO: learning about the primary supernova neutrino fluxes and neutrino properties. *Journal of Cosmology and Astroparticle Physics*, 10:19, October 2011.

[187] C Rubbia, M Antonello, P Aprili, B Baibussinov, M Baldo Ceolin, L Barzè, P Benetti, E Calligarich, N Canci, F Carbonara, et al. Underground operation of the icarus t600 lar-tpc: first results. *Journal of Instrumentation*, 6(07):P07011, 2011.

[188] Ines Gil Botella and A. Rubbia. Oscillation effects on supernova neutrino rates and spectra and detection of the shock breakout in a liquid argon TPC. *JCAP*, 0310:009, 2003.

[189] Kate Scholberg. Supernova observations with globes. http://www.phy.duke.edu/schol/snowglobes.

[190] Jerome Gava, James Kneller, Cristina Volpe, and GC McLaughlin. Dynamical collective calculation of supernova neutrino signals. *Physical review letters*, 103(7):071101, 2009.

[191] K Abe, T Abe, H Aihara, Y Fukuda, Y Hayato, K Huang, AK Ichikawa, M Ikeda, K Inoue, H Ishino, et al. Letter of intent: The hyper-kamiokande experiment—detector design and physics potential—. *arXiv preprint arXiv:1109.3262*, 2011.

[192] Michael Wurm, John F Beacom, Leonid B Bezrukov, Daniel Bick, Johannes Blümer, Sandhya Choubey, Christian Ciemniak, Davide D'Angelo, Basudeb Dasgupta, Alexander Derbin, et al. The next-generation liquid-scintillator neutrino observatory lena. *Astroparticle Physics*, 35(11):685–732, 2012.

[193] The IceCube-PINGU Collaboration. Letter of intent: The precision icecube next generation upgrade (pingu). *arXiv preprint arXiv:1401.2046*, 2014.

[194] L. Demiroers, M. Ribordy, and M. Salathe. Novel technique for supernova detection with icecube. *ArXiv e-prints*, June 2011.

[195] Marco Salathe. Novel search methodology for supernovae with icecube. Master's thesis, Laboratory of High Energy Physics Ecole Polytechnique F?d?rale de Lausanne, 2011.

[196] D. Heereman, K. Hanson, M. Labare, and N. van Eijndhoven. Study of noise HLC hits in DeepCore. *IceCube Internal report*, February 2011.

[197] J. Sopher, D. Williams, and J. Stezelberger. IceCube Internal Documentation: Delta Compressor data format and processes. `https://docushare.icecube.wisc.edu/dsweb/Get/Document-20568`, May 2008.

[198] Various Authors. The fabric library for python. `http://www.fabfile.org/`.

[199] Marcel Zoll. *Preparations for the next solar WIMP Analysis with IceCube: Advances in simulation, filtering, event topology identification and analysis approach*. Licentiate thesis, Stockholm Universitet, Fysikum, February 2014.

[200] D. Chirkin and Ch. Weaver. Topologicalsplitter. `code.icecube.wisc.edu/svn/projects/TopologicalSplitter/`, 2012.

[201] Olaf Schulz. *The design study of IceCube DeepCore: Characterization and veto studies*. PhD thesis, Max-Planck Institute für Kernphysik, 2010.

[202] M Larson. Simulation and identification of non-Poissonian noise triggers in the IceCube Neutrino Detector. Master's thesis, University of Alberta, 2013.

[203] Carl Wernhoff. An FPGA implementation of neutrino track detection for the IceCube telescope. Master's thesis, Stockolms Universiteit, Linköpings Tekniska Högskola, 2010.

[204] CORSIKA Homepage. `https://web.ikp.kit.edu/corsika/`.

[205] Thomas K. Gaisser, Todor Stanev, and Serap Tilav. Cosmic Ray Energy Spectrum from Measurements of Air Showers. *Front.Phys.China*, 8:748–758, 2013.

[206] Berghaus, P. for the IceCube Collaboration. Characterization of the atmospheric muon flux in IceCube. *submitted to Astrophisical Journal*, to be published, 2015.

[207] Desiati et al. Seasonal atmospheric variations and K/π ratio. *Proceedings of the 32nd ICRC, BEIJING 2011*, November 2011.

[208] National Oceanic and Atmospheric Administration . South Pole, Antarctica Balloon-Borne Ozonesonde Profile Measurment Program. http://www.esrl.noaa.gov/gmd/ozwv/ozsondes/spo.html.

[209] National Aeronautics and Space Administration. http://airs.jpl.nasa.gov.

[210] Nick Stanisha. Characterization of low-dt non-poisson noise in the icecube neutrino detector. Master's thesis, THE PENNSYLVANIA STATE UNIVERSITY SCHREYER HONORS COLLEGE, 2014.

[211] The Amanda Collaboration. Light emission in amanda pressure spheres. *Amanda Internal Report*, 2003.

[212] P Buford Price, Oleg V Nagornov, Ryan Bay, Dmitry Chirkin, Yudong He, Predrag Miocinovic, Austin Richards, Kurt Woschnagg, Bruce Koci, and Victor Zagorodnov. Temperature profile for glacial ice at the south pole: Implications for life in a nearby subglacial lake. *Proceedings of the National Academy of Sciences*, 99(12):7844–7847, 2002.

[213] HO Meyer. Dark rate of a photomultiplier at cryogenic temperatures. *arXiv preprint arXiv:0805.0771*, 2008.

[214] H. O. Meyer. Spontaneous electron emission from a cold surface. *EPL (Europhysics Letters)*, 89(5):58001, 2010.

[215] D. Chirkin. Fluxes of Atmospheric Leptons at 600 GeV - 60 TeV. *ArXiv High Energy Physics - Phenomenology e-prints*, July 2004.

[216] Dmitry Chirkin and Wolfgang Rhode. Muon monte carlo: a high-precision tool for muon propagation through matter. *arXiv preprint hep-ph/0407075*.

[217] J-H Koehne, Katharina Frantzen, Martin Schmitz, Tomasz Fuchs, Wolfgang Rhode, D Chirkin, and J Becker Tjus. Proposal: A tool for propagation of charged leptons. *Computer Physics Communications*, 184(9):2070–2090, 2013.

[218] S Flis and Ch. Weaver. DOMLauncher IceTray Project. http://code.icecube.wisc.edu/svn/projects/DOMLauncher/.

[219] Marcel Zoll. MCPulseSeparator. http://code.icecube.wisc.edu/svn/sandbox/mzoll/MCPulseSeparator/.

[220] Daniele Fargion. Detecting solar neutrino flares and flavors. *JHEP*, 0406:045, 2004.

[221] GE Kocharov, GA Kovaltsov, and IG Usoskin. Solar flare neutrinos. *Il Nuovo Cimento C*, 14(4):417–422, 1991.

[222] G. de Wasseige, P. Evenson, K. Hanson, N. van Eijndhoven, and K.-L. Klein. Evaluation of expected solar flare neutrino events in the IceCube observatory. *Proceeding of the 34th International Cosmic Ray Conference*, 2015.

[223] JK Rowley, BT Cleveland, and R Davis Jr. Chlorine solar neutrino experiment. 1984.

[224] John N Bahcall. Solar flares and neutrino detectors. *Physical review letters*, 61(23):2650, 1988.

[225] ME Machado, EH Avrett, JE Vernazza, and RW Noyes. Semiempirical models of chromospheric flare regions. *The Astrophysical Journal*, 242:336–351, 1980.

[226] V. Kurt, B. Yushkov, and V. Grechnev. The onset time of the pion-decay gamma-ray emission of major solar flares. *Proceesings of the 32nd International Cosmic Ray Conference , Bejing 2011*, 2011.

[227] G. de Wasseige, K. Hanson, N. van Eijndhoven, P. Evenson, and K. L. Klein. On the detection of neutrinos from solar flares using pion-decay photons to provide a time window template. 2015.

[228] National Aeronautics and Space Administration. SDO: The Solar Dynamics Observatory. `http://sdo.gsfc.nasa.gov/`.

[229] National Aeronautics and Space Administration. Stereo Mission. `http://stereo.gsfc.nasa.gov/`.

[230] National Aeronautics and Space Administration. Stereo Science Center. `http://stereo-ssc.nascom.nasa.gov/`.

[231] The Fermi LAT Collaboration. The Fermi Large Area Telescope. `http://www-glast.stanford.edu/`.

[232] National Aeronautics and Space Administration. Fermi Solar Flare X-Ray and Gamma-Ray Observations. `http://hesperia.gsfc.nasa.gov/fermi_solar/`.

[233] National Oceanic and Atmospheric Administration (NOAA). `http://www.goes.noaa.gov/goesfull.html`.

[234] National Oceanic and Atmospheric Administration (NOAA). GOES XRAY events for 2014. `http://hesperia.gsfc.nasa.gov/goes/`, Januar 2015.

[235] National Aeronautics and Space Administration. Reuven Ramaty High Energy Solar Spectroscopic Imager (RHESSI). `http://hesperia.gsfc.nasa.gov/rhessi3/`.

[236] M Salathe, M Ribordy, and L Demiroers. Novel technique for supernova detection with icecube. *Astroparticle Physics*, 35(8):485–494, 2012.

[237] The IceCube Collaboration. The IceCube Neutrino Observatory VI: Neutrino Oscillations, Supernova Searches, Ice Properties. *Proceeding of the 32nd International Cosmic Ray Conference, Bejing, China*, 2011.

[238] for the IceCUbe Collaboration Ronald Bruijn. Supernova detection in icecube: Status and future. *Nuclear Physics B Proceedings Supplemenet 00 (2012) 1-3*, 2012.

[239] DR Lorimer, Matthew Bailes, MA McLaughlin, DJ Narkevic, and Froney Crawford. A bright millisecond radio burst of extragalactic origin. *Science*, 318(5851):777–780, 2007.

[240] LG Spitler, JM Cordes, JWT Hessels, DR Lorimer, MA McLaughlin, S Chatterjee, F Crawford, JS Deneva, VM Kaspi, RS Wharton, et al. Fast radio burst discovered in the arecibo pulsar alfa survey. *The Astrophysical Journal*, 790(2):101, 2014.

[241] Heino Falcke and Luciano Rezzolla. Fast radio bursts: the last sign of supramassive neutron stars. *Astronomy & Astrophysics*, 562:A137, 2014.

[242] A. Perego, Stephan Rosswog, Ruben M. Cabezón, Oleg Korobkin, Roger Käppeli, et al. Neutrino-driven winds from neutron star merger remnants. *Mon.Not.Roy.Astron.Soc.*, 443(4):3134–3156, 2014.

[243] MARTIN J REES. A better way of searching for black-hole explosions? *Nature*, 266(5600):333–334, 1977.

[244] The IceCube Collaboration. First observation of pev-energy neutrinos with icecube. *Physical review letters*, 111(2):021103, 2013.

[245] Joachim Kopp, Jia Liu, and Xiao-Ping Wang. Boosted dark matter in icecube and at the galactic center. *Journal of High Energy Physics*, 2015(4):1–31, 2015.

[246] J. Va'vra. Molecular excitations: a new way to detect Dark matter. *ArXiv e-prints*, February 2014.

[247] David N. Spergel. Motion of the earth and the detection of weakly interacting massive particles. *Phys. Rev. D*, 37:1353–1355, Mar 1988.

[248] K. Hanson and D. Heereman. Basic Scripts for HitSpool Data Decoding. `http://code.icecube.wisc.edu/svn/sandbox/dheereman/HitSpoolScripts/build/`.

[249] Ch. Weaver. HitSpool Reader. `http://code.icecube.wisc.edu/svn/sandbox/cweaver/hitspool-reader/`.

[250] D. Heereman. HitSpool Data Mass Processing. `http://code.icecube.wisc.edu/svn/sandbox/dheereman/HsMassProcess/`.

[251] David Heereman. Processing of HITSPOOL type Simulation Data . `http://code.icecube.wisc.edu/svn/sandbox/dheereman/HsSimProcess/`.

[252] David Heereman. Processing of HITSPOOL Data for Supernova. `http://code.icecube.wisc.edu/svn/sandbox/dheereman/HsLightcurveProcess/`.